Mechanosensitive ion channels: from membrane mechanics to channel structural dynamics

Author:
Bavi, Navid

Publication Date:
2017

DOI:

License:

Mechanosensitive Ion Channels: From Membrane Mechanics to Channel Structural Dynamics

Navid Bavi

A Submission to the Faculty of Medicine,
University of New South Wales for the Degree of

Doctor of Philosophy

June 2017

THE UNIVERSITY OF NEW SOUTH WALES

Thesis/Dissertation Sheet

Surname or Family name: **Bavi**

First name: **Navid**

Abbreviation for degree as given in the University calendar: **PhD**

School: **St Vincent's Clinical School**   Faculty: **Medicine**

Title: **Mechanosensitive Ion Channels: From Membrane Mechanics to Channel Structural Dynamics**

Lipid bilayers of cellular membranes play a key role in modulation of membrane proteins, particularly mechanosensitive (MS) channels. Thus, it is imperative to characterise their mechanical properties. In Chapter 2, a novel conceptual framework is introduced, based on excised patch fluorometry. This framework includes a new hyper-elastic model, which is superior to existing models at describing the overall behaviour of lipid bilayers. Importantly, my computational data illustrates that, contrary to the widely-used Laplace's equation that manifests in uniform tension across the membrane, tension is heterogeneous throughout the liposome patch. Here, I describe another significant finding, that there is a substantial difference in tension between the outer and inner monolayers of the lipid bilayer in an excised patch configuration that is absent in cell-attached configuration. These results highlight the need for caution against extrapolation of MS channel behaviour from one patch configuration to another.

In chapter 3, I explore the MS channel structural dynamics building upon my previous findings from chapter 2. Specifically, a multidisciplinary approach was used involving both experimental and computation methods to study the gating cycle of MscL in response to membrane tension. It has unequivocally been shown that the intracellular amphipathic N-terminal helix of MscL is a crucial mechanosensing element that acts as a linker between membrane dynamics and conformational changes to the channel protein. Such intracellularly located horizontal force-coupling helices may represent an important conserved structural entity that underlies mechanosensitivity of most currently known MS channels.

In Chapter 4, I characterise the MscL mechanical properties as a protein scaffold using molecular dynamics (MD) simulation. The Young's modulus of the alpha-helices of Mycobacterium MscL and E. coli MscL was calculated to be between 0.2 and 12.5 GPa. Finally, results from extensive steered MD simulations demonstrate that constant-force method is more reliable than constant-velocity method for measuring Young's moduli of alpha-helices.

Overall, this study advances our understanding of the basic physical principles underlying mechanotransduction on both cellular and molecular levels.

FOR OFFICE USE ONLY   Date of completion of requirements for Award:

Copyright Statement

'I hereby grant the University of New South Wales or its agents the right to archive and to make available my thesis or dissertation in whole or part in the University libraries in all forms of media, now or here after known, subject to the provisions of the Copyright Act 1968. I retain all proprietary rights, such as patent rights. I also retain the right to use in future works (such as articles or books) all or part of this thesis or dissertation. I also authorise University Microfilms to use the 350 word abstract of my thesis in Dissertation Abstract International (this is applicable to doctoral theses only). I have either used no substantial portions of copyright material in my thesis or I have obtained permission to use copyright material; where permission has not been granted I have applied/will apply for a partial restriction of the digital copy of my thesis or dissertation.'

Signed

Date   2/7/2017

Authenticity Statement

'I certify that the Library deposit digital copy is a direct equivalent of the final officially approved version of my thesis. No emendation of content has occurred and if there are any minor variations in formatting, they are the result of the conversion to digital format.'

Signed

Date   2/7/2017

Originality Statement

'I hereby declare that this submission is my own work and to the best of my knowledge it contains no materials previously published or written by another person, or substantial proportions of material which have been accepted for the award of any other degree or diploma at UNSW or any other educational institution, except where due acknowledgement is made in the thesis. Any contribution made to the research by others, with whom I have worked at UNSW or elsewhere, is explicitly acknowledged in the thesis. I also declare that the intellectual content of this thesis is the product of my own work, except to the extent that assistance from others in the project's design and conception or in style, presentation and linguistic expression is acknowledged.'

Signed

Date   2/7/2017

Acknowledgment

First, I thank the almighty God for providing me the opportunity to step into the amazing world of science and granting me the capability to explore a tiny portion of the universe and its mysteries.

This PhD study would not be possible without the assistance and guidance of several wonderful people. I would therefore like to sincerely thank all of them.

Prof. Boris Martinac, my supervisor, my sincere thanks to you for giving me the honour to be your Ph.D student. I appreciate your constant encouragements, unconditional support and insightful guidance along with critical comments during the whole period of my PhD. Especially for your trust that made me - who came from an engineering background - confident to pursue my studies in mechanobiology discipline.

I also express my deep thanks to my co-supervisors **Dr Adam Hill** and **Prof. Qinghua Qin** for their help, insightful discussions, offering valuable advice and for your warm support.

I sincerely thank my friend and mentor **Dr Charles D Cox**, for his advice, intellectual discussions and his willing assistance with various problems at all times, especially for teaching me several "wet lab" techniques including patch-clamp electrophysiology. I also thank him for critically reading this thesis.

I would also like to express my gratitude and deepest appreciation to my lovely friends, first Miss Suzy Hur, for her intellectual and spiritual support as well as lots of incredible life and science wisdoms. Abolghasem Hedayatkhah, Yury Nikolaev, Paul R Rohde, Pietro Ridone, Dr Yoshitaka Nakayama, Maki Nakayama, Saeideh Ebrahimkhani, Hananeh Fonoudi, Nona Farbehi, Justin Szot, Dr Shaista Shaikh, Dr Kadla Rosholm, Adam D Martinac, Dr Louise Dunn, Dr Di Zhang, Dr Hafizah Hamid, Dr Cacang Suarna, Noushin Nasiri, Nastran Nemati, Leila Khanjani and Haleh Allameh Haeri, thank you all for your help in various ways. You have been my family here in Australia and I will never forget the excellent time that we had together. All the Martinac lab members and all Victor Chang (VCCRI) staff, thank you very much for making the atmosphere of our working environment as friendly as possible.

I cannot finish without thanking my family in Iran. I warmly thank and appreciate my parents for their material and spiritual support in all aspects of my life. I also would like to thank my brothers and sisters, especially Sina and Omid for their support and assistance in numerous ways. Omid, I cannot thank you enough for teaching me how to do Molecular Dynamics simulation in addition to several fruitful collaborations that we have had to date.

Navid Bavi,
Darlinghurst, Sydney NSW 2010

Abstract

Lipid bilayers of cellular membranes play a key role in modulation of membrane proteins, particularly mechanosensitive (MS) channels. Thus, it is imperative to characterise their mechanical properties. In Chapter 2, a novel conceptual framework is introduced, based on excised patch fluorometry. This framework includes a new hyper-elastic model, which is superior to existing models at describing the overall behaviour of lipid bilayers. Importantly, my computational data illustrates that, contrary to the widely-used Laplace's equation that manifests in uniform tension across the membrane, tension is heterogeneous throughout the liposome patch. Here, I describe another significant finding, that there is a substantial difference in tension between the outer and inner monolayers of the lipid bilayer in an excised patch configuration that is absent in cell-attached configuration. These results highlight the need for caution against extrapolation of MS channel behaviour from one patch configuration to another. In chapter 3, I explore the MS channel structural dynamics building upon my previous findings from chapter 2. Specifically, a multidisciplinary approach was used involving both experimental and computation methods to study the gating cycle of MscL in response to membrane tension. It has unequivocally been shown that the intracellular amphipathic N-terminal helix of MscL is a crucial mechanosensing element that acts as a linker between membrane dynamics and conformational changes to the channel protein. Such intracellularly located horizontal force-coupling helices may represent an important conserved structural entity that underlies mechanosensitivity of most currently known MS channels.

In Chapter 4, I characterize the MscL mechanical properties as a protein scaffold using molecular dynamics (MD) simulation. The Young's modulus of the alpha-helices of

Mycobacterium tuberculosis MscL and *E. coli* MscL channels was calculated to be between 0.2 and 12.5 GPa. Finally, results from extensive steered MD simulations demonstrate that constant-force method is more reliable than constant-velocity method for measuring Young's moduli of alpha-helices.

Overall, this thesis advances our understanding of the basic physical principles underlying mechanotransduction on both cellular and molecular levels.

TABLE OF CONTENTS

LIST OF FIGURES

Publications, honors and awards arising from this thesis

HONOURS, AWARDS & FUNDING

- Young Scientists' Travel Award from the 19th International Union of Pure and Applied Biophysics (IUPAB) 2017 (800 €).
- Chicago Fellowship, University of Chicago (2 years from December 2017).
- Gibson / Cox Prize for Best Student Poster Presentation at 2017 Gage Conference on Ion Channels and Transporters
- Finalist for the Young Biophysicist Award (YBA), ASB/AuPS 2016 Australia.
- Australian Physiological Society and Australian Society for Biophysics (AUPS/ASB) joint meeting 2016-Student Travel Award ($200)
- International Travel Award for the 60th US Biophysical Meeting, 2016 ($750)
- Australian Society for Biophysics Meeting, Student Travel Award, 2015 ($100)
- Finalist for the Thomson Prize at Sydney Protein Group meeting (December 2014)
- Student Winner of Paul Korner Seminar Series (Faculty Choice), Victor Chang Cardiac Research Institute (December 2014)
- Postgraduate Research Support Scheme Travel Fund, 2014 ($2100)
- Australian Society for Biophysics Meeting, Student Travel Award, 2013 ($200)
- Victor Chang Cardiac Research Institute Top up Scholarship (2013)
- The University of New South Wales Postgraduate Award (UIPA, 2013)

NATIONAL AND INTERNATIONAL CONFERENCES

- 2017 Gage Conference on Ion Channels & Transporters, Canberra, Australia "Surface tension differentially modulates mechanosensitive ion channels" (**Poster**).
- 61st Biophysical Society Meeting, New Orleans, USA 2017, "Perturbation of bilayer surface tension differentially modulates mechanosensitive ion channels" (**Poster**).
- Australian Physiological Society and Australian Society for Biophysics (AUPS/ASB) joint meeting 2016, Adelaide, Australia, "Perturbation of bilayer surface tension differentially modulates mechanosensitive ion channels" (**Oral**).

● The 24th annual St Vincent's Campus Research Symposium, 2016, "Structural dynamics of MscL C-terminal domain" (**Poster**).

● 60th Biophysical Society Meeting, LA, USA. 2016, "The N-terminal helix acts as a dynamic membrane coupler in the gating cycle of the mechanosensitive channel MscL" (**Poster**).

● Australian Society for Biophysics (ASB) meeting 2015, Armidale, Australia, "The N-terminal helix acts as a dynamic membrane anchor in the gating cycle of a mechanosensitive channel" (**Poster**).

● The 23rd annual St Vincent's Campus Research Symposium, 2015, "The membrane anchoring role of the N-terminal helix in the gating of the mechanosensitive channel MscL" (**Fast Forward talk & Poster**).

● Participation in the 2015 Gage Conference on Ion Channels & Transporters.

● Mechanosensory Transduction Satellite-IUPAB 2014, Gold Coast, Australia, "The effect of lipid bilayer on gating of mechanosensitive ion channels" (**Oral**)

● The 5th International Conference on Nanostructures (ICNS5), 2014, Kish Island, Iran, "Finite Element Simulation and Patch Fluorometry of Azolectin Lipid Vesicles" (**Poster**).

● Australian Society for Biophysics (ASB) meeting 2013, Melbourne, Australia, "Mechanical properties of Azolectin liposomes examined by Patch fluorometry and Finite element modeling" (**Oral**).

● The 4th International Conference on Smart Materials and Nanotechnology in Engineering SMN2013, Gold Coast, Australia, "Finite element simulation of the gating mechanism of mechanosensitive ion channels" (**Oral**).

ORIGINAL RESEARCH ARTICLES

1. Martinac, Adam D., **Navid Bavi,** Omid Bavi and Boris Martinac. " Turning MscL into a magnetically-triggered nanovalve: A computational study", _Plos One_ (Under review).

2. **Bavi, Navid**, Adam D. Martinac, Marien D. Cortes, Omid Bavi, Adam P. Hill, Takeshi Nomura, Boris Martinac, and Eduardo Perozo. "Structural Dynamics of MscL C-terminal Domain", _Scientific Reports_ (Under review).

3. Nakayama, Yoshitaka, Kosuke Komazawa, **Navid Bavi**, Kazuhiro Nobata, Ken-ichi Hashimoto, Hisashi Kawasaki, Boris Martinac. "Electrophysiological characterization of mechanosensitive channels in the native membrane using Corynebacterium glutamicum giant spheroplasts" _Nature Microbiology_ (In preparation).

4. Nakayama, Yoshitaka, Radomir Slavchov, **Navid Bavi**, Martinac, Boris, "The energy of liposome patch adhesion to the pipette glass determined by confocal

fluorescence microscopy" *Journal of Physical Chemistry Letters* 7, no. 22 (2016): 4530-4534.

5. **Bavi, Navid**, Omid Bavi, Manoucher Vossoughi, Reza Naghdabadi, Adam P. Hill, Boris Martinac, and Yousef Jamali. "Nanomechanical properties of MscL alpha helices: A steered molecular dynamics study." *Channels* 11(3): 209-223, DOI: 10.1080/19336950.2016.1249077.

> ***New & Views*** on this article by Anishkin, Andriy, and Sergei Sukharev. "Channel disassembled: Pick, tweak, and soak parts to soften." Channels (2017): 1-3

6. **Bavi, Navid**, D. Marien Cortes, Charles D. Cox, Paul R. Rohde, Weihong Liu, Joachim W. Deitmer, Omid Bavi et al. "The role of MscL amphipathic N terminus indicates a blueprint for bilayer-mediated gating of mechanosensitive channels." *Nature Communications* 7 (2016).

> ***Autocommentary*** on this article by **Bavi, Navid**, Charles D. Cox, Eduardo Perozo, and Boris Martinac. "Toward a structural blueprint for bilayer-mediated channel mechanosensitivity." Autocommentary *Channels* 7 (2016): 1-3.

7. Nomura, Takeshi, Charles D. Cox, **Navid Bavi**, Masahiro Sokabe, and Boris Martinac. "Unidirectional incorporation of a bacterial mechanosensitive channel into liposomal membranes." *The FASEB Journal* 29, no. 10 (2015): 4334-4345.

8. **Bavi, Navid**, Yoshitaka Nakayama, Omid Bavi, Charles D. Cox, Qing-Hua Qin, and Boris Martinac. "Biophysical implications of lipid bilayer rheometry for mechanosensitive channels." *Proceedings of the National Academy of Sciences* 111, no. 38 (2014): 13864-13869.

REVIEW ARTICLES

9. Battle, Andrew R., Pietro Ridone, **Navid Bavi**, Yoshitaka Nakayama, Yury A. Nikolaev, and Boris Martinac. "Lipid–protein interactions: Lessons learned from stress." *Biochimica et Biophysica Acta (BBA)-Biomembranes* 1848, no. 9 (2015): 1744-1756.

10. **Bavi, Navid**, Charles D. Cox, Eduardo Perozo, and Boris Martinac. "Toward a structural blueprint for bilayer-mediated channel mechanosensitivity." Autocommentary *Channels* 11, no. 2 (2017): 91-93.

11. Cox, Charles D.*, **Navid Bavi***, and Boris Martinac. "Bacterial mechano-sensors." *Annual Review of Physiology* (Under review). * Equal first author contribution.

PROCEEDINGS

12. **Bavi, Navid.**, Qinghua. Qin, and Boris Martinac, "Finite element simulation of the gating mechanism of mechanosensitive ion channels." *International Society for Optics and Photonics*, (2013).

13. Bavi, Omid, Manochehr Vosoughi, **Navid Bavi,** and Yousef Jamali, " Investigation of Local Curvature and Lateral Pressure Profile in Mechanosensitive Ion Channels", In: Proceedings of the 21st Annual (International) Conference on Mechanical Engineering, 2013, K. N. Toosi University of Technology, Tehran, Iran.

14. **Bavi, Navid**, Yoshitaka Nakayama, Qinghua. Qin, Omid Bavi and Boris Martinac, " Finite Element Simulation and Patch Fluorometry of Azolectin Lipid Vesicles", In: Proceedings of the 5th International Conference in Nanostructures (ICNS5), 2014, Kish Island, Iran.

15. Bavi, O., **Navid Bavi**, Manochehr Vosoughi, Reza Naghdabadi, and Yousef Jamali, "Water screening effects on the mechanical properties of TM1 alpha helix of *E. coli*_MscL studied by steered molecular dynamic" In: Proceedings of the 6th International Conference in Nanostructures (ICNS6), 2016, Kish Island, Iran.

BOOK CHAPTERS

16. Cox, Charles D., **Navid Bavi**, and Boris Martinac. "Origin of the Force: The Force-From-Lipids Principle Applied to Piezo Channels." *Current Topics in Membranes* (2016).

17. **Bavi, Navid**, Yury Nikolaev,…, and Boris Martinac. "Principles of mechano-sensing at the membrane interface." *Springer Series in Biophysics* (In Press).

ABSTRACTS

● **Bavi, Navid**, Charles D. Cox, Omid Bavi, and Boris Martinac. "Perturbation of Bilayer Surface Tension Differentially Modulates Mechanosensitive Ion Channels." *Biophysical Journal* 112, no. 3 (2017): 416a.

● Cox, Charles D., Chai Ann Ng, **Navid Bavi**, and Boris Martinac. "Mechanically-Induced Gating in PKD2L1 (Trpp2): Calcium-Induced Activation Masquerading as Force Sensitivity?." *Biophysical Journal* 112, no. 3 (2017): 311a.

● Nakayama, Yoshitaka, Kosuke Komazawa, **Navid Bavi**, Ken-ichi Hashimoto, Hisashi Kawasaki, and Boris Martinac. "Electrophysiological Characterization of Mechanosensitive Channels in the Native Membrane of *Corynebacterium Glutamicum*." *Biophysical Journal* 112, no. 3 (2017): 534a.

● Martinac, Adam D., **Navid Bavi**, Marien D. Cortes, Omid Bavi, Takeshi Nomura, Boris Martinac, and Eduardo Perozo. "Structural Dynamics of the MSCL C-Terminal Domain." *Biophysical Journal* 112, no. 3 (2017): 413a.

● **Bavi, Navid**, et al. "The N-Terminal Helix Acts as a Dynamic Membrane Coupler in the Gating Cycle of the Mechanosensitive Channel MscL." *Biophysical Journal* 110.3 (2016).

● **Bavi, Navid**, et al. "The N-Terminal Domain Acts as an Anchor during the Gating Cycle of MscL." *Biophysical Journal* 108.2, (2015).

● **Bavi, Navid**, et al. "Gating Mechanism of Mechanosensitive Ion Channels Studied by Continuum Mechanics." *Biophysical Journal* 106.2 (2014): 554a-555a.

CHAPTER 1

1. Introduction

1.1   Mechanotransduction

Mechanotransduction refers to the processes through which living cells sense and respond to mechanical stimuli by converting them into electrochemical signals that in turn elicit specific cellular responses [1]. In bacteria and plants, mechanotransduction is mainly involved in osmoregulation and gravitropism. In mammals, it is involved in a variety of processes including cellular differentiation, cell migration, anoikis, and a complex repertoire of sensory systems such as the sensation of touch, sound, acceleration, and fluctuations in blood pressure [1-15].

1.1.1   Mechanotransduction in bacteria

While numerous studies have focused on the effects of mechanical cues (e.g., fluid flow and surface mechanics) on mammalian cells [16-18], those in bacteria remain largely underexplored. Microbiologists have predominantly focused on the effects of chemical cues on bacterial behaviour. However, a subject of considerable importance lies in the fact that most bacteria grow and adapt to various surfaces (e.g. biofilms) and mechanical environments. In this sense, various types of stress such as those caused by

fluid flow, cell-cell cohesion and cell-surface adhesion are equally influential features governing bacterial physiology [19].

Moreover, unlike the majority of cell types in multicellular organisms, bacteria are regularly subjected to changes in environmental osmolarity [20,21]. As a result of a reduction in external osmolarity, high membrane tension can develop in the inner membrane. If left unchecked, this can exceed the lytic tension of the cell membrane. [1,22-24]. Thus, the osmosensory mechanisms controlling membrane-based K^+ transporters, transcriptional regulators, osmoprotectant transporters, and mechano-sensitive (MS) channels have been under intense investigation over the past few decades. In bacteria, MS channels belonging to the mechanosensitive channel families of large conductance (MscL) and small conductance (MscS) are critical for protection of bacterial cells from hypo-osmotic shock [25]. These ion channels are pore-forming membrane proteins that gate in response to mechanical force and allow ions and other osmolytes to flow across the cell membrane. When external osmolarity suddenly decreases (transfer to medium of low osmolarity, i.e., hypo-osmotic shock), water inflow causes a substantial increase in the cellular turgor pressure, which may cause cell lysis. Here, MS channels form a major path for osmolyte efflux and the release of turgor pressure [24,26-30]. This allows bacteria to survive dramatic osmotic down-shocks (such shocks can generate 20-30 atm of pressure) [23,24] by transducing a potentially lethal physical stress into a timely cellular response (**Figure 1**).

Given that there are no other known mechanotransducers in bacteria, bacterial MS channels present an excellent tool for studying the basic principles of mechanosensory transduction. Mechanosensitive ion channels, as molecules of mechanosensory transduction, are discussed in detail in section 1.2.
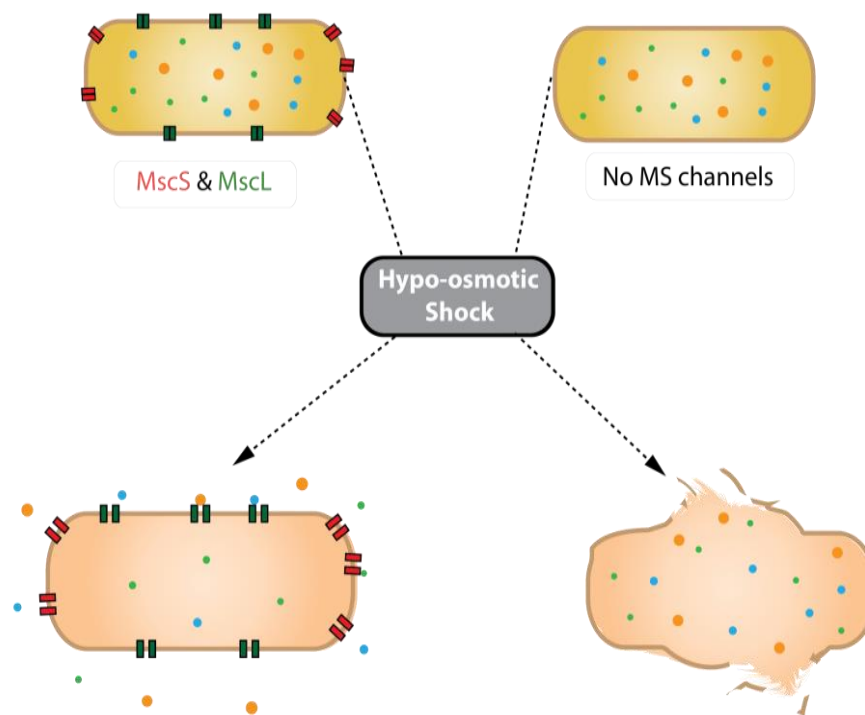
Figure 1. MscL and MscS act as pressure safety valves in bacterial cells. After osmotic downshock, the wild-type *E. coli* cells expand quickly as a result of water influx into the cells causing the cell membrane to stretch to the extent sufficient to activate MscS and MscL channels. Hypo-osmotic shock assay carried out on mutants of *E. coli* lacking MscS and MscL shows that MS channels are designed to open before the cell lysis due to excessive turgor pressure [26,31].

1.1.2   Mechanotransduction in eukaryotes

Mechanotransduction is well-documented in various eukaryotic cellular processes, including cellular differentiation, sensory processes and structural behavior at different length scales [16,17,32,33]. It is well known that eukaryotic cells respond to various forms of mechanical force as part of normal physiology and homeostasis. For example, red blood cells undergo morphological changes when passing through the small diameter of blood capillaries [34-37]; cartilage cells regulate gene expression in response to hydrostatic pressures and fluid shear forces [38], and vascular endothelial cells (ECs) undergo structural remodeling and direct molecular signaling of pro-inflammatory and proliferative pathways in response to mechanical stimuli associated with circulatory pressure and flow (**Figure 2**) [38-42]. In addition, there are pathophysiological force cues (usually with higher

stress values compared to normal physiological cues), that may modulate cellular activity in various organs.
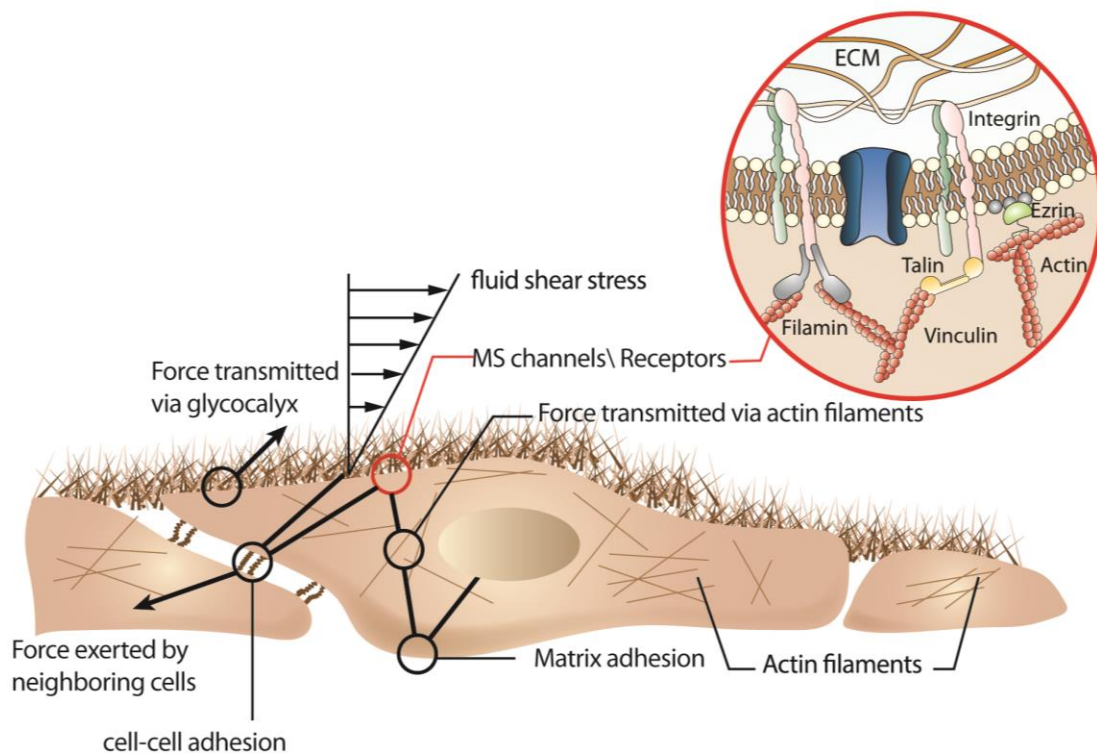
Figure 2. Forces sensed by vascular endothelial cells. Various types of force transmission pathways in endothelial cells including extracellular and cytoskeletal elements, cell-cell adhesions, cell matrix adhesions and MS channels (modified from Mofrad and Kamm 2006 [18] and Cox et al. 2016 [43]).

Eukaryotic cells sense diverse mechanical cues via different types of "mechanosensors". Mechanosensors described in this thesis are structures that link external mechanical stimuli at the cell surface to intracellular signalling events and downstream effectors during mechanotransduction. There are three main known mechanosensors in eukaryotes: (i) those formed by invagination or bulging of the cell membrane (e.g., caveolae, microvilli, and possibly cilia), (ii) intra- or extracellular elements such as integrins, a cadherin rich cell-cell junction and (iii) mechanosensitive ion channels. Mechanosensor-driven pathways often involve positive/negative feedback regulation in response to different cell-type specific stimuli (**Figure 3**) [17]. For example, cells can exhibit different behaviors such as stress stiffening (reinforcement), fluidization through cytoskeletal re-organization in

response to different mechanical stimuli (both magnitude and type) and thus transmission/amplification or dissipation of mechanical forces [44]. This could be a mechanism for several cellular processes such as cell migration or structural remodeling akin to what happens in an artery under high blood pressure [45,46].
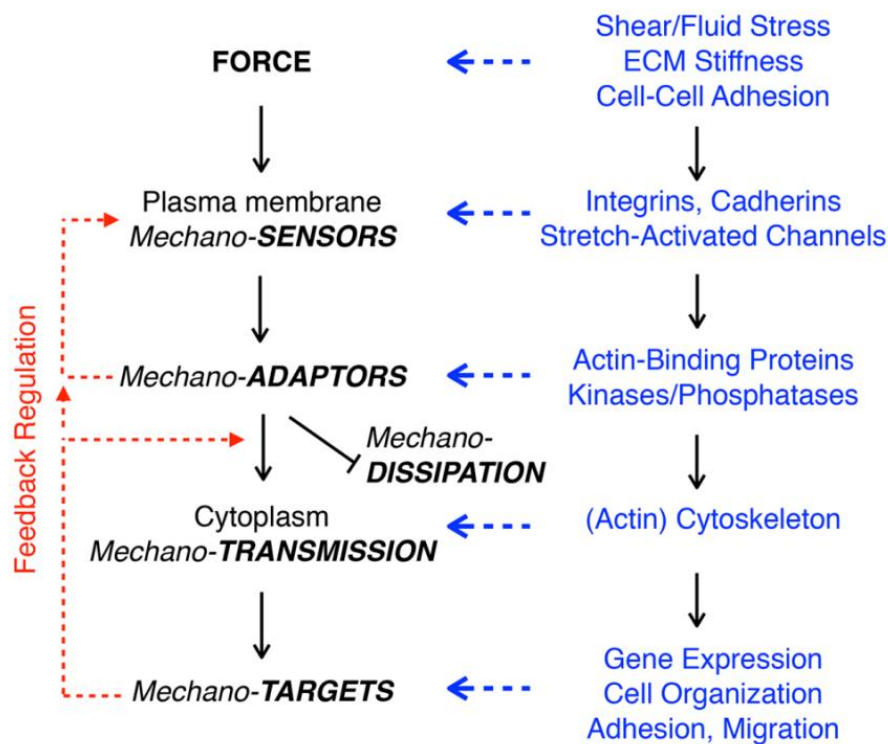
Figure 3. Pathways linking mechanical force at the cell surface to intracellular signalling and downstream effectors. *Left:* External force is detected by mechano-sensors in the plasma membrane, which is linked to extra- and intracellular adaptors that transmit mechanical signals to targets in the cell. These pathways may exhibit positive/negative feedback regulation. *Right:* Examples of processes and proteins involved in each step (adapted with permission from Pruitt et al. 2014 [17]).

Among the aforementioned mechanosensors, MS channels are known to be the fastest mechanotransducers by responding to mechanical stimuli on sub-millisecond time scales [5,47]. MS channels can serve as both sensors and effectors (i.e., mechano-adaptors and -transmitters) as they modify the membrane potential of the cell by mediating a flux of specific ions, such as Ca^{2+}, across the plasma membrane [5,47,48]. Ca^{2+} influx through MS channel activation may in turn be coupled to gene regulation through a myriad of pathways e.g. calcium/calmodulin-dependent pathways [49]. Unlike MS channels, mechanotransduction through other cellular mechanotransducers occur over longer

time scales (e.g., ~1s), such as Src activation in response to localized mechanical stress [50]. That is why as the fastest mechanotransducers, MS channels are ubiquitously present in rapid mechanotransduction loci such as somatosensory neurons.

1.2 Mechanosensitive ion channels: structure, function and gating paradigms

MS channels are involved in numerous physiological processes including osmoregulation (in plants and bacteria), hearing, touch and pain sensation (somatosensation), cell volume and blood flow regulation [5,6,12,51-57].

Classification of MS channels from the other types of ion channels, based on the stimulus type (e.g., mechanical force) is not trivial. This is given that the function of many membrane proteins, which are not known as classical mechanosensors, can also be modulated by the application of mechanical force [58-60]. Nevertheless, with respect to the degree of sensitivity to mechanical force, a mechanical spectrum can be envisioned on which all channels reside from highly sensitive (e.g., TWIK Related Arachidonic Acid K channel, TRAAK) to almost insensitive (Two-pore Domain Weak Inward Rectifying K Channel, TWIK-1). **Figure 4** shows a continuum for channel mechanosensitivity based on previous patch-clamp electrophysiology data [43]. It should be considered that a mechanical stimulus does not elicit the same response in all channels. For instance, a channel may display increased sensitivity towards either membrane stretch or curvature, as demonstrated for *E. coli* (Ec)MscL versus *M. tuberculosis* (Mt)MscL [61]. Moreover, it has been shown that Piezo1 channels can be activated by membrane stretch applied via a high speed pressure clamp as well as stimulation of the cell-substrate interface, while TRPV4 is activated only when the cell-substrate is locally stimulated [62].
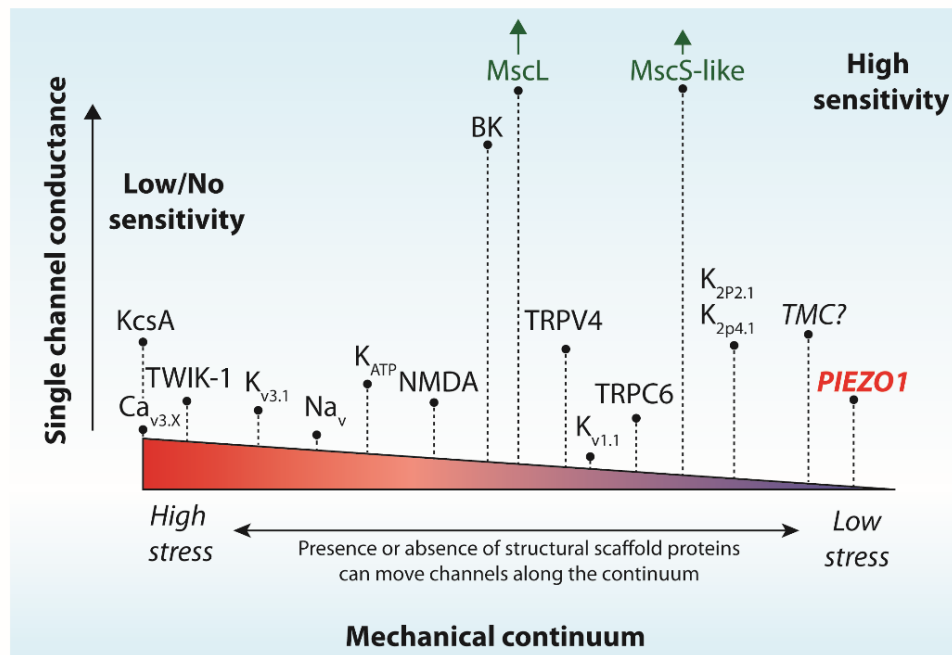
Figure 4. Ion channels sensitivity to mechanical force probed by the patch-clamp technique. All ion channels can be placed on a stress continuum from highly sensitive (e.g., Piezo1) to those that are almost insensitive to mechanical stress (e.g., KcsA). Several factors such as presence or absence of extracellular/intracellular network and experimental paradigm (i.e., stimulus type) may shift channels along the continuum. Note that it is still unknown whether transmembrane-like channels (TMCs) are pore forming channels (see [53,63]; adapted with permission from Cox et al. 2016 [43]).

With all these complexities, if most integral membrane proteins can be modulated by mechanical stimuli, what characteristics constitute a mechanosensitive channel? The presently used criteria for defining whether achannel's mechanosensitivity is physiologically relevant are as follows [64]:

 i. *Localization:* The channel must be broadly expressed in the relevant specialized mechanosensory cells and localized at the correct position within the cell (e.g., Piezo2 in Merkel cells).

ii. *Function:* The channel must be the primary mechanosensor that elicits the initial electrical response of the sensory cell. It is best to be able to modulate channel function (e.g., activation, kinetics and inhibition) by introducing genetic mutations.

iii. *'Mimicry':* When the putative MS channel is expressed in heterologous expression systems, in culture or reconstituted in lipid bilayers, the channel current should largely recapitulate the properties of the native channel current. Such properties include conductance, kinetics, activation by agonists, inhibition by antagonists, and

in particular ion selectivity. It is possible that some of the channel characteristics such as activation threshold are modulated by the change in the physico-chemical properties of the cell membrane.

iv. *Mechanosensitivity:* mechanical force (alone) should activate the channel under the similar conditions used to determine 'mimicry'.

Nevertheless, it should be noted that only a few known MS channels fulfil these criteria, mainly due to the practical challenges associated with examining all these factors for an MS channel candidate.

MS channels are present in both eukaryotic and prokaryotic kingdoms. In prokaryotes, there are two main MS channel families, namely MscL-like and MscS-like channels. MscL-like channels are mostly found in bacterial cells. Although MscL homologues have been identified in some fungi (e.g., Neurospora), fungus-like organisms (Phytophthora), and Archaea (e.g., Methanosarcina) [65]. In *E. coli,* as a representative bacterial species, there are seven MS channels (one MscL-like and six MscS –like channels) that can be distinguished based on their conductance, selectivity and sensitivity to membrane tension. The channels belonging to the MscS-like family are found in cell-walled eukaryotes such as fungi and plants and eukaryotic parasites such as *Plasmodium* [5].

Bacterial MS channels cab also be classified according to their conductance, namely MscM (M for mini), MscS (S for small) and MscL (L for large) [1,66]. MscM (a member of MscS-like family) has a conductance of ~ 200-370 pS and is cation selective [1,66-68]; MscS conductance is ~ 1 nS and is weakly anion selective; MscL conductance is ~ 3 nS and nonselective. MscS channels are distinguishable from MscL channels as their activation threshold is lower than the activation threshold of MscL channels.

The presence of MS channels is not limited to bacteria, Archaea, fungus and plants. Thus far, four families of channel proteins have been implicated in mechanosensation in vertebrates and invertebrates, animals including: DEG/ENaC proteins, the Transient Receptor Potential (TRP) proteins (NOMPC, and the heat sensitive TRPV1, TRPV2 and TRPV4 receptors) [57,69-71], the two-pore-domain K^+ channel (K_{2P}) proteins and most recently Piezo channels [72-76]. Despite this, the evidence for TRPV1 and TRPV2 being primary mechanotransducers is less conclusive than for the other MS channels [5,43].

Each individual MS channel has its specific structure and hence differentially interacts with its surrounding (i.e. lipids, extracellular matrix and cytoskeleton). Among all known MS channels, we have structural information regarding the molecular architecture of *M. tuberculosis* MscL (PDB: 2OAR) [77,78], *E. coli* MscS (PDB: 2OAU)[77], TRAAK (PDB: 3UM7) [79], TREK-2 (PDB: 4XDJ) [80] and Piezo1 (PDB: 3JAC) [81], which have been resolved by either X-ray crystallography or cryo-electron microscopy (cryo-EM). MscL forms a homopentameric structure, while MscS and TRAAK form homoheptameric and homodimeric structures, respectively. In addition, an increasing number of studies have suggested that TRPV1 (PDB: 2PNN) and TRPV2 (PDB: 5AN8) are involved in osmosensation and mechanosensation and structural information also exists for these channels [71,82,83].

The structures of MS channels are very diverse and there is little to no structural identity among different families of MS channels. Despite the recent array of structural data yielded from X-ray crystallography and Cryo-electron microscopy, the exact gating mechanism of MS channels remains elusive. In the next section, the two main gating mechanisms proposed for MS channels will be discussed in detail (**Figure 5**).

1.2.1 Force-from-lipids

The force-from-lipids concept (bilayer model) [84-86] means that force is directly transmitted through the lipid bilayer to an MS channel (**Figure 5A**). This principle originated from the observation that the lipid bilayer alone can transfer the mechanical force to prokaryotic MS channels [86-88]. In a pioneering study, prokaryotic MscL and MscS channels reconstituted into artificial lipid bilayers were shown to maintain their mechanosensitivity comparable to that displayed in the native bacterial membrane [87,89]. This provided firm evidence that the force-from-lipids principle is the main gating paradigm of prokaryotic MS channels. Furthermore, given prokaryotic cells do not possess an animal cell-like cytoskeleton, it is reasonable to assume that all prokaryotic MS channels obey the force-from-lipids principle. Inspired by the pioneering studies on prokaryotic MS channels (purification and reconstitution into lipid bilayers) [89-91], it has recently been demonstrated that force-from-lipids principle also applies to some eukaryotic MS ion channels, most notably TREK and TRAAK [80,92-94] and Piezo1 [95,96].
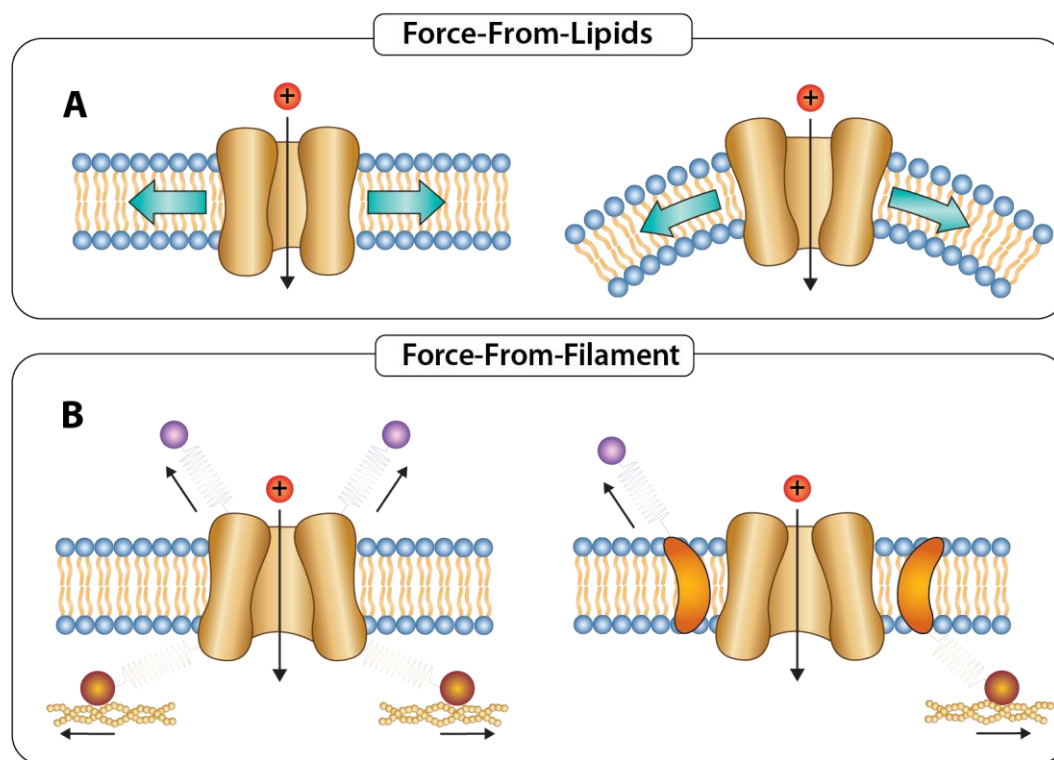
Figure 5. Gating mechanisms of MS channels; A) force-from-lipids (bilayer) paradigm; B) force-from-filament (tether) mechanism.

For other channels the gating paradigm is less clear. An example is a member of the TRP family, TRPV4 channel, which is involved in a number of mechanosensory processes [5,43,97,98], but it is still unclear how mechanical stimuli are transmitted to the channel. Although recordings of TRPV4 currents from *Xenopus* oocytes indicate a direct link with the lipid bilayer [70,99], other work suggests more reliance on tethers [100]. Therefore, unlike the K_{2P} MS channels, no definitive evidence exists for TRPV4, or any other TRP channel, supporting a force-from-lipids type gating model.

None of the above exclusively precludes the possibility of these MS channels being activated by a tether-like molecule. They simply indicate the evolutionary conservation of the force-from-lipids principle from prokaryotes to eukaryotes. It is therefore, likely that MS channels depending on their physiological role can be gated by more than one mechanism. Also energetic calculations of gating free energy shows that the two mechanisms are not mutually exclusive [101]. Nevertheless, one mechanism could be occasionally more efficient than another or act as a complementary mechanism depending on the channel type and their specific physiological roles.

1.2.2 Force-from-filament

The second gating paradigm is the force-from-filament (also called tethered model or swing model), whereby force is transmitted to an MS channel via an auxiliary structural element or tether from the intra- or extracellular environment (Figure 5B, C) [1,64,76].

So far the only strong case for the force-from-filament mechanism is NompC, a member of TRPN channel family which is involved in various mechanosensitive responses in *Drosophila* including gentle touch in larvae (**Figure 6**) [102,103]. NompC is present at the dendritic tips of mechanosensory neurons in the fly halteres, where it converts forces transmitted through the deformation of the overlying cuticle into neuronal depolarization. This channel has 29 ankyrin repeats in its N-terminus, which directly associate with microtubules attached to the plasma membrane. It has been robustly shown that this channel can be activated by applying pulling forces (imitation of gentle touch) on the ankyrin repeats which acts as a tether [57]. Although pulling force is directly transmitted from the tether to the protein, it does not necessarily exclude the potential role of membrane lipids in TRPN gating.
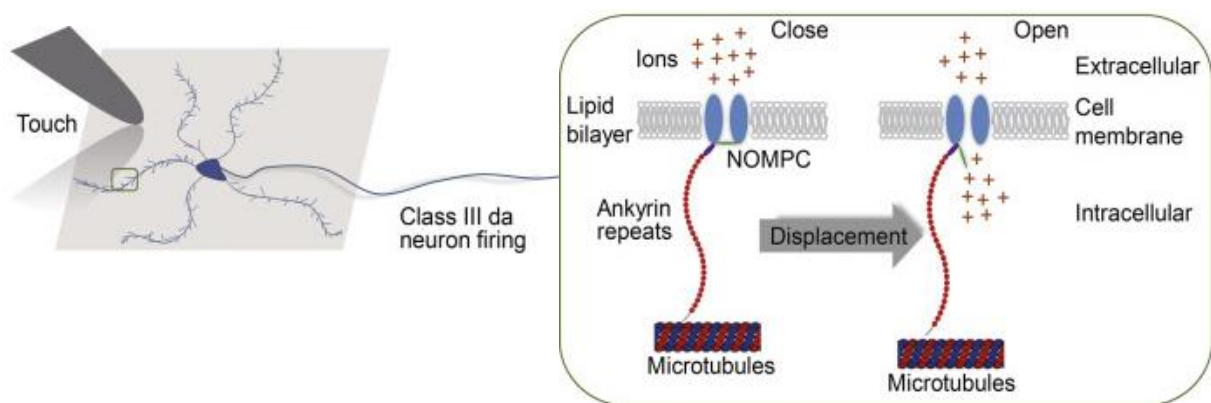
Figure 6. Model for force-from-filament (tethered) gating of the fly NompC cation channels. Fly NompC channel senses mechanical stimuli using its N-terminal tail as a tether between the cell membrane and microtubules. Ankyrin repeats and microtubule association are essential for NOMPC mechanogating in vitro and in vivo. NOMPC is mainly connected to microtubules via ankyrin repeats helping convey force. Attaching the NOMPC N-terminus (ankyrin repeats) to voltage-gated potassium channels confers mechanosensitivity. Adapted with permission from Zhang et al. 2015 [57].

Not as conclusively but similar to TRPN, it has been shown that TRPV1 channel activation can occur according to the force-from-filament principle again via ankyrin

repeats being tethered directly to microtubules [69]. However, recently Julius and Cheng labs have revealed a cryo-EM structure of TRPV1 in a native bilayer using lipid nanodiscs [104]. Using a toxin activator from the Chinese bird spider, they showed that the toxin dislodges a lipid from a protein pocket enabling a structural transition to the open state. They speculated entropy driven removal of lipids from this region by heat may also underlie TRPV1 heat induced gating. It thus indicates modulation of the gating of some mechanically-gated TRPs via their lipid environment.

The classic MS channel that is thought to follow the force-from-filament gating principle is the channel complex responsible for auditory transduction [105-108] [109]. Cadherin 23 and protocadherin 15 are the main components of the "tip-links", which connect the stereocilia, and they couple hair bundle movement to MS channel activation during hearing or head positioning [11,55]. However, despite increasing efforts, the precise pore-forming subunit of the channel complex remains unknown [53,63,110]. For more information on how the force-from-filament paradigm may be relevant to hearing mechanotransduction readers are referred to the following articles (See [11,53,54,111,112]).

 Members of the DEG/ENaC family of MS channels, which are involved in a whole host of physiological processes (such as gentle touch in *C. elegans* and regulatory volume increases in brain cells) [76,113-116] are also believed to be activated by a single or dual tether mechanism [117]. Nevertheless, the fact that the regulation of the lipid environment, particularly the presence of cholesterol, is crucial for the function of channels like DEG/ENaC in *C. elegans*, indicates that the effect of lipid bilayer in force transmission to these channels is important [117,118].

1.3   Mechanical force alters MS channels conformational equilibrium

MS channels as a case in point for integral membrane proteins exist in a conformational equilibrium, where different states are populated according to their relative energies. For a system in equilibrium in a canonical ensemble, the probability of the system being in state with energy G is proportional to $exp\left(-G/k_BT\right)$ [119]. Consider a channel in equilibrium between closed A and open B conformations. Then,

$$\frac{n_B}{n_A} = exp(-\frac{\Delta G}{k_BT}) \tag{1}$$

ΔG is the free energy difference between the states, where k_B is Boltzmann's constant and T is absolute temperature. External mechanical force shifts the equilibrium among pre-existing states by the amount of work done on the system. This leads to a new equilibrium state,

$$\frac{n_B}{n_A} = \ exp(\frac{-\Delta G+W}{k_B T}) \tag{2}$$
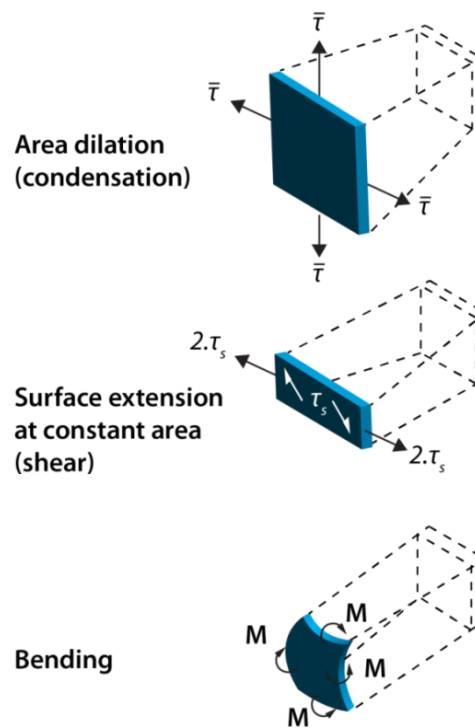
Figure 7. Active physical forces on a membrane patch. Stress and strain of each type, defined as force per unit area and deformation per unit length respectively, are basic quantities that allow characterization of the mechanical response of materials. Channels may deform differently under compressive, tensile, and shear forces [44].

As described above, the mechanical work, W, can be transferred to a channel by the lipid bilayer (force-from-lipids), intra- or extra cellular structures (force-from-filament) or a combination of both. In thermodynamics, the free energy of a system or work done on a system is expressed in terms of pairs of conjugate variables such as membrane tension and areal expansion (Eq. 3) or force and displacement (Eq. 4) (**Figure 8**). In fact, all thermodynamic potentials are expressed in terms of conjugate pairs.

Numerous forms of forces (stress) may act on MS channels with their environment and their own inherent structure dictating their sensitivity to these forces. MS channels are

gated by different types of mechanical stimuli that can be divided into three distinct stress types namely stretch-compression, shear and bending (**Figure 7**) [62,120]. If it is uniform bilayer stretch, then

$$W = -\tau \Delta A^{A \to B} \tag{3}$$

With τ being the membrane tension and $\Delta A^{A \to B}$ being area change of the protein in response to membrane tension (**Figure 8A**). If the force f is directly conveyed from an intra- or extra-cellular structure to the MS channel, and causes a conformational distance δ then,

$$W = -f \delta^{A \to B} \tag{4}$$

The latter model is called the 'swing model', 'force-from-filament' or 'gating by linear force' (**Figure 8A**). It is noted that external force in forms of a moment or shear force may also activate the channel. Then, the external work for a linear bending moment is:

$$W = -M \theta^{A \to B} \tag{5}$$

M is bending moment, θ could be for example degree of out-of-bilayer plane rotation of a structurally crucial transmembrane helix (e.g., pore lining helix). And if it is by a pure linear shear (torsional) force S, then

$$W = -S \varphi^{A \to B} \tag{6}$$

Where φ is the degree of rotation of a structurally crucial transmembrane helix in the bilayer plane and S is the shear force.

Based on Eq. 2, it is likely that a channel activity will increase if applied mechanical force (i.e. work is done on the system, W) is sufficient to overcome a certain energy threshold (i.e. gating energy barrier). Examples of gating energy barriers for MS channels are; TREK-1 is ~ 5 k_BT [121] and MscL is ~50 k_BT [1,122]. Given that one k_BT is equal to ~ 4.2 pN·nm at physiological temperature, this means pN forces acting over nm distances are sufficient to meaningfully shift the equilibrium between closed and open conformations of an MS channel.

A

B
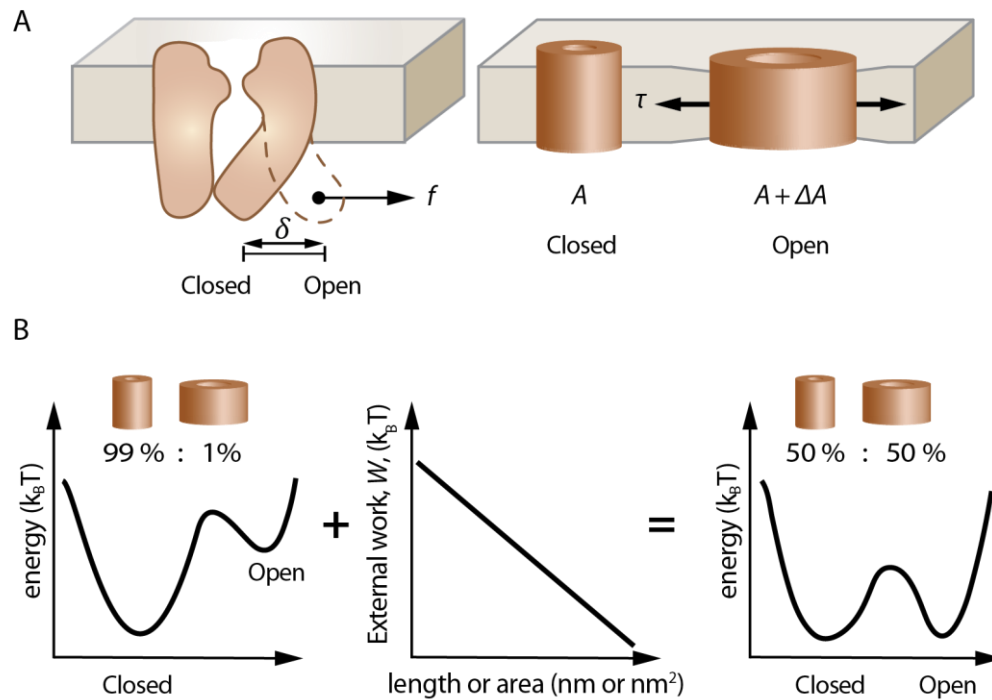
Figure 8. Mechanical force affects channel conformational equilibrium [17]. A) Schematic figure illustrating MS channel gating due to the external work done by force-from-filament (left) or force-from-lipids (right) [123,124]. B) External work overcomes the energy barrier between the closed and open state of the channel, and thus increases the open probability.

1.4   Importance of cell membrane mechanics

Common among all cells, the intracellular environment is separated from the outer space via the cell membrane. Membranes of living cells have been under mechanical force throughout evolution [125], thus they have been reinforced by a cell wall (e.g. in bacteria, yeast and plants) or by a cytoskeleton (in animal cells) to better withstand environmental stresses [126].

Consequently, studying the mechanics of the cell membrane is inescapable for a number of reasons, including: 1) how and to what extent ECM and cytoskeleton reinforce the membrane bilayer to protect it from excessive mechanical stimuli, 2) how cells interact with each other and/or move (cell migration) and 3) to determine the interplay between different membrane components (lipid bilayer, ECM, cytoskeleton) and membrane proteins (e.g. MS channels) in various biological processes. This is important because assessing cellular elasticity and viscosity provides useful information for comparative characterization between different membrane-mediated processes [44]. This is given that

genetic mutations and pathogens that disrupt the cytoskeletal architecture can result in changes of cell mechanical properties such as elasticity, adhesiveness, and viscosity [44,127].
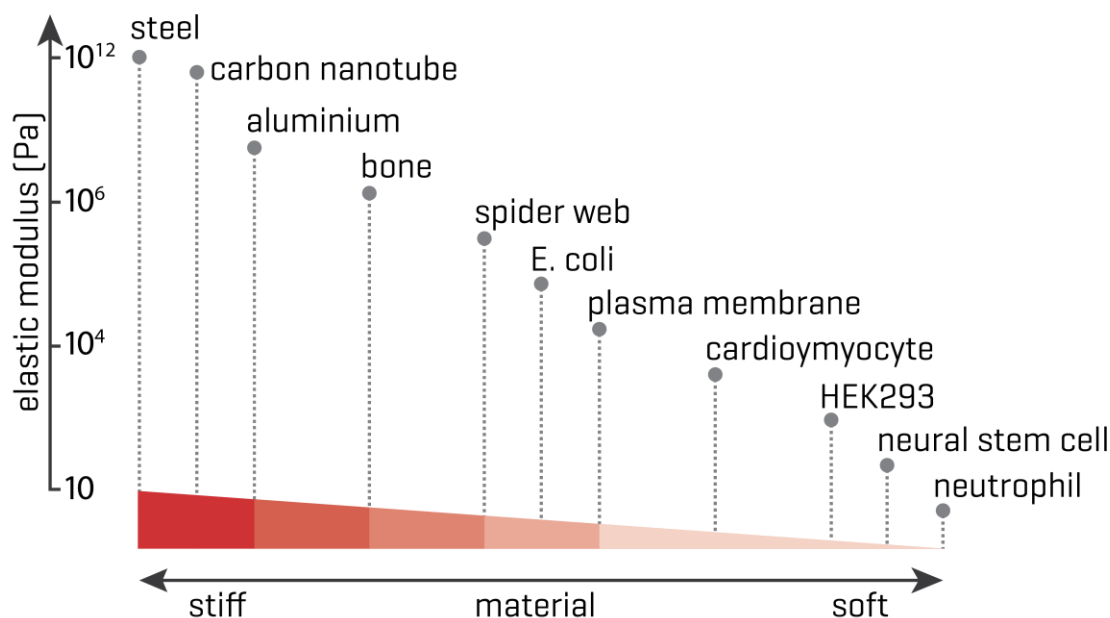
Figure 9. Broad spectrum of mechanical properties of different materials from soft matters (e.g., living cells) to hard condensed matter (e.g., steel) [44,128-131].

The choice of experimental and computational tools requires consideration of the length and the timescale of the measurement and the level of forces (or intrinsic mechanical properties of the system). A reasonable estimate of these three factors indicates which characterization tool is the most appropriate technique for mechanical study of a particular system [132]. A large body of recent research indicates that some of the cellular rheological behaviors are empirically similar to the rheology of soft materials such as foams, emulsions, pastes, and slurries (**Figure 9**).

Given the central role lipids play in mechanosensation [133,134] a detailed understanding of the lipid bilayer rheometry is essential [131]. The key question to be addressed is about how mechanical stimuli affect molecular interactions between the lipid bilayer and membrane proteins to result in physiologically relevant structural changes of these membrane constituents. This question is of critical importance due to the increasing evidence of the role that MS channels play in health and disease [5,125].

1.5 Mechanical coupling between the membrane and embedded MS channels

Membrane protein function can be modulated by a host of lipid mechanical properties. Membrane forces can modulate the activity of various membrane proteins such as MS, voltage-, ligand-, or Ca^{2+}-gated channels. Lipid molecules are able to selectively interact with specific sites on integral membrane proteins, and modulate their structure and function (a key example being Phosphatidylinositol 4,5-bisphosphate or PIP_2). This modulation may depend on specific chemical interactions between membrane proteins and individual molecules in the bilayer (at the lipid-protein interface). This includes affinity and/or avidity of certain lipid molecules to the lipid-protein interface which has direct influence on the structure and function of the membrane proteins [135]. Different proteins, however, exhibit different degrees of selectivity and promiscuity in their binding to lipids. This has recently been studied using an elegant approach called "ion mobility mass spectrometry", which reports gas-phase collision cross sections [135]. In this study, the lipid binding selectivity and strength to the mechanosensitive channel of large conductance (MscL), aquaporin Z (AqpZ), and the ammonia transporter (AmtB) were investigated. It was shown that the degree of selectivity for specific lipid types for these proteins are AmtB>AqpZ>MscL. MscL binds lipids non-selectively, without strong affinity to a particular headgroup or chain length, and binding of any lipid imparts comparable stability (**Figure 10**). Although *E. coli* MscL responds almost non-selectively to lipid composition, MtMscL has been shown to have a slight preference for phosphatidylinositol (PI) binding [135,136]. Given that all MS channels are embedded in the lipid bilayer, it is possible that this difference in their local lipid environment holds the answer for the difference observed between their activation thresholds [61,136]. AqpZ and AmtB on the other hand have been shown to be highly selective for cardiolipin (CDP) and phosphatidylglycerol (PG), respectively [135].
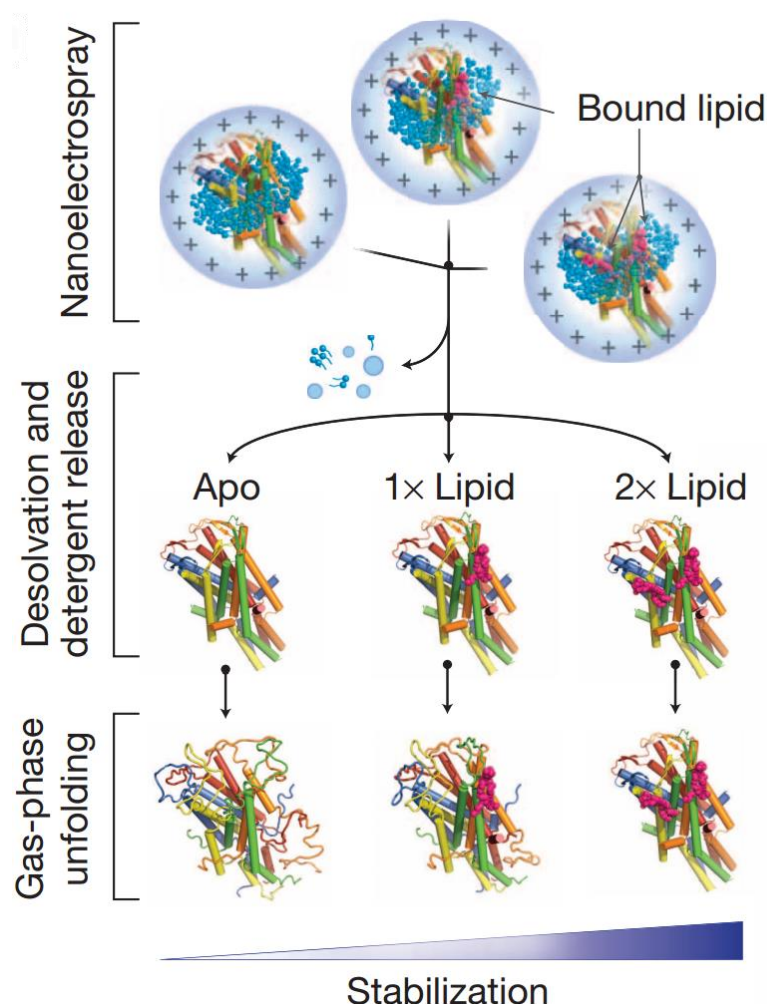
Figure 10. The mechanosensitive channel of large conductance (MscL) in electrospray droplets, within a lipid-detergent micelle, undergoes desolvation and activation. MscL resists unfolding and thus is more stable in the presence of lipids (adapted with permission from Laganowsky et al. 2014 [135]).

In "membrane-mediated" protein modulation (e.g. MS channel activation), the bilayer can be influential by showing collective physical properties such as area and bending elastic moduli, intrinsic monolayer curvature and thickness. Variation in acyl chain length, degree and position of chain unsaturation, head group repulsion, and incorporation of amphipathic molecules and interactions of co-surfactants is accompanied by a redistribution of the lateral pressure profile of the lipid bilayer [137,138]. Therefore, these factors are likely to modulate MS channel function as well.

Before discussing how mechanical properties of the lipid bilayer can impact on an MS channel function, it is first required to clarify some central concepts in this research area.

1.5.1 Transbilayer pressure profile, chain repulsion, surface tension, membrane tension

Lipid bilayers are a unique medium for membrane proteins and water has an immense influence on the structural and functional properties of lipid bilayers and in turn on membrane proteins. Due to the "hydrophobic effect", the amphipathic nature of the lipids drives membrane self-assembly by minimizing the surface exposure of the tails to water. The self-assembled lipid bilayer comes with a set of properties including its strong anisotropic internal stress, termed the "transbilayer pressure profile", and at the same time being chemically or physically malleable [137]. The pressure profile maybe simplified into three zones, a region with positive lateral pressure caused by repulsion of the hydrophilic headgroups, a surface tension area (negative pressure) which prevents water exposure of the hydrophobic tails and an area characterized by the entropic (steric) repulsion between the lipid tails (**Figure 11**). The hydrophilic lipid headgroups are in fact squeezed together to prevent water exposure of the hydrophobic tails and repel each other, both electrostatically and sterically. The steric repulsion of tails can be further understood by comparing fluctuations of a lipid chain in a bilayer and in empty space. In the bilayer, the chain fluctuations are strongly suppressed by the neighboring chains with respect to a free lipid molecule. The amplitude of chain fluctuations in the bilayer under natural conditions (**Figure 11**) is attenuated by one order of magnitude with respect to a free chain [138,139]. Suppression of chain fluctuations leads to a decrease of conformational entropy and, in turn, results in the enhancement of entropic pressure. The most significant relative reduction in the fluctuation amplitude takes place at the chain free end. The suppression of fluctuations is noticeable too at the head group region as lipid heads are not fixed. At the midchain region, deviations of the free chain are smaller due to segment connectivity and restriction of the fluctuation freedom of central segments by their peripheral neighbors. Consequently, the decrease of fluctuations for midchain in the bilayer is less pronounced [139]. The lipid tails also tend to repel each other to maximize their entropy and occupy a greater bilayer volume. To avoid water entry to hydrophobic tail area, an acute lateral "surface tension" develops at the water-lipid interior interface.

Stress/pressure distributions across the bilayer are difficult to measure experimentally, though they have been estimated for different lipid compositions using a variety of computational approaches [137,140]. Some successes have been reported using NMR and X-ray crystallography [141,142]. The main method for pressure profile characterization has however, been the use of computational approaches such as Monte Carlo, mean-field theory (MFT) [137,143,144] and molecular dynamics (MD) simulations [140,145,146]. This has allowed researchers to probe the effect of lipid composition on MS channel function using both atomistic [140,147,148], and continuum approaches [60,131,149-152]. Nevertheless, one should be cautious about the common methodological problems in pressure profile calculations for lipid bilayers using these methods [138,153].

Based on MD simulations of POPE bilayers, a typical surface tension in each "stress free" monolayer is estimated to be 50 mN/m [140]. In a stress-free bilayer, there is a balance between the tension generated at the water-lipid interface and the repelling pressure between the tails, and thus the mean membrane tension is zero. A typical value for the peak pressure inside the lipid bilayer is about 300 atm whereas around the head groups it can be up to 1000 atm [140,143]. Hence, given such huge pressure values across the bilayer thickness, it is not surprising that integral membrane proteins can be sensitive to the changes in the intrinsic transbilayer pressure profile [58,154]. It should be noted however, that proteins can reciprocally redistribute the transbilayer pressure profile depending on their interaction with the lipid [137,143,155]. For example using MD simulations, **Figure 11B** illustrates the changes in the pressure profile of a POPE lipid bilayer in the presence of *E. coli* MscL, with and without applied tension [156]. Firstly, of note is the asymmetry in the pressure profile and the reduction of the pressure peaks in the hydrophobic core after MscL has been inserted into the bilayer. As shown, when the bilayer has been stretched, the pressure profile of the lipid in the presence of MscL changes particularly at the lipid-water interface (Peak A and Peak B). In this scenario, compared to a non-stressed bilayer and based on the area under the pressure profile, one may estimate the equivalent mean "membrane tension" required for the activation of MscL. In Chapter 3, the pressure profile redistribution due to the presence of MscL and under different surface tensions will be discussed in detail [156].
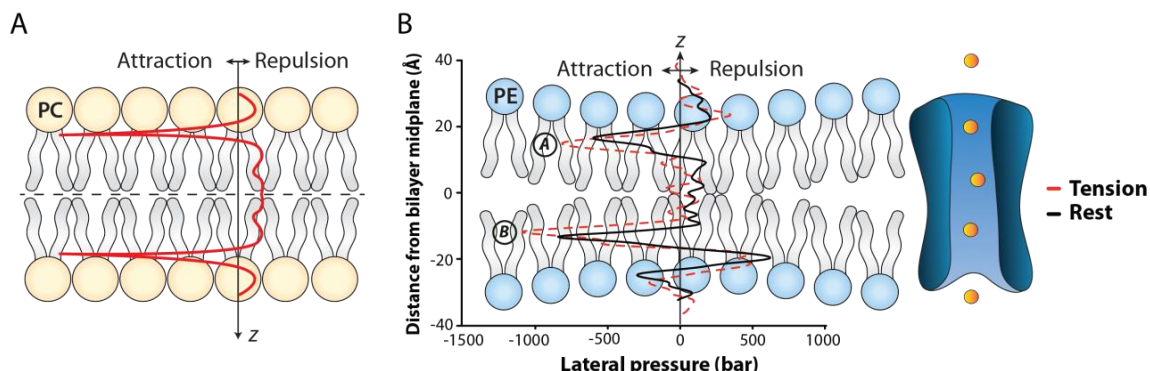
Figure 11. The transbilayer pressure profile. Even in "pure" lipid bilayers, the transbilayer pressure profile is largely inhomogeneous due to the amphipathic nature of the lipid molecules and the presence of water. (A) A symmetrical transbilayer pressure profile of a POPC bilayer showing characteristic negative (attractive) peaks at the water-lipid interface and repulsive positive peaks in the headgroup and tail region. Due to the shape of POPC lipids, their intrinsic curvature is zero. (B) Transbilayer pressure profiles from molecular dynamics simulation of a POPE bilayer with *E. coli* MscL embedded in it (black trace is the lateral pressure profile at rest, and red trace is in the presence of applied tension). Note how in the presence of the protein (e.g., MscL) the pressure profile in a symmetrical lipid bilayer has become clearly asymmetric. Peak A and peak B represent the increase in the pressure profile at lipid solvent interface (for more details see Chapter 3 [156]; modified from Cox et al. 2016 [43]).

1.5.1.1 Measuring membrane area and bending elasticity

Multiple experimental and computational approaches have been employed for characterizing area and bending elasticity of different lipid bilayers. There is an extensive literature discussing each method in detail [157,158]. Computational approaches include atomistic, coarse grained and implicit solvent models. Experimental paradigms include shape fluctuation optical analysis, vesicle electrode formation, AFM-based methods, X-ray scattering, spectroscopic approaches and micropipette aspiration [159-172]. While similar in concept, most of these methods vary depending on the tools employed to exert force on the membrane and/or the scale that the force has been applied to. As a result, they often yield different values for the same lipid membranes under similar conditions. Similar issues are encountered among computational studies, where different methods and/or different energetic models have been adapted [157].

The most popular approach for measuring mechanical properties of various lipid types is the micropipette aspiration (MA) technique. This method was mainly developed by Evans and Needham to ubiquitously measure the area and bending elasticity of membranes of different composition [170]. Here, the membrane tension τ generated via a suction pressure through the glass micropipette can be estimated using Laplace's Law.

$$\tau = \frac{PR_p}{2\left(1-\frac{R_p}{R_v}\right)} \tag{7}$$

This equation is applicable to liposome patches both inside (with the inner radius of R_p) and outside (with the radius of R_v) the micropipette. P is the pressure difference between the inside and outside of the patched membrane (**Figure 12**). The resulting membrane strain, α, which is the area change, ΔA, normalized by the initial area, A_0, is calculated as follows:

$$\alpha = \frac{\Delta A}{A_0} \sim \frac{1}{2}\left(\left(\frac{R_p}{R}\right)^2 - \left(\frac{R_p}{R}\right)^3\right)\frac{\Delta L}{R_p} \tag{8}$$

ΔL is the change in protrusion length of the lipid inside the pipette (**Figure 12**). Equation (8) has been deduced based on the assumption that internal volume of the vesicle during the MA remains constant (due to the incompressibility of the aqueous solution inside the vesicle) [160,173]. Following a typical MA protocol, the areal elasticity modulus under high membrane tensions (when $\tau > 0.5$ mN/m [174,175]), K_a, is calculated using Equation 9.

$$K_a = \frac{\tau}{\alpha} \tag{9}$$

In the low-tension regime ($\tau < 1$ mN/m), the slope of the area dilation versus the logarithm of the tension yields the bending rigidity.

Although this method is commonly adopted for measuring mechanical properties of various lipids, the long-standing quest for the "material reality" of lipid bilayers remain unresolved. Some of the caveats to this technique will be discussed in the following section.
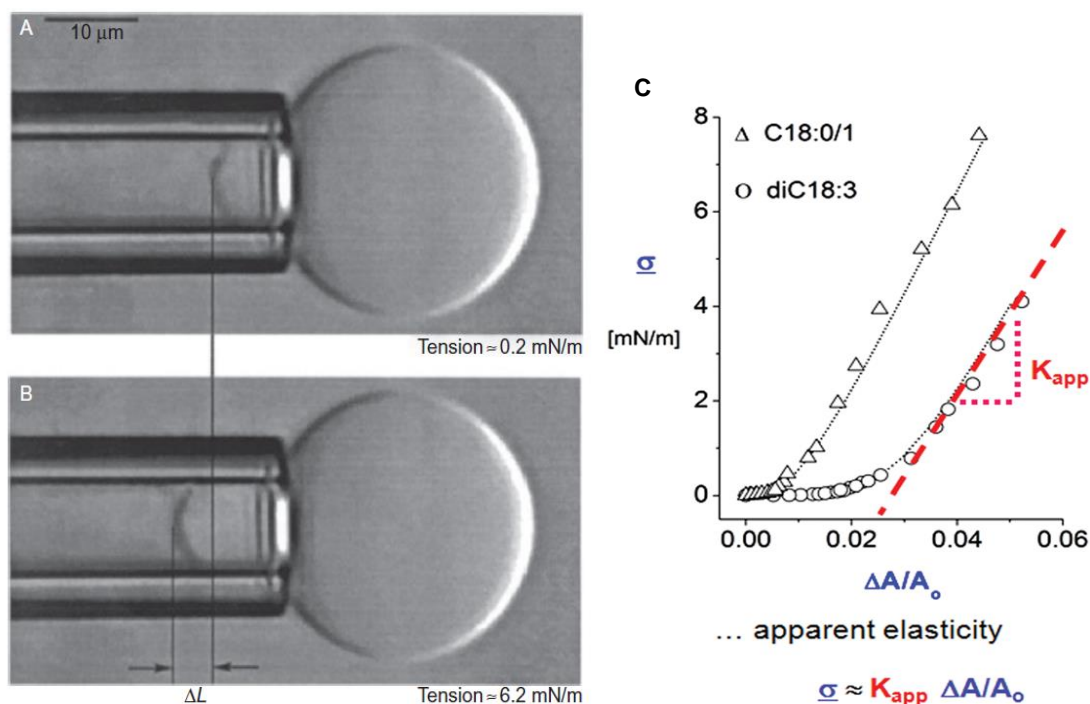
Figure 12. A giant unilamelar vesicle (GUV) has been aspirated into a glass pipette in order to measure its mechanical properties. A, B) The GUV composed of PC-lipid has been aspirated into the pipette entry. Changes in aspiration length is represented by Δ*L*. C) Membrane tension versus area dilation results for two PC vesicles with different chain unsaturation, C18:0/1 and diC18:3, indicating different apparent area elasticity moduli (slopes) K_{app}. The inner diameter of the glass capillary is approximately 10 μm. (Reproduced from Ref. [138] with permission from the Royal Society of Chemistry).

1.5.1.2 Limitations of micropipette aspiration technique

As previously mentioned, MA is the most versatile and widely-used approach for characterizing lipid bilayer properties. This method has particular importance for patch-clamp electrophysiology, as the application of force on the membrane is identical in these two techniques.

However, there are several limitations associated with the current usage of this technique as listed below:

1. MA technique lacks both consistency and accuracy when measuring mechanical properties of a lipid type, as indicated by the following examples. First, the Young's modulus values of DOPC lipid bilayer reported by several studies vary widely from 13 to 150 MPa [138,172,174]. Second, current area elasticity values obtained from MA experiments for lipids constituting bacterial membranes (e.g., the mixture of POPE and POPG) is ~ 300 mN/m [174,176]. This is higher than the reported values for the bacterial

cell wall (i.e., ~ 100 mN/m) [177,178]. This is inconsistent with the well-established knowledge of bacterial cell structure, as the peptidoglycan layer of the cell wall is much stiffer than its inner membrane, an essential structure that protects bacteria against acute volume expansion associated with hypo-osmotic shocks.

2.   MA experiments typically rely on phase contrast microscopy, which has lower precision in tracking cell/liposome protrusions compared to fluorescent microscopy. This precludes the use of a fluorescent dye (e.g., Rhodamine PE) that can be employed to label the lipid bilayer without changing its mechanical properties that can allow easier tracing of the membrane geometry inside the pipette [179,180].

3.   Adhesion of the lipid membrane to the glass pipette during MA can interfere with measuring its bending rigidity [131,180]. Adhesion tension reported for different lipid systems varies widely from 0.3 mN/m to 4 mN/m [181,182], as it is influenced by ionic strength, lipid type, and pH [180] to a varying extent. Given that small tensions (i.e., <0.5 mN/m) can supress thermal fluctuations, measuring bending rigidity of the membranes based on this can cause inaccuracy in the presence of glass-lipid adhesion tension. Subsequently, glass-lipid adhesion must first be removed by, for example, coating the capillary [131].

4.   The accuracy of Laplace's law used in MA techniques can be influenced by various experimental factors. Such factors include the existence of adhesion tension, lipid behaviour (e.g. treating the bilayer as a 2-dimensional fluid or quasi-solid entity at different temperatures) or the degree of freedom of monolayers to slide against each other [131,170].

5.   The stress distribution of MA technique is highly dependent on vesicle size. Vesicle size can dramatically change the properties of the lipid bilayers having the same composition [131,183]. Moreover, it is difficult to perform experiments on small vesicles while remaining in the cell-attached configuration.

6.   Mechanical properties of lipid bilayers (e.g., areal strain reported from MA experiments) are vastly different from what is reported at the nanoscale (e.g. reported from MD simulations). This is mainly because local strains at the nanoscale can always be larger than the nonlocal strains (microscale) [184,185]. Interestingly, even within the same length-scale, the resulting mechanical properties for a lipid type could be very dependent on the utilised approach. For instance, for DMPC, the results from the computational models of Cooke and Brannigan are remarkably different from those

obtained from atomistic and MARTINI CG simulations [186]. The source of discrepancy among these approaches is unclear. Moreover, given the length scale relevant for MA (>1 μm), local phenomena (< 100 nm) such as lipid tilt, ordering or raft formation are unlikely to contribute to the resulting bulk mechanical properties. These local effects are relevant to bilayer mechanical properties at smaller scales (e.g., for the interpretation of X-ray scattering data). Currently, however, there is no comprehensive method that can be applied to microscale measurements while taking into account such detailed contributions [186].

These issues mean that improvement of the conventional micropipette aspiration technique is required, particularly in terms of experimental ease and reliability (Chapter 2) [131].

1.6   MscL structure and function: a prototypical MS channel

Interactions with the lipid environment are particularly important for bacterial MS channel function, because they are gated by bilayer tension with no extra- or intracellular involvement. As previously mentioned, the bacterial MscL and MscS play crucial roles in osmoprotection [26].

MscL is the first cloned MS channel from bacteria [87], and its functional characteristics have been extensively studied using liposomal reconstitution [1,65,87,89,187-189]. This channel forms a homopentamer. Each monomer consists 136 amino acids (in EcMscL, and 151 amino acids in MtMscL) with two transmembrane helices [77]. The channel displays no selectivity for molecules less than 6.5 kDa, with a unitary conductance of ~3 nS. MscL has a C-terminal domain at the cytoplasmic side which aligns co-axially to the transmembrane pore.

Despite emerging structural data on several MS channels, the key structural element that links the membrane mechanics to channel structural dynamics remains unknown. Among all MS channels, MscL is the most studied channel which has repeatedly provided structural and functional principles underlying the bilayer-mediated gating of MS channels [134,190].

There are two competing gating mechanisms proposed for MscL; they differ in which role for the cytoplasmic N-terminal region has been proposed in the literature. One proposal claims that the N-terminus forms a cytoplasmic bundle and thus acts as a second gate [191], while the other one, based on a refined crystal structure [77], claims that

N-terminal is anchored in the membrane [192]. The second proposal has been further reinforced by showing that compared to WT, mutation of phenylalanine residues (F7 and F10) of the N-terminus markedly decreased the mechanosensitivity of MscL and bacterial survival rate against acute osmotic down-shock MscL [192]. Furthermore, due to the amphipathic nature of the N-terminus it seems logical to assume that this helix resides at the bilayer-water interface.

In Chapter 3, it is shown that the short amphipathic N-terminus of MscL is a crucial structural element conferring mechanosensitivity to the channel during membrane tension-induced gating (**Figure 13**) [156]. Furthermore, it is proposed that an amphipathic anchor domain buried in the membrane, which directly transfers the membrane stress to the pore forming helices of an MS channel, is the unifying feature of bilayer-mediated mechanosensitivity [95,193].
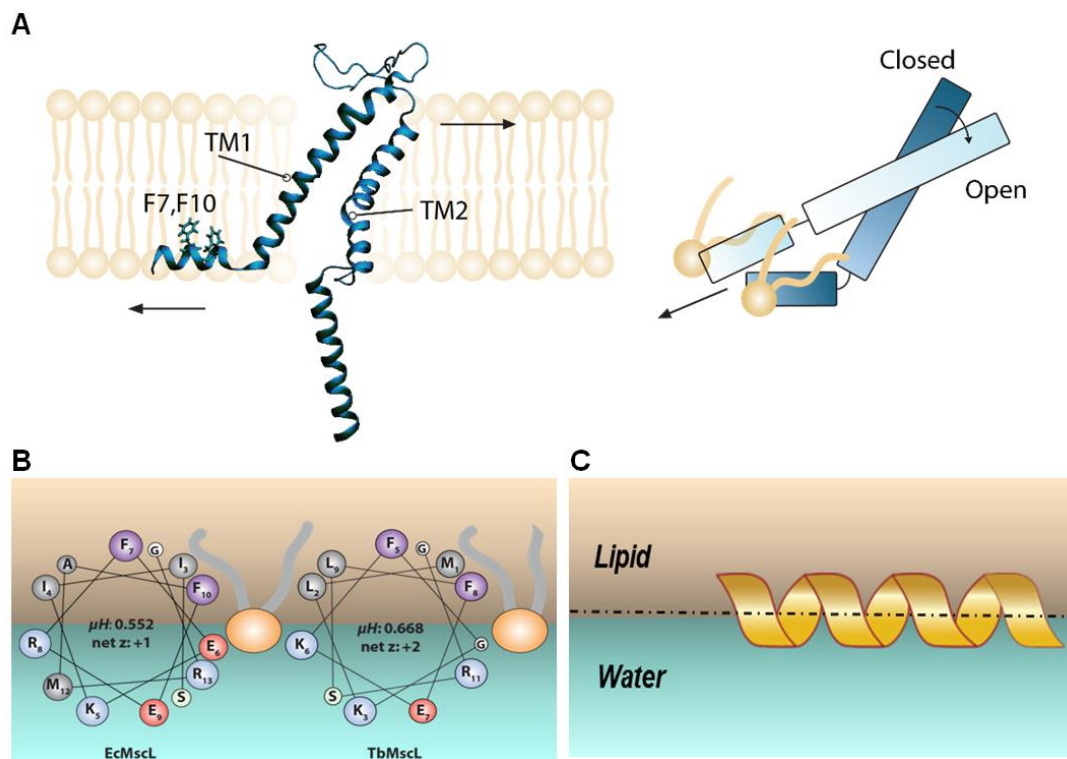
Figure 13. During MscL gating, force-from-lipids is transmitted via the N-terminus to the pore-lining helix TM1. A) It is hypothesized that the N-terminal helix aligns with theTM1 helix during the channel gating. B) In the EcMscL and MtMscL, the hydrophobic residues (e.g., F7 and F10 in EcMscL) face the lipid core while the hydrophilic residues (e.g., K5 and E9 in EcMscL) face the water [156]. C) The N-terminus resides at the lipid-water interface.

1.7   Methods to study mechanosensitive ion channels

The structure and function of ion channels have been studied, over the past three decades, using various experimental and computational approaches. Three main approaches used in this thesis include molecular dynamics (MD) simulations, continuum modelling, and the patch-clamp technique.

1.7.1   Molecular dynamics (MD) simulations

MD simulations account for the interactions between atoms and molecules. These interactions are calculated by solving the Newtonian equations of motion $F = m \cdot a$ for all particles in the simulated system. F is the force acting on the particle (e.g., atom), m is the mass of the particle and a is the acceleration of the particle. The interaction energies and masses are defined in a force field, and are used to calculate the new acceleration vector of a molecule or atom, typically for intervals of 1 or 2 femtoseconds. The choice of time step depends on whether the covalent bonds between hydrogens and heavier atoms are frozen or not. Despite all assumptions and/or simplifications made, it has often been shown that results from MD simulations are in good agreement with experimental data. Therefore, MD adds very useful information on the structural dynamics of the system studied, so that it is considered as a "computational microscope" [194], which provides structural views beyond what is achievable from current imaging methods. While their core functionality is similar, multiple MD software packages are available including CHARMM, AMBER, NAMD, GROMACS, Desmond, OpenMM. NAMD and GROMACS are commonly used in biological simulations. For more information about the equations used and the approximations made, the NAMD or GROMACS manual contains an informative introduction [195-197]. There are three major force fields most used in MD simulations: CHARMM, AMBER and OPLS-AA. Information and protocols on how to setup and run MD simulations of membrane protein systems is also provided in several recent review articles [198-202].

Relevant for this thesis, MD simulations have become an important tool to study the gating cycle of MS channels embedded in various bilayer systems. Over the past few decades, meaningful MD simulations of MS channels in lipid membranes have enabled better understanding of their function and physical properties. Specifically, MD

simulations have been used to probe gating of MS channels such as MscL [140,203-208], MscS [189,209,210], TREK-2 [211] and TRPV4 channels [70,212].

Using all-atom MD simulations Gullingsrud and Schulten [140] measured the lateral pressure profile for in bilayers of different lipid compositions and concluded that gating of MtMscL depends on the second moment of the bilayer pressure profile in a tension dependent manner. They showed that changing lipid composition from DOPC to DOPE lowers the activation threshold by 2 to 4 k_BT, which is a very small share of the total free gating energy (~ 50 k_BT [213]). Using the same approach, Elmore and Dougherty [147] reported the effect of chain length on the gating of MscL function and showed that MscL adjusts to membrane thinning, which is consistent with experimental data [214]. Using all-atom MD simulations, Meyer et al. 2006 [215] embedded *E. coli*-MscL in a curved bilayer composed of single and double tailed lipids in absence of any external force. Although this stress redistribution due to the initial curvature and the single tail lipid did not fully gate the channel in their relatively short simulation, they showed a rearrangement of the periplasmic loops as a result. Based on their result, they suggested that depending on the geometry and composition of the bilayer, the protein structure can be affected even on short timescales. In all-atom molecular dynamics (MD) simulations, membranes usually only consist of one or two different lipids and may include sterols. Detailed membranes made of a more diverse lipid population have been developed to model Chlamydia, yeast and *E. coli* membranes by Klauda group [176,216,217]. More recently, Ingólfsson et al., 2014 have provided a coarse grain (CG) model consisting of 63 different lipid species asymmetrically distributed across the two leaflets, mimicking an idealized mammalian plasma membrane [218].

In MD simulations of bacterial membrane proteins, it is common to use a membrane model consisting of only POPE [140,156] lipids [140,219]. In some cases, this is also done in combination with 1-palmitoyl-2-oleoyl-sn-glycero-3-phosphoglycerol (POPG) lipids [61,133].

Most computational studies have been focused on examining the membrane proteins, without paying enough attention to the membrane [176]. However, it should be noted that the composition of, for example, bacterial membranes varies depending on the bacterial species, strain, nutrients, and growth phase. Therefore, it is quite likely that membrane proteins, in particular MS channels, may respond differently in different lipid

environments, as discussed in previous sections. Hence, it is essential to develop an accurate representation of the relevant plasma membrane, e.g. an *E. coli* cytoplasmic membrane, for use in further simulation studies of ion channels.

1.7.1   Continuum mechanics approaches

Continuum approaches are usually adopted in mechanobiology for two main reasons: i) they are not usually computationally expensive, and ii) it is more straightforward to describe/interpret the parametric dependence of a quantity (e.g., free energy) on its possible variable(s) (e.g., membrane thickness). However, atomistic detail or resolution are usually overlooked in modeling different protein molecules using continuum approaches.

There are several applications of continuum mechanics approaches to study of MS channels. Wiggins and Phillips (2005) [150,151], developed an analytical model to qualitatively describe the free energy of the protein-bilayer system. They suggested that hydrophobic mismatch could be a physical mechanism that controls MS channel gating. This model was further improved by adding triggers (besides the channel radius change) in the transition from the closed to the open state [150]. They showed that, for MscL, the share of hydrophobic mismatch, surface tension, spontaneous curvature and elasticity moduli in gating free energy can be up to 10 k_BT whereas the share of Gaussian curvature and line tension were much less (~1 k_BT). However, the low contribution of line tension could be due to the lack of a proper mathematical model and/or overlap between line tension and surface tension.

In another study, Markin and Sachs (2004), simplified the bilayer forces down to membrane tension, line tension and membrane torque. They deduced a general thermodynamic formalism to relate the open probability to the physical factors including membrane stiffness, thickness and spontaneous curvature [149]. They also predicted that the contribution of line tension in total gating energy of a channel such as MscL is negligible.

Modelling packages based on continuum theories such as finite element (FE) provide additional approaches to energetic experiments. In FE modeling, the bulk mechanical properties (e.g., Young's modulus and Poisson's ratio) of different constitutes are applied to compute the deformation and strain energies. In the field of cell biology, FE

models typically capture the dynamics of large biological molecules such as multi-protein assemblies, cytoskeleton, cell membrane, cell wall, extracellular matrix and chromatin [220,221]. Additionally, FE modeling has been used to simulate smaller structures such as MS channels [220,222-225].

Using FE modelling, a representative volume element (RVE) for MscL was designed by Bavi et al. (2014), [226] to gain insights into the gating of MS channels in response to local membrane bending. The proposed continuum model of MscL was designed to be consistent with channel conformation in three conditions: i) in detergent, ii) in closed and iii) in open state. Furthermore, their implicit membrane model incorporated the lipid pressure profile. From this, it was calculated that global bending of the membrane, such as the curvature of the patch inside a micropipette, has a negligible effect on the MscL conformation. In contrast, another study reported that the local curvature (e.g. with the curvature radii < 25 nm) has a considerable effect on stress profile of the lipid bilayer and thus modulation of the MS channel. In this study [227], MscL was shown to respond differently to various local curvature directions, although the external work in both curvature directions was very similar. Compared to the outward curvature (periplasmic), inward (cytoplasmic) curvature was shown to be more effective at opening MscL. It was also concluded that concave and convex local curvatures can produce different effects on the channel activity. Such effects were shown to be influenced by the shape of the MS channel pore, and largely by the location of the constriction gate along the bilayer thickness.

Overall, continuum simulations have provided valuable insights in understanding the bulk effect of the membrane on MscL. However, these models are not comprehensive enough to capture the atomistic details underlying channel gating including inter-helical degrees of freedom and interactions. To address this, improvements can be made by including important bulk interactions as well as an accurate 3D structure of the MS channel of interest. This can be achieved by combining FE modeling with the atomistic or coarse interactions obtained from MD simulations (MD-FE).

Recently, MscL was simulated *in silico* using the FE method where the alpha helices were modeled as elastic rods and the membrane as an orthotropic slab [222]. The inter-helical interactions obtained from these MD simulations were introduced to regions called "chemical nodes". The effect of the "wetting" [228] process on gating of MscL was

examined using a continuum solvation model where the effect of water molecules was implicitly reflected on the surfaces at the channel pore. It was shown that wetting has a dominant role in determining the gating kinetics of MscL, which is in agreement with the previous experimental and MD simulation studies [203,209].

This is a compelling example that meaningful continuum simulations can advance our understanding of gating of an MS channel without expensive computational cost. Consequently, in conjunction with other computational and experimental techniques, a similar approach was adopted in Chapter 3 [156] to study the role of the N-terminus in the gating cycle of WT and mutant MscL channels.

1.7.2   Patch-clamp electrophysiology

To detect ionic currents from MS channels in response to mechanical force, several experimental methods have been developed that apply various mechanical stimuli to cells. Patch-clamp electrophysiology is the most versatile approach and "gold standard" technique for functional studies of ion channels, as it provides quantitative information on the relationship between membrane tension and channel open probability [229,230]. It is also one of the main techniques employed to study the activity of MscL and MscS co-reconstituted into liposomes and in native *E. coli* membranes as described in Chapter 3 [156] of this thesis.

A simplified schematic of a patch-clamp amplifier in voltage clamp mode has been illustrated in **Figure 14 A,B**. The cell can be modeled as a set of capacitors and resistors. Based on Ohm's law ($V=IR$), voltage (V) is related to current (I) in proportion to the resistance (R) of the circuit. Current and voltage are both controlled through the electrode shown in **Figure 14**. In the voltage clamp mode, membrane potential can be set at any level (i.e., clamped), while recording the current flux through the membrane patch (e.g., through ion channels). This is achieved by a feedback circuitry within the patch-clamp amplifier [229,231]. The physical process in the current clamp is similar to the voltage clamp, except that in a voltage clamp the voltage is set to a value and the current flux is measured, whereas in a current clamp the current is preset while the change in the voltage (e.g. action potential) is being measured.

In a patch-clamp electrophysiology set up, after formation of a tight seal (giga-seal [180,182]), the membrane patch can be stimulated by hydrostatic or osmotic pressure gradients applied across the patch membrane [232,233]. As an example, a patch-clamp recording of MscS and MscL reconstituted into an azolectin liposome is shown in **Figure 14C**. Upon application of negative pressure (suction) to the micropipette, the patched membrane is stretched to the extent that can activate the embedded MS channels. The key equation used to calculate the resulting membrane tension due to application of pressure on the patch is Young-Laplace's equation (pr/2; another version of Eq. 7). MscS requires a lower tension for 50% activation ($P_o = 0.5$) (~ 6 mN/m) compared to MscL (~ 12 mN/m) [179]. Therefore, as the pressure rises (the red trace), first the MscS channels present in the patch activate and then the MscL channels (**Figure 14C**). As the pressure decreases first the MscL channels close followed by closure of the MscS channels. The trend is similar when an *E. coli* spheroplast is patched, except that the tension necessary for 50% activation of the channels is higher due to the difference between the lipid composition and/or presence of the remnant cell wall in spheroplasts compared to azolectin [179,234].

Cells can be patched in various configurations such as cell-attached, whole-cell and excised-patch mode. The choice of patch configuration usually depends on a number of factors including the number of channels (i.e., single channel or cohort current) [232,233] and the accessibility to either side of a patch (intra- or extracellular). The computational analysis provided in Chapter 2 enables us to decipher the stress differences among different electrophysiological patch configurations [131].
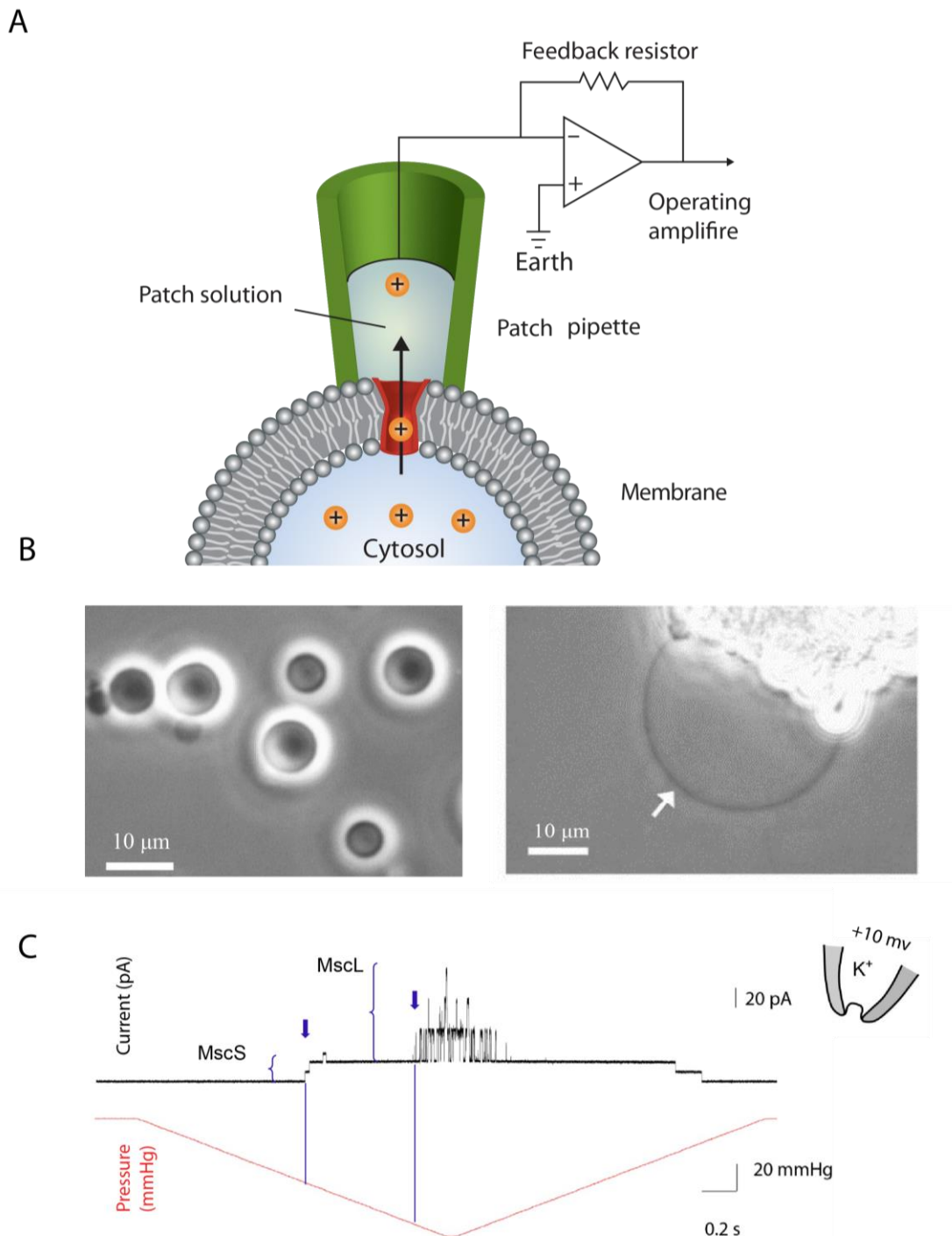
Figure 14. Patch-clamp electrophysiology of MS channels in cells and reconstituted liposomes. A) Schematic of a simplified patch-clamp set up in the voltage clamp mode. Pressure is applied through a micropipette to the patch membrane. Geometry of the membrane patch can be outwardly or inwardly bent upon application of negative or positive pressure, respectively. B) *E. coli* spheroplasts (left) and azolectin liposome (right) containing reconstituted channels amenable for patch-clamp electrophysiology. C) Patch-clamp electrophysiology recording of MscS and MscL channels, reconstituted into azolectin lipid bilayers, from an inside-out configuration.

The pipette voltage is set to +10 mV and the maximum applied pressure is ~ -80 mmHg. The current has been shown in black and pressure in red. As the pressure (suction) increases, membrane tension increases, which first activates MscS channels and then MscL channels. The blue dashed lines indicate the activation thresholds of MscS and MscL that are ~ 45 and 70 mmHg, respectively.

References

1.	Hamill, O.P. & Martinac, B. Molecular basis of mechanotransduction in living cells. *Physiol Rev* **81**, 685-740 (2001).
2.	Hamilton, E.S., Schlegel, A.M. & Haswell, E.S. United in diversity: mechanosensitive ion channels in plants. *Annu Rev Plant Biol* **66**, 113-37 (2015).
3.	Haswell, E.S. & Verslues, P.E. The ongoing search for the molecular basis of plant osmosensing. *J Gen Physiol* **145**, 389-94 (2015).
4.	Monshausen, G.B. & Haswell, E.S. A force of nature: molecular mechanisms of mechanoperception in plants. *J Exp Bot* **64**, 4663-80 (2013).
5.	Martinac, B. & Cox, C.D. Mechanosensory transduction: Focus on ion channels. in *Comprehensive Biophysics* (Elsevier, 2016).
6.	Ranade, S.S., Syeda, R. & Patapoutian, A. Mechanically Activated Ion Channels. *Neuron* **87**, 1162-79 (2015).
7.	Nilius, B. & Honore, E. Sensing pressure with ion channels. *Trends Neurosci* **35**, 477-86 (2012).
8.	Arnadottir, J. & Chalfie, M. Eukaryotic mechanosensitive channels. *Annu Rev Biophys* **39**, 111-37 (2010).
9.	Kocer, A. Mechanisms of mechanosensing - mechanosensitive channels, function and re-engineering. *Curr Opin Chem Biol* **29**, 120-7 (2015).
10.	Nikolaev, Y.A., Dosen, P.J., Laver, D.R., Van Helden, D.F. & Hamill, O.P. Biophysical Factors that Promote Mechanically-Induced Action Potentials in Neocortical and Hippocampal Pyramidal Neurons. *Biophysical Journal* **110**, 349a (2016).
11.	Sotomayor, M., Weihofen, W.A., Gaudet, R. & Corey, D.P. Structure of a force-conveying cadherin bond essential for inner-ear mechanotransduction. *Nature* **492**, 128-132 (2012).
12.	Wu, Z. et al. Mechanosensory hair cells express two molecularly distinct mechanotransduction channels. *Nat Neurosci* **20**, 24-33 (2017).
13.	Maksimovic, S. et al. Epidermal Merkel cells are mechanosensory cells that tune mammalian touch receptors. *Nature* **509**, 617-21 (2014).
14.	Poole, K., Herget, R., Lapatsina, L., Ngo, H.D. & Lewin, G.R. Tuning Piezo ion channels to detect molecular-scale movements relevant for fine touch. *Nat Commun* **5**, 3520 (2014).
15.	Ranade, S.S. et al. Piezo2 is the major transducer of mechanical forces for touch sensation in mice. *Nature* **516**, 121-5 (2014).
16.	Fritton, S.P. & Weinbaum, S. Fluid and solute transport in bone: flow-induced mechanotransduction. *Annual review of fluid mechanics* **41**, 347 (2009).
17.	Pruitt, B.L., Dunn, A.R., Weis, W.I. & Nelson, W.J. Mechano-transduction: from molecules to tissues. *PLoS Biol* **12**, e1001996 (2014).
18.	Mofrad, M.R. & Kamm, R.D. *Cytoskeletal mechanics: models and measurements in cell mechanics*, (Cambridge University Press, 2006).
19.	Persat, A. et al. The mechanical world of bacteria. *Cell* **161**, 988-997 (2015).
20.	Wood, J.M. Bacterial osmoregulation: a paradigm for the study of cellular homeostasis. *Annu Rev Microbiol* **65**, 215-38 (2011).
21.	Wood, J.M. Osmosensing by bacteria: signals and membrane-based sensors. *Microbiology and Molecular Biology Reviews* **63**, 230-262 (1999).
22.	Kung, C., Saimi, Y. and Martinac, B. . Mechanosensitive ion channels in microbes and the early evolutionary origin of solvent sensing. . in *Current Topics in Membranes and Transport* (ed. Claudio, T.) 9451-9455 (Academic Press, New York, 1990).

23. Booth, I.R. Bacterial mechanosensitive channels: progress towards an understanding of their roles in cell physiology. *Curr Opin Microbiol* **18**, 16-22 (2014).
24. Booth, I.R., Miller, S., Muller, A. & Lehtovirta-Morley, L. The evolution of bacterial mechanosensitive channels. *Cell Calcium* **57**, 140-50 (2015).
25. Lieber, A.D., Yehudai-Resheff, S., Barnhart, E.L., Theriot, J.A. & Keren, K. Membrane tension in rapidly moving cells is determined by cytoskeletal forces. *Curr Biol* **23**, 1409-17 (2013).
26. Levina, N. et al. Protection of Escherichia coli cells against extreme turgor by activation of MscS and MscL mechanosensitive channels: identification of genes required for MscS activity. *EMBO J* **18**, 1730-7 (1999).
27. Berrier, C., Coulombe, A., Szabo, I., Zoratti, M. & Ghazi, A. Gadolinium ion inhibits loss of metabolites induced by osmotic shock and large stretch-activated channels in bacteria. *European Journal of Biochemistry* **206**, 559-565 (1992).
28. Poolman, B. & Glaasker, E. Regulation of compatible solute accumulation in bacteria. *Molecular microbiology* **29**, 397-407 (1998).
29. Poolman, B., Spitzer, J.J. & Wood, J.M. Bacterial osmosensing: roles of membrane structure and electrostatics in lipid–protein and protein–protein interactions. *Biochimica et Biophysica Acta (BBA)-Biomembranes* **1666**, 88-104 (2004).
30. Naismith, J.H. & Booth, I.R. Bacterial mechanosensitive channels--MscS: evolution's solution to creating sensitivity in function. *Annu Rev Biophys* **41**, 157-77 (2012).
31. Buda, R. et al. Dynamics of Escherichia coli's passive response to a sudden decrease in external osmolarity. *Proceedings of the National Academy of Sciences* **113**, E5838-E5846 (2016).
32. Hoffman, B.D., Grashoff, C. & Schwartz, M.A. Dynamic molecular processes mediate cellular mechanotransduction. *Nature* **475**, 316-323 (2011).
33. Rahimzadeh, J. et al. Real-time observation of flow-induced cytoskeletal stress in living cells. *Am J Physiol Cell Physiol* **301**, C646-52 (2011).
34. Leverett, L., Hellums, J., Alfrey, C. & Lynch, E. Red blood cell damage by shear stress. *Biophysical journal* **12**, 257 (1972).
35. Dao, M., Lim, C.T. & Suresh, S. Mechanics of the human red blood cell deformed by optical tweezers. *Journal of the Mechanics and Physics of Solids* **51**, 2259-2280 (2003).
36. Secomb, T.W., Hsu, R. & Pries, A. Motion of red blood cells in a capillary with an endothelial surface layer: effect of flow velocity. *American Journal of Physiology-Heart and Circulatory Physiology* **281**, H629-H636 (2001).
37. Savin, T., Bandi, M. & Mahadevan, L. Pressure-driven occlusive flow of a confined red blood cell. *Soft matter* **12**, 562-573 (2016).
38. Grodzinsky, A.J., Levenston, M.E., Jin, M. & Frank, E.H. Cartilage tissue remodeling in response to mechanical forces. *Annual review of biomedical engineering* **2**, 691-713 (2000).
39. Guilak, F. & Mow, V.C. The mechanical environment of the chondrocyte: a biphasic finite element model of cell–matrix interactions in articular cartilage. *Journal of biomechanics* **33**, 1663-1673 (2000).
40. Mow, V., Bachrach, N., Setton, L. & Guilak, F. Stress, strain, pressure and flow fields in articular cartilage and chondrocytes. in *Cell Mechanics and Cellular Engineering* 345-379 (Springer, 1994).
41. Frangos, J.A., Eskin, S.G., McIntire, L.V. & Ives, C. Flow effects on prostacyclin production by cultured human endothelial cells. *Science* **227**, 1477-1479 (1985).
42. Chatzizisis, Y.S. et al. Role of endothelial shear stress in the natural history of coronary atherosclerosis and vascular remodeling: molecular, cellular, and vascular behavior. *Journal of the American College of Cardiology* **49**, 2379-2393 (2007).
43. Cox, C., Bavi, N. & Martinac, B. Origin of the Force: The Force-From-Lipids Principle Applied to Piezo Channels. *Current Topics in Membranes* (2016).

44. Moeendarbary, E. & Harris, A.R. Cell mechanics: principles, practices, and prospects. *Wiley Interdisciplinary Reviews: Systems Biology and Medicine* **6**, 371-388 (2014).

45. Iadecola, C. & Davisson, R.L. Hypertension and cerebrovascular dysfunction. *Cell metabolism* **7**, 476-484 (2008).

46. Intengan, H.D. & Schiffrin, E.L. Vascular remodeling in hypertension roles of apoptosis, inflammation, and fibrosis. *Hypertension* **38**, 581-587 (2001).

47. Martinac, B. Mechanosensitive ion channels: an evolutionary and scientific tour de force in mechanobiology. *Channels (Austin)* **6**, 211-3 (2012).

48. Sukharev, S. & Sachs, F. Molecular force transduction by ion channels: diversity and unifying principles. *J Cell Sci* **125**, 3075-83 (2012).

49. Wang, W. et al. Fluid shear stress stimulates phosphorylation-dependent nuclear export of HDAC5 and mediates expression of KLF2 and eNOS. *Blood* **115**, 2971-2979 (2010).

50. Na, S. et al. Rapid signal transduction in living cells is a unique feature of mechanotransduction. *Proceedings of the National Academy of Sciences* **105**, 6626-6631 (2008).

51. Honore, E., Martins, J.R., Penton, D., Patel, A. & Demolombe, S. The Piezo Mechanosensitive Ion Channels: May the Force Be with You! *Rev Physiol Biochem Pharmacol* **169**, 25-41 (2015).

52. Freund, J.B. & Vermot, J. The wall-stress footprint of blood cells flowing in microvessels. *Biophysical journal* **106**, 752-762 (2014).

53. Fettiplace, R. Is TMC1 the Hair Cell Mechanotransducer Channel? *Biophysical Journal* **111**, 3-9 (2016).

54. Fettiplace, R. & Kim, K.X. The physiology of mechanoelectrical transduction channels in hearing. *Physiological reviews* **94**, 951-986 (2014).

55. Vollrath, M.A., Kwan, K.Y. & Corey, D.P. The micromachinery of mechanotransduction in hair cells. *Annual review of neuroscience* **30**, 339 (2007).

56. Corns, L.F., Johnson, S.L., Kros, C.J. & Marcotti, W. Tmc1 Point Mutation Affects Ca2+ Sensitivity and Block by Dihydrostreptomycin of the Mechanoelectrical Transducer Current of Mouse Outer Hair Cells. *J Neurosci* **36**, 336-49 (2016).

57. Zhang, W. et al. Ankyrin Repeats Convey Force to Gate the NOMPC Mechanotransduction Channel. *Cell* **162**, 1391-403 (2015).

58. Jensen, M.O. & Mouritsen, O.G. Lipids do influence protein function-the hydrophobic matching hypothesis revisited. *Biochim Biophys Acta* **1666**, 205-26 (2004).

59. Cantor, R.S. The lateral pressure profile in membranes: a physical mechanism of general anesthesia. *Toxicol Lett* **100-101**, 451-8 (1998).

60. Marsh, D. Lateral pressure profile, spontaneous curvature frustration, and the incorporation and conformation of proteins in membranes. *Biophysical journal* **93**, 3884-3899 (2007).

61. Mukherjee, N. et al. The activation mode of the mechanosensitive ion channel, MscL, by lysophosphatidylcholine differs from tension-induced gating. *FASEB J* **28**, 4292-302 (2014).

62. Servin-Vences, M.R., Moroni, M., Lewin, G.R. & Poole, K. Direct measurement of TRPV4 and PIEZO1 activity reveals multiple mechanotransduction pathways in chondrocytes. *eLife* **6**, e21074 (2017).

63. Beurg, M., Kim, K.X. & Fettiplace, R. Conductance and block of hair-cell mechanotransducer channels in transmembrane channel-like protein mutants. *J Gen Physiol* **144**, 55-69 (2014).

64. Katta, S., Krieg, M. & Goodman, M.B. Feeling force: physical and physiological principles enabling sensory mechanotransduction. *Annu Rev Cell Dev Biol* **31**, 347-71 (2015).

65. Martinac, B. et al. Bacterial Mechanosensitive Channels: Models for Studying Mechanosensory Transduction. *Antioxid Redox Signal* (2013).

66. Berrier, C., Besnard, M., Ajouz, B., Coulombe, A. & Ghazi, A. Multiple mechanosensitive ion channels from Escherichia coli, activated at different thresholds of applied pressure. *Journal of Membrane Biology* **151**, 175-187 (1996).

67. Perozo, E. & Rees, D.C. Structure and mechanism in prokaryotic mechanosensitive channels. *Current opinion in structural biology* **13**, 432-442 (2003).

68. Schumann, U. et al. YbdG in Escherichia coli is a threshold-setting mechanosensitive channel with MscM activity. *Proceedings of the National Academy of Sciences* **107**, 12664-12669 (2010).

69. Prager-Khoutorsky, M., Khoutorsky, A. & Bourque, C.W. Unique interweaved microtubule scaffold mediates osmosensory transduction via physical interaction with TRPV1. *Neuron* **83**, 866-78 (2014).

70. Teng, J., Loukin, S.H., Anishkin, A. & Kung, C. L596-W733 bond between the start of the S4-S5 linker and the TRP box stabilizes the closed state of TRPV4 channel. *Proc Natl Acad Sci U S A* **112**, 3386-91 (2015).

71. Huynh, K.W. et al. Structure of the full-length TRPV2 channel by cryo-EM. *Nat Commun* **7**, 11130 (2016).

72. Ronan, D. & Gillespie, P. Metazoan mechanotransduction mystery finally solved. *Nature neuroscience* **8**, 7-8 (2005).

73. Gillespie, P.G. & Muller, U. Mechanotransduction by hair cells: models, molecules, and mechanisms. *Cell* **139**, 33-44 (2009).

74. Coste, B. et al. Piezo proteins are pore-forming subunits of mechanically activated channels. *Nature* **483**, 176-81 (2012).

75. Coste, B. et al. Piezo1 and Piezo2 are essential components of distinct mechanically activated cation channels. *Science* **330**, 55-60 (2010).

76. Chalfie, M. Neurosensory mechanotransduction. *Nature reviews Molecular cell biology* **10**, 44-52 (2009).

77. Steinbacher, S., Bass, R., Strop, P., and Rees, D.C. Structures of the prokaryotic mechanosensitive channels MscL and MscS. in *Mechanosensitive Ion Channels, Part A* (ed. Hamill, O.P.) 1–24 (Elsevier Academic Press, Inc., San Diego, 2007).

78. Chang, G., Spencer, R.H., Lee, A.T., Barclay, M.T. & Rees, D.C. Structure of the MscL homolog from Mycobacterium tuberculosis: a gated mechanosensitive ion channel. *Science* **282**, 2220-6 (1998).

79. Brohawn, S.G., del Marmol, J. & MacKinnon, R. Crystal structure of the human K2P TRAAK, a lipid- and mechano-sensitive K+ ion channel. *Science* **335**, 436-41 (2012).

80. Dong, Y.Y. et al. K2P channel gating mechanisms revealed by structures of TREK-2 and a complex with Prozac. *Science* **347**, 1256-9 (2015).

81. Ge, J. et al. Architecture of the mammalian mechanosensitive Piezo1 channel. *Nature* **527**, 64-9 (2015).

82. Zubcevic, L. et al. Cryo-electron microscopy structure of the TRPV2 ion channel. *Nat Struct Mol Biol* **23**, 180-6 (2016).

83. Liao, M., Cao, E., Julius, D. & Cheng, Y. Structure of the TRPV1 ion channel determined by electron cryo-microscopy. *Nature* **504**, 107-12 (2013).

84. Teng, J., Loukin, S., Anishkin, A. & Kung, C. The force-from-lipid (FFL) principle of mechanosensitivity, at large and in elements. *Pflügers Archiv-European Journal of Physiology* **467**, 27-37 (2015).

85. Kung, C. A possible unifying principle for mechanosensation. *Nature* **436**, 647-54 (2005).

86. Martinac, B., Adler, J. & Kung, C. Mechanosensitive ion channels of E. coli activated by amphipaths. *Nature* **348**, 261-3 (1990).

87. Sukharev, S.I., Blount, P., Martinac, B., Blattner, F.R. & Kung, C. A large-conductance mechanosensitive channel in E. coli encoded by mscL alone. *Nature* **368**, 265-8 (1994).

88. Sukharev, S. Purification of the small mechanosensitive channel of Escherichia coli (MscS): the subunit structure, conduction, and gating characteristics in liposomes. *Biophys J* **83**, 290-8 (2002).

89. Hase, C.C., Le Dain, A.C. & Martinac, B. Purification and functional reconstitution of the recombinant large mechanosensitive ion channel (MscL) of Escherichia coli. *J Biol Chem* **270**, 18329-34 (1995).

90. Delcour, A.H., Martinac, B., Adler, J. & Kung, C. Modified reconstitution method used in patch-clamp studies of Escherichia coli ion channels. *Biophys J* **56**, 631-6 (1989).

91. Sukharev, S.I., Martinac, B., Arshavsky, V.Y. & Kung, C. Two types of mechanosensitive channels in the Escherichia coli cell envelope: solubilization and functional reconstitution. *Biophys J* **65**, 177-83 (1993).

92. Brohawn, S.G., Campbell, E.B. & MacKinnon, R. Physical mechanism for gating and mechanosensitivity of the human TRAAK K+ channel. *Nature* **516**, 126-30 (2014).

93. Brohawn, S.G., Su, Z. & MacKinnon, R. Mechanosensitivity is mediated directly by the lipid membrane in TRAAK and TREK1 K+ channels. *Proc Natl Acad Sci U S A* **111**, 3614-9 (2014).

94. Berrier, C. et al. The purified mechanosensitive channel TREK-1 is directly sensitive to membrane tension. *J Biol Chem* **288**, 27307-14 (2013).

95. Cox, C.D. et al. Removal of the mechanoprotective influence of the cytoskeleton reveals PIEZO1 is gated by bilayer tension. *Nat Commun* **7**, 10366 (2016).

96. Syeda, R. et al. Chemical activation of the mechanotransduction channel Piezo1. *Elife* **4**(2015).

97. Zheng, J. Molecular mechanism of TRP channels. *Compr Physiol* **3**, 221-42 (2013).

98. O'Conor, C.J., Leddy, H.A., Benefield, H.C., Liedtke, W.B. & Guilak, F. TRPV4-mediated mechanotransduction regulates the metabolic response of chondrocytes to dynamic loading. *Proc Natl Acad Sci U S A* **111**, 1316-21 (2014).

99. Loukin, S., Zhou, X., Su, Z., Saimi, Y. & Kung, C. Wild-type and brachyolmia-causing mutant TRPV4 channels respond directly to stretch force. *J Biol Chem* **285**, 27176-81 (2010).

100. Liedtke, W. et al. Vanilloid receptor-related osmotically activated channel (VR-OAC), a candidate vertebrate osmoreceptor. *Cell* **103**, 525-35 (2000).

101. Sabass, B. & Stone, H.A. Role of the membrane for mechanosensing by tethered channels. *arXiv preprint arXiv:1603.05751* (2016).

102. Zhang, W., Yan, Z., Jan, L.Y. & Jan, Y.N. Sound response mediated by the TRP channels NOMPC, NANCHUNG, and INACTIVE in chordotonal organs of Drosophila larvae. *Proc Natl Acad Sci U S A* **110**, 13612-7 (2013).

103. Yan, Z. et al. Drosophila NOMPC is a mechanotransduction channel subunit for gentle-touch sensation. *Nature* **493**, 221-5 (2013).

104. Gao, Y., Cao, E., Julius, D. & Cheng, Y. TRPV1 structures in nanodiscs reveal mechanisms of ligand and lipid action. *Nature* **534**, 347-351 (2016).

105. Pan, B. et al. TMC1 and TMC2 are components of the mechanotransduction channel in hair cells of the mammalian inner ear. *Neuron* **79**, 504-15 (2013).

106. Kim, K.X. & Fettiplace, R. Developmental changes in the cochlear hair cell mechanotransducer channel and their regulation by transmembrane channel-like proteins. *J Gen Physiol* **141**, 141-8 (2013).

107. Gao, X. et al. Novel compound heterozygous TMC1 mutations associated with autosomal recessive hearing loss in a Chinese family. *PLoS One* **8**, e63026 (2013).

108. Kawashima, Y., Kurima, K., Pan, B., Griffith, A.J. & Holt, J.R. Transmembrane channel-like (TMC) genes are required for auditory and vestibular mechanosensation. *Pflugers Arch* **467**, 85-94 (2015).

109. Chatzigeorgiou, M., Bang, S., Hwang, S.W. & Schafer, W.R. tmc-1 encodes a sodium-sensitive channel required for salt chemosensation in C. elegans. *Nature* **494**, 95-9 (2013).

110. Delling, M. et al. Primary cilia are not calcium-responsive mechanosensors. *Nature* **531**, 656-60 (2016).

111. Hudspeth, A. Integrating the active process of hair cells with cochlear function. *Nature Reviews Neuroscience* **15**, 600-614 (2014).

112. Zhao, B. & Müller, U. The elusive mechanotransduction machinery of hair cells. *Current opinion in neurobiology* **34**, 172-179 (2015).

113. O'Hagan, R., Chalfie, M., Goodman, M.B.. The MEC-4 DEG/ENaC channel of Caenorhabditis elegans touch receptor neurons transduces mechanical signals. *Nature Neurosci.* **8**, 43-50 (2005).

114. Kellenberger, S. & Schild, L. Epithelial sodium channel/degenerin family of ion channels: a variety of functions for a shared structure. *Physiol Rev* **82**, 735-67 (2002).

115. Stockand, J.D. Degenerin/ENaC channels. in *Handbook of Ion Channels* (eds. Zheng, J. & Trudeau, M.C.) (Taylor & Francis Group, FL, USA, 2015).

116. Ross, S.B., Fuller, C.M., Bubien, J.K. & Benos, D.J. Amiloride-sensitive Na+ channels contribute to regulatory volume increases in human glioma cells. *American Journal of Physiology-Cell Physiology* **293**, C1181-C1185 (2007).

117. Martinac, B. The ion channels to cytoskeleton connection as potential mechanism of mechanosensitivity. *Biochim Biophys Acta* (2013).

118. Eastwood, A.L. et al. Tissue mechanics govern the rapidly adapting and symmetrical response to touch. *Proc Natl Acad Sci U S A* **112**, E6955-63 (2015).

119. Atkins, P. & De Paula, J. *Physical chemistry for the life sciences*, (Oxford University Press, USA, 2011).

120. Poole, K., Moroni, M. & Lewin, G.R. Sensory mechanotransduction at membrane-matrix interfaces. *Pflugers Arch* **467**, 121-32 (2015).

121. Maksaev, G., Milac, A., Anishkin, A., Guy, H.R. & Sukharev, S. Analyses of gating thermodynamics and effects of deletions in the mechanosensitive channel TREK-1: comparisons with structural models. *Channels (Austin)* **5**, 34-42 (2011).

122. Sukharev, S.I., Sigurdson, W.J., Kung, C. & Sachs, F. Energetic and spatial parameters for gating of the bacterial large conductance mechanosensitive channel, MscL. *J Gen Physiol* **113**, 525-40 (1999).

123. Sukharev, S. & Corey, D.P. Mechanosensitive channels: multiplicity of families and gating paradigms. *Sci STKE* **2004**, re4 (2004).

124. Phillips, R., Ursell, T., Wiggins, P. & Sens, P. Emerging roles for lipids in shaping membrane-protein function. *Nature* **459**, 379-385 (2009).

125. Battle, A.R. et al. Lipid–protein interactions: Lessons learned from stress. *Biochimica et Biophysica Acta (BBA)-Biomembranes* **1848**, 1744-1756 (2015).

126. Boal, D. & Boal, D.H. *Mechanics of the Cell*, (Cambridge University Press, 2012).

127. Gruenheid, S. & Finlay, B.B. Microbial pathogenesis and cytoskeletal function. *Nature* **422**, 775-781 (2003).

128. Satcher Jr, R.L. & Dewey Jr, C.F. Theoretical estimates of mechanical properties of the endothelial cell cytoskeleton. *Biophysical journal* **71**, 109 (1996).

129. Knowles, T.P. et al. Role of intermolecular forces in defining material properties of protein nanofibrils. *Science* **318**, 1900-1903 (2007).

130. Giesa, T., Arslan, M., Pugno, N.M. & Buehler, M.J. Nanoconfinement of spider silk fibrils begets superior strength, extensibility, and toughness. *Nano letters* **11**, 5038-5046 (2011).

131. Bavi, N. et al. Biophysical implications of lipid bilayer rheometry for mechanosensitive channels. *Proc Natl Acad Sci U S A* **111**, 13864-9 (2014).

132. Bertaud, J., Hester, J., Jimenez, D.D. & Buehler, M.J. Energy landscape, structure and rate effects on strength properties of alpha-helical proteins. *Journal of Physics: Condensed Matter* **22**, 035102 (2009).

133. Pliotas, C. et al. The role of lipids in mechanosensation. *Nat Struct Mol Biol* **22**, 991-8 (2015).

134. Bavi, N., Cox, C.D., Perozo, E. & Martinac, B. Towards a structural blueprint for bilayer-mediated channel mechanosensitivity. *Channels* **11**, 91-93 (2016).

135. Laganowsky, A. et al. Membrane proteins bind lipids selectively to modulate their structure and function. *Nature* **510**, 172-5 (2014).

136. Zhong, D. & Blount, P. Phosphatidylinositol is crucial for the mechanosensitivity of Mycobacterium tuberculosis MscL. *Biochemistry* **52**, 5415-20 (2013).

137. Cantor, R.S. Lipid composition and the lateral pressure profile in bilayers. *Biophys J* **76**, 2625-39 (1999).

138. Evans, E., Rawicz, W. & Smith, B. Concluding remarks back to the future: mechanics and thermodynamics of lipid biomembranes. *Faraday discussions* **161**, 591-611 (2013).

139. Mukhin, S.I. & Baoukina, S. Analytical derivation of thermodynamic characteristics of lipid bilayer from a flexible string model. *Physical Review E* **71**, 061918 (2005).

140. Gullingsrud, J. & Schulten, K. Lipid bilayer pressure profiles and mechanosensitive channel gating. *Biophys J* **86**, 3496-509 (2004).

141. Gawrisch, K. & Holte, L.L. NMR investigations of non-lamellar phase promoters in the lamellar phase state. *Chemistry and physics of lipids* **81**, 105-116 (1996).

142. Templer, R.H., Castle, S.J., Curran, A.R., Rumbles, G. & Klug, D.R. Sensing isothermal changes in the lateral pressure in model membranes using di-pyrenyl phosphatidylcholine. *Faraday discussions* **111**, 41-53 (1999).

143. Cantor, R.S. The lateral pressure profile in membranes: a physical mechanism of general anesthesia. *Biochemistry* **36**, 2339-44 (1997).

144. Harries, D. & Ben-Shaul, A. Conformational chain statistics in a model lipid bilayer: comparison between mean field and Monte Carlo calculations. *The Journal of chemical physics* **106**, 1609-1619 (1997).

145. Baoukina, S., Marrink, S.J. & Tieleman, D.P. Lateral pressure profiles in lipid monolayers. *Faraday discussions* **144**, 393-409 (2010).

146. Lindahl, E. & Edholm, O. Mesoscopic undulations and thickness fluctuations in lipid bilayers from molecular dynamics simulations. *Biophysical journal* **79**, 426-433 (2000).

147. Elmore, D.E. & Dougherty, D.A. Investigating lipid composition effects on the mechanosensitive channel of large conductance (MscL) using molecular dynamics simulations. *Biophysical journal* **85**, 1512-1524 (2003).

148. Yoo, J. & Cui, Q. Curvature generation and pressure profile modulation in membrane by lysolipids: insights from coarse-grained simulations. *Biophys J* **97**, 2267-76 (2009).

149. Markin, V.S. & Sachs, F. Thermodynamics of mechanosensitivity. *Phys Biol* **1**, 110-24 (2004).

150. Wiggins, P. & Phillips, R. Membrane-protein interactions in mechanosensitive channels. *Biophys J* **88**, 880-902 (2005).

151. Wiggins, P. & Phillips, R. Analytic models for mechanotransduction: gating a mechanosensitive channel. *Proceedings of the National Academy of Sciences* **101**, 4071-4076 (2004).

152. Im, W., Feig, M. & Brooks, C.L. An implicit membrane generalized born theory for the study of structure, stability, and interactions of membrane proteins. *Biophysical journal* **85**, 2900-2918 (2003).

153. Sonne, J., Hansen, F.Y. & Peters, G.H. Methodological problems in pressure profile calculations for lipid bilayers. *The Journal of chemical physics* **122**, 124903 (2005).

154.   Lee, A.G. How lipids affect the activities of integral membrane proteins. *Biochim Biophys Acta* **1666**, 62-87 (2004).

155.   Lundbaek, J.A., Collingwood, S.A., Ingolfsson, H.I., Kapoor, R. & Andersen, O.S. Lipid bilayer regulation of membrane protein function: gramicidin channels as molecular force probes. *J R Soc Interface* **7**, 373-95 (2010).

156.   Bavi, N. et al. The role of MscL amphipathic N terminus indicates a blueprint for bilayer-mediated gating of mechanosensitive channels. *Nat Commun* **7**, 11984 (2016).

157.   Bochicchio, D. & Monticelli, L. Chapter Five-The Membrane Bending Modulus in Experiments and Simulations: A Puzzling Picture. *Advances in Biomembranes and Lipid Self-Assembly* **23**, 117-143 (2016).

158.   Dimova, R. Recent developments in the field of bending rigidity measurements on membranes. *Advances in colloid and interface science* **208**, 225-234 (2014).

159.   Evans, E. & Rawicz, W. Entropy-driven tension and bending elasticity in condensed-fluid membranes. *Physical Review Letters* **64**, 2094 (1990).

160.   Henriksen, J., Rowat, A.C. & Ipsen, J.H. Vesicle fluctuation analysis of the effects of sterols on membrane bending rigidity. *European Biophysics Journal* **33**, 732-741 (2004).

161.   Esposito, C. et al. Flicker spectroscopy of thermal lipid bilayer domain boundary fluctuations. *Biophysical journal* **93**, 3169-3181 (2007).

162.   Mecke, K.R., Charitat, T. & Graner, F. Fluctuating lipid bilayer in an arbitrary potential: theory and experimental determination of bending rigidity. *Langmuir* **19**, 2080-2087 (2003).

163.   Gracià, R.S., Bezlyepkina, N., Knorr, R.L., Lipowsky, R. & Dimova, R. Effect of cholesterol on the rigidity of saturated and unsaturated membranes: fluctuation and electrodeformation analysis of giant vesicles. *Soft Matter* **6**, 1472-1482 (2010).

164.   Lee, C.-H., Lin, W.-C. & Wang, J. All-optical measurements of the bending rigidity of lipid-vesicle membranes across structural phase transitions. *Physical Review E* **64**, 020901 (2001).

165.   Schönherr, H., Johnson, J.M., Lenz, P., Frank, C.W. & Boxer, S.G. Vesicle adsorption and lipid bilayer formation on glass studied by atomic force microscopy. *Langmuir* **20**, 11600-11606 (2004).

166.   Genova, J., Vitkova, V. & Bivas, I. Registration and analysis of the shape fluctuations of nearly spherical lipid vesicles. *Physical Review E* **88**, 022707 (2013).

167.   Monzel, C. & Sengupta, K. Measuring shape fluctuations in biological membranes. *Journal of Physics D: Applied Physics* **49**, 243002 (2016).

168.   Bouvrais, H., Holmstrup, M., Westh, P. & Ipsen, J.H. Analysis of the shape fluctuations of reconstituted membranes using GUVs made from lipid extracts of invertebrates. *Biology open* **2**, 373-378 (2013).

169.   Heftberger, P., Kollmitzer, B., Rieder, A.A., Amenitsch, H. & Pabst, G. In situ determination of structure and fluctuations of coexisting fluid membrane domains. *Biophysical journal* **108**, 854-862 (2015).

170.   Evans, E. & Needham, D. Physical properties of surfactant bilayer membranes: thermal transitions, elasticity, rigidity, cohesion and colloidal interactions. *Journal of Physical Chemistry* **91**, 4219-4228 (1987).

171.   Li, J. et al. Piezo1 integration of vascular architecture with physiological force. *Nature* **515**, 279-82 (2014).

172.   Et-Thakafy, O. et al. Mechanical properties of membranes composed of gel-phase or fluid-phase phospholipids probed on liposomes by atomic force spectroscopy. *Langmuir* (2017).

173.   Evans, E. & Rawicz, W. Elasticity of ``Fuzzy''Biomembranes. *Physical review letters* **79**, 2379 (1997).

174. Rawicz, W., Olbrich, K., McIntosh, T., Needham, D. & Evans, E. Effect of chain length and unsaturation on elasticity of lipid bilayers. *Biophysical journal* **79**, 328-339 (2000).

175. Needham, D. & Nunn, R.S. Elastic deformation and failure of lipid bilayer membranes containing cholesterol. *Biophysical journal* **58**, 997 (1990).

176. Pandit, K.R. & Klauda, J.B. Membrane models of E. coli containing cyclic moieties in the aliphatic lipid chain. *Biochimica et Biophysica Acta (BBA)-Biomembranes* **1818**, 1205-1210 (2012).

177. Deng, Y., Sun, M. & Shaevitz, J.W. Direct measurement of cell wall stress stiffening and turgor pressure in live bacterial cells. *Physical Review Letters* **107**, 158101 (2011).

178. Cayley, D.S., Guttman, H.J. & Record, M.T. Biophysical characterization of changes in amounts and activity of Escherichia coli cell and compartment water and turgor pressure in response to osmotic stress. *Biophysical Journal* **78**, 1748-1764 (2000).

179. Nomura, T. et al. Differential effects of lipids and lyso-lipids on the mechanosensitivity of the mechanosensitive channels MscL and MscS. *Proc Natl Acad Sci U S A* **109**, 8770-5 (2012).

180. Nakayama, Y., Slavchov, R.I., Bavi, N. & Martinac, B. The Energy of Liposome Patch Adhesion to the Pipette Glass Determined by Confocal Fluorescence Microscopy. *The Journal of Physical Chemistry Letters* (2016).

181. Opsahl, L.R. & Webb, W.W. Lipid-glass adhesion in giga-sealed patch-clamped membranes. *Biophys J* **66**, 75-9 (1994).

182. Slavchov, R.I., Nomura, T., Martinac, B., Sokabe, M. & Sachs, F. Gigaseal mechanics: creep of the gigaseal under the action of pressure, adhesion, and voltage. *The Journal of Physical Chemistry B* **118**, 12660-12672 (2014).

183. Sun, Y., Sun, T.-L. & Huang, H.W. Physical properties of Escherichia coli spheroplast membranes. *Biophysical journal* **107**, 2082-2090 (2014).

184. Feller, S.E. Molecular dynamics simulations of lipid bilayers. *Current opinion in colloid & interface science* **5**, 217-223 (2000).

185. Feller, S.E. & Pastor, R.W. Constant surface tension simulations of lipid bilayers: the sensitivity of surface areas and compressibilities. *The Journal of chemical physics* **111**, 1281-1287 (1999).

186. Iglič, A., Kulkarni, C. & Rappolt, M. Advances in Biomembranes and Lipid self-assembly-volume 23. (Elsevier, 2016).

187. Nomura, T., Cox, C.D., Bavi, N., Sokabe, M. & Martinac, B. Unidirectional incorporation of a bacterial mechanosensitive channel into liposomal membranes. *FASEB J* **29**, 4334-45 (2015).

188. Blount, P., Sukharev, S.I., Moe, P. & Kung, C. Mechanosensitive channels of E. coli: a genetic and molecular dissection. *Biol Bull* **192**, 126-7 (1997).

189. Vasquez, V., Sotomayor, M., Cordero-Morales, J., Schulten, K. & Perozo, E. A structural mechanism for MscS gating in lipid bilayers. *Science* **321**, 1210-4 (2008).

190. Perozo, E., Kloda, A., Cortes, D.M. & Martinac, B. Physical principles underlying the transduction of bilayer deformation forces during mechanosensitive channel gating. *Nat Struct Biol* **9**, 696-703 (2002).

191. Sukharev, S., Betanzos, M., Chiang, C.S. & Guy, H.R. The gating mechanism of the large mechanosensitive channel MscL. *Nature* **409**, 720-4 (2001).

192. Iscla, I., Wray, R. & Blount, P. On the structure of the N-terminal domain of the MscL channel: helical bundle or membrane interface. *Biophys J* **95**, 2283-91 (2008).

193. Syeda, R. et al. Piezo1 channels are inherently mechanosensitive. *Cell reports* **17**, 1739-1746 (2016).

194. Lee, E.H., Hsin, J., Sotomayor, M., Comellas, G. & Schulten, K. Discovery through the computational microscope. *Structure* **17**, 1295-1306 (2009).

195. Phillips, J.C. et al. Scalable molecular dynamics with NAMD. *Journal of computational chemistry* **26**, 1781-1802 (2005).

196.   van der Spoel, D. et al. GROMACS user manual version 3.3. (2008).
197.   Lindahl, E., Hess, B. & Van Der Spoel, D. GROMACS 3.0: a package for molecular simulation and trajectory analysis. *Journal of molecular modeling* **7**, 306-317 (2001).
198.   Sansom, M.S., Scott, K.A. & Bond, P.J. Coarse-grained simulation: a high-throughput computational approach to membrane proteins. *Biochemical Society Transactions* **36**, 27-32 (2008).
199.   Sansom, M. & Hedger, G. Lipid interaction sites on channels, transporters and receptors: recent insights from molecular dynamics simulations. *BBA-Biomembranes* (2016).
200.   Zhuang, X., Dávila-Contreras, E.M., Beaven, A.H., Im, W. & Klauda, J.B. An extensive simulation study of lipid bilayer properties with different head groups, acyl chain lengths, and chain saturations. *Biochimica et Biophysica Acta (BBA)-Biomembranes* **1858**, 3093-3104 (2016).
201.   Pavlova, A., Hwang, H., Lundquist, K., Balusek, C. & Gumbart, J.C. Living on the edge: Simulations of bacterial outer-membrane proteins. *Biochimica et Biophysica Acta (BBA)-Biomembranes* **1858**, 1753-1759 (2016).
202.   Van Der Spoel, D. et al. GROMACS: fast, flexible, and free. *Journal of computational chemistry* **26**, 1701-1718 (2005).
203.   Sawada, Y. & Sokabe, M. Molecular dynamics study on protein–water interplay in the mechanogating of the bacterial mechanosensitive channel MscL. *European Biophysics Journal* **44**, 531-543 (2015).
204.   Sawada, Y., Murase, M. & Sokabe, M. The gating mechanism of the bacterial mechanosensitive channel MscL revealed by molecular dynamics simulations: from tension sensing to channel opening. *Channels* **6**, 317-331 (2012).
205.   Vanegas, J.M. & Arroyo, M. Force transduction and lipid binding in MscL: a continuum-molecular approach. *PloS one* **9**, e113947 (2014).
206.   Corry, B. et al. An improved open-channel structure of MscL determined from FRET confocal microscopy and simulation. *J Gen Physiol* **136**, 483-94 (2010).
207.   Gullingsrud, J. & Schulten, K. Gating of MscL studied by steered molecular dynamics. *Biophysical journal* **85**, 2087-2099 (2003).
208.   Gullingsrud, J., Kosztin, D. & Schulten, K. Structural determinants of MscL gating studied by molecular dynamics simulations. *Biophys J* **80**, 2074-81 (2001).
209.   Anishkin, A., Akitake, B., Kamaraju, K., Chiang, C.S. & Sukharev, S. Hydration properties of mechanosensitive channel pores define the energetics of gating. *J Phys Condens Matter* **22**, 454120 (2010).
210.   Anishkin, A. & Sukharev, S. Water dynamics and dewetting transitions in the small mechanosensitive channel MscS. *Biophys J* **86**, 2883-95 (2004).
211.   Aryal, P. et al. Bilayer-Mediated Structural Transitions Control Mechanosensitivity of the TREK-2 K2P Channel. *Structure* **25**, 708-718. e2 (2017).
212.   Teng, J., Loukin, S.H., Anishkin, A. & Kung, C. A competing hydrophobic tug on L596 to the membrane core unlatches S4–S5 linker elbow from TRP helix and allows TRPV4 channel to open. *Proceedings of the National Academy of Sciences* **113**, 11847-11852 (2016).
213.   Chiang, C.S., Anishkin, A. & Sukharev, S. Gating of the large mechanosensitive channel in situ: estimation of the spatial scale of the transition from channel population responses. *Biophys J* **86**, 2846-61 (2004).
214.   Perozo, E., Cortes, D.M., Sompornpisut, P., Kloda, A. & Martinac, B. Open channel structure of MscL and the gating mechanism of mechanosensitive channels. *Nature* **418**, 942-8 (2002).
215.   Meyer, G.R., Gullingsrud, J., Schulten, K. & Martinac, B. Molecular dynamics study of MscL interactions with a curved lipid bilayer. *Biophysical journal* **91**, 1630-1637 (2006).

216. Jo, S., Lim, J.B., Klauda, J.B. & Im, W. CHARMM-GUI Membrane Builder for mixed bilayers and its application to yeast membranes. *Biophysical journal* **97**, 50-58 (2009).
217. Lim, J.B. & Klauda, J.B. Lipid chain branching at the iso-and anteiso-positions in complex chlamydia membranes: A molecular dynamics study. *Biochimica et Biophysica Acta (BBA)-Biomembranes* **1808**, 323-331 (2011).
218. Ingólfsson, H.I. et al. Lipid organization of the plasma membrane. *Journal of the american chemical society* **136**, 14554-14559 (2014).
219. Sotomayor, M. & Schulten, K. Molecular dynamics study of gating in the mechanosensitive channel of small conductance MscS. *Biophys J* **87**, 3050-65 (2004).
220. Bathe, M. A finite element framework for computation of protein normal modes and mechanical response. *Proteins: Structure, Function, and Bioinformatics* **70**, 1595-1609 (2008).
221. Liu, W.K. et al. Immersed finite element method and its applications to biological systems. *Computer methods in applied mechanics and engineering* **195**, 1722-1749 (2006).
222. Zhu, L. et al. Gating mechanism of mechanosensitive channel of large conductance: a coupled continuum mechanical-continuum solvation approach. *Biomechanics and modeling in mechanobiology*, 1-20 (2016).
223. Chen, X., Cui, Q., Tang, Y., Yoo, J. & Yethiraj, A. Gating mechanisms of mechanosensitive channels of large conductance, I: a continuum mechanics-based hierarchical framework. *Biophys J* **95**, 563-80 (2008).
224. Sodt, A.J., Beaven, A.H., Andersen, O.S., Im, W. & Pastor, R.W. Gramicidin A Channel Formation Induces Local Lipid Redistribution II: A 3D Continuum Elastic Model. *Biophysical Journal* **112**, 1198-1213 (2017).
225. Chatzieleftheriou, S., Adendorff, M.R. & Lagaros, N.D. Generalized Potential Energy Finite Elements for Modeling Molecular Nanostructures. *Journal of Chemical Information and Modeling* **56**, 1963-1978 (2016).
226. Bavi, O., Vossoughi, M., Naghdabadi, R. & Jamali, Y. The effect of local bending on gating of MscL using a representative volume element and finite element simulation. *Channels (Austin)* **8**, 344-9 (2014).
227. Bavi, O., Vossoughi, M., Naghdabadi, R. & Jamali, Y. The Combined Effect of Hydrophobic Mismatch and Bilayer Local Bending on the Regulation of Mechanosensitive Ion Channels. *PLoS One* **11**, e0150578 (2016).
228. Beckstein, O. & Sansom, M.S. Liquid-vapor oscillations of water in hydrophobic nanopores. *Proc Natl Acad Sci U S A* **100**, 7063-8 (2003).
229. Sakmann, B. *Single-channel recording*, (Springer Science & Business Media, 2013).
230. Nilius, B. Pflugers Archiv and the advent of modern electrophysiology. From the first action potential to patch clamp. *Pflugers Arch* **447**, 267-71 (2003).
231. Safronov, B.V. & Vogel, W. Electrical activity of individual neurons: patch-clamp techniques. in *Modern Techniques in Neuroscience Research* 173-192 (Springer, 1999).
232. Hamill, O. Twenty odd years of stretch-sensitive channels. *Pflügers Archiv* **453**, 333-351 (2006).
233. Hamill, O.P., Marty, A., Neher, E., Sakmann, B. & Sigworth, F.J. Improved patch-clamp techniques for high-resolution current recording from cells and cell-free membrane patches. *Pflugers Arch* **391**, 85-100 (1981).
234. Shaikh, S., Cox, C.D., Nomura, T. & Martinac, B. Energetics of gating MscS by membrane tension in azolectin liposomes and giant spheroplasts. *Channels (Austin)* **8**(2014).

CHAPTER 2

In the first chapter, it was reviewed that lipid bilayers have a central role in structural integrity (stability) and function of not only mechanosensitive (MS) channels but membrane proteins in general. In this chapter, a multidisciplinary approach was used, combining continuum mechanics theories and computer simulation with experimental methodologies such as patch fluorometry and single molecule patch-clamp electrophysiology, to characterise the overall rheological behaviour of lipid bilayers. This information is essential to understand the basics of cell mechano-transduction, wherein the lipid bilayer plays a key role. Specifically, this study introduces a novel conceptual framework, based on excised patch fluorometry. This new superior experimental paradigm enables the study of the mechanical properties of lipid bilayers more accurately, which is also free of the issues encountered when using the traditional micropipette aspiration technique (as discussed in section 5.1.2 of Chapter 1). This study also proposes a new hyper-elastic model, which is superior at describing the overall behavior of lipid bilayers, in comparison to the traditional model used in conjunction with micropipette aspiration. These findings are important when considering patch-clamp electrophysiology as a paradigm for the study of all types of ion channels, in particular MS channels.

Biophysical implications of lipid bilayer rheometry for mechanosensitive channels

Navid Bavi[a,b], Yoshitaka Nakayama[b], Omid Bavi[c], Charles D. Cox[b], Qing-Hua Qin[d], and Boris Martinac[a,b,1]

[a]St. Vincent's Clinical School, Faculty of Medicine, University of New South Wales, Darlinghurst, NSW 2010, Australia; [b]Molecular Cardiology and Biophysics Division, Victor Chang Cardiac Research Institute, Darlinghurst, NSW 2010, Australia; [c]Institute for Nanoscience and Nanotechnology, Sharif University of Technology, 8969414588 Tehran, Iran; and [d]Research School of Engineering, Australian National University, Canberra, ACT 0200, Australia

The lipid bilayer plays a crucial role in gating of mechanosensitive (MS) channels. Hence it is imperative to elucidate the rheological properties of lipid membranes. Herein we introduce a framework to characterize the mechanical properties of lipid bilayers by combining micropipette aspiration (MA) with theoretical modeling. Our results reveal that excised liposome patch fluorometry is superior to traditional cell-attached MA for measuring the intrinsic mechanical properties of lipid bilayers. The computational results also indicate that unlike the uniform bilayer tension estimated by Laplace's law, bilayer tension is not uniform across the membrane patch area. Instead, the highest tension is seen at the apex of the patch and the lowest tension is encountered near the pipette wall. More importantly, there is only a negligible difference between the stress profiles of the outer and inner monolayers in the cell-attached configuration, whereas a substantial difference (~30%) is observed in the excised configuration. Our results have far-reaching consequences for the biophysical studies of MS channels and ion channels in general, using the patch-clamp technique, and begin to unravel the difference in activity seen between MS channels in different experimental paradigms.

MscL | azolectin | electrophysiology | finite element modeling

Liposome reconstitution has been used for both functional and structural studies of bacterial mechanosensitive (MS) channels (MscL and MscS) for many years (1–4) and also more recently for the study of eukaryotic MS channels (5–8). Most frequently azolectin, a crude extract of phospholipids from animal and plant tissue consisting mainly of phosphatidylcholine (PC), phosphatidylethanolamine (PE), and phosphatidylinositol (PI) (9), has been used for liposome preparations. Given the frequent use of azolectin bilayers for the study of MS channels and the importance of protein–lipid interactions in MS channel gating it is imperative to consider the best way to accurately calculate and assess its material properties. This is also essential for studies of voltage- and ligand-gated ion channels as the activity of these proteins can also be modulated by membrane tension (6–8, 10–12).

The mechanical properties of different types of lipids have been studied extensively using the micropipette aspiration (MA) approach (13–18). These experiments have shown that the mechanical properties of lipids differ considerably and that lipid bilayers exhibit elastic behavior (14, 15, 18, 19). The MA technique is versatile and has the advantage of exerting a wide range of aspiration pressures on a specific portion of a bilayer (20–23). Here we use this technique in combination with finite-element (FE) simulation to examine in depth the mechanical properties of azolectin bilayers in both cell-attached and excised patch configurations (SI Materials and Methods). It is widely known that lipid behavior is vastly different at low (<0.5 mN/m) compared with high tensions, due to thermal shape fluctuations (24). Given that the midpoint activation of most MS channels is higher than 1 mN/m [e.g., ~12 mN/m for MscL (25, 26) and ~6.0 mN/m for MscS (26, 27)], characterizing the behavior of lipid bilayers at high-tension ranges is a necessity and is the focus of this study. To do this we introduce two alternative models (elastic and hyperelastic). These models have the advantage, over the traditional

model, of including in the calculations the boundary conditions caused by a rigid cylindrical pipette and no assumption for volume conservation during MA. The material properties resulting from these models were imported separately into a continuum FE model (Fig. S1 A–C). This permitted comparisons between the FE model parameters and experimentally derived results to define the best description of the continuum behavior of azolectin bilayers. Using our alternative models, we compare the membrane tension in an azolectin liposome patch estimated using Laplace's law with the membrane tension obtained from our computations. Furthermore, the stress–strain distribution within the patch area for cell-attached and excised configurations has been compared. We discuss how these findings may provide integral information about a widely used experimental and theoretical paradigm used to study MS channels.

Results and Discussion

To probe the material properties of azolectin bilayers we used patch fluorometry. This technique involves slowly aspirating a lipid membrane into a micropipette, measuring the geometry of the patch, recording the pressure inside the pipette during aspiration, P, and then calculating the liposome's surface tension and areal strain to determine its mechanical properties, i.e., areal elastic modulus. In this study, to estimate material parameters from patch fluorometry data, the experimental deformation history was fitted to three different analytical models. These models represent different assumptions, namely, (i) model 1, traditionally used in conjunction with MA (28) (based on an equibiaxial tension assumption); (ii) model 2, linear elastic (based on a uniaxial tension assumption); and (iii) model 3, hyperelastic (neo-Hookean)

> **Significance**
>
> Given the extensive use of lipid bilayer reconstitution for the study of mechanosensitive channels, it is imperative to understand the biophysical properties of lipid bilayers. We have theoretically and experimentally proven that the traditional micropipette aspiration method fails to accurately describe these properties. Herein we introduce a superior framework, which combines computational modeling with patch fluorometry for the assessment of bilayer properties. Our results show the limitations of Laplace's law for estimation of tension within a patch membrane. We also demonstrate, in contrast to the cell-attached configuration, there is a significant difference between the stress developed in the outer and in the inner monolayers of the bilayer in the excised patch configuration. These results are of critical importance for patch-clamp electrophysiology in general.

(*SI Materials and Methods*). For each model we describe the physical parameters calculated for azolectin membrane bilayers under mechanical stress. Although cell membranes are composed of various lipids and proteins and as such are not homogeneous, in this study we examined the continuum behavior of azolectin lipid bilayers, which are a good model, mimicking the basic mechanical properties of cell membranes (26). The framework set out can be applied to any type of lipid bilayer.

Cell-Attached Patch Fluorometry. Initially we investigated the material properties of azolectin liposomes containing 0.1% rhodamine-PE, using cell-attached patch fluorometry. During these experiments, due to the shear rigidity of lipid vesicles, below a certain pressure, the vesicle was only marginally deformed by suction. Above this threshold pressure, however, the vesicle moved into the pipette until it reached a point of equilibrium, specifically a pressurized spherical geometry, where area dilation was required for further entry (14). After equilibrium, liposomes were aspirated by applying negative pressure up to a maximum pressure of −20 mmHg in increments of −5 mmHg (Movie S1). At each pressure, the length of liposome patches inside the pipette was measured (Fig. 1 *A* and *B*). Our experiments indicated that in some cases the radius of curvature of the liposome patch was slightly larger than the radius of the pipettes used. Hence, to provide an accurate estimation, the method used to calculate membrane tension in stretched membrane patches based on Laplace's law (14, 16) had to be modified with regard to the radius of the liposome patch (*SI Materials and Methods* and Fig. S1 *D–F*).

After modification of Laplace's law for the tension calculation, we first assessed the material properties, using model 1. Linear slopes in measurements of area dilation at high tensions were used in the early 1980s as elastic (Hookean) moduli, characterizing the bilayer area-stretch response (28). The membrane area increases linearly as the membrane undulations are reduced by the increasing pressure difference across the pipette opening. Using model 1, from the slopes of the plots of applied tension vs. areal

strain, the areal elasticity modulus, K_A, of ∼45.5 ± 5 mN/m was calculated (Fig. S2*A*). Thus, we calculated the average Young's modulus of azolectin to be ∼13 MPa for small vesicles in the diameter range of 5–8 μm (Table 1 and Fig. S2*A*). Surprisingly, these values increased with vesicle size, i.e., 14–20 μm. Elastic modulus is related to bending rigidity, k_b, through $k_b = Et^3/24$, where t is the bilayer thickness (18, 29, 30). Therefore, the k_b for small vesicles (diameter 5–8 μm) was 2.32 × 10⁻²⁰ J (Table 1). These values were much smaller than those of larger azolectin vesicles as well as values previously reported for other types of lipids (15).

Although a patch fluorometry experiment does not exhibit all of the ideal uniaxial conditions, one could consider this experiment as a uniaxial tensile test. If we look at the liposome behavior on the patch scale (>1 μm, range of pipette radius) rather than on the lipid raft scale (10–200 nm) (31), the cylindrical pipette disallows the expansion of lipid in the radial direction. Hence, a uniaxial assumption is more appropriate than an equibiaxial assumption for obtaining the stress–strain relationship (*SI Materials and Methods*). Using the elastic uniaxial assumption (model 2), the nominal stress–strain experimental results are presented in Fig. S2*B*. From the slopes of these plots we calculated a Young's modulus of ∼2.5 MPa, which was much lower than that determined by the traditional MA approach (model 1) (Table S1) but very close to what has been measured for egg yolk lipid bilayers (32). This means that model 1 described much stiffer behavior for small azolectin vesicles.

Given that elastic material models are intended for elastic strains that usually remain small (<5–10%) and hyperelastic material models are more appropriate for most biological materials, particularly at large strain magnitudes (>5%) (33), we fitted a linear constitutive hyperelastic model, the neo-Hookean model (model 3, *SI Materials and Methods*), to our experimental data (Fig. 1*C*). In this model, the strain energy density, U, is a linear function of deviatoric strain invariants, $\bar{I}_1$, and can be derived as

$$U = \frac{G(\bar{I}_1 - 3)}{2}, \qquad [1]$$

where G is the shear modulus. Unlike the liposome areal change in the longitudinal direction, the area of the patch dome within the pipette does not change notably at any equilibrium position. As a result, one may simplify the boundary and loading conditions inside the pipette as illustrated in Fig. S3. Because the rigid cylindrical pipette does not allow any growth of the patch area in the radial direction, $\lambda_1 = 1$. Consequently, due to the boundary conditions of the liposome bilayer within the pipette and the incompressibility of azolectin lipid, $\lambda_3 = 1/\lambda_2 = 1/\lambda$. Hence, the stress in the longitudinal direction could be expressed as (*SI Materials and Methods* and Fig. S3)

$$\sigma = \frac{\partial U}{\partial \lambda} = G\left(\lambda - \frac{1}{\lambda^3}\right). \qquad [2]$$

Based on Eq. **2**, the slope of stress vs. a function of the longitudinal stretch ratio, $\lambda - 1/\lambda^3$, shows the shear modulus of the azolectin bilayer (∼1 MPa; Fig. 1*C* and Table 1).

Next, we imported the material properties estimated using models 1–3 into our computational model to see which were the best for describing the continuum behavior of azolectin lipids during aspiration (Fig. 2 *A* and *B*). This was achieved by comparing the computed liposome projection lengths, ΔL, with those observed during patch fluorometry (Table S1). All FE computations were carried out using identical geometries, meshes, loads, and boundary conditions typical of experimental patch fluorometry conditions, including identical liposome diameters, micropipette diameters, and applied pressures (*SI Materials and Methods*). FE solutions were obtained successfully for all three models at corresponding pressures to those used in the cell-attached patch fluorometry experiments (Table S1 and Movie S2). Model 1 predicted
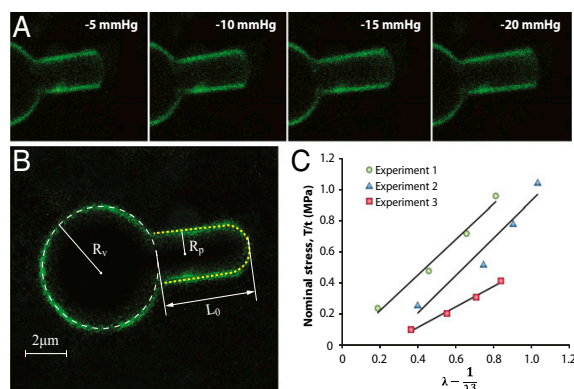

Fig. 1. Representative cell-attached patch fluorometry experiment. (*A*) Confocal images of azolectin liposomal membranes fluorescently labeled by addition of 0.1% rhodamine-PE being stretched by applying four negative pressure steps of −5 to −20 mmHg. (*B*) L_0 is the initial projection length, and R_v and R_p denote the radius of the liposome and the micropipette, respectively. (*C*) Stress–strain relationship from the patch fluorometry experiment shows the variation of the nominal in-plane stress in the membrane with respect to a function of the longitudinal stretching ratio, $\lambda - 1/\lambda^3$, for three azolectin lipid vesicles of similar diameter (6–8 μm). The relationship is fitted using the linear neo-Hookean hyperelastic model (model 3). λ is the stretching ratio in the longitudinal direction (along the length of the micropipette). These diagrams demonstrate a linear relation between the change in the nominal stress of lipid and the term $\lambda - 1/\lambda^3$. The slope allows us to calculate the shear modulus, which is ∼1.0 MPa. R^2 values are 0.98, 0.94, and 0.99 for experiments 1, 2, and 3, respectively.

BIOPHYSICS AND
COMPUTATIONAL BIOLOGY

Table 1. Material parameters obtained from curve fitting of patch fluorometry data (cell-attached and excised patch configurations)

Models	Linear elastic, biaxial	Linear elastic, uniaxial	Hyperelastic, neo-Hookean
Small vesicles, diameter 5–8 μm			
C_{10}, MPa	—	—	0.5 ± 0.15
E(MPa)	13.0 ± 1.5	3.0 ± 0.7	10.5 ± 3
K_A, mN/m	45.5 ± 5	3.0 ± 0.8	10.5 ± 3
k_b (J) $\times 10^{21}$	23 ± 3	5.4 ± 1.3	5.4 ± 1.6
Large vesicles, diameter 14–20 μm			
C_{10}, MPa	—	—	0.7 ± 11
E(MPa)	32.1 ± 8.0	4.2 ± 1.5	4.1 ± 0.7
K_A, mN/m	112.2 ± 29	14.6 ± 5	14.4 ± 2
k_b (J) $\times 10^{21}$	57.0 ± 15	7.4 ± 1.9	7.3 ± 1.2
Excised patches			
C_{10}, MPa	—	—	0.7 ± 0.07
E(MPa)	4.5 ± 0.6	4.4 ± 0.5	4.3 ± 0.4
K_A, mN/m	15.8 ± 2	15.5 ± 2	15.0 ± 2
k_b (J) $\times 10^{21}$	8.1 ± 1.1	7.9 ± 0.9	7.6 ± 0.8

C_{10} is the neo-Hookean material parameter. E and G represent Young's and the shear moduli, respectively. In the case of lipids, the Poisson ratio is assumed to be 0.5, and then $E = 3G$. k_b denotes the bending rigidity. All of the data are presented in the form of mean $\pm$ SEM.

ΔL values that were far below the experimental values at all pressures. These results clearly show that the material properties obtained based on model 1 (assuming the lipid bilayer as a single elastic slab) are much stiffer than the real behavior of the azolectin lipid bilayers during aspiration. Use of model 2 resulted in ΔL values that were in better agreement with those obtained using patch fluorometry. The neo-Hookean material model (model 3) was the most appropriate model for describing the continuum behavior of the azolectin liposomes (Table S1). The principal difference between models 2 and 3 is the consideration of more realistic boundary conditions during derivation of the equations. The main difference between the introduced models (models 2 and 3) and the traditional model (model 1) is the lack of assumption of preserved internal vesicle volume and inclusion of boundary conditions in our calculations for the membrane patch inside the micropipette (15, 34) with both of these being important for the calculation of areal strain (*SI Materials and Methods*).

Although models 2 and 3 provided an excellent representation of the continuum behavior of azolectin liposomes, there were minor discrepancies between the computational and experimental results. These small differences possibly originate from the adhesion tension (35) dependency on the applied pressures within the pipette (36), which for simplicity our FE models did not consider.

Excised Patch Fluorometry. Due to the wide use of the excised patch configuration in the electrophysiological studies of MS channels, we also investigated the material properties of azolectin bilayers, using excised patch fluorometry (Movie S3). There has been a discussion in the literature (37, 38) about the existence of pretension in lipid vesicles (without any concentration or pressure gradient across the membrane). Our results indicate considerable pretension even in small vesicles, which is magnified in larger vesicles (Table S2). Aside from experimental simplicity, excised patch fluorometry has the major benefit of reducing this pretension and more importantly allows suppression of the thermodynamic effects related to volume changes and thermal undulations ("wiggles") (19, 24, 28, 34, 39), which may affect the rheological behavior of liposomal membranes. Importantly, unlike the cell-attached technique (Fig. 2 and Table S2), in excised patch fluorometry experiments the material properties obtained from all three theoretical models were very similar (Fig. 3 *A* and *B*, Fig. S4 *A* and *B*, and Table 1). The areal elasticity modulus, K_A, for excised azolectin bilayers is ~15 mN/m. Moreover, comparisons performed between the experimentally measured aspiration lengths of azolectin lipid and those simulated using the neo-Hookean model (model 3) were in very good agreement (Fig. 3C and Fig. S4 *C* and *D*).

Tension Distribution in Cell-Attached Membrane Patches. As model 3 resulted in the best description of azolectin rheometry in both configurations, it was used in the following computational stress analysis, which includes investigating tension distribution and deformation of azolectin liposome patches during aspiration. The maximum in-plane stress is highest in the apex, reducing to zero around the site where the micropipette is normally connected to the liposome (Fig. 2*A* and Movie S2). The largest effective stress field was found in the vicinity of the membrane normal contact with the edge of the micropipette as well as in the apex (Fig. 2*B*). From this we suggest that these two areas are the most likely places for lipid rupture initiation during aspiration. Given that we assumed the pipette to have a smooth tip, which it does not (40), the most likely place for the rupture initiation in a cell-attached system is near the pipette tip rather than the apex of the patch. From comparison of the vertical displacement field and the in-plane maximum principal strain the apex of the patch had the greatest vertical displacement whereas the elements near the liposome–pipette contact region had the largest strain (Fig. S5). This implies that when a local stress is produced in this area, the lipid membrane is unable to reconfigure itself and reduce the strain. Consequently, it restricts the movement of the elements (in FE simulation) and likely the phospholipids of the membrane (in reality) (18), thereby facilitating membrane rupture (Fig. S3). Hence, the computational results show that the response is mostly dominated by local stretching of the liposome rather than by its shear and/or bending effects near this normal contact area. In fact, the lipid membrane expands in the principal in-plane directions and shrinks in the thickness direction to maintain a constant volume; i.e., $\Delta A/A = -\Delta t/t$, where A and t are the area and the thickness of the bilayer, respectively. These stress and deformation analyses of geometrically realistic liposomes could be used for an accurate estimation of stresses and strains and to facilitate prospective studies of the role of stress in lipid bilayer rupture during aspiration, particularly relevant for patch-clamp electrophysiology.

Subsequently, we compared the tension values acquired from our FE simulations with those estimated by two widely used forms of Laplace's law (Eqs. S1 and S18) to assess their levels of accuracy (Fig. 2C). The maximum in-plane tension variation in the membrane, obtained from FE simulations, at three negative pressure steps of −10 mmHg, −20 mmHg, and −30 mmHg in the whole patch area is shown in Fig. 3C. Based on the geometry of
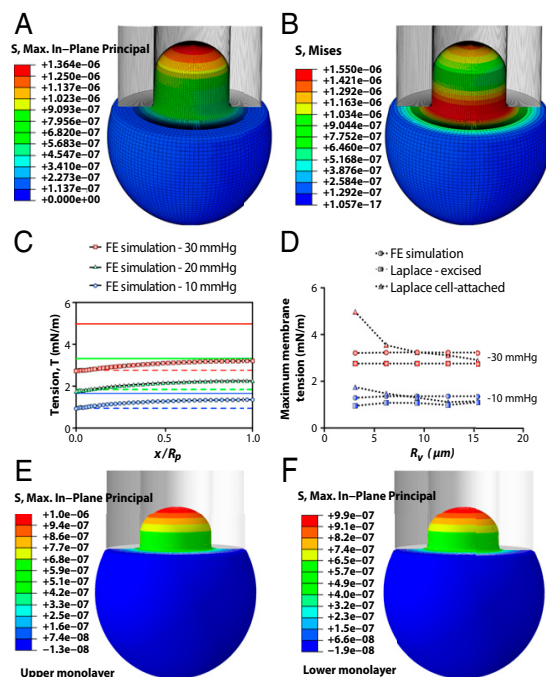
Fig. 2. Spatial profiles of an aspirated liposome calculated using FE simulation. The vesicle has a diameter of 6.2 μm. The inner diameter of the micropipette is 2.8 μm (both are typical sizes encountered experimentally). The suction starts from 0 and reaches a value of −30 mmHg (~4 kPa), instantaneously (in 0.01 s), and is then kept constant for 0.01 s. The computations are performed for the material parameters of C_{10} = 0.5 MPa and k_b = 5.36 × 10^{-21} J (neo-Hookean model). (A) In-plane maximum principal stress (N/μm² distribution; maximum membrane tensional stress, σ_{max}, in the apex and the minimum membrane tension, 0.6 σ_{max}, close to the pipette wall has also been illustrated). (B) Effective stress (von Mises stress) field. (C) Comparison of membrane tension, T, at different points in the patch area using FE analysis in conjunction with the relevant Laplace's equations for excised patch and cell-attached configurations. FE results demonstrate that there is a differential distribution of tension within a patch; with the above-mentioned geometrical properties, the cell-attached Laplace equation (solid lines) (Eq. S1) is an overestimation of the membrane tension, whereas the excised patch equation (dashed lines) (Eq. S18) underestimates the tension developed in the patch area (x axis: 0, membrane–pipette contact point; 1, patch apex). (D) Comparison of the maximum membrane tensions (in the apex) obtained from FE computation and Laplace's law formulation at two negative pressures (blue, 10 mmHg; red, 20 mmHg) and for different vesicle sizes, R_v. This result illustrates that R_v is not affecting the actual tension distribution in the patch. However, as R_v increases, the accuracy of Eq. S1 improves up to the point where R_v = ~9 μm. For much larger vesicles (i.e., R_v > 15 μm), the results from both forms of Laplace's equation are equal and both underestimate the actual distributed tension in the patch (Fig. S6). (E and F) Spatial profiles of the in-plane stress in an aspirated liposome illustrated in the upper (outer) monolayer and the lower (inner) monolayer, respectively. It is the same model as described in A and B, except that here, each monolayer of the bilayer has been modeled as a separate shell that can slide against another shell. Moreover, the material behavior of the inner and outer layers in the current computational model has two more material constants: their relaxation time of 0.01 and their relaxation shear modulus ratio of 0.9 (SI Materials and Methods).

the deformed patch from our simulations at each pressure, we calculated the theoretical tension using Laplace's formulation for the cell-attached configuration using Eq. S1, as well as the relevant form for excised patches using Eq. S18. Our results indicate that the tension value estimated by Eq. S18 was always an underestimation of the maximum actual tension developed in the patch (Fig. 2 C and D). In contrast, the value obtained from Eq. S1 was always above the actual tension for relatively small

vesicles (i.e., R_v < 9 μm) and was below the actual tension for larger vesicles. However, both equations provided similar results when the radius of the vesicle was much greater than the micropipette radius, i.e., R_v/R_p > 15 (Fig. 2D and Fig. S6). In contrast to the assumption provided by both equations, the membrane tensional stress was not uniform at different points within the patch area. The highest value is found in the patch apex and the lowest near the pipette wall. These findings were true of a wide range of vesicles, from 3 μm to 16 μm, and are important for the study of MS channels using the patch-clamp technique. Additionally, we modeled the liposome membrane as two independent monolayers being able to slide relative to each other and normally restrained by van der Waals force. We compared the stress–strain profile in the two monolayers under ramp pressure, considering the internal and intermonolayer damping of our model bilayer (SI Materials and Methods). Our results indicate a negligible difference (<2%)
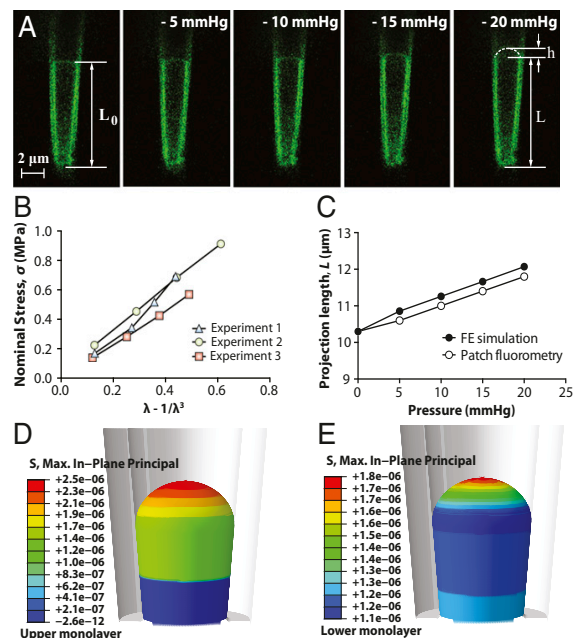

Fig. 3. Excised patch fluorometry. (A) Confocal images of a representative excised liposome patch fluorometry experiment. Rhodamine-PE–labeled azolectin liposome excised patch membranes were stretched by applying four negative pressure steps of −5 mmHg to −20 mmHg through the micropipette. L_0 is the initial projection length, L is the deformed projection length of the liposome membrane, and h is the height of the patch dome. (B) Variation of the nominal in-plane stress in the membrane with respect to the unidirectional strain term $\lambda - 1/\lambda^3$ based on the neo-Hookean hyperelastic model. λ is the unidirectional stretching ratio in the longitudinal direction. These diagrams demonstrate a linear relation between the change in the nominal stress of lipid and the strain term $\lambda - 1/\lambda^3$. (C) Validation of the simulations with the observations from patch fluorometry experiments. Comparisons were made between the measured aspiration lengths of azolectin lipid inside the pipette and those simulated using the neo-Hookean hyperelastic model. The inner diameters of the micropipette are typical sizes encountered experimentally. The computations were performed for the material parameters of C_{10} = 0.71 MPa and k_b = 5.36 × 10^{-21} J (SI Materials and Methods). (D and E) Spatial profiles of the in-plane stress in an excised liposome patch shown in the upper (outer) monolayer and the lower (inner) monolayer, respectively. The computations were performed for the material parameters of C_{10} = 0.71 MPa and k_b = 5.36 × 10^{-21} J (SI Materials and Methods). It is the same model as model described in C, except that here, each monolayer of the bilayer has been modeled as a separate surface that can slide against another surface. Moreover, the material behavior of the inner and outer layers in the current computational model has two more material constants: their relaxation time of 0.01 and their relaxation shear modulus ratio of 0.9 (SI Materials and Methods).

BIOPHYSICS AND COMPUTATIONAL BIOLOGY

between the stress profiles of the two monolayers in the cell-attached model (Fig. 2 *E* and *F*). These results are valid for different loading rates and/or material properties (*SI Materials and Methods*).

Tension Distribution in Excised Membrane Patches. As well as investigating the stress distribution in the membrane in the cell-attached configuration we also studied simulations of the excised patch configuration (Figs. 3 *D* and *E* and 4*A*). Similar to what we simulated for the cell-attached configuration, we modeled the liposome bilayer as two separate monolayers in an excised patch system. Interestingly, unlike the cell-attached results (Fig. 2 *E* and *F*), the peak stress in the upper leaflet is ∼30% higher than that in the inner leaflet (Fig. 3 *D* and *E*). This dissimilarity may explain differences in activity seen for some MS channels between the cell-attached and excised patch configurations. For example, it may explain the apparent adaptation upon a sustained pressure pulse observed experimentally with both MscL (1) and MscS channels (41) in excised liposome patches. In this experiment we pressurized an excised patch lipid bilayer containing MscL with a tapered pipette. Analogous to cell-attached results, membrane tension reduced from a maximum value in the apex of the patch to its minimum close to the pipette wall (Fig. 4*A*). In Movie S4 we illustrate how the distribution of tension changed in the membrane during the application of negative pressure. This observation together with our patch-clamp results may explain the very interesting biophysical phenomenon of sequential gating of MscL (Fig. 4 *B* and *C*), which may well be relevant for other MS channels. Our electrophysiology recordings demonstrated that when we gradually increased the pressure up to a certain point (i.e., −35 mmHg), the resulting tension was just enough to activate a few channels probably clustered in the apex (highly stressed). As the pressure rose, the area that had reached or passed the activation threshold of MscL increased and thus there was a higher probability for a larger cohort of channels in the patch area to gate. This trend continued until the stress value in the whole patch area exceeded the activation threshold of MscL. At this point the maximum saturating

current, a composite of the activity of all functional channels in the patch area, was recorded (Fig. 4*B*). Moreover, the gating kinetics of MscL under ramp pressure were shown as an S-like activation of the cohort of channels in the patch area. Moreover, we examined how MscL was activated under constant pressure close to the activation threshold. When the negative pressure steps increased gradually, first a single channel opened and then several channels were suddenly activated (Fig. 4*C*). This "flare-up activation" also seems consistent with the finding that MscL forms clusters in the liposome membrane as previously shown (42).

It has previously been reported that acyl chain length (and hence initial bilayer thickness) affects the gating of numerous channels including MscL; in the case of MscL shorter acyl chains (PC16) facilitate opening, whereas longer chains (PC20) stabilize the closed state (43). Surprisingly, previous work has shown that altering acyl chain length (PC13–PC22) does not appreciably affect the areal elasticity modulus of a lipid bilayer (19, 28). Thus, we performed a set of simulations to investigate the effect of initial membrane thickness on the stress and tension distribution within the membrane patch area (Figs. S7 and S8). The results show that the initial thickness had no effect on membrane tension, but it had a remarkable impact on bilayer stress. The thinner the lipid bilayer, the higher the stress was at any given pressure. Moreover, the stress variation over the patch area was also steeper. We believe that these simulations complement and compound the previous reports of lipid chain length on MscL activity by explaining the effect of bilayer thickness on tensional stress (43, 44).

Conclusions

In summary, patch fluorometry in combination with continuum mechanics modeling has clearly shown that the traditional widely used model (model 1) describes much stiffer continuum behavior for azolectin liposomes, and likely other lipids, during aspiration. The alternative elasticity models we introduce (models 2 and 3) differ principally from the old model (model 1) in the calculation of areal strain, resulting in a more realistic description of the rheological behavior of azolectin lipids. To make sure that the inaccuracy arises from the calculation of areal strain in the traditional approach (model 1), we used excised patch fluorometry, to remove this assumption during the calculation of areal strain. The material properties obtained from these experiments were very similar for all three theoretical models. This confirms the notion that the way that areal strain is calculated in the traditional model is not accurate. Thus, we require new theoretical models to interpret data obtained from the cell-attached MA technique, with our neo-Hookean model (model 3) being a good example. In addition, excised patch fluorometry seems to be an excellent experimental paradigm for investigating the mechanical properties of lipids. Based on our FE simulations we also conclude that although Laplace's law gives a good approximation of membrane tension in a patch membrane by assuming a constant tension within the patch area, this is not a true reflection of the experimental scenario. First, application of Laplace's law leads to an overall underestimation of the bilayer tension in excised patch membranes, whereas for the cell-attached equation its accuracy depends on the radius of the individual liposome. Furthermore, Laplace's law neglects the integral fact that membrane tension is actually decreasing from its maximum value in the apex of the patch dome to its minimum value near the pipette wall. This may be one of the reasons for sequential activation of MscL channels when their activity is recorded upon application of a pressure ramp. More importantly, we showed that unlike in cell-attached configuration, the difference between the stress profiles of the two monolayers of a liposome bilayer is significantly different in the excised patch configuration (∼30%). There is higher stress in the upper monolayer in comparison with the lower one. These results should facilitate prospective studies on the role of bilayer stress not only in the gating of MS channels, but also of voltage- and ligand-gated ion channels. They also caution against the
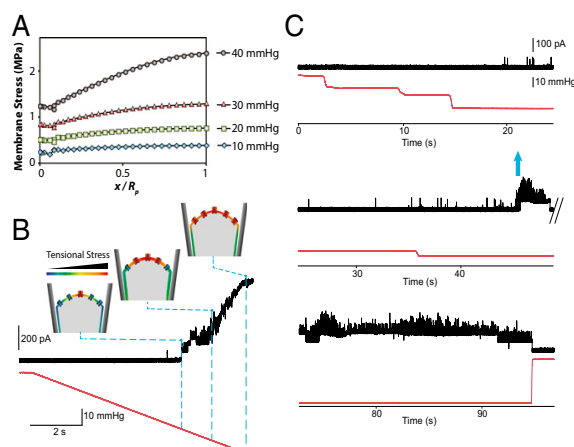

Fig. 4. MS channels in the center of the patch sense a higher tensional stress than the channels close to the pipette wall. (*A*) In-plane maximum principal stress (MPa) distribution in a conical pipette. FE results demonstrate that there is a differential distribution of tensional stress within a patch: maximum membrane tensional stress, σ_{max}, in the apex and minimum tensional stress, $0.6\ \sigma_{max}$, close to the pipette wall (more details about the FE computations in Figs. S7 and S8). (*B*) Activation of MscL under a pressure ramp. Currents were recorded at a pipette voltage of +20 mV in a recording solution containing 200 mM KCl, 40 mM MgCl$_2$, and 5 mM Hepes-KOH, the gating kinetics of MscL under ramp pressure applied to the patch membrane. (*C*) "Flare-up" activation of MscL under the application of increasing pressure steps (blue arrow). Applied pressure (mmHg) is shown in red.

extrapolation of MS channel behavior from one experimental paradigm to another.

Materials and Methods

Liposome Preparation and Patch Fluorometry. Liposomes made of azolectin [99.9% (wt/wt)] and rhodamine-PE [0.1% (wt/wt)] were prepared using the Nanion Vesicle Prep Pro device. Lipids dissolved in chloroform were placed on electrodes and an electrical field of 5 Hz and 3 V was applied for 120 min. For visualizing the creep, the tips of glass pipettes were bent ~30°, using a microforge (Narishige) to make them parallel to the bottom of the chamber, and images of patch membranes were taken using a confocal microscope (*SI Materials and Methods*). All of the data are expressed in the form of mean ± SEM. To suppress adhesion tension between the glass and lipid bilayer, we coated the pipette with 0.1% BSA (Movie S5).

Electrophysiology. Liposomes were prepared by the dehydration/rehydration (D/R) method and the MscL proteins were incorporated in the ratio of protein to lipids (1:1,000) as previously described (1, 45). Channel currents were recorded with an AxoPatch 1D amplifier and negative pressure was applied with a syringe or a High Speed Pressure Clamp-1 apparatus (HSPC-1; Ala Scientific) (*SI Materials and Methods*).

Finite-Element Modeling. Details of the computational models can be found in *SI Materials and Methods*. Given the geometric nonlinearities that had to be taken into consideration, we used commercial finite-element analysis (FEA) software (Abaqus/Standard; Dassault Systemes Simulia) for simulations as well as for prediction of the stress and strain distribution in azolectin liposomes exposed to pipette aspiration (Movies S2, S4, S6 and S7). To address the limitations of applying all of the forms of Laplace's law to calculate membrane tension in membrane patches, FE models of pure azolectin liposomes for both cell-attached (MA technique) and excised patch (patch-clamp experiment) configurations based on their related patch fluorometry data were developed. This approach has been widely used to model micropipette aspiration for several different cell types (46–50).

1. Häse CC, Le Dain AC, Martinac B (1995) Purification and functional reconstitution of the recombinant large mechanosensitive ion channel (MscL) of Escherichia coli. *J Biol Chem* 270(31):18329–18334.
2. Cruickshank CC, Minchin RF, Le Dain AC, Martinac B (1997) Estimation of the pore size of the large-conductance mechanosensitive ion channel of Escherichia coli. *Biophys J* 73(4):1925–1931.
3. Martinac B (2011) Bacterial mechanosensitive channels as a paradigm for mechanosensory transduction. *Cell Physiol Biochem* 28(6):1051–1060.
4. Cox CD, et al. (2013) Selectivity mechanism of the mechanosensitive channel MscS revealed by probing channel subconducting states. *Nat Commun* 4:2137.
5. Maroto R, et al. (2005) TRPC1 forms the stretch-activated cation channel in vertebrate cells. *Nat Cell Biol* 7(2):179–185.
6. Brohawn SG, Su Z, MacKinnon R (2014) Mechanosensitivity is mediated directly by the lipid membrane in TRAAK and TREK1 K+ channels. *Proc Natl Acad Sci USA* 111(9):3614–3619.
7. Kloda A, Martinac B, Adams DJ (2007) Polymodal regulation of NMDA receptor channels. *Channels* 1(5):334–343.
8. Berrier C, et al. (2013) The purified mechanosensitive channel TREK-1 is directly sensitive to membrane tension. *J Biol Chem* 288(38):27307–27314.
9. Hamill OP, Martinac B (2001) Molecular basis of mechanotransduction in living cells. *Physiol Rev* 81(2):685–740.
10. Schmidt D, del Mármol J, MacKinnon R (2012) Mechanistic basis for low threshold mechanosensitivity in voltage-dependent K+ channels. *Proc Natl Acad Sci USA* 109(26):10352–10357.
11. Shcherbatko A, Ono F, Mandel G, Brehm P (1999) Voltage-dependent sodium channel function is regulated through membrane mechanics. *Biophys J* 77(4):1945–1959.
12. Tabarean IV, Juranka P, Morris CE (1999) Membrane stretch affects gating modes of a skeletal muscle sodium channel. *Biophys J* 77(2):758–774.
13. Evans E, Needham D (1986) Giant vesicle bilayers composed of mixtures of lipids, cholesterol and polypeptides. Thermomechanical and (mutual) adherence properties. *Faraday Discuss Chem Soc* (81):267–280.
14. Evans E, Needham D (1987) Physical properties of surfactant bilayer membranes: Thermal transitions, elasticity, rigidity, cohesion and colloidal interactions. *J Phys Chem* 91(16):4219–4228.
15. Needham D, Evans E (1988) Structure and mechanical properties of giant lipid (DMPC) vesicle bilayers from 20 degrees C below to 10 degrees C above the liquid crystal-crystalline phase transition at 24 degrees C. *Biochemistry* 27(21):8261–8269.
16. Evans E, Rawicz W (1997) Elasticity of "fuzzy" biomembranes. *Phys Rev Lett* 79(12):2379–2382.
17. Boumann HA, et al. (2009) Biophysical properties of membrane lipids of anammox bacteria: I. Ladderane phospholipids form highly organized fluid membranes. *Biochim Biophys Acta* 1788(7):1444–1451.
18. Rodowicz KA, Francisco H, Layton B (2010) Determination of the mechanical properties of DOPC:DOPS liposomes using an image procession algorithm and micropipette-aspiration techniques. *Chem Phys Lipids* 163(8):787–793.
19. Rawicz W, Olbrich KC, McIntosh T, Needham D, Evans E (2000) Effect of chain length and unsaturation on elasticity of lipid bilayers. *Biophys J* 79(1):328–339.
20. Evans EA, La Celle PL (1975) Intrinsic material properties of the erythrocyte membrane indicated by mechanical analysis of deformation. *Blood* 45(1):29–43.
21. Evans EA (1985) Molecular structure and viscoelastic properties of biomembranes. *Festkörperprobleme 25* (Springer, Berlin), pp 735–745.
22. Evans EA (1983) Bending elastic modulus of red blood cell membrane derived from buckling instability in micropipet aspiration tests. *Biophys J* 43(1):27–30.
23. Olbrich K, Rawicz W, Needham D, Evans E (2000) Water permeability and mechanical strength of polyunsaturated lipid bilayers. *Biophys J* 79(1):321–327.
24. Needham D, Nunn RS (1990) Elastic deformation and failure of lipid bilayer membranes containing cholesterol. *Biophys J* 58(4):997–1009.
25. Sukharev SI, Sigurdson WJ, Kung C, Sachs F (1999) Energetic and spatial parameters for gating of the bacterial large conductance mechanosensitive channel, MscL. *J Gen Physiol* 113(4):525–540.
26. Nomura T, et al. (2012) Differential effects of lipids and lyso-lipids on the mechanosensitivity of the mechanosensitive channels MscL and MscS. *Proc Natl Acad Sci USA* 109(22):8770–8775.
27. Shaikh S, Cox CD, Nomura T, Martinac B (2014) Energetics of gating MscS by membrane tension in azolectin liposomes and giant spheroplasts. *Channels* 8(4):321–326.
28. Evans E, Rawicz W, Smith BA (2013) Back to the future: Mechanics and thermodynamics of lipid biomembranes. *Faraday Discuss* 161:591–611.
29. Allen KB, Layton BE (2009) Determination of the forces imposed by micro and nanopipettes during DOPC: DOPS liposome manipulation. *Chem Phys Lipids* 162(1–2):34–52.
30. Bloom M, Evans E, Mouritsen OG (1991) Physical properties of the fluid lipid-bilayer component of cell membranes: A perspective. *Q Rev Biophys* 24(3):293–397.
31. Lingwood D, Simons K (2010) Lipid rafts as a membrane-organizing principle. *Science* 327(5961):46–50.
32. Smeulders JB, Blom C, Mellema J (1990) Linear viscoelastic study of lipid vesicle dispersions: Hard-sphere behavior and bilayer surface dynamics. *Phys Rev A* 42(6):3483–3498.
33. Holzapfel GA, Ogden RW (2006) *Mechanics of Biological Tissue* (Springer, Berlin).
34. Henriksen JR, Ipsen JH (2004) Measurement of membrane elasticity by micro-pipette aspiration. *Eur Phys J E Soft Matter* 14(2):149–167.
35. Suchyna TM, Markin VS, Sachs F (2009) Biophysics and structure of the patch and the gigaseal. *Biophys J* 97(3):738–747.
36. Ursell T, Agrawal A, Phillips R (2011) Lipid bilayer mechanics in a pipette with glass-bilayer adhesion. *Biophys J* 101(8):1913–1920.
37. White SH (1980) Small phospholipid vesicles: Internal pressure, surface tension, and surface free energy. *Proc Natl Acad Sci USA* 77(7):4048–4050.
38. Jähnig F (1996) What is the surface tension of a lipid bilayer membrane? *Biophys J* 71(3):1348–1349.
39. Evans E, Rawicz W (1990) Entropy-driven tension and bending elasticity in condensed-fluid membranes. *Phys Rev Lett* 64(17):2094–2097.
40. Malboubi M, Y Gu, Jiang K (2010) Experimental and simulation study of the effect of pipette roughness on giga-seal formation in patch clamping. *Microelectronic Engineering* 87.5:778–781.
41. Belyy V, Kamaraju K, Akitake B, Anishkin A, Sukharev S (2010) Adaptive behavior of bacterial mechanosensitive channels is coupled to membrane mechanics. *J Gen Physiol* 135(6):641–652.
42. Grage SL, et al. (2011) Bilayer-mediated clustering and functional interaction of MscL channels. *Biophys J* 100(5):1252–1260.
43. Perozo E, Kloda A, Cortes DM, Martinac B (2002) Physical principles underlying the transduction of bilayer deformation forces during mechanosensitive channel gating. *Nat Struct Biol* 9(9):696–703.
44. Phillips R, Ursell T, Wiggins P, Sens P (2009) Emerging roles for lipids in shaping membrane-protein function. *Nature* 459(7245):379–385.
45. Delcour AH, Martinac B, Adler J, Kung C (1989) Modified reconstitution method used in patch-clamp studies of Escherichia coli ion channels. *Biophys J* 56(3):631–636.
46. Sato M, Theret DP, Wheeler LT, Ohshima N, Nerem RM (1990) Application of the micropipette technique to the measurement of cultured porcine aortic endothelial cell viscoelastic properties. *J Biomech Eng* 112(3):263–268.
47. Vaziri A, Mofrad MR (2007) Mechanics and deformation of the nucleus in micropipette aspiration experiment. *J Biomech* 40(9):2053–2062.
48. Jafari Bidhendi A, Korhonen RK (2012) A finite element study of micropipette aspiration of single cells: Effect of compressibility. *Comput Math Methods Med* 2012, 10.1155/2012/192618.
49. Zhou E, Lim C, Quek S (2005) Finite element simulation of the micropipette aspiration of a living cell undergoing large viscoelastic deformation. *Mech Adv Mater Structures* 12(6):501–512.
50. Trickey WR, Baaijens FP, Laursen TA, Alexopoulos LG, Guilak F (2006) Determination of the Poisson's ratio of the cell: Recovery properties of chondrocytes after release from complete micropipette aspiration. *J Biomech* 39(1):78–87.

BIOPHYSICS AND COMPUTATIONAL BIOLOGY

Supporting Information

Bavi et al. 10.1073/pnas.1409011111

SI Materials and Methods

Liposome Preparation and Patch Fluorometry. Liposomes made of azolectin [99.9% (wt/wt)] (P5638; Sigma) and rhodamine-PE [0.1% (wt/wt)] were prepared using a Nanion Vesicle Prep Pro. Briefly, 20 µL of 5 mM lipid dissolved in chloroform and 350 µL of 520 mM D-sorbitol were placed on indium tin oxide (ITO) slides. An alternating electrical field of 5 Hz and 3 V was applied for 120 min to produce liposomes, which were stored at 4 °C. Images of creeping patch membranes were taken using a confocal microscope (LSM 700; Carl Zeiss) equipped with a long working distance water immersion objective (×63; NA 1.15; Carl Zeiss). A 555-nm laser was used to excite the fluorophore and creep of the patch membrane was detected using a long-pass 560-nm filter. Borosilicate glass pipettes (Drummond Scientific) were pulled using a Flaming/Brown pipette puller (P-87; Sutter Instruments) and the tip of each pipette was cut with a microforge (Narishige; MF-900) to a diameter of ∼2 µm. For visualizing the creep, the tip was bent ∼30°, using the microforge to make it parallel to the bottom of the chamber when the pipette was mounted on a micromanipulator (1). Negative pressure steps of −5 mmHg were generated by a High Speed Pressure Clamp-1 apparatus (HSPC-1; ALA Scientific Instruments) and monitored by a piezoelectric pressure transducer (PM015R; World Precision Instruments). To remove adhesion tension, the pipette was filled with 0.1% BSA. After incubation for 30 min at room temperature, the pipette was washed several times with distilled water.

Electrophysiological Experiments. Liposomes were prepared by the dehydration/rehydration (D/R) method (1). Briefly, 2 mg of azolectin lipids (P5638; Sigma) was dissolved in CHCl₃, and nitrogen gas was applied to form lipid films. After suspension in 200 µL D/R buffer [200 mM KCl, 5 mM Hepes (pH 7.2, adjusted with KOH)], the solution was subjected to sonication for 5 min to make lipid clouds, and purified MscL protein was added in the ratio of protein to lipid of 1:1,000 (wt/wt). D/R buffer was added up to 3 mL and the mixture was incubated for 1 h, after which biobeads (Bio-Rad) were added and incubated for a further 3 h to remove the detergent. The solution was centrifuged at $250,000 \times g$ and the pellet was resuspended in 60 µL D/R buffer, spotted onto a glass slide, and dehydrated under vacuum overnight at 4 °C. The dried film was rehydrated with D/R buffer at 4 °C for 3 h and used for the patch-clamp experiment. The channel currents were amplified with an AxoPatch 1D amplifier (Axon Instruments) and data were acquired at a sampling rate of 5 Hz with 2-kHz filtration in the patch solution [200 mM KCl, 40 mM MgCl₂, and 5 mM Hepes (pH 7.2, adjusted with KOH)]. Pressure was applied manually with a syringe for flare-up experiments; ramp pressures were generated by a High Speed Pressure Clamp-1 apparatus (HSPC-1; ALA Scientific Instruments).

Finite-Element Simulation. Finite-element (FE) simulation has been used widely to model the micropipette aspiration technique to study the mechanical behavior of several different cell types (2–6). Given the geometric nonlinearities that had to be taken into consideration, we used commercial finite-element analysis (FEA) software (Abaqus/Standard; Dassault Systems Simulia) for simulations as well as for prediction of the stress and strain distribution in azolectin liposomes and excised membrane patches exposed to pipette aspiration. As the inertial forces were negligible during suction, the procedure was considered quasistatic. The lipid vesicles were assumed to be deformable thin-walled spheres for cell-attached configuration (Fig. S1A). Thin L-shaped shells were used

for the excised patch configuration (Fig. S1 *B* and *C*). All models had a thickness of 3.5 nm (unless otherwise specified), having isotropic and homogeneous material properties, for which the bending deformations are important. Hence, internal pressure causes negligible stretching and shell permeability is less important to the deformation (7) (Fig. S1). We used shell theory for our computational model, because a shell element can sustain bending moments and maintain irregular geometry. Membrane theory failed to explain the deformation of the lipid bilayer under aspirating pressure for either cell-attached or excised patch configurations. This is because, by definition, a membrane cannot sustain a bending moment. Thus, irregular undulations on the membrane surface cannot remain stable without proper constraints. In fact, when membrane elements were used for typical patch geometries, we could not converge to a solution under any reasonable load. Further, even in very low pressures, the patch deforms like a bell rather than having a parabolic or hemispheric shape (typical shapes that can be found in typical experiments). The two-node SAX1 element was used, which is two-node stress/displacement element that uses one point integration of the linear interpolation function for the distribution of loads (ABAQUS 6.11-2). The FE model consisted of 297 and 112 linear axisymmetric elements (SAX1) for the cell-attached and excised patch configurations, respectively. Sensitivity to mesh density (total number of elements and nodes in the computational model) was also studied, meaning the original model was remeshed to obtain meshes of different density. The results were seen to be independent of mesh size, beyond the number of elements stated for each FE model. Our results were also independent of the type of element. For instance, the quadratic three-node element, SAX2, could also be used. Although compared with SAX1 elements, a lower number of SAX2 elements are needed to converge to the results, the chance of simulation abortion (due to severe distortion of elements) was seen to be much higher for SAX2. A finer mesh (maximum aspect ratio of ∼1:7) was used in the current study to accommodate the highly curved geometry near the pipette tip and to avoid distortion of elements. Due to the axisymmetric feature of the problem, we modeled an axisymmetric wire in our FE model. A fillet radius was considered at the opening of the micropipette to mimic the experimentally used micropipettes and to reduce element distortion that would prevent termination of the FE computation (Fig. S1A). Moreover, the fillet radius appeared to have no significant effect on the results as long as the pipette was large enough (3). Symmetrical boundary conditions were used on the liposome, restricting its horizontal movement in the axis of symmetry. As illustrated in Fig. S1, because the micropipette was significantly stiffer than the liposomes, the micropipette was assumed to be rigid and fixed at its reference point (restricted from moving in all translational and rotational directions). Frictionless, hard contact (penalty method), finite sliding, surface-to-surface contact was implemented between the micropipette and the liposome surface. For patch fluorometry experiments in all FE simulations, suction was increased from 0 to its maximum value within 0.05 s for each step. ABAQUS requires Young's modulus, E, and the Poisson ratio, ν, for elastic models, and neo-Hookean material parameters can be expressed in terms of C_{10} and $D1$. E and C_{10} could be obtained experimentally and ν and $D1$ were assumed to be 0.5 and 0, respectively, as lipid bilayers can be considered as almost incompressible materials (8–12). All these values are stated in the relevant legends for each FE simulation.

For viscoelastic materials, ABAQUS uses a Prony series expansion of the dimensionless relaxation modulus. ABAQUS inputs for

viscosity are shear relaxation modulus ratio, bulk modulus, and relaxation time. A parametric set of simulations has been performed. Assuming lipid bilayers as incompressible materials, wide ranges of shear relaxation modulus ratio, g_i (0.1–0.9), and relaxation time, tau_i (10 μs to 1 s), have been considered in our simulations to cover the rheometry of different lipids with different characteristics. When we increase g_i, it means that the long-term shear modulus decreases (more fluid behavior) and if we decrease tau_i, we reduce the rate of transition from the short-term to the long-term modulus. The ABAQUS Analysis User's Manual covers viscoelasticity in detail.

Micropipette Aspiration Technique (Constitutive Model Based on an Equibiaxial Tension Assumption for Liposome Elongation in the Pipette, Model 1). A popular structural model for liposomes assumes that they have mostly elastic behavior. They cannot be simply modeled as a thin liquid film because the hydrocarbon-chain interior of the membrane exhibits elastic behavior when its thickness is varied (13). The use of static analysis was justified here because the timescale of relaxation from viscoelastic effects is on the order of tens of microseconds (10, 14).

During deformation, lipid bilayers bear external loads and resist bending deformation. Membrane mechanical properties have been extensively studied by application of pressure across an aspirated liposome in a glass pipette (micropipette aspiration technique). In those experiments, however, the lipid glass adhesion and seal formation were overlooked (10, 15, 16). Thus, the traditional analytical model used to estimate membrane tension in stretched membrane patches based on Laplace's law had to be modified with regard to the radius of the liposome patch to calculate accurately the membrane tension, T. The membrane tension in the presence of the adhesion tension is expressed as (17, 18)

$$T = \frac{PR_d}{2(1 - R_d/R_v)}. \qquad [\text{S1}]$$

This equation was applied to both the portion of the vesicle inside the micropipette with the inner radius of R_p and that outside the pipette with the radius of R_v. P is the pressure difference between the outside and the inside of the patch; R_d is the local radius of curvature of the patch area, which is equal to $(R_p^2 + h^2)/2h$, and h is the height of the patch dome (Fig. S1 D–F). In the absence of the adhesion tension, a simpler form of Eq. **S1** can be derived for micropipette analysis, where $R_d = R_p$ (7, 15). Obviously the stretching modulus resulting from Eq. **S1** will be higher than the resulting stretching modulus when we use $T = PR_p/2(1 - R_p/R_v)$ to calculate the tension. This is because R_d is always greater than R_p. Thus, for the same strain, higher values of T were obtained at the corresponding tensions.

The resulting membrane strain, α, which is the area change, ΔA, normalized by the initial area, A_0, was calculated as follows:

$$\alpha = \frac{\Delta A}{A_0} \sim \frac{1}{2}\left(\left(\frac{R_p}{R}\right)^2 - \left(\frac{R_p}{R}\right)^3\right)\frac{\Delta L}{R_p}. \qquad [\text{S2}]$$

ΔL is the change in projection length produced by an increase in applied pressure (Fig. S1). Eq. **S2** was deduced with the viable assumption that the internal volume of the vesicle during micropipette aspiration remains constant due to incompressibility of aqueous solution inside the vesicle (15, 19). Following a typical micropipette aspiration protocol, the area stretch elasticity modulus under a high membrane tension regime [when $T > 0.5$ mN/m (20, 21)], K_A, was calculated as follows:

$$K_A = \frac{\Delta T}{\alpha}. \qquad [\text{S3}]$$

ΔT is the change in tension due to the change of negative pressure at each pressure step. Depending on the thickness of the lipid bilayer, we can relate the area stretch elasticity to Young's modulus, using the following expression (Fig. S2A):

$$E = \frac{2K_A(1 - \nu)}{t}. \qquad [\text{S4}]$$

In cases of uniform stretching and bending, the bilayer behaves as an incompressible elastic body (13). Thus, ν is the Poisson ratio that can be assumed to be near 0.5 (8–11) and t is the thickness of the unstressed lipid bilayer. For lipid bilayers (assuming uniform lateral pressure distribution with depth in the uncoupled monolayers), the elastic modulus is related to the bending rigidity, k_b, through $k_b = Et^3/24$, where t is the bilayer thickness (10, 22, 23).

Constitutive Model Based on Uniaxial Linear Elastic Assumption (Model 2). Although the patch fluorometry experiment did not exhibit all ideal uniaxial test conditions, one could consider this experiment as a uniaxial test. If we look at the liposome behavior on the patch scale (>1 μm, range of pipette radius) rather than on the lipid raft scale (10–200 nm) (24), the cylindrical pipette precludes expansion of lipid in the radial direction. Hence, a uniaxial assumption was more appropriate than an equibiaxial assumption for obtaining a stress–strain curve of the lipid during patch fluorometry experiments. In both the traditional and the alternative models, it was assumed that there was no substantial slippage of the lipid molecules from outside the pipette into the pipette during suction (after the initial equilibrium position). Moreover, the effect of the normal force that the pipette exerted on the lipid inside the pipette was disregarded. Although the azolectin lipid showed almost linear elastic behavior, to improve the accuracy of our calculations, the nominal longitudinal strain was linearized as

$$\varepsilon_i = \varepsilon_{i-1} + \frac{\Delta L_i}{L_{i-1}} \quad (\varepsilon_0 = 0 \text{ and } i = 1, 2, 3, 4), \qquad [\text{S5}]$$

where L_0 is the initial projection length and ΔL_i is the change of corresponding projection lengths at each pressure step. Using Eq. **S1**, the nominal tensile stress was also calculated as

$$\sigma = \frac{T}{t}. \qquad [\text{S6}]$$

From the slopes of the plots of the applied tension vs. the nominal longitudinal strain of all of the experimental data obtained in this study, Young's modulus of azolectin lipid could be calculated (Fig. S2B).

Large-Strain Isotropic Hyperelastic Constitutive Model (Model 3). It is important to mention that a hyperelastic material is still an elastic material, which means that it returns to its original form after deformation forces have been removed. The linear elastic coefficients of azolectin liposomes were discussed in the previous section. Given that elastic material models are intended for elastic strains that usually remain small (<5%) and hyperelastic material models are more appropriate for most biological materials, particularly at large strain magnitudes (>5%) (25), we fitted a hyperelastic model to our experimental data and introduced the corresponding coefficients. In fact, herein we show that liposomes could be modeled as a large-strain isotropic hyperelastic material. Hyperelastic materials also are Cauchy elastic, which means that

the stress is determined by the current state of deformation, not by the path or history of deformation. The Cauchy stress can be derived from the strain energy function, which is given by (26)

$$U = \sum_{i+j=1}^{N} C_{ij}(\bar{I}_1 - 3)^i (\bar{I}_2 - 3)^j + \sum_{i=1}^{N} \frac{1}{D_i}(J^{\text{el}} - 1)^{2i} \qquad \textbf{[S7]}$$

(Deviatoric part)   (Volumetric part),

where U is the strain energy per unit of reference volume and i and j are integer numbers. As shown in Eq. **S7**, U contains a deviatoric part and a volumetric part. N is the polynomial order, C_{ij} and D_i are temperature-dependent material parameters, $\bar{I}_i$ are deviatoric strain invariants of the left Cauchy–Green deformation tensor, and J^{el} is the elastic volume ratio. In this section we summarize briefly the equations of incompressible isotropic nonlinear elasticity that are required for comparing the theory with patch fluorometry data. We assume homogeneous deformations that can be classified as pure homogeneous strain, i.e., deformations of the form

$$x_1 = \lambda_1 X_1, \quad x_2 = \lambda_2 X_2, \quad x_3 = \lambda_3 X_3, \qquad \textbf{[S8]}$$

where X_1, X_2, and X_3 are rectangular Cartesian coordinates that identify material particles in some unstressed reference configuration. x_1, x_2, and x_3 are the corresponding coordinates after deformation with respect to the same axes. $\lambda_i (i = 1, 2, 3)$ are the stretch ratios in the principal directions. The first and second deviatoric strain invariants in Eq. **S7** are defined as

$$\bar{I}_1 = \lambda_1^2 + \lambda_2^2 + \lambda_3^2, \quad \bar{I}_2 = \lambda_1^2 \lambda_2^2 + \lambda_2^2 \lambda_3^2 + \lambda_1^2 \lambda_3^2. \qquad \textbf{[S9]}$$

The principal stretch ratios $\lambda_i (i = 1, 2, 3)$ are related to the principal nominal strain ε_i through $\varepsilon_i = \lambda_i - 1$. The principal stretch λ_i can be linearized, as previously explained in Eq. **S5**, to achieve more accuracy. With the assumption of full incompressibility for lipid membranes (7),

$$J^{\text{el}} = \lambda_1 \lambda_2 \lambda_3 = 1. \qquad \textbf{[S10]}$$

Thus, the volumetric part of strain energy (U) becomes equal to zero. The principal Cauchy stresses σ_i ($i = 1, 2, 3$) [defined as force per unit deformed cross-sectional area normal to the x_i ($i = 1, 2, 3$) axis in the deformed configuration] are related to the stretches through U according to the equations

$$\sigma_i = \lambda_i \frac{\partial U}{\partial \lambda_i} - P \quad i = 1, 2, 3. \qquad \textbf{[S11]}$$

However, for calculation of the Cauchy stresses, we need to know the exact thickness at different parts of the patch area during aspiration of the liposomes. To avoid this at this juncture, the corresponding nominal stresses (defined as per unit undeformed cross-sectional area) are the stresses that are often measured directly in experiments and thus are given by (26)

$$\sigma_i = \frac{\partial U}{\partial \lambda_i} - P \lambda_i^{-1} \quad i = 1, 2, 3. \qquad \textbf{[S12]}$$

For an incompressible material it is always possible to superimpose a hydrostatic stress without producing strain and Eq. **S12** changes to

$$\sigma_i = \frac{\partial U}{\partial \lambda_i} \quad i = 1, 2, 3. \qquad \textbf{[S13]}$$

As presented in the following sections, the results show linear behavior for azolectin lipid bilayer (Fig. S2), and we were unable to

perform enough different standard experiments on the liposome vesicles (because of their sensitive properties, size, and form). Here we use the simplest constitutive model, the neo-Hookean model. The neo-Hookean model is the first-order polynomial form of the general hyperelastic model with $N = 1$. It uses only linear functions of the invariants. In this model, the strain energy density is a linear function of deviatoric strain invariants, $\bar{I}_1$ and $\bar{I}_2$, and can be derived from Eq. **S7** as follows:

$$U = C_{10}(\bar{I}_1 - 3). \qquad \textbf{[S14]}$$

In the neo-Hookean model, shear modulus, G, is

$$G = 2C_{10}. \qquad \textbf{[S15]}$$

As a result, we may simplify the boundary and loading conditions inside the pipette as illustrated in Fig. S3. Also the geometry and membrane stresses of the lipid bilayer during a micropipette aspiration experiment are indicated. R_P and σ represent the inner radius of the pipette and the longitudinal stress of the membrane, respectively. L is the length of projection of the lipid inside the micropipette. λ_1 and λ_2 are the stretching ratios in directions 1 (horizontal) and 2 (vertical), respectively. Fig. S3, *Right* depicts the planar form of a liposome with the associated boundary conditions caused by the rigid micropipette. The rigid cylindrical pipette around the patch area prevents any growth of the radius in the portion of the liposome within the pipette, $\lambda_1 = 1$ (Fig. S3). Also, due to the boundary conditions of the liposome bilayer within the pipette and the incompressibility of azolectin lipid, $\lambda_3 = 1/\lambda_2 = 1/\lambda$. Hence, Eq. **S14** can be expressed in terms of λ as

$$U = \frac{G}{2}\left(\lambda^2 + \frac{1}{\lambda^2} - 2\right). \qquad \textbf{[S16]}$$

Thus, using Eq. **S13**, the nominal stress in the main direction 2 can be expressed as

$$\sigma = G\left(\lambda - \frac{1}{\lambda^3}\right), \qquad \textbf{[S17]}$$

where $\sigma = T/t$ ($t = 3.5$ nm). T can be calculated from Eq. **S1**. The slope of the nominal stress and $\lambda - 1/\lambda^3$ indicate the shear modulus (Fig. 1*C*).

Equations for Excised Patch Configuration. To suppress unknown thermodynamic effects such as membrane pretension (27) and thermal undulations (19–21) involved in the mechanical behavior of liposomes and, more importantly, to study the rheological behavior of the lipid in the excised patch configuration, micropipette aspiration was performed on three different excised patches (Fig. 3). This method has several advantages over the cell-attached configuration, including simplicity and accuracy. For tension in the excised patch membrane, T, in Eq. **S1**, based on a principle of surface chemistry (Laplace's law) is changed as follows (12, 27–31):

$$T = \frac{P R_d}{2}. \qquad \textbf{[S18]}$$

R_d is the radius of curvature of the patch (Fig. S1 *D–F*). Note that there is no attached liposome part in the excised patch configuration. Therefore, the fundamental assumption of a conserved internal volume for the vesicle due to the incompressibility of the water inside the liposome during micropipette aspiration is no longer viable. Membrane deformations in excised patch experiments are conventionally characterized by the relative change

in the visible area measured with respect to a somewhat arbitrarily chosen initial state area, A_0. The areal strain (fractional area change) is defined by

$$\alpha = \frac{A - A_0}{A_0}, \qquad \text{[S19]}$$

where A is the total deformed area of the patch. Using very basic geometric relations, the deformed area can be calculated from the cylindrical length, L; the pipette radius, R_p; and the height of the dome of the patch, h (Fig. 3) by

$$A = 2\pi R_p L + \pi \left(R_p^2 + h^2 \right). \qquad \text{[S20]}$$

Because the other models discussed in this paper (uniaxial and hyperelastic models) do not deal with the attached part of the vesicle in the cell-attached configuration (and thus the constant volume assumption), they are all still valid also for the excised patch configuration. In those models, however, for the calculation of membrane tension, Eq. **S18** should be used instead of Eq. **S1**. The material properties obtained from different models (models 1–3) for excised patch configuration are demonstrated (Fig. S4 and Fig. 3*C*).

Supporting Patch Fluorometry Data Without Adhesion Tension. To calculate the bilayer material properties (i.e., K_A) we used ΔT, which is the change in tension due to the change of negative pressure at each pressure step (Eq. **S3**). We believe this reduces the potential influence of adhesion tension, assuming this value stays constant during pressure application. Furthermore, we carried out additional patch-fluorometry experiments, using BSA to reduce adhesion tension. As mentioned in the literature, we used 0.02% BSA (32) and the result was similar to what we previously measured. However, this concentration failed to completely remove adhesion tension. Using only 0.1% BSA allowed complete removal of adhesion tension (Movie S5). The corresponding value calculated for K_A using model 1 is ∼91 mN/m, which is similar to that calculated in the absence of BSA (∼112 mN/m; Table 1). The corresponding value of K_A using model 3 is 10 mN/m (∼14 mN/m without BSA; Table 1), given that 0.1% might affect the membrane properties and increase the irreproducibility of K_A (32–35).

Thus, a small amount of adhesion tension aids experimental simplicity and is likely present in a large number of the published micropipette aspiration (MA) reports, which is signified clearly by the radius of curvature being larger than the radius of the pipette, which can be seen in the initial equilibrium state of the patch in previous studies (7, 21, 36). Importantly, this adhesion tension does not seem to affect our calculated values for K_A.

Supporting Computational Data. As mentioned, shell theory was used in our computations, which is a more advanced theory for estimation of tension in thin-walled shells compared with Laplace's law. The spatial profiles of the aspirated liposome calculated by the FE simulation are presented in Fig. 2 *A* and *B* and Fig. S5. The vesicle has a diameter of 6.2 μm with the inner diameter of the micropipette being 2.8 μm (both are typical sizes encountered experimentally). The suction begins from 0 and reaches a value of −30 mmHg (∼4 kPa), instantaneously (in 0.01 s), and is then kept constant for 0.01 s. The computations were performed for the material parameters of $C_{10} = 0.5$ MPa and $k_b = 5.36 \times 10^{-21}$ (neo-Hookean model). The in-plane maximum and effective (von Mises) stress fields are represented in Fig. 2 *A* and *B*. Von Mises stress, S_v, is an equivalent stress of distortion energy of a material, which in principal directions can be calculated from

$$S_v = \sqrt{\frac{(S_1 - S_2)^2 + (S_1 - S_3)^2 + (S_1 - S_2)^2}{2}}, \qquad \text{[S21]}$$

where S_i ($i = 1, 2, 3$) are the stress components in the principal directions. Von Mises stress is used for fracture analysis of ductile materials. The stress distributions were nonuniform, with continuous regions of high and low stress. Moreover, to distinguish the role of the rigid micropipette in the movement of lipid molecules during micropipette aspiration, the vertical displacement field and in-plane maximum principal strain field in the azolectin vesicle were calculated and are shown in Fig. S5. By comparing the vertical displacement field and the in-plane maximum principal strain field it can be observed that, although the apex of the patch has the largest vertical displacement, the elements within the liposome–pipette normal contact region have the greatest strains (Fig. S5). This implies that when a local stress is produced in this area, the lipid membrane is unable to reconfigure itself and reduce the strain. Consequently, movement of the elements (in an FE simulation) or the phospholipids of the membrane (in reality) (10) is restricted and this facilitates membrane rupture (Figs. S3 and S5). The computational results show that the response is mostly dominated by local stretching of the liposome rather than its shear and/or bending effects near this normal contact area. No substantial result sensitivity to the contact conditions between the liposome and the pipette is observed, as the stress and the resulting deformation are mainly dominated by force regime and longitudinal movement of membrane within the pipette rather than by normal and tangential effects near the pipette opening.

A set of FE computations was performed to study the effects of the radius of the vesicle on tension, thickness variation, and in-plane stress field of the patch in the cell-attached configuration (Fig. S6). The vesicle size ranged from 3.1 μm (small vesicles that could be found abundantly in each sample) to 12.4 μm (rare typical sizes encountered experimentally). We showed that the radius of the vesicle outside liposome had no substantial effect on tension distribution, thickness variation, and stress field in the patch area within the pipette (Fig. S6). This is consistent with what we had assumed for deducing our mathematical elastic and hyperelastic equations. The tensions estimated from the Laplace equation for the cell-attached configuration (Eq. **S1**) and the excised patch configuration (Eq. **S18**) were compared with the FE results. On the basis of our computational results, for relatively small vesicles (i.e., $R_v < 9$ μm) the estimated tension obtained from Eq. **S1** is always an overestimation. On the other hand, for larger vesicles, like the tension estimated from Eq. **S18**, the results were always lower than the (FE) values (Fig. 2*D*). This also allowed us to choose the more appropriate equation (between Eqs. **S1** and **S18**) for tension estimation in the process of calculating the mechanical properties of lipid bilayer.

Previously, we showed that a micropipette aspiration protocol based on an equibiaxial tension assumption results in overestimation of lipid elastic moduli. Moreover, the mechanical properties of larger liposomes are shown to be stiffer than those of smaller vesicles. However, unlike the cell-attached configuration, the mechanical properties obtained from an isolated patch in micropipette aspiration (excised patch configuration) are very similar using all three different material models (Fig. S4 *A* and *B*, Fig. 3*B*, and Table S2). In a similar manner to that performed for the cell-attached configuration, we also modeled the excised patch experiment (Fig. S1 *B* and *C*). The mechanical properties obtained were used as input data for our computational model to see whether we could observe the same rheological behavior for our lipid bilayer model under experimental conditions (i.e., typical patch and pipette geometry in conjunction with similar load and boundary conditions). Thus, the length of lipid membrane

within the pipette at four different pressures was compared with experimentally derived values and very good agreement was found between the two approaches (Fig. S4 *C* and *D* and Fig. 3*C*). We believe that the relatively small difference between the two is mainly attributable to the adhesion tension between lipid and micropipette, which was not taken into account in our computational model.

Both typical pipette shapes, cylindrical and tapering, were simulated to see whether there was any difference in rheological behavior between the two during aspiration. Furthermore, a set of calculations was performed, considering similar computational conditions to indicate the effect of initial membrane thickness on the maximum membrane stress (in the apex of the patch), up to suction pressure 40 mmHg (Figs. S7 and S8). The initial thickness of the lipid bilayer did not affect the tension distribution but it had a considerable effect on the membrane stress distribution within the patch area. The thinner the membrane, the higher was the stress at any given pressure.

Effect of Membrane Fluidity (Internal Dissipation) on the Stress–Strain Distribution of Patched Lipid Bilayers. Visco-hyperelasticity is the property of materials that exhibit both viscous and hyperelastic characteristics when undergoing large deformation. Given that fluid–lipid biomembranes show both liquid-like and solid-like behavior, numerous researchers have adopted viscoelastic models for describing the behavior of different lipid bilayers and cell membranes (3, 6, 14, 37–42).

Although for azolectin we and others (1) have seen negligible stiffness nonlinearity (Figs. 1*C* and 3*B* and Figs. S2 and S4 *A* and *B*) and hysteresis (Movie S5), we considered a low viscous (fluidic) behavior for lipids in addition to the lipid hyperelasticity to see how this changes the stress distribution in the patch area. In other words, a hyperelasticity model was used to study the result of the reversible bond stretching along the crystallographic planes of the lipid bilayer. Herein, viscosity was added to our previous (hyperelastic) model to capture the influence of the fluidity (internal damping) and creep of lipid molecules inside the pipette during micropipette aspiration. This enabled us to investigate the influence of lipid internal viscosity on the stress–strain distribution within the patch area during micropipette aspiration of the bilayer.

In the previous hyperplastic model (Figs. 2 and 3), the results from finite-element simulations predict that there is a persistent heterogeneity in tension with the maximum at the top of the patch dome of highly viscous membranes. In our introduced alternative visco-hyperelastic model, we assume a surface viscosity as the internal dissipative mechanisms of the bilayer. Our results indicate that for the membranes with low viscosity (high fluidity), such nonuniform distribution of tension is still feasible for different loading conditions (step or ramp), various fluidities, and typical experimental time courses. In a time course of 5 s (a typical experimental time) the maximum tension in the patch starts to expand over the patch area due to the relaxation along the tension gradient (Movies S6 and S7). This happens in both cell-attached and excised bilayer models. As shown, after 5 s the difference between the stress in the dome (maximum) and the stress near the wall (minimum) is about 50% (Movie S6). Hence, comparing results from the visco-hyperelastic model with our previous results, not only is the heterogeneous distribution of the stress valid with the existence of membrane fluidity but also it introduces a new time-dependent axisymmetric growth of the high-stress region (at the patch center) toward the low-stress area (near the pipette wall). This tense area in the center of the patch develops to the sides of the patch area (adjacent to the pipette wall) as the lipid creeps inside the pipette during the simulated experimental time. Thus, stress heterogeneity is valid for a wide range of instantaneous and long-term shear modulus and relaxation times.

Effect of Intermonolayer Dissipation: Modeling the Bilayer as Two Sliding Slabs. Previous models (models 1–3) were conceptualized on the basis of the mechanical behavior for a unit membrane structure for simplicity. This assumption is quite viable when there is a rapid displacement between layers (i.e., applying instantaneous suction). In this case, their relative lateral motion will be opposed by a considerable viscous drag at the bilayer midplane, which will lead to "dynamic coupling" of the monolayers, causing them to behave as a single slab (43). However, the monolayers are able to slide one relative to another in the case of regular displacements. This is because monolayers are tied together by a weak van der Waals (vdw) attraction at the midplane, stemming from the aqueous half spaces surrounding the bilayer (43).

Given that the boundary and loading conditions are different between the monolayers during micropipette aspiration, herein, we examine to what extent this affects the stress distribution between the monolayers in both cell-attached and excised configurations. The interlayer drag has been assumed to be velocity dependent and it follows the postulated constitutive relation for interlayer coupling $\tau = b \Delta v_s$. This assumption has been used in many other continuum mechanics (coarse grain) models of lipid bilayers, where b represents the magnitude of coupling embodied in a constant drag coefficient (of order 10^8 $N - s/m^3$). Δv_s represents the relative rate that molecules (nodes in our continuum model) in opposite monolayers slip past each other as the bilayer deforms (43).

As mentioned before, the monolayers are in contact with each other via a weak force stemming from vdw interaction between the two hydrophobic surfaces. The interlayer pressure as a function of the distance can be computed, adopting the vdw stress between two parallel bilayers,

$$S = \frac{-A_H}{6\pi D^3}. \qquad \textbf{[S22]}$$

Here S is the stress, A_H is the Hamaker constant, and D is the distance between the two monolayers. For lipid bilayers in water the Hamaker constant is ~5 (± 2) $\times 10^{-21}$ J (7, 44). Let us consider this number for hydrocarbons in the monolayers. The normal tractions can be positive, indicating an attractive interaction between the surfaces, or negative, in the case of repulsive forces.

The resulting expression of the interlayer contact interactions has been implemented in an ABAQUS user subroutine for simulating the vdw force. In ABAQUS/Standard, user subroutine UINTER can be used to define the constitutive interaction between two deforming surfaces. Monolayers are defined as the master and slave surfaces, and the UINTER is called for each slave node at each time increment of the analysis. Inputs to this subroutine are the initial and incremental relative positions of each slave node with respect to its closest point on the master surface and the material properties defined for the monolayers. The constitutive calculation thus involves computing the tractions based on the increments in relative position of the slave node with respect to the master surface.

Interestingly, our results indicate that higher membrane stress values are developed in the outer leaflet compared with the inner one by considering the lipid bilayer as two sliding surfaces. The asymmetry in the stress profiles of the two leaflets exists in both excised and cell-attached systems. However, we showed that for similar characteristics and conditions, the dissimilarity between the stress profiles of two monolayers is much more noticeable in the excised configuration compared with the cell-attached one. In the excised patch system, the maximum stress that arises in the upper monolayer (the one that is in contact with the pipette) is about 30% larger than the maximum stress in the inner monolayer (Fig. 3 *D* and *E*), whereas in the cell-attached configuration, the difference in the monolayers' maximum stress is less than 2% (Fig. 2 *E* and *F*). The difference between monolayers stems

from the fact that the inner leaflet in the excised patch has a higher degree of freedom for lateral movement and relaxation than the inner leaflet in the cell-attached conformation. Based on these results, we can suggest that depending on the location of the pore in different MS channels (close to or away from the mid-plane), the dissimilarity between the distributed stresses in the monolayers can affect activation of MS channels reconstituted and investigated in an excised patch system (45, 46).

1. Nomura T, et al. (2012) Differential effects of lipids and lyso-lipids on the mechanosensitivity of the mechanosensitive channels MscL and MscS. *Proc Natl Acad Sci USA* 109(22):8770–8775.
2. Sato M, Theret DP, Wheeler LT, Ohshima N, Nerem RM (1990) Application of the micropipette technique to the measurement of cultured porcine aortic endothelial cell viscoelastic properties. *J Biomech Eng* 112(3):263–268.
3. Vaziri A, Mofrad MR (2007) Mechanics and deformation of the nucleus in micropipette aspiration experiment. *J Biomech* 40(9):2053–2062.
4. Jafari Bidhendi A, Korhonen RK (2012) A finite element study of micropipette aspiration of single cells: Effect of compressibility. *Comput Math Methods Med* 2012, 10.1155/2012/192618.
5. Zhou E, Lim C, Quek S (2005) Finite element simulation of the micropipette aspiration of a living cell undergoing large viscoelastic deformation. *Mech Adv Mater Structures* 12(6):501–512.
6. Trickey WR, Baaijens FP, Laursen TA, Alexopoulos LG, Guilak F (2006) Determination of the Poisson's ratio of the cell: Recovery properties of chondrocytes after release from complete micropipette aspiration. *J Biomech* 39(1):78–87.
7. Evans E, Needham D (1987) Physical properties of surfactant bilayer membranes: Thermal transitions, elasticity, rigidity, cohesion and colloidal interactions. *J Phys Chem* 91(16):4219–4228.
8. Kirk GL, Gruner SM, Stein D (1984) A thermodynamic model of the lamellar to inverse hexagonal phase transition of lipid membrane-water systems. *Biochemistry* 23(6):1093–1102.
9. Kuzmin PI, Akimov SA, Chizmadzhev YA, Zimmerberg J, Cohen FS (2005) Line tension and interaction energies of membrane rafts calculated from lipid splay and tilt. *Biophys J* 88(2):1120–1133.
10. Rodowicz KA, Francisco H, Layton B (2010) Determination of the mechanical properties of DOPC:DOPS liposomes using an image procession algorithm and micropipette-aspiration techniques. *Chem Phys Lipids* 163(8):787–793.
11. Akimov SA, Kuzmin PI, Zimmerberg J, Cohen FS (2007) Lateral tension increases the line tension between two domains in a lipid bilayer membrane. *Phys Rev E Stat Nonlin Soft Matter Phys* 75(1 Pt 1):011919.
12. Hamill OP, Martinac B (2001) Molecular basis of mechanotransduction in living cells. *Physiol Rev* 81(2):685–740.
13. Kralchevsky PA, Paunov VN, Denkov ND, Nagayama K (1995) Stresses in lipid membranes and interactions between inclusions. *J Chem Soc Faraday Trans* 91(19):3415–3432.
14. Earnshaw JC, Crawford GE (1989) Viscoelastic relaxation of bilayer lipid membranes: II. Temperature dependence of relaxation time. *Biophys J* 55(5):1017–1021.
15. Evans E, Rawicz W (1997) Elasticity of "fuzzy'" biomembranes. *Phys Rev Lett* 79(12):2379–2382.
16. Kwok R, Evans E (1981) Thermoelasticity of large lecithin bilayer vesicles. *Biophys J* 35(3):637–652.
17. Mitchison J, Swann M (1954) The mechanical properties of the cell surface I. The cell elastimeter. *J Exp Biol* 31(3):443–460.
18. Bowman CL, Gottlieb PA, Suchyna TM, Murphy YK, Sachs F (2007) Mechanosensitive ion channels and the peptide inhibitor GsMTx-4: History, properties, mechanisms and pharmacology. *Toxicon* 49(2):249–270.
19. Henriksen JR, Ipsen JH (2004) Measurement of membrane elasticity by micro-pipette aspiration. *Eur Phys J E Soft Matter* 14(2):149–167.
20. Needham D, Nunn RS (1990) Elastic deformation and failure of lipid bilayer membranes containing cholesterol. *Biophys J* 58(4):997–1009.
21. Rawicz W, Olbrich KC, McIntosh T, Needham D, Evans E (2000) Effect of chain length and unsaturation on elasticity of lipid bilayers. *Biophys J* 79(1):328–339.
22. Allen KB, Layton BE (2009) Determination of the forces imposed by micro and nanopipettes during DOPC: DOPS liposome manipulation. *Chem Phys Lipids* 162(1–2):34–52.
23. Bloom M, Evans E, Mouritsen OG (1991) Physical properties of the fluid lipid-bilayer component of cell membranes: A perspective. *Q Rev Biophys* 24(3):293–397.
24. Lingwood D, Simons K (2010) Lipid rafts as a membrane-organizing principle. *Science* 327(5961):46–50.
25. Holzapfel GA, Ogden RW (2006) *Mechanics of Biological Tissue* (Springer, Berlin).
26. Ogden R, Saccomandi G, Sgura I (2004) Fitting hyperelastic models to experimental data. *Comput Mech* 34(6):484–502.
27. White SH (1980) Small phospholipid vesicles: Internal pressure, surface tension, and surface free energy. *Proc Natl Acad Sci USA* 77(7):4048–4050.
28. Tanford C (1979) Hydrostatic pressure in small phospholipid vesicles. *Proc Natl Acad Sci USA* 76(7):3318–3319.
29. Opsahl LR, Webb WW (1994) Lipid-glass adhesion in giga-sealed patch-clamped membranes. *Biophys J* 66(1):75–79.
30. Suchyna TM, Markin VS, Sachs F (2009) Biophysics and structure of the patch and the gigaseal. *Biophys J* 97(3):738–747.
31. Ursell T, Agrawal A, Phillips R (2011) Lipid bilayer mechanics in a pipette with glass-bilayer adhesion. *Biophys J* 101(8):1913–1920.
32. Zhou Y, Raphael RM (2005) Effect of salicylate on the elasticity, bending stiffness, and strength of SOPC membranes. *Biophys J* 89(3):1789–1801.
33. Shoemaker SD, Vanderlick TK (2002) Intramembrane electrostatic interactions destabilize lipid vesicles. *Biophys J* 83(4):2007–2014.
34. Wu Y, Fletcher GL (2000) Efficacy of antifreeze protein types in protecting liposome membrane integrity depends on phospholipid class. *Biochim Biophys Acta* 1524(1):11–16.
35. Yokouchi Y, et al. (2001) Effect of adsorption of bovine serum albumin on liposomal membrane characteristics. *Colloids Surf B Biointerfaces* 20(2):95–103.
36. Evans E, Rawicz W, Smith BA (2013) Back to the future: Mechanics and thermodynamics of lipid biomembranes. *Faraday Discuss* 161:591–611.
37. Waugh R, Evans EA (1976) Viscoelastic properties of erythrocyte membranes of different vertebrate animals. *Microvasc Res* 12(3):291–304.
38. Jamali Y, Azimi M, Mofrad MR (2010) A sub-cellular viscoelastic model for cell population mechanics. *PLoS ONE* 5(8):pii:e12097.
39. Canham PB (1970) The minimum energy of bending as a possible explanation of the biconcave shape of the human red blood cell. *J Theor Biol* 26(1):61–81.
40. Mills JP, Qie L, Dao M, Lim CT, Suresh S (2004) Nonlinear elastic and viscoelastic deformation of the human red blood cell with optical tweezers. *Mech Chem Biosyst* 1(3):169–180.
41. Lubarda V, Marzani A (2009) Viscoelastic response of thin membranes with application to red blood cells. *Acta Mech* 202(1–4):1–16.
42. Smeulders JB, Blom C, Mellema J (1990) Linear viscoelastic study of lipid vesicle dispersions: Hard-sphere behavior and bilayer surface dynamics. *Phys Rev A* 42(6):3483–3498.
43. Evans E, Yeung A (1994) Hidden dynamics in rapid changes of bilayer shape. *Chem Phys Lipids* 73(1):39–56.
44. De Haas K, et al. (1997) Rheological behavior of a dispersion of small lipid bilayer vesicles. *Langmuir* 13(25):6658–6668.
45. Belyy V, Kamaraju K, Akitake B, Anishkin A, Sukharev S (2010) Adaptive behavior of bacterial mechanosensitive channels is coupled to membrane mechanics. *J Gen Physiol* 135(6):641–652.
46. Häse CC, Le Dain AC, Martinac B (1995) Purification and functional reconstitution of the recombinant large mechanosensitive ion channel (MscL) of Escherichia coli. *J Biol Chem* 270(31):18329–18334.
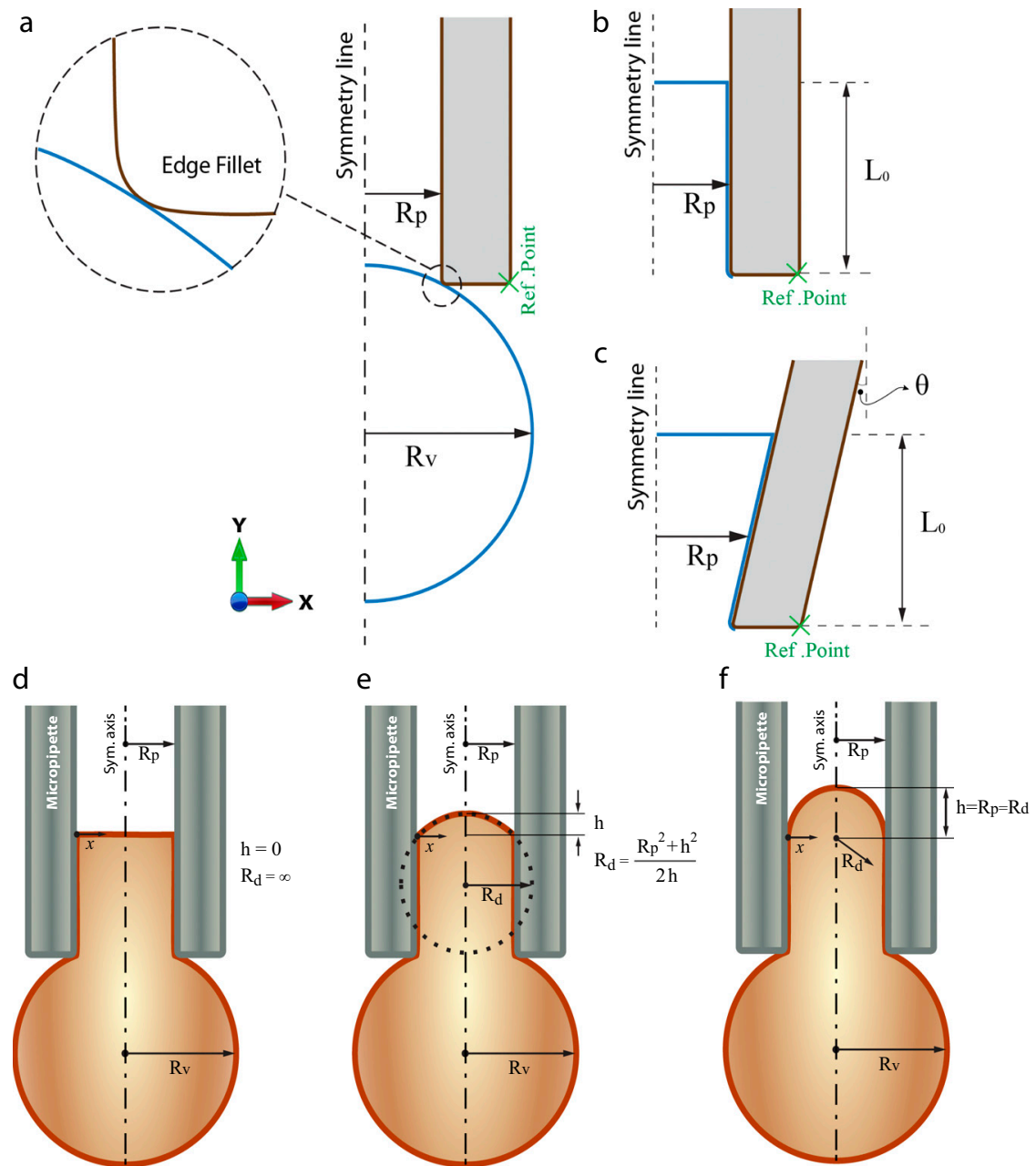
Supplementary Information

Fig. S1. Finite-element (FE) model of a lipid bilayer and a micropipette including schematic diagrams of the geometry of cell-attached micropipette aspiration. (*A*) For the FE model of cell-attached configuration, a liposome is modeled as a 2D axisymmetric semicircle with the radius of R_v. R_p is the inner radius of the micropipette. An edge fillet at the opening of the micropipette is used to mimic the experimentally used micropipettes and to avoid element distortion in this region. (*B* and *C*) FE model of excised patch membrane, where the lipid bilayer is modeled as a thin shell in flat form according to the realistic prestressed shape of the lipid bilayer at resting state, within a cylindrical pipette with the radius R_p, and a tapering pipette with the normal angle of θ, respectively. (*D*) Flat state of the patch area when the adhesion tension is much higher than the tension caused by the applied pressure within the pipette. (*E*) A general state of the patch area. R_d is the radius of the dome (radius of curvature), which can be calculated from the geometry of the patch using $((R_p^2 + h^2)/2h)$; h is the height of the patch dome. (*F*) A special case where the adhesion tension is negligible and thus the patch area has a hemispherical shape.
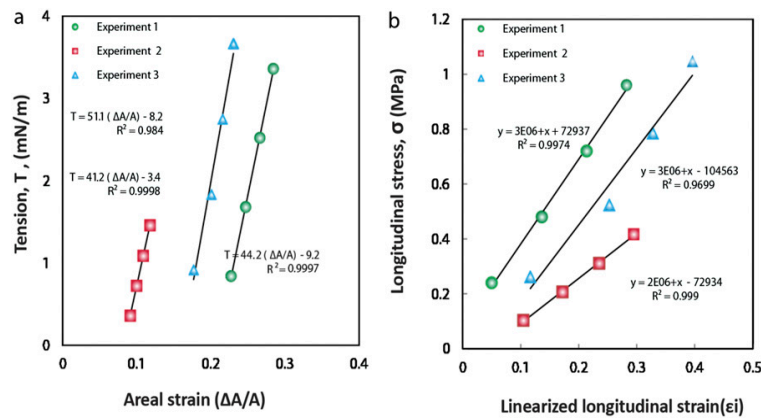
Fig. S2. Patch fluorometry results for three azolectin lipid vesicles of similar diameter (6–8 μm). (*A*) Variation of the membrane tension plotted against corresponding areal strain. Shown is how the membrane tension changes almost linearly with respect to areal strain; plots are fitted with linear regression lines. (*B*) Variation of the nominal longitudinal in-plane membrane stress vs. the linearized longitudinal strain fitted with linear regression lines. The diagram demonstrates the almost linear change of the nominal stress–strain field in the longitudinal direction.
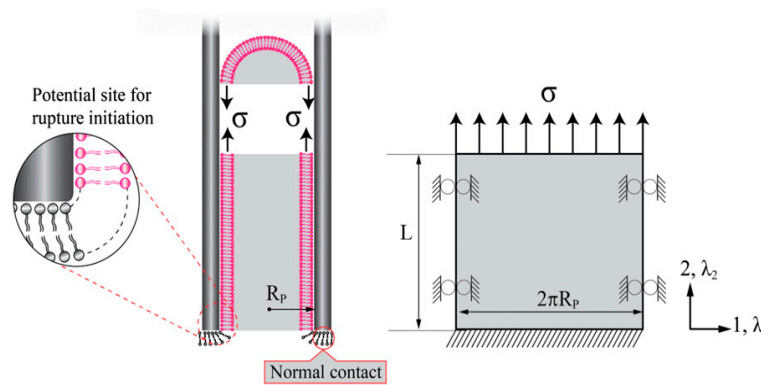
Fig. S3. Membrane stresses and boundary conditions of the lipid bilayer during a micropipette aspiration experiment. R_P and σ represent the inner radius of the pipette and the longitudinal stress of the membrane, respectively. λ_1 and λ_2 are the stretching ratios in directions 1 (horizontal) and 2 (vertical), respectively. L is the length of projection of the lipid within the micropipette. (*Right*) The planar form of a liposome with the associated boundary conditions caused by the rigid micropipette. (*Left*) The normal contact area between the liposome and the micropipette as well as one of the potential regions for rupture initiation in the liposome during micropipette aspiration.
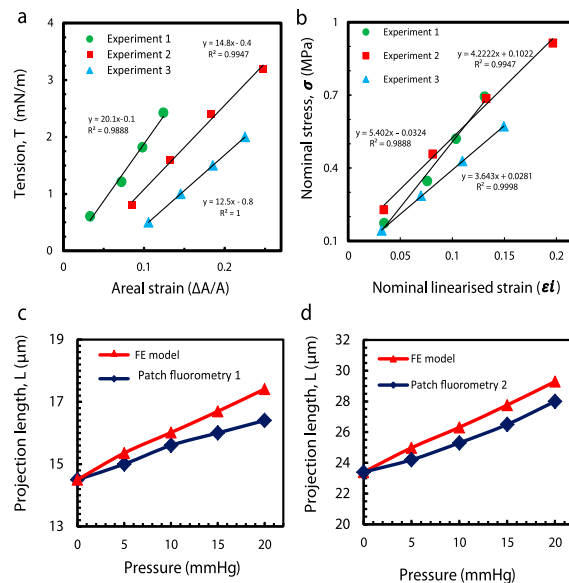
Fig. S4. Patch fluorometry results for three excised membrane patches and validation of simulations with observations from patch fluorometry experiments. (*A*) Variation of the membrane tension plotted against corresponding areal strain. Shown is how the membrane tension changes almost linearly with respect to the areal strain in the excised configuration; plots are fitted with linear regression lines. (*B*) Alteration of the nominal longitudinal in-plane membrane stress vs. the linearized longitudinal strain fitted with linear regression lines. The diagram demonstrates the almost linear change of the nominal stress–strain field in the longitudinal direction. (*C* and *D*) Comparisons between the measured aspiration lengths of azolectin lipid within the pipette and those simulated using the neo-Hookean hyperplastic model. The inner diameters of the micropipette are typical sizes encountered experimentally. The suction begins from 0 and reaches a value of −20 mmHg (−5 mmHg increments) instantaneously (in 0.01 s) and is then kept constant for 0.01 s. The computations are performed for the material parameters of $C_{10} = 0.71$ MPa and $k_b = 5.36 \times 10^{-21}$.
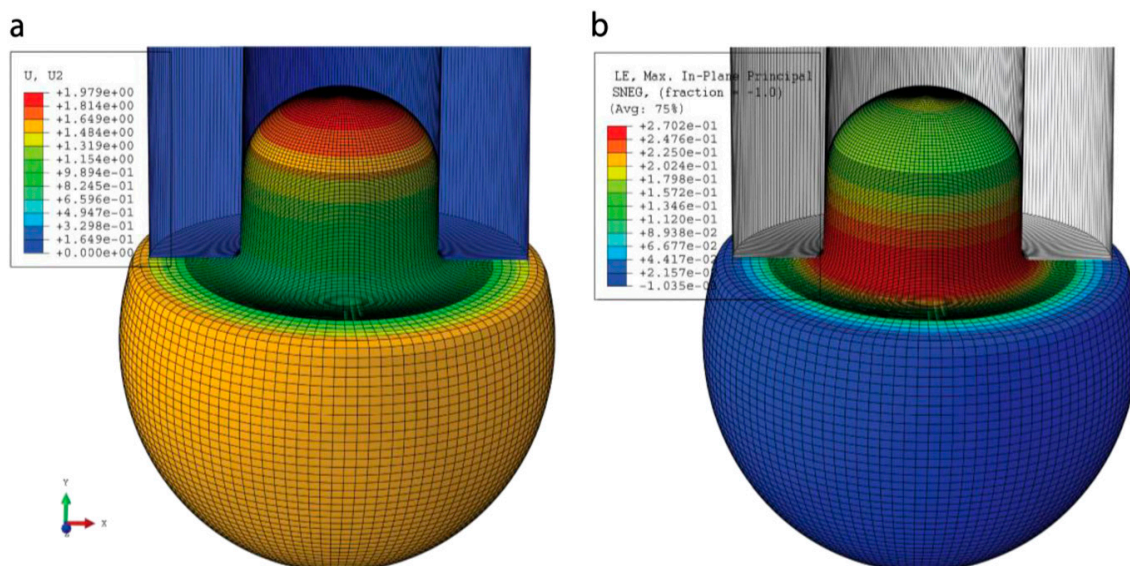
Fig. S5. Membrane stresses and displacement fields of lipid bilayer during a micropipette aspiration experiment. (*A*) Spatial profiles of the aspirated liposome calculated by FE simulation. The vesicle has a diameter of 6.2 μm. The inner diameter of the micropipette is 2.8 μm (both are typical sizes encountered experimentally). The suction begins from 0 and reaches a value of −30 mmHg (~4 kPa) instantaneously (in 0.01 s) and is then kept constant for 0.01 s. The computations are performed for the material parameters of $C_{10} = 0.5$ MPa and $k_b = 5.36 \times 10^{-21}$ J (neo-Hookean model). Shown are (*A*) the vertical displacement field (μm) and (*B*) in-plane maximum principal strain field in the azolectin vesicle.

Normalised distance from the pipette wall to the apex of the patch, x/Rp
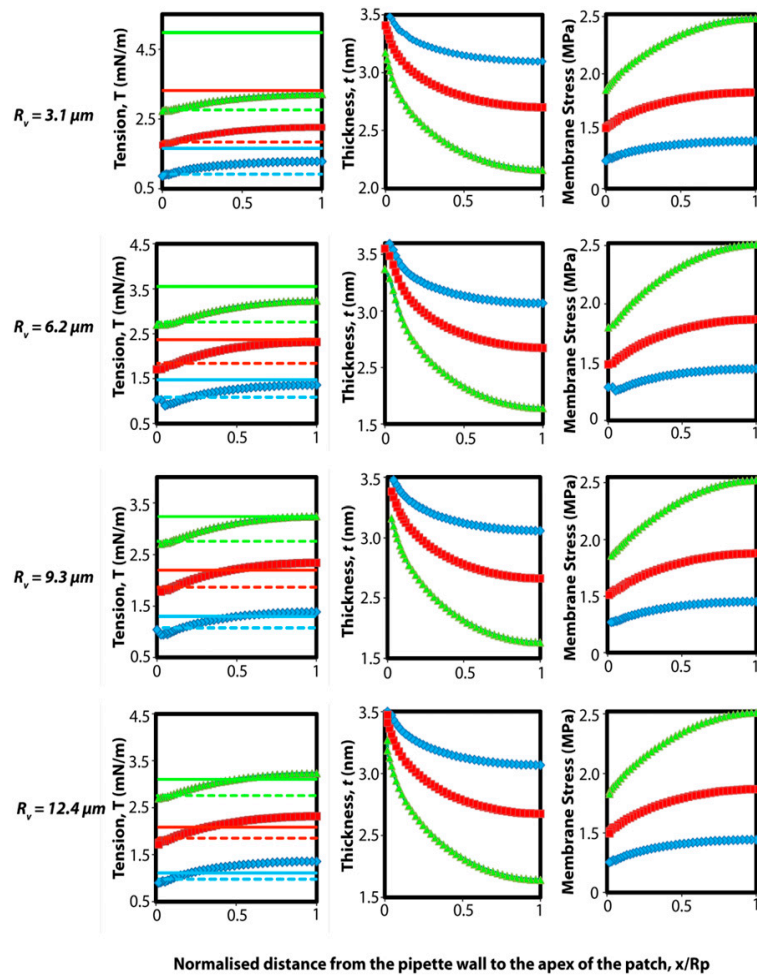
Fig. S6. FE results (tension, bilayer thickness, and in-plane stress) of a patch in the cell-attached configuration. The inner diameter of the micropipette is 2.8 μm (a typical size encountered experimentally). The suction begins from 0 and reaches a value of −30 mmHg (∼4 kPa), instantaneously (in 0.01 s), and is then kept constant for 0.01 s. The computations are performed for the material parameters of $C_{10} = 0.5$ MPa and $k_b = 5.36 \times 10^{-21}$ J (model 3: neo-Hookean model). Each row shows the bilayer tension variation, the bilayer thickness change, and the membrane stress distribution within the patch area for different radii of vesicle, $R_v = 3.1$ μm (*First Row*), $R_v = 6.2$ μm (*Second Row*), $R_v = 9.3$ μm (*Third Row*), and $R_v = 12.4$ μm (*Fourth Row*). Solid line in *Left* column represents tension estimated using Eq. **S1** (cell-attached), and the dashed line represents tension estimated using Eq. **S18** (excised patch).
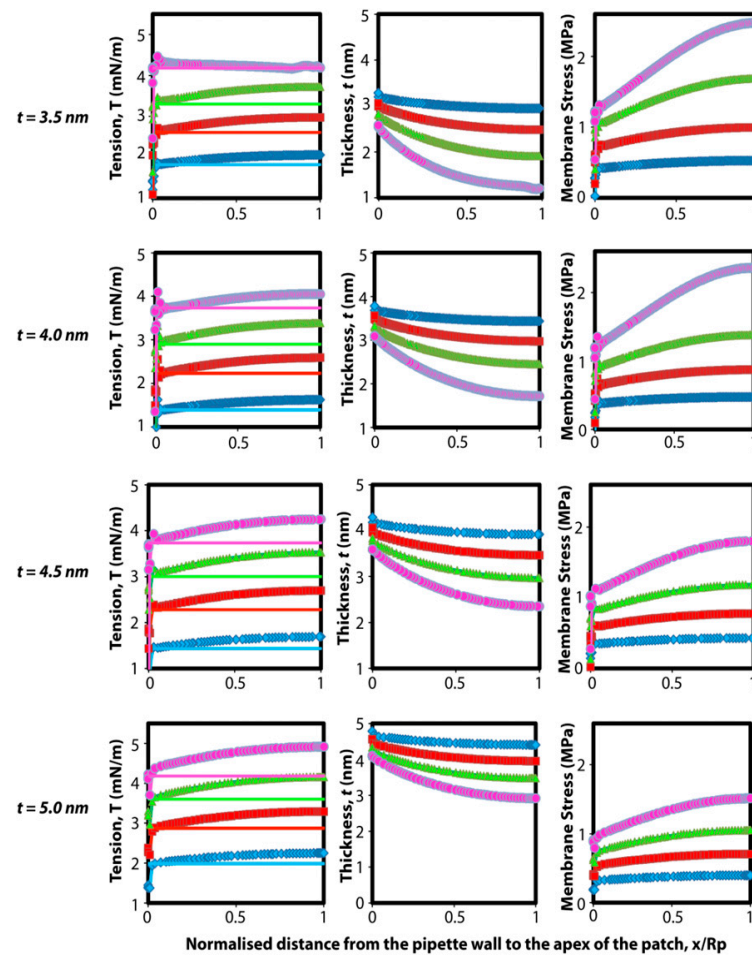
Fig. S7. Effect of initial thickness of bilayer on tension, thickness variations, and in-plane stress within the patch area in the excised patch configuration (using a cylindrical pipette). In these FE models, the inner diameter of the cylindrical micropipette is 2.8 μm (a typical size encountered experimentally). The suction begins from 0 and reaches a value of −40 mmHg (∼5.3 kPa) instantaneously (in 0.01 s) and is then kept constant for 0.01 s. The computations are performed for the material parameters of $C_{10} = 0.5$ MPa and $k_b = 5.36 \times 10^{-21}$ J (neo-Hookean model). Each row shows the bilayer tension variation, the thickness change, and the membrane stress distribution within the patch area for different bilayer thicknesses, $t = 3.5$ nm (*First Row*), $t = 4$ nm (*Second Row*), $t = 4.5$ nm (*Third Row*), and $t = 5$ nm (*Fourth Row*). Solid lines in *Left* column represent tension estimated using Eq. **S18** (excised patch).

Normalised distance from the pipette wall to the apex of the patch, x/Rp
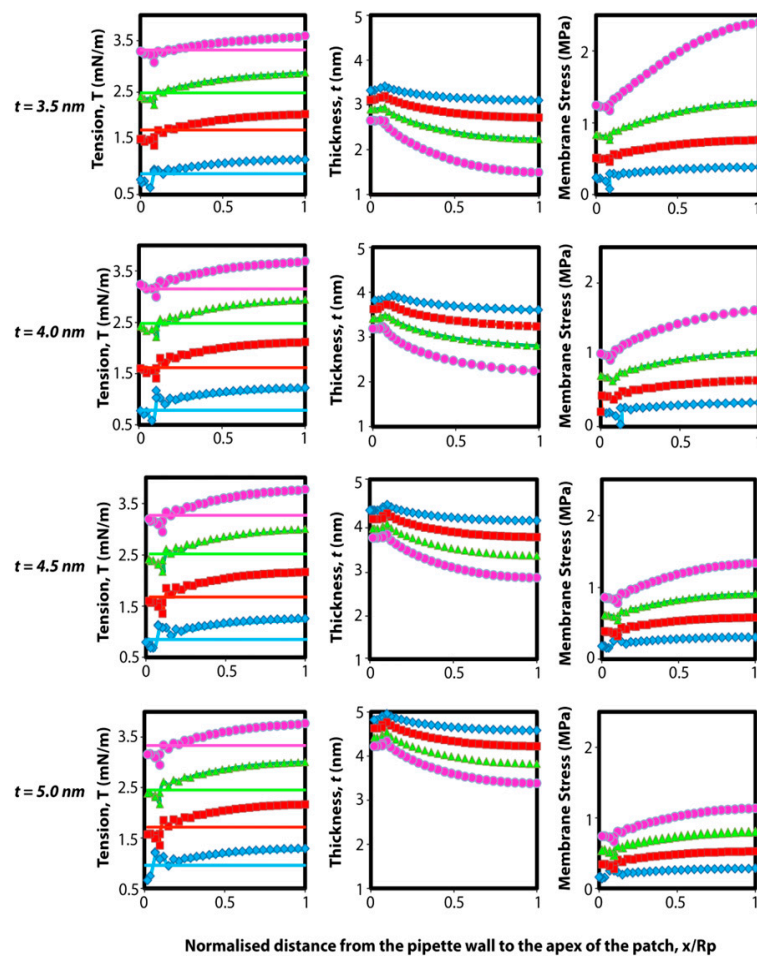
Fig. S8. Effect of initial thickness of bilayer on tension, thickness variations, and in-plane stress within the patch domain in excised patch configuration (using a conical pipette). All of the model properties are the same as those of the patch model with a cylindrical pipette (Fig. S7), except that the initial inner diameter of the conical micropipette is 1.2 μm before applying suction and the angle of the pipette is 10° (these are typical values encountered experimentally). Thus, the suction begins from 0 and reaches a value of −40 mmHg (∼5.3 kPa) instantaneously (in 0.01 s) and is then kept constant for 0.01 s. The computations are performed for the material parameters of $C_{10} = 0.5$ MPa and $k_b = 5.36 \times 10^{-21}$ J (neo-Hookean model). Each row shows the bilayer tension variation, the thickness change, and the membrane stress distribution within the patch area for the bilayer thickness, $t = 3.5$ nm (*First Row*), $t = 4$ nm (*Second Row*), $t = 4.5$ nm (*Third Row*), and $t = 5$ nm (*Fourth Row*). Solid lines in *Left* column represent tension estimated using Eq. S18 (excised patch).

Table S1. Validation of the proposed material properties of azolectin liposomes by comparing computational and experimentally derived values of the change in projection length, ΔL, at two different pressures (μm)

Different approaches	ΔL, in −10 mmHg	ΔL, in −20 mmHg
FE: linear elastic, model 1	0.4	0.6
FE: linear elastic, model 2	0.7	1.2
FE: neo-Hookean, model 3	0.8	1.6
Patch fluorometry experiment	0.8	1.7

Table S2. Pretension in the lipid within the pipette before pressurizing

Experiment no.	Excised patch	Cell-attached, small vesicles	Cell-attached, large vesicles
1	0.1	8.2	5.3
2	0.4	3.4	13.2
3	0.8	8.2	—

Extrapolations back to zero area dilation gave a value for the tension in the resting membrane of up to 13 ± 3 mN/m for very large vesicles, in close agreement with earlier measurements. Pretension values for the excised patch configuration may indicate the adhesion tension between the glass and azolectin lipid bilayer, whereas those of the vesicles are not just attributable to the adhesion tension. As can be seen, the pretensions in excised patches are much lower than those found in vesicles. All values are in mN/m.
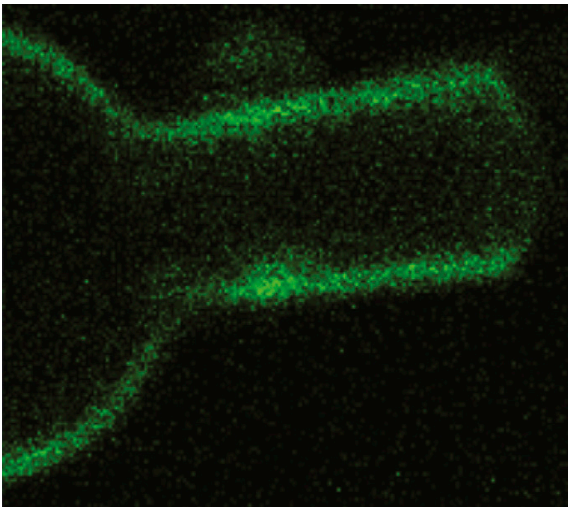
Movie S1. Movement of fluorescent-labeled azolectin liposomes (cell-attached configuration) during micropipette aspiration using confocal microscopy. Liposomes were aspirated by applying a negative pressure of −20 mmHg (5-mmHg increments).

Movie S1
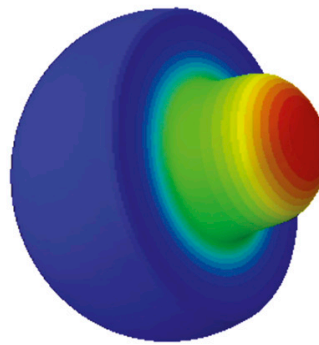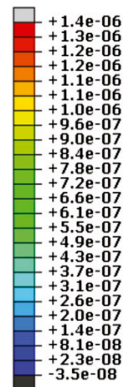
Movie S2. Simulation of the movement of a liposome patch (cell-attached configuration) and stress distribution during micropipette aspiration, using the finite-element method. A hyperelastic material model has been adopted here.
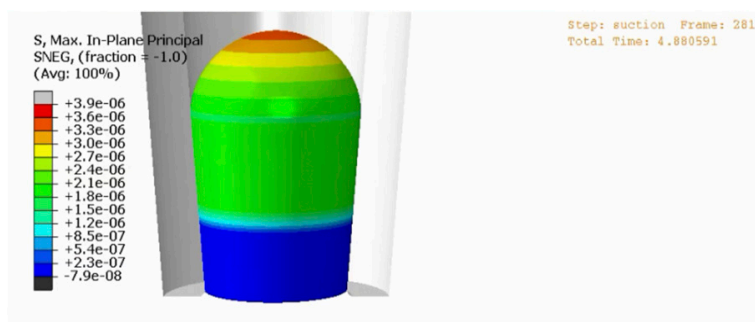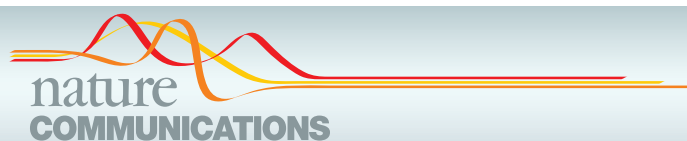
Movie S2
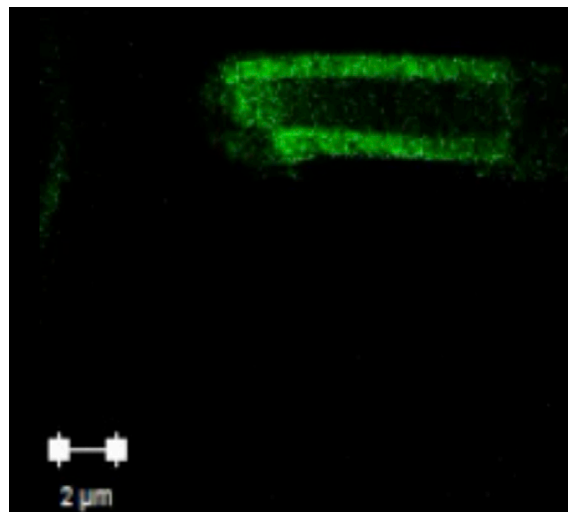
Movie S3. Movement of fluorescent-labeled azolectin lipid (excised patch configuration) during micropipette aspiration, using confocal microscopy. The membrane patches were aspirated by applying a negative pressure of −20 mmHg (5-mmHg increments).

Movie S3
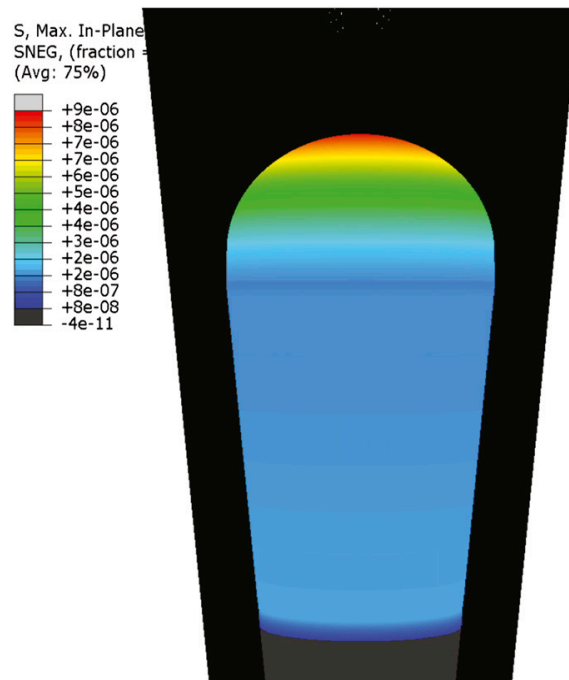
Movie S4. Simulation of the movement of azolectin lipid (excised patch configuration) and stress distribution during patch clamping, using the finite-element method. A hyperelastic material model has been adopted here.

Movie S4
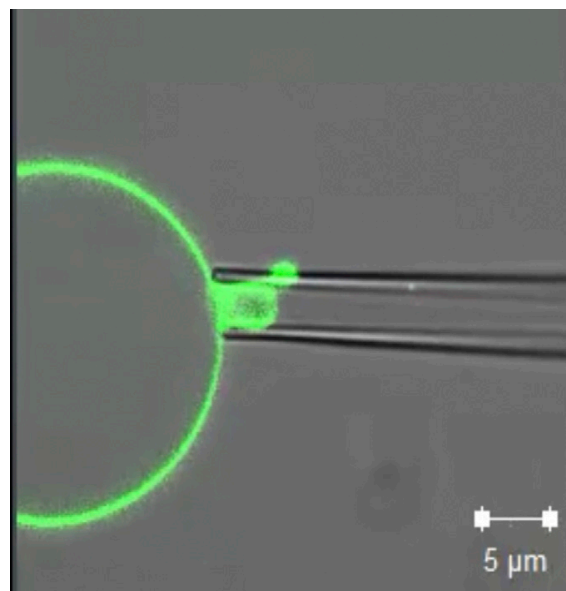
Movie S5. Movement of fluorescent-labeled azolectin liposome (cell-attached configuration) during aspiration, using a micropipette coated with 0.1% BSA. Liposomes were aspirated by applying a negative pressure of −15 mmHg (ramp) and then the pressure was released stepwise.

Movie S5
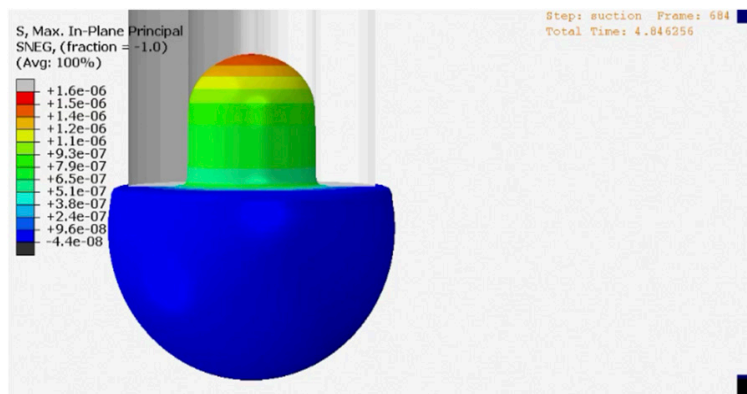
Movie S6. Simulation of the movement of a liposome patch (cell-attached configuration) and stress distribution during micropipette aspiration, using the finite-element method. The material model is visco-hyperelastic.

Movie S6

Movie S7. Simulation of the movement of a liposome patch (excised patch configuration) and stress distribution during patch clamping, using the finite-element method. The material model is visco-hyperelastic.

Movie S7

CHAPTER 3

Mechanical force is an omnipresent stimulus in biology, yet our understanding of the molecular workings of cellular mechanotransducers is limited. As reviewed in Chapter 1, one ubiquitous type of molecular mechanotransducers are mechanosensitive (MS) ion channels. These channel families are vastly diverse in structure with little to no sequence similarity among organisms of different evolutionary provenance. While 3D structures of five MS channels have been resolved to date, the key structural element that links mechanical stress from the membrane to MS channel dynamics remain a mystery. As a prototypical mechanosensitive channel MscL has continually provided insights into the basic biophysical principles of mechanosensory transduction despite its structural simplicity. In this chapter, the molecular mechanism underlying the fundamental mechanotransduction process that couples membrane tension to the pore expansion in MscL is investigated. Using an interwoven multidisciplinary approach of experiment and computational modelling, it is shown that the short amphipathic N-terminal helix of MscL acts as a horizontal coupling helix linking membrane bilayer dynamics to changes in protein conformation. Providing such an architectural blueprint for mechanosensitivity (conserved amphipathic or membrane attached anchor domain), aids identifying/ classifying genes that encode for mechanotransduction channels. In other words, there would be a unique structural criterion for fulfilling mechanosensitivity.

ARTICLE

OPEN

The role of MscL amphipathic N terminus indicates a blueprint for bilayer-mediated gating of mechanosensitive channels

Navid Bavi[1,2], D. Marien Cortes[3,†], Charles D. Cox[1,2], Paul R. Rohde[1], Weihong Liu[4,†], Joachim W. Deitmer[5], Omid Bavi[1,6], Pavel Strop[7,†], Adam P. Hill[1,2], Douglas Rees[7], Ben Corry[8], Eduardo Perozo[3] & Boris Martinac[1,2]

The bacterial mechanosensitive channel MscL gates in response to membrane tension as a result of mechanical force transmitted directly to the channel from the lipid bilayer. MscL represents an excellent model system to study the basic biophysical principles of mechanosensory transduction. However, understanding of the essential structural components that transduce bilayer tension into channel gating remains incomplete. Here using multiple experimental and computational approaches, we demonstrate that the amphipathic N-terminal helix of MscL acts as a crucial structural element during tension-induced gating, both stabilizing the closed state and coupling the channel to the membrane. We propose that this may also represent a common principle in the gating cycle of unrelated mechanosensitive ion channels, allowing the coupling of channel conformation to membrane dynamics.

[1] Division of Molecular Cardiology and Biophysics, Victor Chang Cardiac Research Institute, Darlinghurst, New South Wales 2010, Australia. [2] St Vincent's Clinical School, Faculty of Medicine, University of New South Wales, Darlinghurst, New South Wales 2010, Australia. [3] Department of Biochemistry and Molecular Biology, Institute for Biophysical Dynamics, University of Chicago, Chicago, Illinois 60637, USA. [4] Department of Pharmacology, University of Western Australia, Nedlands, Western Australia 6009, Australia. [5] FB Biologie, University of Kaiserslautern, Kaiserslautern D-67663, Germany. [6] Institute for Nanoscience and Nanotechnology, Sharif University of Technology, Tehran 1458889694, Iran. [7] Division of Chemistry and Chemical Engineering, Howard Hughes Medical Institute, California Institute of Technology, Pasadena, California 91125, USA. [8] Research School of Biology, The Australian National University, Acton, Australian Capital Territory 2601, Australia. † Present address: Department of Cell Physiology, Texas Tech University Health Sciences Center, Lubbock, Texas 79430, USA (M.D.C.); Marion Domain Medical and Dental Centre, Oaklands Park, South Australia 5046, Australia (W.L.); Pfizer Inc., New York, New York 10017, USA (P.S.). Correspondence and requests for materials should be addressed to E.P. (email: eperozo@uchicago.edu) or to B.M. (email: b.martinac@victorchang.edu.au).

Mechanosensitive channels (MSs) are a ubiquitous type of molecular force sensor[1–3]. They convert the various mechanical forces that regulate and define life at all levels into electrical signals[4]. For this to occur, the applied mechanical force must generate a conformational change that leads to channel gating[5]. Current knowledge suggests that force maybe transmitted via the lipid bilayer as shown for bacterial MS channels, two-pore domain potassium channels and Piezo channels or via tethering of the channel to structural scaffold proteins[6–10]. Indeed, MS channels represent a structurally diverse class of proteins, a fact that has largely precluded the identification of a universal 'force-sensing' motif[11–14]. Despite this lack of structural similarity much of the knowledge of the basic biophysical principles that govern bilayer-mediated gating of this class of channels comes from studies of the MS channel of large conductance (MscL) from *Escherichia coli* and its homologues[15,16]. MscL is a homopentamer, each monomer consisting of two transmembrane (TM) helices: TM1 lines the pore and TM2 interacts with the lipid bilayer and is connected to a coiled-coil C-terminal helical bundle[14,17,18]. The last structural feature is an amphipathic N-terminal helix, previously named S1 that is connected to the pore-lining TM1 helix via a glycine hinge (G14). During gating and in response to forces transmitted directly from the bilayer, the channel undergoes a large in-plane area expansion[15,19–22], where the pore-lining TM1 helix tilts and rotates in response to tension, culminating in solvation of a hydrophobic gate[23,24]. MscL activation results in the development of a large non-selective pore with a diameter approaching ∼3 nm and a unitary conductance in the range of ∼3 nS (refs 15,20).

While there is a consensus on most of the major global conformational changes that occur during gating, the critical role of the N-terminal helix in MscL gating cycle remains controversial[19,25]. Two competing models have been proposed. The first model suggests that the N-terminal domain acts as a second gate, providing an additional constriction point on top of the hydrophobic lock formed principally by L19 and V23 (refs 24,26). This model was largely built on the initial MscL crystal structure[14] that was later refined, particularly concerning the position of the N-terminal helix[17]. The second model suggested by Blount and co-workers[25] is one in which the N terminus has a close association with the lipid bilayer and acts as a crucial mechanosensing element.

Here using patch-clamp electrophysiology, site-directed spin-labelling electron paramagnetic resonance (EPR) spectroscopy and multiple computational approaches we show that the N-terminal helix of MscL acts as a dynamic membrane-coupling element. In its dual role, the N-terminal helix both associates with the bilayer at the lipid–solvent interface and drives the tilting of the pore-lining TM1 helix, leading to the radial expansion of the pore. The juxtaposition of an amphipathic coupling helix (for example, N terminus) with a pore-lining helix (for example, TM1) through a flexible linker might also be the architectural foundation underlying bilayer force transmission in MscS-like and two-pore domain K$^+$ (K$_{2P}$) channels[11,27–30]. This mechanism might also be involved in force transduction for some members of the TRP channel family[31]. Our data suggest that the gating mechanism of MscL, a primordial MS, might reveal a unifying fundamental blueprint that underlies the mechanosensitivity of structurally unrelated ion channels.

Results

Conservation of the N-terminal helix. The N-terminal helix of *E. coli* MscL (EcMscL) is widely conserved throughout its homologues. While the absolute length of the helix varies among bacterial species (∼10–14 amino acids), there is a conserved amphipathic region at the distal end of the N-terminal helix,

preceding the pore-lining TM1 helix, with the consensus sequence F-[K,R]-x-F-[A,I,L]-x-[K,R]-G (Fig. 1a). These helices have a relatively high % of charged residues (∼20–30 %) indicative of interfacial helices (*c.f.* 5–10 % in TM helices). In addition, all these N-terminal helices have a net positive charge with the exception of AbMscL, as one would expect from an intracellular helix, in agreement with the positive inside rule. These helices also have a high hydrophobic moment ($<\mu H>$), again a characteristic of interfacial amphipathic helices (Fig. 1b). Using the consensus sequence shown in Fig. 1a as a search motif identifies a number of proteins known to associate and bind to membranes, for example, phycobiliprotein ApcE, C2 domain containing proteins and bacterial glucosyltransferase enzymes.

This interfacial positioning is supported by our equilibrated molecular dynamics (MD) simulations, which are discussed fully later in the text (Fig. 1c–e).

Interfacial positioning and dynamics of the N-terminal helix. Although the N-terminal segment could not be modelled in the original crystallographic analysis of the *Mycobacterium tuberculosis* MscL (MtMscL), a subsequent re-refinement of the original diffraction data revealed ordered density for this region[14,17]. MscL crystals were obtained from a construct with an additional 23 residues at the N terminus, including a decahistidine tag, and removal of this tag was not necessary for crystal growth. These residues are presumably disordered in the crystal structure.

To probe both the interfacial nature of the N terminus and the influence of the N-terminal tag on structure and dynamics, we generated three different constructs (Supplementary Fig. 1a) with histidine tags at the N- and C termini, plus an additional construct with a deleted C-terminal helical bundle (Δ110). Individual cysteine mutants were introduced in each construct background at positions 2–12. In all cases, mutants were purified as detergent-stabilized (*n*-Dodecyl β-D-maltoside) pentamers and were stable at room temperature, as has been the case in previous studies for the majority of cysteine mutants of EcMscL[15,32]. This is taken as an indication that, overall, cysteine mutagenesis does not have major consequences for the structural integrity of this region of the channel molecule. However, this is not to suggest that these mutations are functionally irrelevant (Supplementary Fig. 1b). Most mutations in the N terminus showed an increased pressure threshold and many displayed frequent subconducting states, with one of the most severe in our hands being K5C. In order to show that, despite this loss of sensitivity, the channel could still adopt the open state we compared K5C with the wild-type (WT)-like mutant I24C (Supplementary Fig. 2). The K5C mutant required more lysophosphatidylcholine (LPC) to gate in EPR experiments but ultimately reached the fully open state. This suggests that under conditions that favour ion flux, attaching spin labels in the N terminus does not preclude the channel from making the closed to open transition. We also confirmed the spin-labelling efficiency at these sites using mass spectrometry (Supplementary Fig. 3).

Initial examination of the EPR spectra derived from the spin-labelled N terminus mutants (Supplementary Fig. 1a) reveals that the overall dynamics of this region increases considerably when the His-tag peptide is covalently attached. Changes in individual probe mobility were assessed from line shape differences (the inverse of width in the central resonant line, ΔH_o^{-1}). In particular, for the N-terminal His-tag constructs spin labels at positions 2–6 show mobility parameter values typically associated with flexible loops or disordered regions ($\Delta H_o^{-1} > 0.3$). When the His-tag peptide was attached to the C terminus, of either the full length or truncated channel, local dynamics were periodic, suggestive of a better-defined secondary structure.
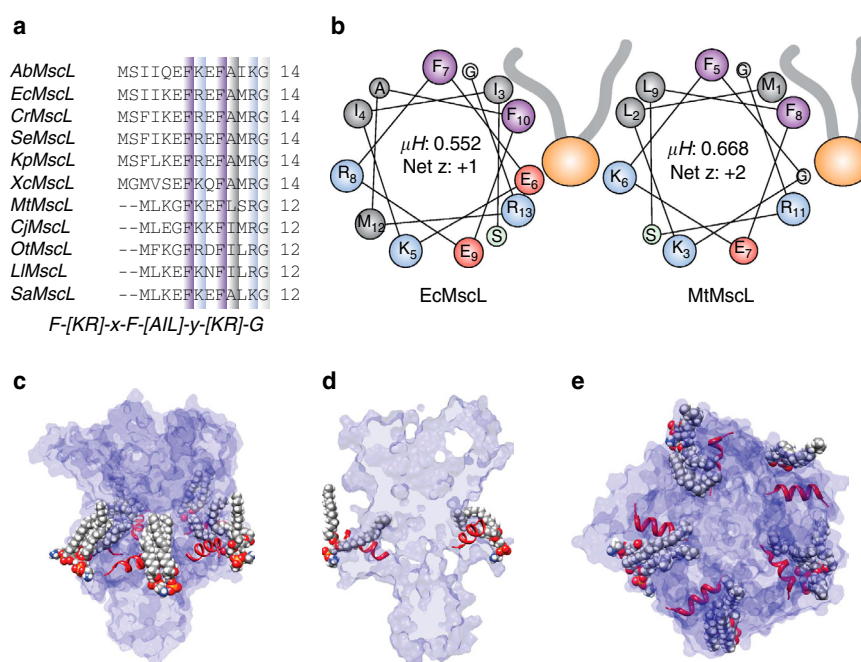
ARTICLE

Figure 1 | Conservation and amphipathic nature of the N-terminal helix in bacterial homologues of MscL. (**a**) Sequence alignment of MscL homologues from different bacterial classes with the consensus sequence shown below. (**b**) Helical wheel diagrams showing the amphipathic nature of the N-terminal helix of both *E. coli* (EcMscL) and *M. tuberculosis* (MtMscL) MscL. Amphipathic helices classically have high hydrophobic moments ($> 0.45\,\mu H$). (**c,d**) This type of helix with a high hydrophobic moment usually interacts at the interfacial region of a lipid bilayer with the hydrophobic face buried. Here the orientation of the N-terminal helix parallel to the membrane plane is shown from an equilibrated MD simulation model of EcMscL (see Fig. 4). Here we can also clearly see how the acyl chains bend over the N-terminal helix and protrude into an inter-subunit cavity. (**e**) Top view of the N-terminal helix showing its orientation and membrane association.

We then looked specifically at the lipid and water accessibility of the N-terminal helix using our C-terminally linked His-tag construct. Figure 2a shows spectra from residues 2 to 12 of the MscL N-terminal region. The probe mobility (ΔH_o^{-1}) at each of these positions in the resting state is shown in the upper panel of Fig. 2b. These values are matched to the individual spectra shown in Fig. 2a to visualize the degree of mobility of each residue. In particular, the mobility parameter is high prior to residue E6, suggesting that even without an N-terminal His-tag the most proximal end of the N terminus is not helical. Of note there are a number of residues that are particularly restricted, including K5, F7 and F10 (Fig. 2b, upper panel). There is also an increase in the periodicity beginning at F7, indicative of a helical structure, which matches well with our consensus sequence for the bacterial N-terminal helices (Fig. 1a). Figure 2b also indicates the degree of membrane lipid accessibility (O_2 collision frequency, ΠO_2) and accessibility to the aqueous environment (ΠNiEdda collision frequency, ΠNiEdda) of residues 2–12 of the N-terminal domain using power saturation experiments[15,33]. When we map the degree of accessibility of all these residues on to the crystal structure of MscL, we observe not only the interfacial positioning of the N-terminal domain but also a lipid-accessible inter-subunit cavity (Fig. 2c). As shown in Fig. 1c–e, this is also supported by our MD simulations, demonstrating that lipid acyl chains protrude into these regions in a similar way to that suggested for MscS[34].

Global rearrangement of the N-terminal helix. As a proof of principle for the dynamic role of the N-terminal domain in the gating of MscL, we created a novel finite element model. Finite element (FE) simulations lack the atomistic resolution and information provided by MD including solvation effects, but the advantage of FE simulations being computationally inexpensive means that larger timescales can be probed. The FE models of MscL presented in this study were developed to provide a structural framework for a mechanistic understanding of the gating mechanism of MS channels at the continuum level (Fig. 3a,b). The FE model displays many of the attributes and features of MscL channel gating, reflecting well the pore expansion, TM tilting and their movement away from the central fivefold axis of the channel that is suggested in other studies (Fig. 3c,d)[15,19–22,35–37]. Moreover, in the open state, the lipid bilayer thins $\sim 15\%$ ($\sim 5\,\text{Å}$), which is in good agreement with previously reported results[38,39]. In response to membrane tension, the TM1 and TM2 helices move together in an outward radial direction tilting towards the plane of the membrane. The helical axis for TM1 tilted by 21° with respect to the central fivefold axis, whereas the TM2 helices tilted by more than 19°. One important point to note is that the N-terminal helix begins to align with TM1 as a contiguous helix in the open state (Fig. 3c). In addition, a stress analysis illustrates a high level of stress in the N-terminal helix, which points towards it being an important structural mechanosensing entity (Fig. 3d).

When we removed the N terminus, the global rearrangements of the channel were very different under the application of membrane tension (Fig. 3e–h). The tilt of TM1 was not as pronounced and the effective pore radius under the same applied force was almost 50% smaller. The model lacking the N terminus also displayed a lack of stability. It is important to note that, because of the instability of the model without the N terminus,
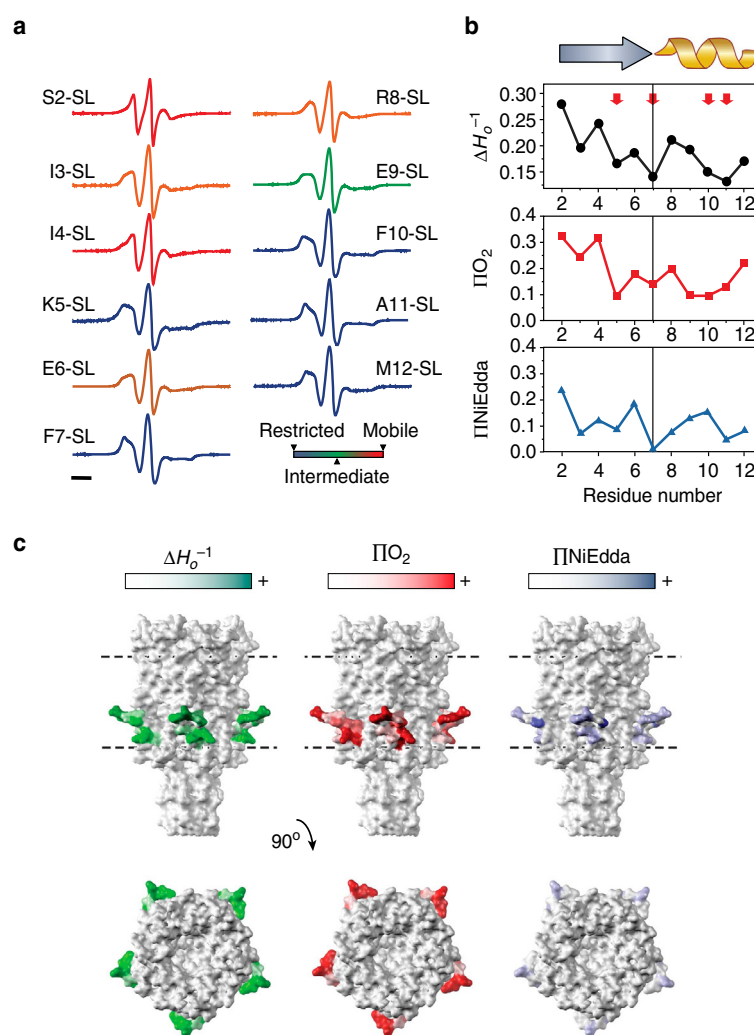
Figure 2 | Site-directed spin-labelling analysis of the MscL N terminus. (**a**) X-band CW-EPR spectra of spin-labelled N-terminal mutants reconstituted into azolectin liposomes. Spectra are colour-coded according to their overall probe dynamics as shown in the colour gradient (bottom right). (**b**) Environmental parameter profiles derived from the spectra in **a** or from power saturation experiments. Mobility parameter ΔH_o^{-1} (top panel, black circles), oxygen-accessibility parameter ΔO_2 (centre panel, red squares) and NiEdda-accessibility parameter Δ_{NiEdda} (bottom panel, blue triangles). A cartoon of the assigned secondary structure for this segment is shown on top. Bar represents 20 G. (**c**) EPR-derived structural data mapped on MtMscL. The side and top (extracellular) views of the mapped EPR data are displayed on solvent-accessible surfaces calculated in UCSF Chimera with a probe radius of 1.4 Å. Green tones, probe mobility (ΔH_o^{-1}). Red tones, oxygen-accessibility parameter (ΔO_2). Blue tones, NiEdda-accessibility parameter (ΔNiEdda). The dotted parallel lines represent the putative location of the lipid bilayer.

the MscL structures shown in Fig. 3e–h were modelled at half of the nondimensional membrane tension required for the full opening. Thus, the structures shown do not represent fully open states of the channel. Moreover, the 'effective' pore only takes into account the backbone of the helices. This is because of the fact that both TM1 and TM2 are modelled as elastic rods with a diameter of 5 Å. Therefore, what we define as the effective pore does not represent the exact diameter of the hydrophobic constriction point of the channel. Despite this, the FE model provides us with insights that can be further probed using EPR, MD and mutational analysis.

Probing the effect of N-terminal deletions. In order to provide unequivocal experimental support for the effects of N-terminal deletion seen in FE simulations, we used sequential deletion of the

N-terminal helix in combination with site-directed spin-labelled EPR spectroscopy (Fig. 4).

First, all truncations produce loss of sensitivity phenotypes where expression of these constructs cannot rescue MJF465 E. coli cells from hypo-osmotic downshock (Fig. 4a)[40]. The most severe loss of sensitivity was seen with the Δ2–7 construct, with all constructs requiring considerably more force to gate when probed using patch-clamp electrophysiology (Fig. 4b and Supplementary Fig. 4)[41,42]. In the crystal structure of MscL, the N terminus of one subunit (i) comes within close proximity of TM2 of the second-next neighbouring channel subunit (i + 2). Using the calculated mobility parameter at position M94-SL, as a surrogate for the mobility of TM2, we see a sharp increase in mobility when more than five residues were deleted from the N terminus. The spectra for the WT channel and the deletion mutants in the resting state are shown in Fig. 4c, and the associated mobility

ARTICLE

parameters (ΔH_o^{-1}) are quantified in Fig. 4d. We also show the spectra associated with the WT channel in the presence of LPC, which stabilizes the open state[16,43]. We can see that once we remove K5 the spectra of the deletions become progressively more like those encountered in the presence of LPC. This suggests that once K5 is removed the TM2 helix becomes more mobile and is consistent with the idea that an interaction between the N terminus and TM2 is lost. When we probed these interactions using MD simulations, we find that in fact a relatively strong electrostatic interaction is present between Glu residues on the N terminus (both E6 and E9) on subunit (i) and a Lys residue on TM2 of the second adjacent subunit ($i+2$; K97), which is $\sim 158.9 \pm 21$ kcal mol^{-1} (Fig. 4e). The K5 residue in fact seems to interact in a molecular triad with a Glu residue that resides in the loops between TM2 and the C-terminal bundle on the adjacent subunit (E108) and the phosphate of the head group of a phosphatidylethanolamine (PE) molecule (Fig. 4f). This image again clearly shows that a lipid acyl chain protrudes into the inter-subunit cavity. This type of interaction with a phosphate group provides the necessary interaction between the channel and the bilayer, although not discriminating against the lipid type, an observation supported by the non-selective binding of lipids to MscL in Laganowsky et al.[44].

Structural rearrangements at the N terminus probed using EPR. Using LPC/PC mixtures, we proceeded to investigate the conformation of the N terminus as it transitions into the open state to complement our FE simulations. Figure 5a shows the spectra of each individual N-terminal domain residue (2–12) in the presence (Red) and absence (Black) of LPC. The difference in the mobility parameter and lipid and aqueous accessibilities are then quantified in Fig. 5b as discussed previously. Here the resting conformation is shown with open grey symbols and the filled symbols represent LPC-treated experiments. There is a large and periodic increase in NiEdda (aqueous) accessibility at positions 5 and 9. This 'face' of the helix is opposite to the side with the large O$_2$ (lipid) exposure, which includes residues 4, 7, 10 and 11. The full periodicity of the N-terminal region shown in the upper panel of Fig. 5b suggests that the N-terminal region is fully helical in the open state. Combined with the lipid and aqueous accessibility shown in Fig. 5b, we show that the N terminus is forming a single contiguous helix with TM1. In light of our structural model of open MscL we suggest that the transition into a fully helical conformation helps extend the now tilted TM1 to span the length of the bilayer[15].

Simulating the extension of the Gly14 linker. All the data so far support the integral role of the interfacial N-terminal helix as an essential force transducing element in the gating cycle of MscL. Given this importance, we wanted to further probe how the connection between the N-terminal domain and TM1 affects force transmission. In order to do this we extended the Gly14 linker that attaches it to the pore-lining TM1 helix. The idea here is that increasing the linker length will impair the transmission of mechanical force from the N terminus to the pore-lining helix. This was achieved by the insertion of extra glycine residues (either $+2$ or $+5$) in addition to the native Gly14 (Supplementary Fig. 5). Glycine was chosen because of its inherent flexibility and low helical propensity.
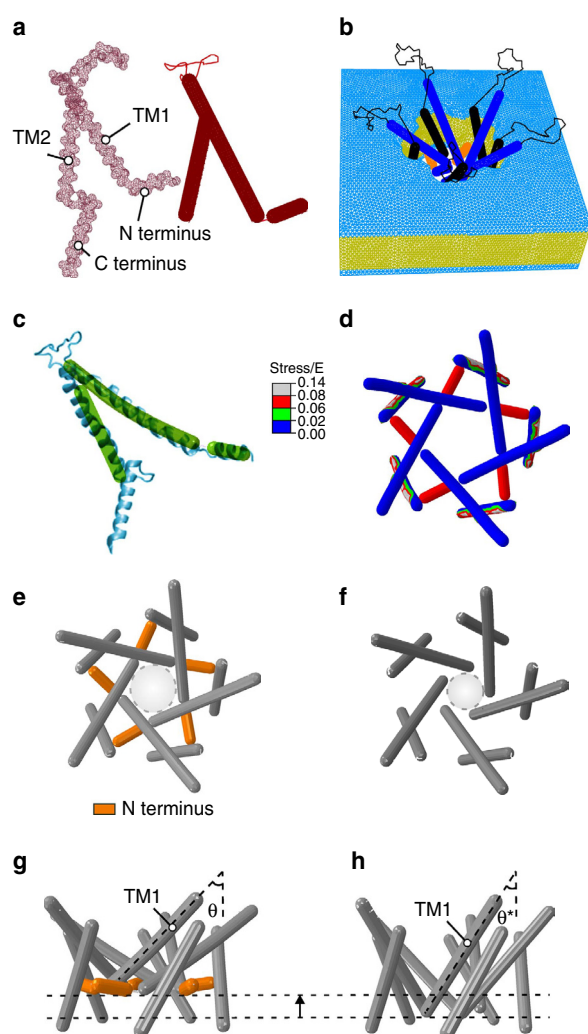

Figure 3 | The crucial role of the N-terminal domain in the gating of MscL shown by a parametric FE simulation. (**a**) Mesh representation of a subunit of WT EcMscL obtained from an EcMscL homology model based on MtMscL (PDB: 2OAR; left panel—red mesh)[17] and the FE model of a subunit of EcMscL without the C-terminal domain (right panel—solid red rods). The α-helices are modelled as elastic rods and the loops are modelled as nonlinear springs. (**b**) The FE structure of EcMscL is embedded into the lipid bilayer with the mesh distribution shown. (**c**) Superposition of FE EcMscL open structure with a previously obtained restrained MD simulation of EcMscL[20]. (**d**) Effective (Von Mises) stress distribution in the open state (top view). The membrane tensional stress is made dimensionless using the Young's modulus of EcMscL, E, that is, stress/E. The nondimensional stress is 0.6. (**e**,**f**) Channel pore in an expanded state, with and without the N terminus (top view). The nondimensional exerted stress on the membrane is 0.3 in both models, and thus they do not represent fully open structures[20,35]. The light grey dashed circles in **e**,**f** represent the position of the effective pore with respect to the plane of the membrane. This diameter is, however, not the actual pore size, since it does not show the side chains on each TM1. The effective pore diameter of the WT model is ~ 24 Å, and the model that lacks the N terminus is ~ 18 Å. (**g**) Side view of a WT subunit showing that the angle between the N-terminal domain and the TM1 helix increases as the channel begins to gate. Moreover, they both tilt upwards towards the membrane midplane as the membrane is stretched. (**h**) TM1 has less out-of-plane tilting in the absence of the N terminus ($\theta^* = 33°$) compared with the WT channel ($\theta = 45°$). Overall, these results suggest that the N-terminal helices have a significant role in transferring the force from the lipid to the pore-lining TM1 helix, guiding both its tilting and expansion.
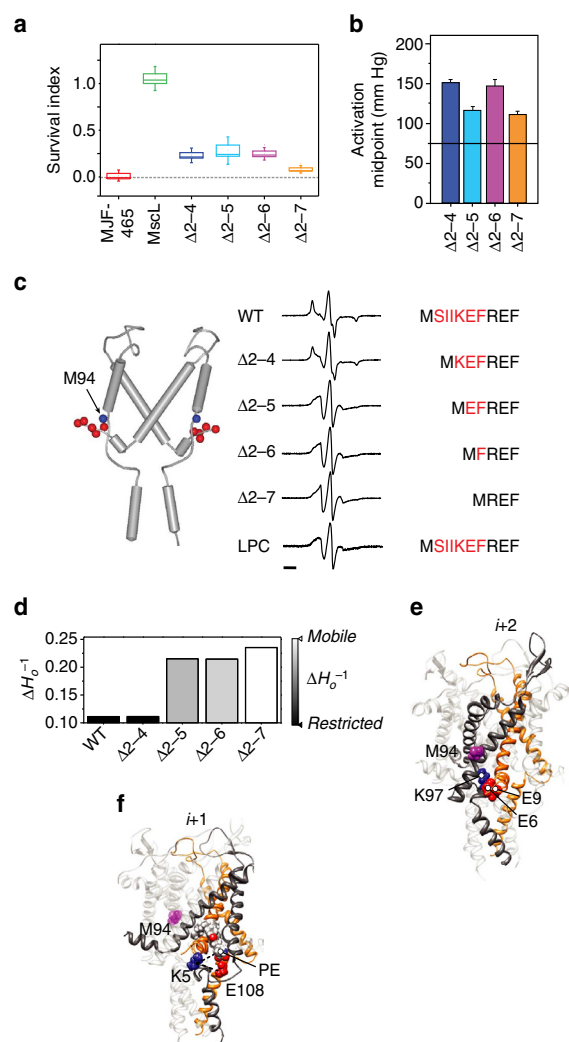
Figure 4 | Probing the functional role of the N-terminal domain and the physical interaction between the N terminus and TM2 by deletion analysis. (**a**) Survival of MJF465 (MscL⁻ MscS⁻ MscK⁻) *E. coli* expressing different deletion constructs of MscL after downshock from LB supplemented with 500 mM NaCl to LB (~1,000 mOsm). Data shown as box plots indicating the mean, 25 and 75 percentile (box) and ± s.d. (capped lines). (**b**) Midpoint of pressure activation of individual deletion constructs determined from multichannel patches (*n* = 4, Δ2–7, *n* = 3; mean ± s.d.). The dotted horizontal line represents the mean value for WT MscL. (**c**) Local dynamics at the intracellular end of TM2 (spin-labelled at position M94) as a function of N-terminal deletions. Left, cartoon representation of subunits *i* and *i* + 2 showing the position of the spin-labelling site (blue sphere) and the individual residues in the N terminus that were deleted (red spheres). Right, EPR spectra of M94-SL in a WT background, four different deletions (Δ2–4, Δ2–5, Δ2–6 and Δ2–7) and the WT background opened in the presence of LPCs. The N-terminal sequence of MscL is shown with the region of deleted residues in red. Bar represents 20 G. (**d**) Calculated mobility parameter at position M94-SL for the different spin-labelled constructs in **a**,**c**. (**e**) A cartoon representation of the electrostatic interaction of the Glu (E6 and E9) residues on subunits *i* with Lys (K97) residue of the second adjacent (*i* + 2) subunit. (**f**) A cartoon representation of the electrostatic interaction of the Lys (K5) residue on subunits *i* with Glu (E108) residue of the adjacent (*i* + 1) subunit and phosphate group of a POPE lipid molecule. The position of M94 has been indicated as a purple sphere with respect to these residues in **e**,**f**.

Our MD simulations were carried out using an optimized homology model of EcMscL based on the crystal structure of MtMscL and the C-terminal region of EcMscL from a recent crystal structure reported by the Rees group[17,18]. We then equilibrated a WT model and a model containing the additional five glycines (+5G) in a POPE (1-palmitoyl-2-oleoyl-sn-glycero-3-phosphoethanolamine) bilayer for 62 ns (Supplementary Fig. 6a,b). POPE was chosen as *E. coli* membranes contain >60% PE. The +5G mutant in the equilibrated closed state (after 62 ns) is more expanded, with an angle between the N-terminal helix and TM1 of 147 ± 3° compared with 136 ± 3° (mean ± s.e.m.) in the WT channel (Fig. 6a–d). The s.e. is measured based on the difference observed among the angles in the five subunits over three repeated simulations (Supplementary Figs 5–7). Consequently, the upper regions of the +5G model in the closed state are substantially more expanded compared with WT because of the increased tilt of TM1 helices (Fig. 6c,d; repeats shown in Supplementary Figs 6 and 7). This also corresponds to a slight movement of the hydrophobic gate, which in the +5G mutant is centred around the V23 residue, whereas in the WT the gate is a composite of both L19 and V23 (Fig. 6 and Supplementary Fig. 7).

In order to see a partial gating transition over the time frame of our simulations (~270 ns), it was necessary to apply higher tensional forces than those defined experimentally, taking into account that the first and midpoint activation tensions of MscL are 9 and 12 mNm⁻¹, respectively[43]. We used 75 and 100 mNm⁻¹ surface tension, but in an NγPzT ensemble[45]. This means when a surface tension of 75 mNm⁻¹ is applied to a POPE bilayer, the bilayer is only stressed by ~25 mNm⁻¹ (Supplementary Fig. 6c). This is because each lipid bilayer has an intrinsic surface tension (for example, ~50 mNm⁻¹ for POPE) to keep its area per lipid constant when it is stress-free[46], otherwise the bilayer would shrink[45]. Therefore, when we set the surface tension to 75 mNm⁻¹, in fact we are increasing the surface tension of the bilayer by ~25 mNm⁻¹. In order to systematically show this, we have calculated the surface tension of the bilayer in the presence of MscL when it is stress-free and when it is stressed. Thus, the highest value we applied on our lipid bilayer is actually 3–5 × of the experimental value. Using higher membrane tension than the experimental range for MscL activation is a common issue with these types of MD simulations. However, it is currently a 'necessary evil' in order to be able to capture full gating transitions, given existing limited computational timescales.

Our expanded structure obtained from MD simulations aligns well with the expanded structure in our FE model (Supplementary Table 1). This is a clear illustration that the FE model shows a similar trajectory to that of MD simulations, in particular, the formation of an almost contiguous helix (Fig. 6a–e and Fig. 3c) and is consistent with our extensive EPR data. It is important to note here that the addition of extra glycines does not affect the total lipid–protein interaction energy of our N-terminal helices, and it is instead a completely mechanistic insertion designed for testing our hypothesis (total interaction energy of the N terminus (the initial 13 residues) with the bilayer; WT 797.7 ± 44 kcal mol⁻¹, +5G mutant 841.3 ± 63 kcal mol⁻¹). Moreover, the interaction of the added five glycine residues with the lipid bilayer is in comparison negligible during our simulations (<1.6 kcal mol⁻¹).

After 268 ns of MD simulation under identical conditions (for the exact force regimen see Methods), the level of upward tilting of TM1 is not as pronounced in the +5G mutant when compared with the WT (Fig. 6b, side view). In addition, the pore of the WT model is substantially more expanded than the pore in the +5G model (Fig. 6b,e). This is because of the significant role
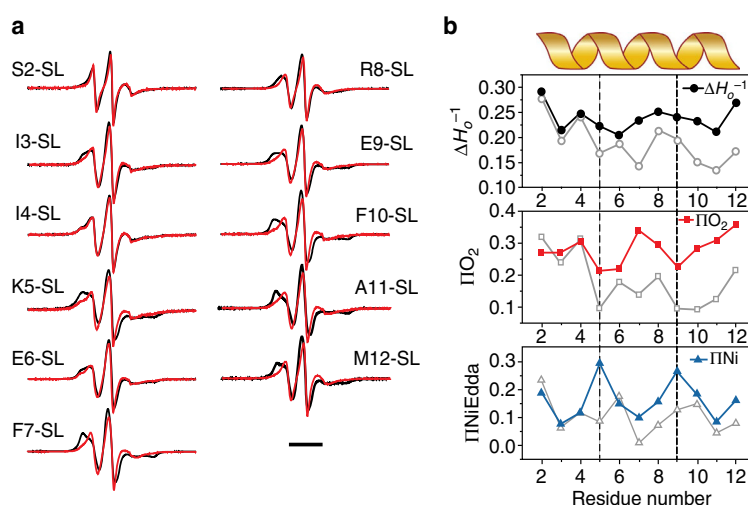
Figure 5 | Conformational changes at the N terminus associated with the channel opening. (**a**) X-band CW-EPR spectra of liposome-reconstituted spin-labelled N-terminal mutants in the presence (red traces) and in the absence (black traces) of 25 mol% LPC to stabilize the open conformation. Experimental conditions as described in Fig. 3. Bar represents 30 G. (**b**) Environmental parameter profiles of the N terminus in the open state, derived from the spectra in **a** or from power saturation experiments. Mobility parameter ΔH_o^{-1} (top panel, black circles), oxygen-accessibility parameter ΔO_2 (centre panel, red squares) and NiEdda-accessibility parameter ΔNiEdda (bottom panel, blue triangles). For comparison, data for the closed state (from Fig. 2) are shown on each panel as grey open symbols. The vertical dashed lines point to the periodic maxima of NiEdda-accessibility and O_2-accessibility minima in the open state.

of the N-terminal domain in tilting TM1 in the membrane plane and in expanding the pore by driving the movement of TM1 away from the central axis of the pore. This ability is impaired by extending the Gly14 linker between the N terminus and TM1. To be able to expand the $+5$G pore to the same level as the WT pore, the same level of tension is needed for a further 5 ns (Fig. 6c–f).

Here we should also note that during the expansion of the WT model the tight association of the lipid molecules with the N-terminal helix is conserved (Fig. 2c–e). While these lipids are 'dragged' away from protruding into the structure (Fig. 1c–e), their interactions with the protein, nevertheless, remain.

Electrophysiological effects of extending the Gly14 linker. In order to examine the functionality of mutant MscL channels with extended Gly14 linkers ($+2$G and $+5$G mutants), we purified the proteins and reconstituted them into azolectin liposomes (Fig. 7a–d). Owing to the complexity of electrophysiological patches and the impact of pipette geometry on membrane tension here we use MscS as a gauge to determine whether the extension of the linker between the N-terminal and the TM1 helix affects the MscL activation threshold[47,48]. When co-reconstituted with MscS, a severe loss of sensitivity to applied force was seen for both the $+2$G and $+5$G mutants (WT $P_{1/2}$ ratio: 1.8 ± 0.07 ($n=6$) $+2$G $P_{1/2}$ ratio: 2.6 ± 0.06 ($n=8$) and $+5$G $P_{1/2}$ ratio: 3.0 ± 0.21 ($n=9$)). In addition to these pronounced effects on opening, the lengthening of the G14 linker also mildly delayed closing (pressure-of-first-opening/pressure-of-last-closing ratio—WT: 1.0 ± 0.03 ($n=11$), $+5$G 1.5 ± 0.12 ($n=19$)) (Fig. 7d,e and Supplementary Fig. 9). However, the effect on closing was not as large as the effect on the mechanical force required to open the channel.

We saw the same loss of sensitivity in native membranes of *E. coli* spheroplasts (MJF612: $MscL^-$, $MscS^-$, $MscK^-$ and $YbdG^-$) when expressed with MscS (Supplementary Fig. 8). In fact, it was extremely difficult to apply sufficient force to gate the

$+5$G mutant in spheroplasts and this is why we chose to characterize these channels in liposomes (Supplementary Fig. 9).

The N terminus dictates the conformational freedom of TM1. One striking feature of extending the glycine linker between the N-terminal helix and the pore-lining TM1 helix is the change in single-channel activity. The $+5$G mutant gates almost exclusively in substates (Fig. 7f), making estimation of the channel unitary conductance difficult. This is indicative of the increased conformational freedom of TM1 enabled by the partial decoupling of the N-terminal helix. In the WT channel this tight link coordinates the movement of single monomers within the channel pentamer by efficiently coupling membrane tension to the TM1 helix of a single subunit.

Further mutational analysis of the Gly14 linker reveals its crucial role and the necessity for a relatively small hydrophilic residue in this region. Substitution with large residues prevented channel function completely (V, W), while the channel continued to function with polar side chains (S, Q, E, R; Fig. 7g). Deletion of G14 resulted in channels that were spontaneously active, giving rise to a 'leaky' phenotype and retarded growth in *E. coli*. The activity represented gating in lower substates, and full channel openings could not be seen even with the application of high pressure to the patch pipette (Fig. 7g). This may well be because of a repositioning of the N-terminal helix as a result of a loss of the 'kink' formed by G14. This is again further support for the stabilizing role of the N-terminal helix in the closed state of MscL.

Discussion

Here we have fully investigated the role of the amphipathic N-terminal helix in the gating cycle of *E. coli* MscL. These types of helices are present in all sorts of membrane-associated proteins (not just membrane-spanning channels) and were first suggested by Segrest *et al.*[49] to interact directly with the lipid bilayer. Mutagenic studies have previously shown the importance of this region in gating, particularly the phenylalanine residues[25,41,50].
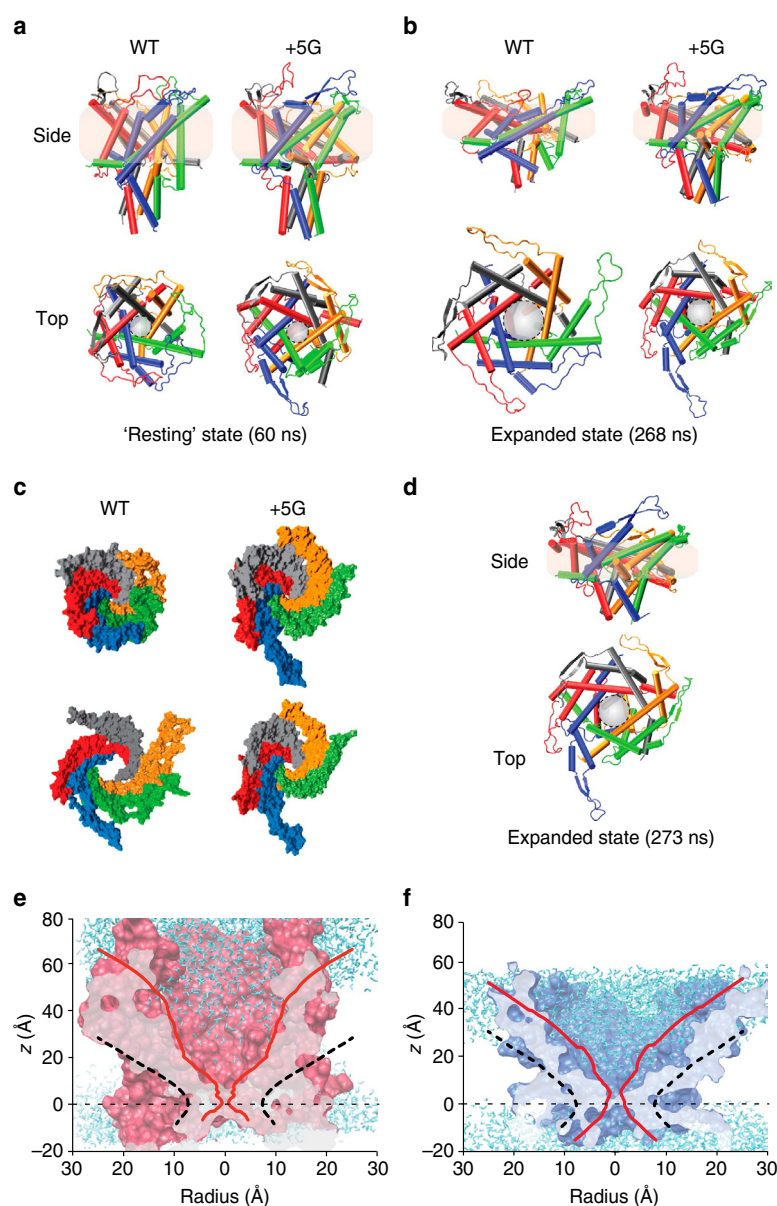
Figure 6 | All-atom MD simulations of WT and +5G mutant EcMscL models. (**a**) Side and top views of WT MscL and +5G MscL in their resting equilibrated states. The TM1 helices in the +5G are slightly more tilted than in the WT model mostly because of the higher degree of freedom of TM1 in the +5G model. (**b**) Side and top views of WT and +5G MscL after 268 ns of simulation (for force regimen see Methods). The pore of the WT model is much more expanded than in the +5G model. This is because of the significant role of the N terminus in tilting TM1 in the membrane plane and in expanding the pore by driving the movement of TM1 away from the central axis. This ability is diminished by extending the Gly linker between the N terminus and TM1. (**c**) A surface representation of WT and +5G models in the resting and expanded states from the top. This clearly shows the difference in the degree of expansion. (**d**) The side and top views of the expanded state of the +5G mutant MscL model. To reach this state, the simulation was run for longer than the WT simulation (additional 5 ns under the high membrane surface tension of 100 mN m^{-1}). (**e**) Closed (solid red) and expanded (dashed black) pore of WT MscL. (**f**) Closed (solid red) and expanded (dashed black) pore of +5G MscL. Comparing **e,f** shows that the upper regions of the +5G model in the closed state are substantially more expanded compared with WT because of an increased tilt of TM1 helices.

Using an interwoven multidisciplinary approach combining experiment and simulation, we show that the short amphipathic N-terminal helix of MscL acts as a horizontal coupling helix linking membrane bilayer dynamics to protein conformation, as initially proposed by Iscla *et al.*[25]. Our simulations and EPR spectroscopy data suggest a firm interaction between the amphipathic N-terminal helices of MscL and the lipid bilayer, with numerous residues buried within the acyl chains (Figs 1 and 2 and Supplementary Fig. 10). This fits well with the work of Blount and colleagues, showing that mutating these buried hydrophobic residues, especially F7 and F10, results in channels with a higher activation threshold[25,51]. Thus, we postulate that the N-terminal helix (or its equivalent) is essential in the process of coupling bilayer forces
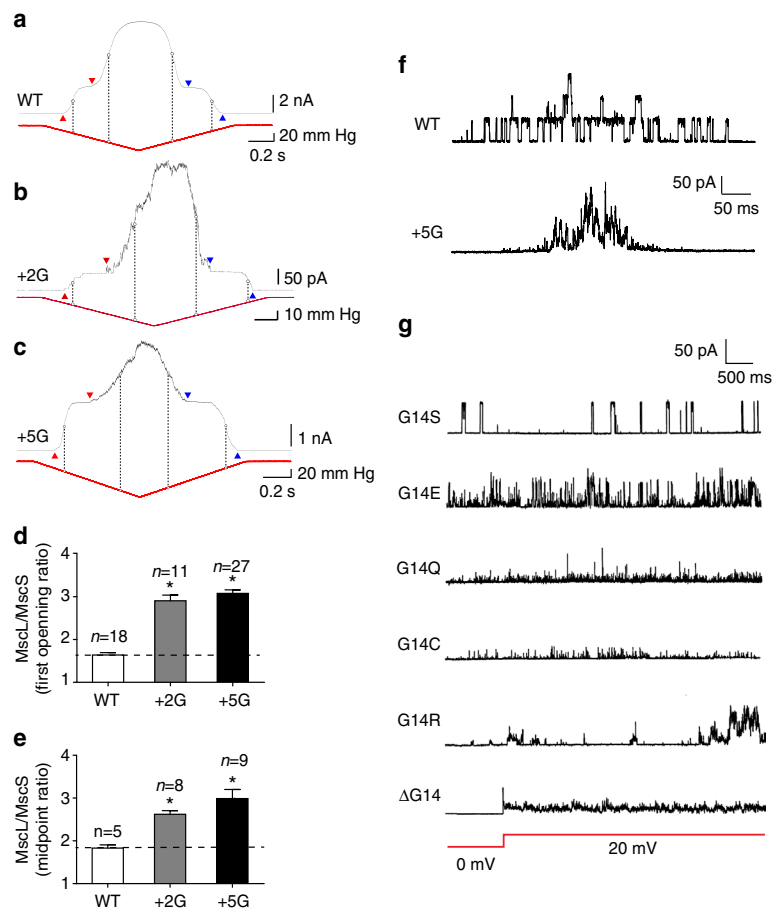
Figure 7 | Effect of extension of the Gly linker between the N terminus and TM1 on MscL activation threshold in liposomes. MscS and MscL are co-reconstituted in 100% azolectin lipid. (**a–c**) Current traces of MscS and MscL recorded at +5-mV pipette potential. Red arrowheads point to the first observed MscS and MscL opening, used to determine the MscL/MscS first opening threshold ratio (TR). Blue arrowheads point to the last observed MscS closure and MscL closure. The vertical dashed line illustrates the midpoint activation threshold of the respective channels. (**d,e**) The comparison between activation TR of WT with +2G and +5G mutant MscL mutants. It can clearly be observed that extension of the G linker increases the activation threshold of MscL by almost 100%. (data points represent mean ± s.e.m. *P-value < 0.01; one-way ANOVA). (**f**) Single-channel recordings from WT MscL (upper panel: 3.04 ± 0.04 nS (n = 5)) and +5G MscL (lower panel: 2.76 ± 0.08 nS (n = 5)) both recorded at +20-mV pipette potential and after application of negative pressure. The +5G mutant channel gates at substates for a large percentage of the time especially when compared with WT, a fact largely because of the greater conformational freedom of the TM1 helix. (**g**) Effect of polar substitutions at position G14 on single-channel activity of MscL. G14S gives almost WT-like activity, whereas deletion of G14 results in a channel that gates spontaneously at substates, giving rise to a 'leaky' toxic phenotype when expressed in E. coli. For ΔG14, the record shows the change in voltage from 0 to 20 mV pipette potential (red line) and the corresponding spontaneous activity.

to the pore-forming helices in a plethora of MS channels, a fact supported by robust experimental and computational data from numerous laboratories[11,27–31,52].

Further, our MD simulations show that the acyl chains of the lipid molecules deform around the N terminus and protrude into an inter-subunit cavity, in agreement with recent observations in the bacterial channel MscS, and suggested for the two-pore domain potassium channel TRAAK (Fig. 8)[11,30,34]. We note that, while the acyl chains are removed from these cavities during gating, they still have a tight association with the N-terminal helix (Supplementary Fig. 11). Therefore, rather than a gating mechanism based on entropy-driven lipid acyl chain removal, MscL appears to open as a result of the direct 'pulling' of structural elements in the channel such as the N-terminal helix. Thus, the 'exclusion' of acyl chains from these cavities seems to be a consequence rather than a cause of MscL gating.

A critical finding in this study was that, during MscL activation, the N-terminal helix becomes a long, contiguous helix with TM1, as shown by EPR spectroscopy and FE/MD simulations (Figs 3 and 5). Overall, the results from FE and MD are very comparable as shown in the Supplementary Table 1. The overall stress map with high intensity in the N-terminal domain is consistent with the stress values determined by our and previous MD simulations (Supplementary Fig. 11)[53]. Complete deletion of the N terminus in our FE model resulted in a channel significantly less sensitive to applied membrane tension. This fact is clearly shown by the reduced pore expansion in our model that lacks the N terminus (Fig. 3e,f) and suggests that the N-terminal helix is an essential mechanosensing entity within the MscL structure. This is supported by electrophysiological data and hypo-osmotic downshock experiments, which demonstrated abrogated function of sequential N-terminal deletion constructs.
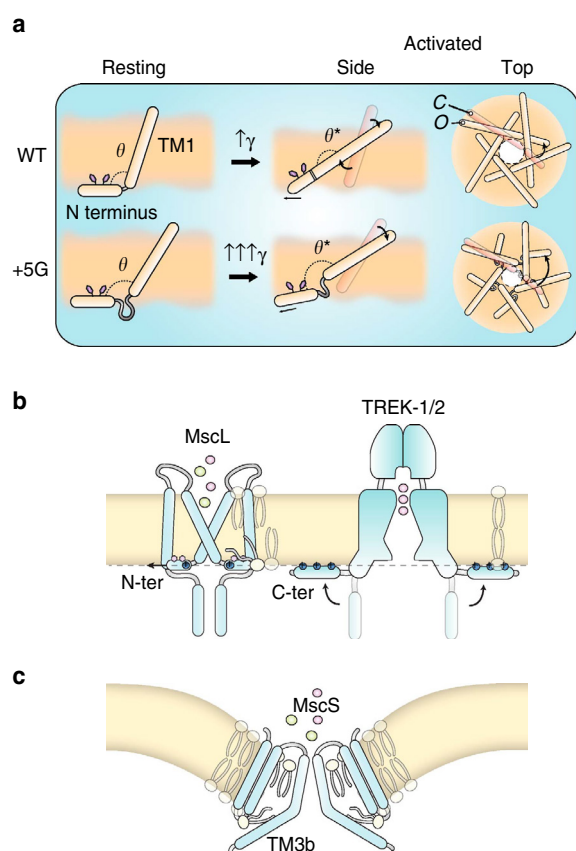
Figure 8 | Crucial role of the N-terminal domain in the gating of MscL.
(**a**) The N-terminal domain interacts tightly with the lipid bilayer. It orients at the lipid–solvent interface on the cytoplasmic side and acts as an anchor in stabilizing the closed state of the channel. As the lipid bilayer is stretched, the N-terminal helix is stretched following the trajectory of its surrounding lipid molecules but never becomes completely buried. Then, force is transmitted via the Gly14 residue to the end of TM1, which causes the alignment of TM1 with the N-terminal domain and the formation of a contiguous helix. If we extend the Gly linker (+ 5 G), we observe that one of the main roles of the N terminus is in expanding the pore. These functions are largely diminished in the + 5G model because of the fact that TM1 does not follow the trajectory of the N-terminal region. (**b,c**) Horizontal membrane-coupling helices seem to be a hallmark of mechanosensitive channels. These helices maybe buried as in the N terminus of MscL, TM3b of MscS and the S4–S5 linker of TRPV4 or adsorbed on the membrane surface as in the C terminus of TREK channels. Owing to the various types of lipids present in different organisms and the divergent ways in which these coupling helices can interact, there is little to no necessity for sequence conservation despite the fact that they play an almost identical role.

EPR and MD simulations reveal that there are also essential interactions between the N terminus and the TM2 helix of the second subunit neighbour ($i + 2$) in addition to the adjacent neighbour. These tight interactions define the conformational freedom of the TM2 helix (Fig. 4).

On the basis of the present data set and simulations, we suggest that the 'force from lipids' is transmitted to the MscL pore-lining TM1 helices via the N terminus. This amphipathic helix would guide the tilting and movement of the five TM1 helices in a coordinated manner, magnifying the resulting pore expansion. Specifically, the conformational rearrangement that establishes

the continuity between the N terminus and the intracellular end of the pore-lining TM1 helix allows a putative radial force on the N terminus to be transduced into increased tilt in the TM1 helix relative to the membrane. In this scenario, the link between the N terminus and TM1 (G14) is likely to play a critical role in mechanical coupling. Indeed, deletion of G14 leads to a 'leaky' phenotype with continuous spontaneous activity at subconducting levels (Fig. 7g). This suggests that G14 likely acts as a hinge, positioning the N-terminal parallel to the membrane plane at the bilayer-solvent interface and that its structural flexibility is crucial for stabilizing TM1 (and thus, the closed state). This proposal is further supported by our site-directed mutagenesis at this position where less flexible residues (*W*, *V*) do not give rise to channel currents but more flexible polar residues do[54], where a serine mutation gives rise to WT-like currents.

By averaging all the subunits, the N-terminal helix moves quite significantly in the radial direction during gating: 8.3 ± 1.3 Å in MD simulations and 10.5 ± 0.5 in FE simulations (Supplementary Table 1 and Supplementary Movie 1 and Supplementary Software 1). To further address the mechanism of force transmission from the N terminus to the TM1 helix, we designed mutants where the N-terminal/TM1 linker was extended by the addition of two or five glycines. In electrophysiology experiments, the linker extension resulted in channels with a much higher gating threshold, with these channels gating almost exclusively in substates because of the lack of coordinated movement of single subunits of the channel pentamer. A simple explanation for this is that the resulting increase in conformational freedom of the TM1 helix associated with this partial decoupling from the N terminus results in an abrogated ability of forces felt by the N terminus to be transferred to the TM1 helix. From MD simulations, the addition of five glycines should not affect the total interaction energy between the N termini and the bilayer. Our equilibrated + 5G model displays a more expanded state, indicative of the partial decoupling of TM1 helices from the N termini, ultimately preventing the N-terminal stabilization of the closed state (Fig. 6). These results are in agreement with the recently published structural data on the role of the N-terminal domain in stabilizing the closed state of an archaeal MscL homologue MaMscL[55]. Therefore, in addition to the mechanosensing residues at the rim of MscL, for example, F78 (ref. 56), we conclusively show that the force transmission from the bilayer to the N terminus and thus to TM1 is an essential driver of both the tilting of TM1 and the radial expansion of the channel pore (Fig. 8a).

Horizontal membrane-coupling helices, such as the N-terminal domain of MscL, appear to be a hallmark of MS channels that gate according to the force from lipid paradigm and seems to be independent of their evolutionary provenance (Fig. 8b). These helices can be partly buried as we have shown here for the N terminus of MscL. This may also be the case for TM3b of MscS (it is important to note here that there are differing schools of thought regarding the exact gating cycle[34,57]) and the S4–S5 linker of TRPV4 (refs 31,52). Alternatively, these mechanical-force-coupling helices may be adsorbed on the membrane surface through electrostatic interactions. Such regions are seen in the current crystal structures of TREK1/2 and TRAAK where the lower half of these channels seem to have a tight association with the lipid bilayer[11,12,30,58]. In addition, the distal C terminus in these force-sensitive K_{2P} channels, which is not seen in any of the TREK crystal structures, is predicted to be an extended amphipathic helix functionally essential for mechanically induced gating[27–29]. Regardless of the complexity of the gating paradigms for these individual classes of channels, these horizontal force-transmitting helices have repeatedly been shown to play integral roles in the transmission of mechanical stimuli according to the force from the lipid concept[12,15,33,59,60].

Owing to the various types of lipids present in different organisms and the divergent ways, these coupling helices can interact (buried, adsorbed); there is little to no expectation for sequence conservation, despite the fact that they play an almost identical mechanical role. Given that Piezo1 has recently been shown to be gated according to the force from the lipid paradigm[10], we speculate, taking into account functional data[61], that the $\alpha 4^{anchor}$, which runs roughly parallel to the inner bilayer leaflet[13], may also serve the same purpose in the gating of Piezo1 channels as the N terminus does for MscL.

Methods

Bioinformatics. Sequence alignments were carried out using Clustal Omega. Motifs were defined using Prosite. The following consensus motif was used to search UniProt for proteins containing a similar sequence: F-[K,R]-x-F-[A,I,L]-x-[K,R]-G. Helical wheel diagrams and hydrophobic moment ($<\mu H>$) were calculated using HeliQuest.

FE model. Owing to large deformations during MscL gating, we employed an FE computational method implemented in the ABAQUS commercial software (Abaqus/Standard; Dassault Systems Simulia Dassault Systemes Simulia Corp., Providence, RI, USA). In our model, the α-helices are modelled as elastic rods and the loops are modelled as nonlinear wires. Elastic rods are fitted to the orientation of backbone carbons of each TM helix, while the loops are modelled as nonlinear wires. Although our FE model shares similarities with the previous FE models[36,38,62], it differs from those in several important aspects as follows. Our model is based on a homology model of a more recent MscL crystal structure (PDB: 2OAR)[17], showing that the N terminus connects the TM1 helix to the lipid bilayer almost perpendicularly to TM1. The C-terminal helices are not included as it has been shown that they have negligible effect on the gating of EcMscL[41,63]. Glycine 14 (G14) between the N terminus and TM1 is modelled by a Hinge Connector available in ABAQUS, reflecting the flexible nature of this residue. To more accurately capture the lipid bilayer behaviour during gating, a mean field-like lateral pressure profile for the bilayer is considered in the tail and head regions (see ref. 47 for further details). This way, unlike the previous FE models[36,38,62], our simulation does not require any assignment of mechanical properties for different areas of the lipid bilayer. Moreover, a nondimensional FE analysis is carried out, which is independent of the protein elasticity modulus. The applied tensional stress on the membrane as well as the stress outputs are also nondimensionalized using the overall Young's modulus of the protein. Pairwise interactions between the lipid and outer surface of the TM helices are defined by a van der Waals (vdw) stress function[64]. The surface interaction stress can be computed as a function of the distance between two hydrophobic surfaces by adopting the following equation[47].

$$S = -A_H / 6\pi D^3 \qquad (1)$$

Here S is the stress, A_H is the Hamaker constant and D is the distance between the two surfaces. The normal tractions can be positive, indicating an attractive interaction between the surfaces, or negative, in the case of repulsive forces. The resulting expression of intralayer contact interactions has been implemented in an ABAQUS-user subroutine called UINTER for computing the vdw stresses. The lipid bilayer inner surface and the outer surface of each TM helix are defined as the master and slave surfaces, respectively. The UINTER subroutine is called for each individual slave node at every time increment through the analysis. Inputs to this subroutine are the initial and the incremental relative positions of each slave node with respect to its closest point on the master surface. The constitutive calculation thus involves computing the tractions based on the increments in relative position of the slave node with respect to the master surface. The energetic interaction constants are obtained from fitting equation (1) to the overall interaction energies obtained from our MD simulation of MscL in a POPE lipid bilayer. As a result, a Hamaker constant of $\sim 21(\pm 3) \times 10^{-21}$ J is obtained at the equilibrium state.

In the EcMscL crystal structure, the TM1 and TM2 helices of adjacent subunits have a very large contact area stabilized by vdw interactions, and their crossing angle is slightly positive ($\sim 10°$). The contacts in the channel area involve the TM1 helices of the two adjacent subunits (crossing angle $\sim -43°$) and two TM2 helices: one within the same subunit (crossing angle $\sim 135°$) and the second from an adjacent subunit (crossing angle $\sim 169°$). The TM2 helices of neighbouring subunits do not directly contact each other, but are separated by ~ 20 Å (refs 14,17). N-terminal helices make an $\sim 95°$ link, with the TM1 close to the pore with the upper half of the N terminus buried in the lipid bilayer. Interhelical interactions are ignored for simplicity and more importantly to check the gating characteristics of MscL when only force transmitted from the membrane is considered. Before any FE analysis, a mesh-sensitivity study was carried out to ensure the independence of the results from the computational mesh. All the FE computational analyses were conducted using a CPU 2.4 GHZ, 8-Gigabyte RAM and at the maximum run time of ~ 5 h.

MD simulations. All MD simulations were performed with NAMD2.10 (ref. 65). Visual MD (VMD)[66], Pymol and UCSF Chimera were used for all visualizations. The three-dimensional structure of E. coli MscL and $+5$G mutant EcMscL were generated based on the crystal structure of the MscL homologue of M. tuberculosis (PDB ID: 2OAR) using Phyre2[,67] and Swiss-Model[68].

The resultant MscL models were embedded into a POPE bilayer comprising 222 lipid molecules using the VMD software. After deletion of lipids inside the channel and those in very close proximity to the protein (<5 Å), the lipid heads and tails were in turn randomized and equilibrated for ~ 1 ns at 298 K, while the rest of the system was fixed. The protein and lipids were next solvated with a $120 \times 120 \times 130$–Å water box and 200 mM KCl. The TIP3P water molecule model was used along with the SOLVATE programme. A further randomization of the POPE lipid tails was performed, with the rest of system being fixed. Lipid, water and ions packed around the protein for 1 ns with the $C\alpha$ atoms of the protein were restrained with a spring constant of 5 KJ mol^{-1} Å^{-2} at constant pressure (1 atm). Then, the whole system was equilibrated for 62 ns with a time step of 2 fs with no restraints. The equilibration step (62 ns) was run three times for each of the WT and the $+5$G mutant models. After equilibration to see the channel expansion, a surface tension of 75 mN m^{-1} was applied on the lipid molecules for 200 ns with a time step of 0.1 nm in an $N\gamma P_z T$ (constant surface tension, constant pressure and constant temperature) ensemble (262 ns total simulation time). To see a partial gating event of the WT and $+5$G mutated channels, a further 25 mNm^{-1} was added to the previous surface tension (100 mNm^{-1} in total) and applied to the membrane for another 6 ns (268 ns in total) and 11 ns (273 ns in total), respectively (1 fs time step). In all the simulations, the particle-mesh Ewald method was used for computing electrostatic interactions beyond a real-space cutoff of 1.2 nm with a Fourier grid spacing of 0.1 nm. A modified Nosé–Hoover Langevin piston pressure control provided in NAMD was utilized to control fluctuations in the barostat (at 1 atm). This method is combined with a method of temperature control (at 298 K; Langevin dynamics) in order to simulate the NPT ensemble. The CHARMM c36 Force field was used for all MD calculations. The pore shape of closed and open MscL channels was interrogated using the HOLE programme with a probe of 1 Å radius using the CHARMM36 vdw radii for the protein and energetic calculations done using the NAMD energy plugin.

We wrote custom tcl codes (Supplementary Software 1) for calculating the interaction energies, thickness, tilt angle and movement of the N-terminal helix. All custom-written codes are available for download.

Mutagenesis and construct generation. In order to probe the role of the N-terminal helix, we created constructs that expressed MscL with a hexahistidine fusion purification tag specifically on the C terminus to prevent the tag from interfering with N-terminal gating mechanisms that were to be analysed by electrophysiology. MscL was subcloned into pETDuet-1 vector (Novagen) by PCR using PfuUltra (Agilent) thermostable DNA polymerase. The PCR primers (IDT; 'BsaI-MscL-F' acttaaGGTCTCcCATGcGCGGGAACGTGGTGGATTT and 'HindIII-MscL-6his-stop' tagctaAAGCTTTTAGTGGTGGTGGTGGTGGTGAGA GCGGTTATTCTGCTCTT) were used to amplify the WT E. coli MscL-coding sequence for the ligation into the NcoI and HindIII sites of pETDuet-1 after the PCR product had been digested with BsaI and HindIII-HF restriction enzymes (New England Biolabs). The reverse primer coded to the last WT amino acid, immediately followed by hexahistidine purification fusion tag and stop codon, while the forward primer allowed translation to start with the native start methionine. The construct allows MscL expression by T7 RNA polymerase-based E. coli extract cell-free synthesis systems (Exiprogen, Bioneer) or by E. coli recombinant culture systems compatible with the T7 RNA polymerase promoter.

Two extra glycines were inserted into the N-terminal MscL domain of the above construct immediately before G14 using a 'Quikchange' site-directed mutagenesis method employing the following primers: 'MscL R13R + GG-S' GAATTTCGCGA ATTTGCGATGCGCGGTGGTGGGAACGTGGTGGATTTGGCGGTG and 'MscL R13R + GG-AS' CACCGCCAAATCCACCACGTTCCCACCACCGCGCATCGCAA ATTCGCGAAATTC.

The construct to encode for five extra glycines adjacent to G14 was constructed by performing megaprimer site-directed mutagenesis to the above ' + 2G' construct. The primary megaprimer PCR reaction used the following primer 'MscL R13R + GGGGG-S' GAATTTCGCGAATTTGCGATGCGCGGTGGTGGTGGTG GTGGGAACGTGGTGGATTTGGCGGTG (to insert three more glycines ahead of the two extra glycines), with the 'HindIII-MscL-6his-stop' primer. The secondary megaprimer PCR reaction used the resulting primary PCR product as a reverse primer with the 'BsaI-MscL-F' primer to create a full-length $+5$G MscL C-terminal hexahistidine insert to be cloned as above into pETDuet-1.

Protein purification and incorporation into liposomes. MscS and MscL were purified using immobilized metal affinity chromatography and either 6 × - or 10 × -His-tag combined with size exclusion chromatography[69]. Final elution buffers contained 1-mM n-Dodecyl β-D-maltoside for both channel proteins. Reconstitution into soybean azolectin (Sigma, CA) liposomes was carried out using the dehydration/rehydration (D/R) method[69,70]. Briefly, mixed lipids were dissolved in chloroform and dried under N$_2$ flow to make a thin lipid film. D/R buffer (200 mM KCl, 5 mM HEPES, adjusted to pH 7.2 with KOH) was added before vortexing and in subsequent 10 min of sonication. MscS and MscL were

ARTICLE

added at a protein-to-lipid ratio of 1:500 (w/w) and incubated at 4 °C for 1 h. Detergent was removed with the addition of Biobeads (Bio-Rad, Hercules, CA) and incubated at 4 °C for further 3 h. The proteoliposomes were collected by ultracentrifugation and resuspended in 30 µl D/R buffer. Aliquots of proteoliposomes were spotted on cover slips and dehydrated overnight under vacuum conditions at 4 °C. The dried proteoliposomes were then rehydrated with D/R buffer at 4 °C for at least 6 h and subsequently used for electrophysiological experimentation.

Spheroplast preparation. *E. coli* spheroplasts were prepared as using a standardized protocol[43,70]. Briefly, MJF465 ($\Delta kefA$::kan,$\Delta yggB$,$\Delta mscL$::Cm) or MJF612 ($\Delta ybdg$::apr,$\Delta kefA$::kan,$\Delta yggB$,$\Delta mscL$::Cm) cells were grown for 1.5 h in the presence of the cephalosporin-type antibiotic cephalexin (final concentration 60 µg ml^{-1}) to form *E. coli* snakes (length $-$ 50 to 150 µm). Cells were then digested for 3–7 min in the presence of 0.8 M sucrose, 60 mM TRIS, pH 7.2, lysozyme (final concentration 0.2 mg ml^{-1}) and EDTA (6.3 mM). A stop solution (0.8 M sucrose, 20 mM MgCl$_2$, 60 mM TRIS pH 7.2) was added, and the spheroplasts were collected by centrifugation.

Electrophysiology. An aliquot of proteoliposomes (1–3 µl) was introduced into the recording chamber. Channel activity of WT MscL and mutant proteins ($+2$G and $+5$G) were co-reconstituted with the WT MscS channel and examined in inside-out azolectin liposome patches using the patch-clamp technique[43]. Borosilicate glass pipettes (Drammond Scientific Co, Broomall, PA) were pulled using a micropipette puller (PP-83; Narishige, Tokyo, Japan). Pipettes with resistance of 3.0–5.0 MΩ were used for the patch-clamp experiments. Pipette and bath solution contained 200 mM KCl, 40 mM MgCl$_2$ and 5 mM HEPES (pH 7.2 adjusted with KOH). In the case of spheroplast patching, the bath solution was supplemented with 400 mM sucrose. The current was amplified with an Axopatch 200B amplifier (Molecular Devices, Sunnyvale, CA), filtered at 5 kHz and data acquired at 20 kHz with a Digidata 1440A interface using pCLAMP 10 acquisition software (Molecular Devices) and stored in a personal computer. Negative pressure was applied manually with a syringe or High-Speed Pressure Clamp-1 apparatus (HSPC-1; ALA Scientific Instruments, Farmingdale, NY) and was monitored with a pressure gauge (PM 015R, World Precision Instruments, Sarasota, FL).

Survivability of MJF465 cells. Survival of MJF465 ($\Delta kefA$::kan,$\Delta yggB$,$\Delta mscL$::Cm) *E. coli* expressing different N-terminal deletion constructs of EcMscL after osmotic downshock from LB supplemented with 500 mM NaCl ($\sim$1,000 mOsm) to LB was carried out using a standardized protocol[40]. Briefly, cells were exposed to osmotic downshock or control conditions for 15 mins, and 10 µl of a fivefold dilution was aliquoted on an agar plate. Plates were incubated overnight and the resulting number of colonies was counted the next day.

Spin-labelling and EPR spectroscopy. The purified MscL mutant proteins were spin-labelled overnight with methanethiosulfonate spin label (Toronto Research) at a 10:1 label/channel molar ratio and were reconstituted at a 500:1 lipid/channel molar ratio by dilution in PBS[16]. Consequently, in a fully labelled channel, each of the five subunits had one spin label attached. EPR spectroscopy was performed using X-band CW EPR spectra obtained in a Bruker EMX spectrometer fitted with a loop-gap resonator at 2-mW incident power, 100 kHz modulation frequency and 1 G modulation amplitude[16]. The accessibility parameter used in this study to quantify the extent of solvent accessibility in a per-residue basis reports on the individual collision frequency of a nitroxide spin label with paramagnetic test compounds, and it is derived from the midpoints of signal saturation at increasing microwave powers. Power saturation curves were obtained for each spin-labelled mutant after equilibration in N$_2$ as control, and air (21% O$_2$), and N$_2$ in the presence of 200 mM NiEdda as relaxing agents. All EPR data were obtained at room temperature.

Statistical analysis. One-way analysis of variance combined with a Holm–Šídák *post hoc* test (Fig. 7 and Supplementary Fig. 8) or Student's *t*-test (Supplementary Fig. 9) were used for statistical analysis and differences were considered significant at $P < 0.01$. Statistical significance was confirmed in groups with low *n* number using non-parametric Kruskal–Wallis test. The number of experiments and replicates is mentioned in the figure legends. The values are mean ± s.e.m., unless otherwise specified.

Data availability. The authors confirm that the data that support the findings of this study are available from the corresponding author upon reasonable request.

References

1. Hamill, O. P. & Martinac, B. Molecular basis of mechanotransduction in living cells. *Physiol. Rev.* **81**, 685–740 (2001).
2. Sukharev, S. & Sachs, F. Molecular force transduction by ion channels: diversity and unifying principles. *J. Cell Sci.* **125**, 3075–3083 (2012).
3. Haswell, E. S., Phillips, R. & Rees, D. C. Mechanosensitive channels: what can they do and how do they do it? *Structure* **19**, 1356–1369 (2011).
4. Ranade, S. S., Syeda, R. & Patapoutian, A. Mechanically activated ion channels. *Neuron* **87**, 1162–1179 (2015).
5. Phillips, R., Ursell, T., Wiggins, P. & Sens, P. Emerging roles for lipids in shaping membrane-protein function. *Nature* **459**, 379–385 (2009).
6. Teng, J., Loukin, S., Anishkin, A. & Kung, C. The force-from-lipid (FFL) principle of mechanosensitivity, at large and in elements. *Pflugers Arch.* **467**, 27–37 (2015).
7. Zhang, W. *et al.* Ankyrin repeats convey force to gate the NOMPC mechanotransduction channel. *Cell* **162**, 1391–1403 (2015).
8. Brohawn, S. G., Su, Z. & MacKinnon, R. Mechanosensitivity is mediated directly by the lipid membrane in TRAAK and TREK1 K+ channels. *Proc. Natl Acad. Sci. USA* **111**, 3614–3619 (2014).
9. Sukharev, S. I., Blount, P., Martinac, B., Blattner, F. R. & Kung, C. A large-conductance mechanosensitive channel in *E. coli* encoded by mscL alone. *Nature* **368**, 265–268 (1994).
10. Cox, C. D. *et al.* Removal of the mechanoprotective influence of the cytoskeleton reveals PIEZO1 is gated by bilayer tension. *Nat. Commun.* 103667 **(2016)**.
11. Brohawn, S. G., del Mármol, J. & MacKinnon, R. Crystal structure of the human K2P TRAAK, a lipid-and mechano-sensitive K+ ion channel. *Science* **335**, 436–441 (2012).
12. Dong, Y. Y. *et al.* K2P channel gating mechanisms revealed by structures of TREK-2 and a complex with Prozac. *Science* **347**, 1256–1259 (2015).
13. Ge, J. *et al.* Architecture of the mammalian mechanosensitive Piezo1 channel. *Nature* **527**, 64–69 (2015).
14. Chang, G., Spencer, R. H., Lee, A. T., Barclay, M. T. & Rees, D. C. Structure of the MscL homolog from *Mycobacterium tuberculosis*: a gated mechanosensitive ion channel. *Science* **282**, 2220–2226 (1998).
15. Perozo, E., Cortes, D. M., Sompornpisut, P., Kloda, A. & Martinac, B. Open channel structure of MscL and the gating mechanism of mechanosensitive channels. *Nature* **418**, 942–948 (2002).
16. Perozo, E., Kloda, A., Cortes, D. M. & Martinac, B. Physical principles underlying the transduction of bilayer deformation forces during mechanosensitive channel gating. *Nat. Struct. Biol.* **9**, 696–703 (2002).
17. Steinbacher, S., Bass, R., Strop, P. & Rees, D. C. Structures of the prokaryotic mechanosensitive channels MscL and MscS. *Curr. Topic Memb.* **58**, 1–24 (2007).
18. Walton, T. A. & Rees, D. C. Structure and stability of the C-terminal helical bundle of the *E. coli* mechanosensitive channel of large conductance. *Protein Sci.* **22**, 1592–1601 (2013).
19. Sukharev, S., Betanzos, M., Chiang, C. S. & Guy, H. R. The gating mechanism of the large mechanosensitive channel MscL. *Nature* **409**, 720–724 (2001).
20. Corry, B. *et al.* An improved open-channel structure of MscL determined from FRET confocal microscopy and simulation. *J. Gen. Physiol.* **136**, 483–494 (2010).
21. Gullingsrud, J. & Schulten, K. Gating of MscL studied by steered molecular dynamics. *Biophys. J.* **85**, 2087–2099 (2003).
22. Gullingsrud, J., Kosztin, D. & Schulten, K. Structural determinants of MscL gating studied by molecular dynamics simulations. *Biophys. J.* **80**, 2074–2081 (2001).
23. Iscla, I. & Blount, P. Sensing and responding to membrane tension: the bacterial MscL channel as a model system. *Biophys. J.* **103**, 169–174 (2012).
24. Blount, P. & Moe, P. C. Bacterial mechanosensitive channels: integrating physiology, structure and function. *Trends Microbiol.* **7**, 420–424 (1999).
25. Iscla, I., Wray, R. & Blount, P. On the structure of the N-terminal domain of the MscL channel: helical bundle or membrane interface. *Biophys. J.* **95**, 2283–2291 (2008).
26. Ou, X., Blount, P., Hoffman, R. J. & Kung, C. One face of a transmembrane helix is crucial in mechanosensitive channel gating. *Proc. Natl Acad. Sci. USA* **95**, 11471–11475 (1998).
27. Maingret, F., Patel, A. J., Lesage, F., Lazdunski, M. & Honoré, E. Mechano-or acid stimulation, two interactive modes of activation of the TREK-1 potassium channel. *J. Biol. Chem.* **274**, 26691–26696 (1999).
28. Patel, A. J. *et al.* A mammalian two pore domain mechano-gated S-like K+ channel. *EMBO J.* **17**, 4283–4290 (1998).
29. Treptow, W. & Klein, M. L. The membrane-bound state of K2P potassium channels. *J. Am. Chem. Soc.* **132**, 8145–8151 (2010).
30. Lolicato, M., Riegelhaupt, P. M., Arrigoni, C., Clark, K. A. & Minor, D. L. Transmembrane helix straightening and buckling underlies activation of mechanosensitive and thermosensitive K 2P channels. *Neuron* **84**, 1198–1212 (2014).
31. Teng, J., Loukin, S. H., Anishkin, A. & Kung, C. L596–W733 bond between the start of the S4-S5 linker and the TRP box stabilizes the closed state of TRPV4 channel. *Proc. Natl Acad. Sci. USA* **112**, 3386–3391 (2015).

ARTICLE

32. Reading, E. *et al.* The effect of detergent, temperature, and lipid on the oligomeric state of MscL constructs: insights from mass spectrometry. *Chem. Biol.* **22,** 593–603 (2015).

33. Vasquez, V., Sotomayor, M., Cordero-Morales, J., Schulten, K. & Perozo, E. A structural mechanism for MscS gating in lipid bilayers. *Science* **321,** 1210–1214 (2008).

34. Pliotas, C. *et al.* The role of lipids in mechanosensation. *Nat. Struct. Mol. Biol.* **22,** 991–998 (2015).

35. Martinac, B., Buechner, M., Delcour, A. H., Adler, J. & Kung, C. Pressure-sensitive ion channel in Escherichia coli. *Proc. Natl Acad. Sci. USA* **84,** 2297–2301 (1987).

36. Chen, X., Cui, Q., Tang, Y., Yoo, J. & Yethiraj, A. Gating mechanisms of mechanosensitive channels of large conductance, I: a continuum mechanics-based hierarchical framework. *Biophys. J.* **95,** 563–580 (2008).

37. Wang, Y. *et al.* Single molecule FRET reveals pore size and opening mechanism of a mechano-sensitive ion channel. *eLife* **3,** e01834 (2014).

38. Tang, Y., Yoo, J., Yethiraj, A., Cui, Q. & Chen, X. Mechanosensitive channels: insights from continuum-based simulations. *Cell Biochem. Biophys.* **52,** 1–18 (2008).

39. Wiggins, P. & Phillips, R. Analytic models for mechanotransduction: gating a mechanosensitive channel. *Proc. Natl Acad. Sci. USA* **101,** 4071–4076 (2004).

40. Levina, N. *et al.* Protection of Escherichia coli cells against extreme turgor by activation of MscS and MscL mechanosensitive channels: identification of genes required for MscS activity. *EMBO J.* **18,** 1730–1737 (1999).

41. Hase, C. C., Le Dain, A. C. & Martinac, B. Molecular dissection of the large mechanosensitive ion channel (MscL) of E. coli: mutants with altered channel gating and pressure sensitivity. *J. Membr. Biol.* **157,** 17–25 (1997).

42. Blount, P. *et al.* Membrane topology and multimeric structure of a mechanosensitive channel protein of Escherichia coli. *EMBO J.* **15,** 4798–4805 (1996).

43. Nomura, T. *et al.* Differential effects of lipids and lyso-lipids on the mechanosensitivity of the mechanosensitive channels MscL and MscS. *Proc. Natl Acad. Sci. USA* **109,** 8770–8775 (2012).

44. Laganowsky, A. *et al.* Membrane proteins bind lipids selectively to modulate their structure and function. *Nature* **510,** 172 (2014).

45. Feller, S. E. & Pastor, R. W. Constant surface tension simulations of lipid bilayer: The sensitivity of surface areas and compressibilities. *J. Chem. Phys.* **111,** 1281–1287 (1999).

46. Gullingsrud, J. & Schulten, K. Lipid bilayer pressure profiles and mechanosensitive channel gating. *Biophys. J.* **86,** 3496–3509 (2004).

47. Bavi, N. *et al.* Biophysical implications of lipid bilayer rheometry for mechanosensitive channels. *Proc. Natl Acad. Sci. USA* **111,** 13864–13869 (2014).

48. Suchyna, T. M., Markin, V. S. & Sachs, F. Biophysics and structure of the patch and the gigaseal. *Biophys. J.* **97,** 738–747 (2009).

49. Segrest, J. P., Jackson, R. L., Morrisett, J. D. & Gotto, A. M. A molecular theory of lipid—protein interactions in the plasma lipoproteins. *FEBS Lett.* **38,** 247–253 (1974).

50. Blount, P., Sukharev, S. I., Schroeder, M. J., Nagle, S. K. & Kung, C. Single residue substitutions that change the gating properties of a mechanosensitive channel in Escherichia coli. *Proc. Natl Acad. Sci. USA* **93,** 11652–11657 (1996).

51. Iscla, I., Wray, R., Eaton, C. & Blount, P. Scanning MscL channels with targeted post-translational modifications for functional alterations. *PLoS ONE* **10,** e0137994–e0137994 (2014).

52. Malcolm, H. R. & Blount, P. Mutations in a conserved domain of E. coli MscS to the most conserved superfamily residue leads to kinetic changes. *PLoS ONE* **10,** e0136756 (2015).

53. Vanegas, J. M. & Arroyo, M. Force transduction and lipid binding in MscL: a continuum-molecular approach. *PLoS ONE* **9,** e113947 (2014).

54. Smith, D. K., Radivojac, P., Obradovic, Z., Dunker, A. K. & Zhu, G. Improved amino acid flexibility parameters. *Protein Sci.* **12,** 1060–1072 (2003).

55. Li, J. *et al.* Mechanical coupling of the multiple structural elements of the large-conductance mechanosensitive channel during expansion. *Proc. Natl Acad. Sci. USA* **112,** 10726–10731 (2015).

56. Yoshimura, K., Nomura, T. & Sokabe, M. Loss-of-function mutations at the rim of the funnel of mechanosensitive channel MscL. *Biophys. J.* **86,** 2113–2120 (2004).

57. Akitake, B., Anishkin, A., Liu, N. & Sukharev, S. Straightening and sequential buckling of the pore-lining helices define the gating cycle of MscS. *Nat. Struct. Mol. Biol.* **14,** 1141–1149 (2007).

58. Brohawn, S. G., Campbell, E. B. & MacKinnon, R. Physical mechanism for gating and mechanosensitivity of the human TRAAK K+ channel. *Nature* **516,** 126–130 (2014).

59. Honoré, E. The neuronal background K2P channels: focus on TREK1. *Nat. Rev. Neurosci.* **8,** 251–261 (2007).

60. Naismith, J. H. & Booth, I. R. Bacterial mechanosensitive channels--MscS: evolution's solution to creating sensitivity in function. *Annu. Rev. Biophys.* **41,** 157–177 (2012).

61. Zhao, Q. *et al.* Ion permeation and mechanotransduction mechanisms of mechanosensitive piezo channels. *Neuron* **89,** 1248–1263 (2016).

62. Tang, Y. *et al.* A finite element framework for studying the mechanical response of macromolecules: application to the gating of the mechanosensitive channel MscL. *Biophys. J.* **91,** 1248–1263 (2006).

63. Anishkin, A. *et al.* On the conformation of the COOH-terminal domain of the large mechanosensitive channel MscL. *J. Gen. Physiol.* **121,** 227–244 (2003).

64. Israelachvili, J. N. *Intermolecular and Surface Forces: Revised* 3rd edn (Academic press, 2011).

65. Phillips, J. C. *et al.* Scalable molecular dynamics with NAMD. *J. Comput. Chem.* **26,** 1781–1802 (2005).

66. Humphrey, W., Dalke, A. & Schulten, K. VMD: visual molecular dynamics. *J. Mol. Graph.* **14,** 33–38 (1996).

67. Kelley, L. A., Mezulis, S., Yates, C. M., Wass, M. N. & Sternberg, M. J. The Phyre2 web portal for protein modeling, prediction and analysis. *Nat. Protoc.* **10,** 845–858 (2015).

68. Biasini, M. *et al.* SWISS-MODEL: modelling protein tertiary and quaternary structure using evolutionary information. *Nucleic Acids Res.* **42,** W252-8 (2014).

69. Häse, C. C., Le Dain, A. C. & Martinac, B. Purification and functional reconstitution of the recombinant large mechanosensitive ion channel (MscL) of Escherichia coli. *J. Biol. Chem.* **270,** 18329–18334 (1995).

70. Nomura, T., Cox, C. D., Bavi, N., Sokabe, M. & Martinac, B. Unidirectional incorporation of a bacterial mechanosensitive channel into liposomal membranes. *FASEB J.* **29,** 10 4334–10 4345 (2015).

Author contributions

N.B., C.D.C, E.P., D.R., W.L. and B.M. designed research; N.B. and O.B. performed the simulations. B.C. and A.P.H. helped and supported MD simulations. N.B., C.D.C., E.P., M.D.C., P.S., J.W.D. and W.L performed the experiments; M.C., B.M. and E.P. carried out all the EPR-related experiments. P.R.R., N.B. and C.D.C. designed and carried out the mutagenesis and spheroplast formation. B.M., A.P.H., B.C., E.P. and D.R. contributed reagents/analytic tools; N.B., M.C., C.D.C., E.P., P.S. and B.M. analysed data; and N.B., C.D.C., A.P.H., E.P. and B.M. wrote the manuscript. All authors read and approved the final manuscript.

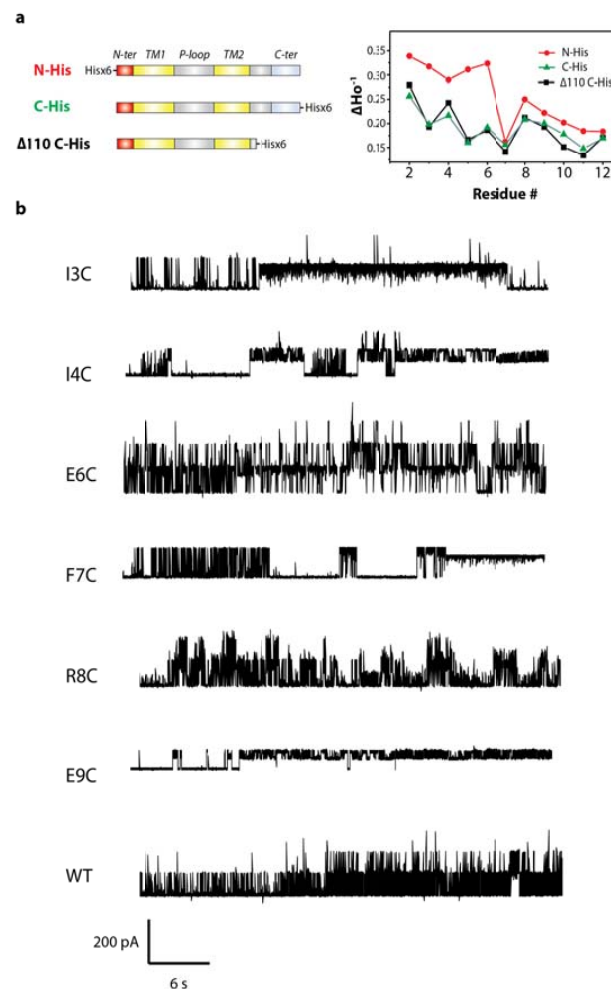## Additional information

Supplementary Information

Supplementary Figure 1 The influence of the N-terminal tag on structure and dynamics of EcMscL. (**a**) Schematic diagrams of the three types of EcMscL constructs used in the present study (left panel) and local mobility profile for the three MscL constructs, as derived from line-shape broadening of spin-labeled mutants (right panel). (**b**) Representative current traces of N-terminal cysteine mutant channels. Except for the mutant K5C all other mutants were functional at the single channel level. Most of them displayed frequent and/or prolonged gating at subconducting levels.
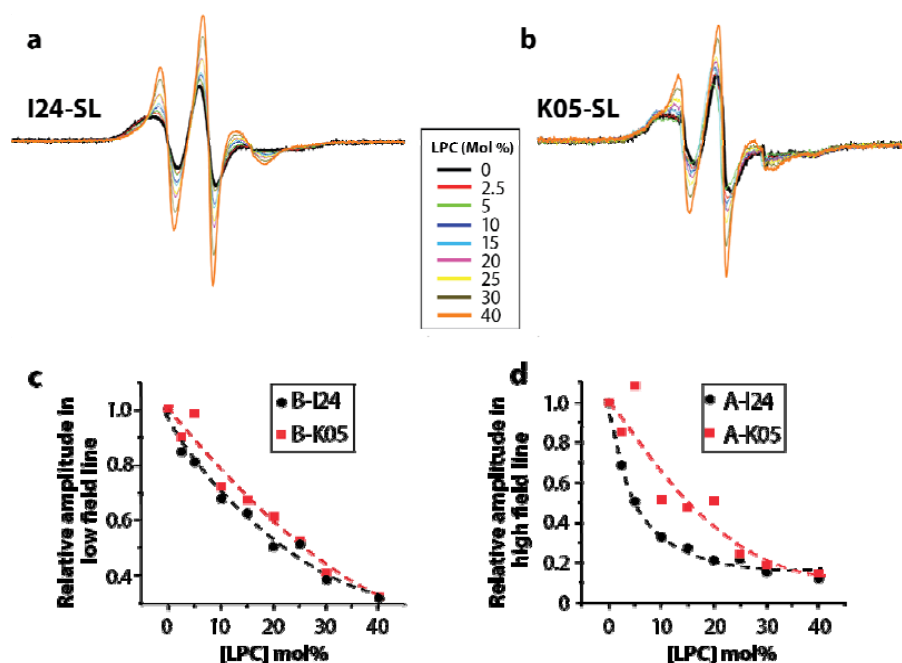
Supplementary Figure 2 Comparison of the loss of function phenotype of K5C with a WT-like mutation in the TM1 helix (I24C). (**a**) X-band CW-EPR spectra of spin-labeled I24C and (**b**) and K5C mutants reconstituted into azolectin liposomes. Spectra are color coded according to the concentration of the LPC used for the MscL activation (middle) (**c,d**) Low and high field response to different concentrations of LPC of K5C and I24C mutants. The figures show that more LPC is required to gate the K5C mutant but nevertheless it can ultimately adopt the fully open state.
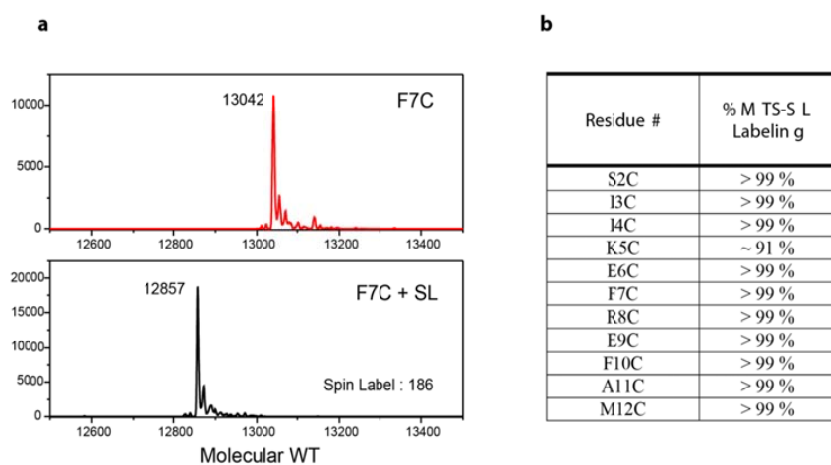
Supplementary Figure 3 Mass spectrometry of the spin labeling efficiency. The extent of labeling of the N-terminal residues was directly determined from their mass spectra by integrating the respective peaks for the expected masses of the labeled and unlabeled (**a**) species using the electrospray ionization technique (31). All N-terminal residues examined by EPR spectroscopy were fully labelled (**b**).
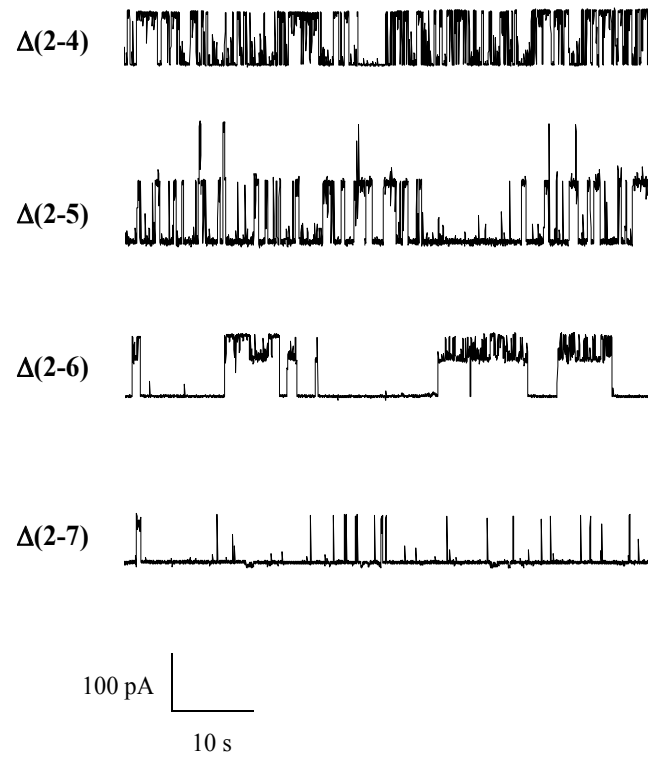
Supplementary Figure 4 Current traces of N-terminal deletion mutants. The activity of the deletion mutants decreased as the size of the deletion was increased. All mutant channels were reconstituted into azolectin liposomes and recorded at a pipette voltage V_p = +30 mV and suction (negative pressure applied to the patch pipette) of 60 mmHg.
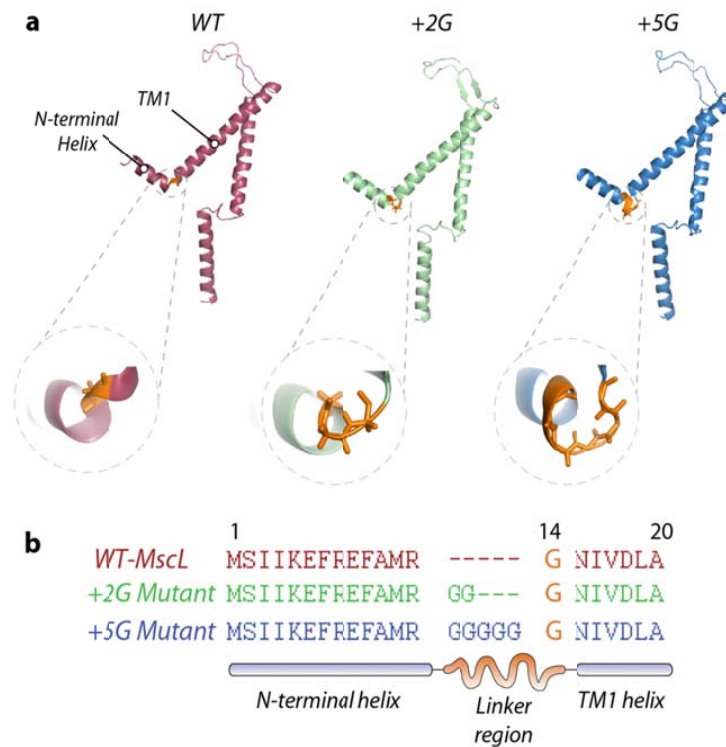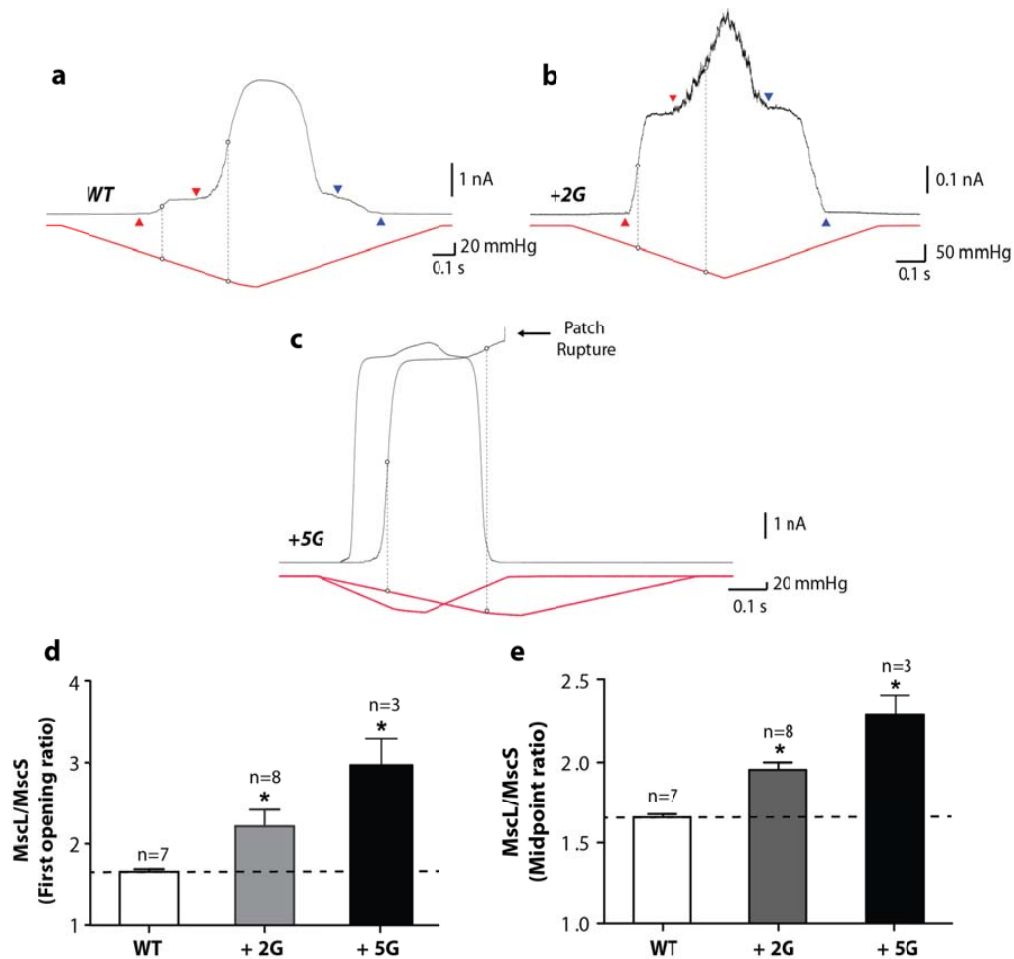
Supplementary Figure 5 Extension of the glycine linker between the N-terminal helix and TM1 helix. (**a**) In addition to the wild type (WT) model (red), two *in silico* models of +2G (green) and +5G mutants (blue) are shown, where two and five extra glycine residues are added to G14, respectively. (**b**) The sequence of the initial amino acids of WT, +2G and +5G mutant models showing the location of the extra glycine residues.
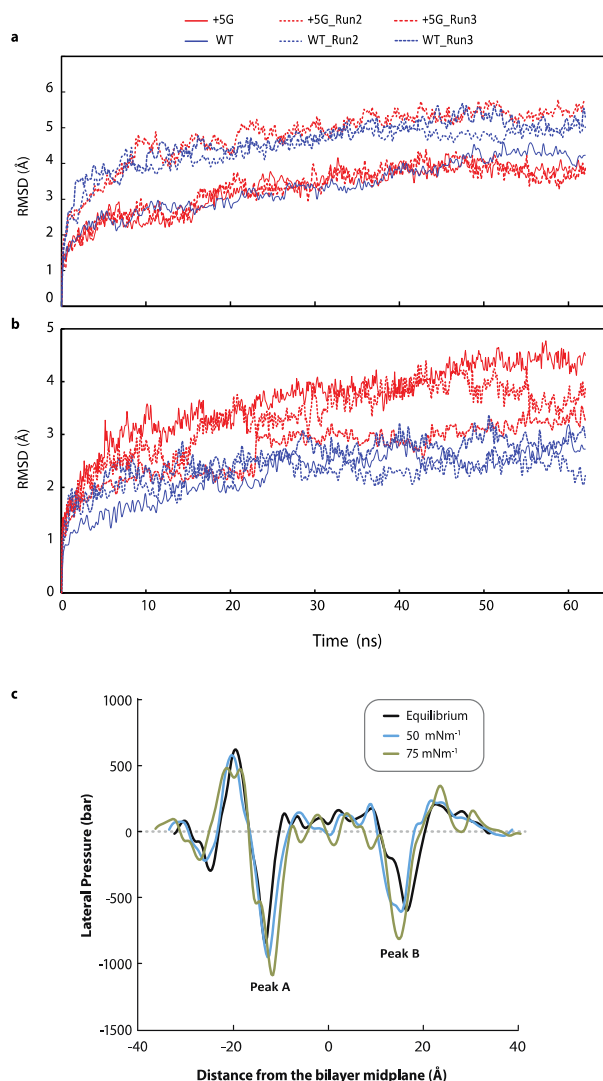
Supplementary Figure 6 Equilibration of WT MscL and +5G mutant in a POPE lipid bilayer in an NPT ensemble using all-atom MD simulation. Simulation for each model (WT and +5G) was carried out three times, each for 62 ns duration. (**a**) Root Mean Square Deviation (RMSD) of the protein backbone carbons plotted against simulation time. Both WT and +5G models are well equilibrated after 62 ns. (**b**) During equilibration, the RMSD of N-terminal domain in WT is lower than the RMSD of +5G N-terminal region as the latter one has more freedom due to the extra added glycines. (**c**) Illustration of how the pressure profile of the lipid bilayer in the presence of MscL changes at different surface tensions of 50 and 75 mNm^{-1} in an NγPzT ensemble. Also of note is the asymmetry in the pressure profile after MscL has been inserted into the bilayer. As shown, when the target surface tension is 50mNm^{-1} the pressure profile of the lipid in the presence of MscL changes negligibly. We only start to see noticeable changes in the pressure profile at 75 mNm^{-1}, particularly at the lipid water interface (Peak A and Peak B). In this condition (target surface tension of 75 mNm^{-1}), compared to a non-stressed bilayer (equilibrium) and based on the area under the pressure profile we estimate a mean membrane tension of 25.5 mNm^{-1} has been applied on the membrane, which is about twice the experimental value.
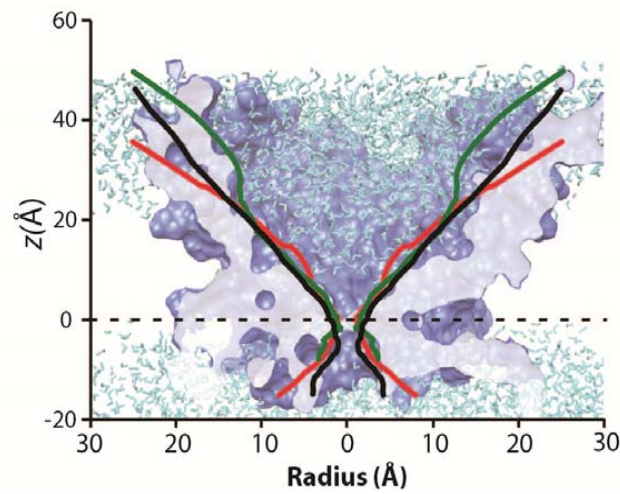
Supplementary Figure 7 Pore shape of +5G mutant MscL equilibrated in a solvated POPE lipid bilayer for 62 ns. The simulation is run three times and the pore shape has been shown for each run. This clearly supports the idea that as the Gly linker between the N-terminus and TM1 helices gets longer, the resting conformation of the channel becomes wider compared to the WT model. The red, green and black lines represent the reproducibility of this expansion in our 1st, 2nd and 3rd simulations respectively. Moreover, the length of the hydrophobic constriction region of the pore is shorter than in the WT MscL largely due to higher degrees of freedom of the N-terminus in the +5G mutant MscL.

Supplementary Figure 8 Effect of extension of the Gly linker between the N-terminus and TM1 on MscL activation threshold in *E. coli* spheroplasts. (**a-c**) Current traces of MscS and MscL recorded at +10 mV (pipette voltage). Upward red arrowheads point to the first observed MscS opening, whereas the downward pointing arrows indicate the first observed MscL opening used to determine the MscL/MscS first opening threshold ratio (TR). The vertical dashed line illustrates the midpoint activation threshold of each channel [(**a**) WT MscL, (**b**) +2G and (**c**) +5G mutant MscL]. (**d**, **e**) Shows the comparison between activation TR of WT with +2G and +5G mutant MscL channels. It can clearly be seen that extension of the Gly linker greatly increases the activation threshold of MscL. Significant differences are indicated by asterisks (*p-value < 0.01; One-way ANOVA). [WT MscL/MscS $P_{1/2}$ 1.7 ± 0.03 (n=7) and first opening 1.7 ± 0.2 (n=7). +2G mutant/MscS $P_{1/2}$ ratio: 2.1 ± 0.06 (n=8), first opening ratio: 2.3±0.15 (n=8) and +5G mutant/MscS $P_{1/2}$ ratio: 2.3 ± 0.20 (n=3), first opening 3.01 ± 0.33 (n=3)]. In addition, the mutants also showed a decreased sensitivity to applied force indicated by an increase in $1/\alpha$ values i.e. a shallower slope of the Boltzmann fit to P_o vs pressure [WT: 5.1 ± 0.6 mmHg (n=3), +2G: 8.7 ± 2.3 mmHg (n=3) and +5G: 12.3 ± 1.4 mmHg (n=3)]; where P_o is the open probability, and α is the slope of the plot ln [$P_o/(1-P_o)$] vs (p-p$_{1/2}$).
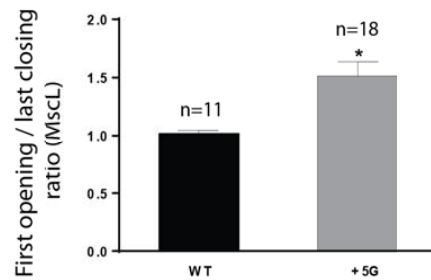
Supplementary Figure 9 First opening over last closing pressure threshold ratio of MscL. Full closing of +5G occurs at lower pressures compared to the WT. This is due to the fact that the reorganisation and closing of the pore by the N-terminal domain and TM1 helix is less effective in +5G mutant as a result of the extended Gly linker (Data represents mean ± S.E.M; p-value <0.01, Student's T-test).
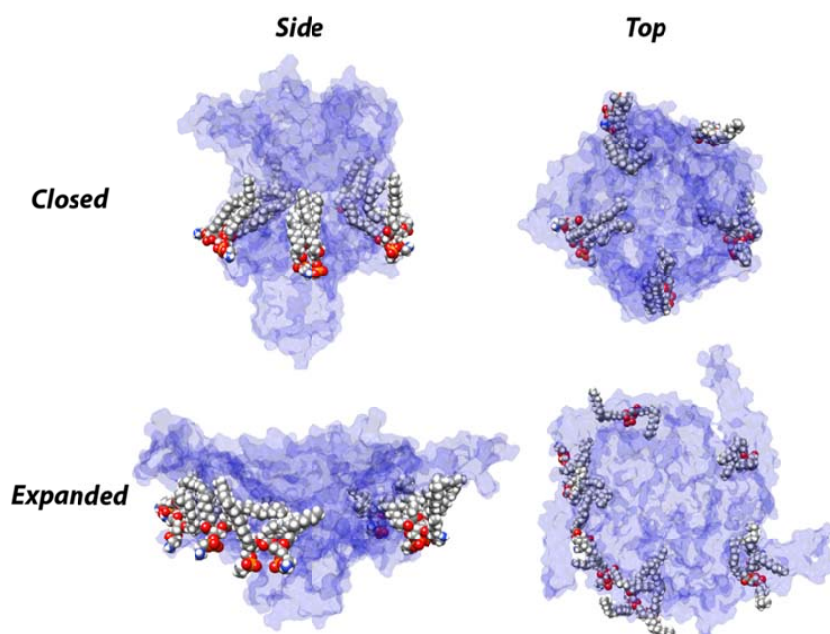
Supplementary Figure 10. Lipid protrusion in the inter-subunit cavities in the closed (resting) state (upper panel) and the open state of the channel (lower panel). From the side and the top views it is clear that the acyl chain of the lipid molecules protrude into the inter-subunit cavities in the resting state of MscL such that they interact tightly with the upper surface of the N-terminus. In the open state the lipid chains are stretched out of the cavities while they drag (guide) the N-terminus with them via their tight coupling.
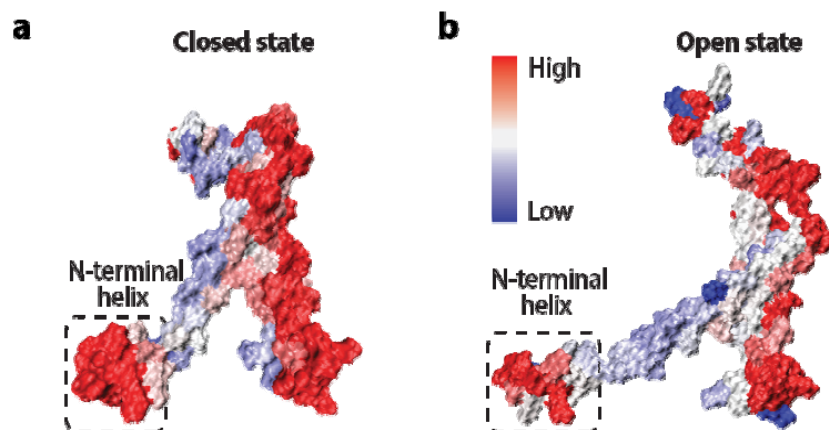
Supplementary Figure 11 Lipid-protein interaction mapped onto an EcMscL subunit from MD simulations. The interaction energy is shown between the lipid and the protein in (**a**) the closed state and in (**b**) the open state. Red shows the highest interactions and blue shows the lowest interaction. This unsurprisingly illustrates the highest level of interaction between the lipid facing part of TM2 and the N-terminal helix. (**a**,**b**) Illustrates that the N-terminal has an intimate interaction with the lipid bilayer in the closed state and that this tight association is conserved throughout the gating cycle. This is commensurate with the idea that the N-terminal is being 'pulled' by the lipid and drives gating.

Tilt about Z axis		MD			FE	
		Initial angle	Final angle	Tilt angle	Final angle	Tilt angle
Tilt about Z axis	N-terminal	76.3 ±6.2	87.3 ±5.7	12.0 ±10.2	88.6 ±1.2	13.9 ±1.2
	TM1	47.0 ±1.0	70.8 ±1.3	23.8 ±1.7	72.1 ±2.9	25.0 ±2.7
	TM2	30.6 ±2.2	60.5 ±3.1	30.0 ±3.5	52.9 ±4.6	26.3 ±2.4
	Pore Diameter (Å)		Bilayer thinning (%)		N-terminal movement (Å)	
MD	28.2		15.3		8.3 ±1.3	
FE	30.1		14.3		10.5 ± 0.5	

Supplementary Table 1 Comparison of the MscL structure obtained from all-atom molecular dynamics (MD) and finite element (FE) simulation in the closed (initial) and the open state (final). The initial angles of FE are exactly the same as in the MD since it was mapped from the MD structure. All the angles are in degrees. Z axis is the direction normal to membrane plane (along the membrane thickness). It is notable that the MscL pore obtained from MD simulation is not completely round in shape (**Fig. 2C**) with a maximum pore diameter of 28.2 Å. The pore shape obtained from FE is more symmetric and the diameter is ~ 30.1 Å. Since the FE structure is modelled based on the backbone carbons (no side chains), the reported values for the pore diameter for both MD and FE simulations are based on the backbone to backbone distance of the constriction pore which structurally encompasses L19 and V23. All the values are Mean ± SEM and n=5. The N-terminal helix movement obtained from the MD simulation is 8.3 ±1.3 Å versus 10.5 ± 0.5 Å obtained from the FE simulation. The bilayer thins 14.3 % after full MscL gating in our FE model. The thickness change due to MscL gating obtained from MD simulation is 15.3 %.

CHAPTER 4

As discussed in Chapter 3, the gating cycle of MscL includes a cascade of movements and deformations of transmembrane helices in response to membrane tension. Therefore, measuring the mechanical properties of the helices as the main building blocks of MscL, further sheds light on the details of MscL gating. More importantly, given the growing interest in using MscL as a nanosensor and/or nanovalve in biotechnology, there are still essential questions left unanswered with regards to the mechanical strength, robustness and function of MscL as a nanovalve. In this chapter of the thesis, using a large number of all-atom molecular dynamics simulations, the mechanical properties of MscL α-helices are estimated. Also, the efficiency of the two widely-used MD approaches called "constant-velocity" and "constant-force" methods for measuring mechanical properties of proteins are compared. Moreover, three questions are addressed regarding MscL channels in *Mycobacterium tuberculosis* and *Escherichia coli*; i) how much force does each α-helix bear during the gating process? ii) how do the helix properties differ in different environments (e.g., vacuum vs. water)? and iii) is there any difference between the mechanical properties of the helices in different MscL homologues?

Our results should be useful not only for studies of MS and other types of ion channels but also for studies of mechanical properties of "soft" biological materials in general.

Taylor & Francis
Taylor & Francis Group

RESEARCH PAPER

Nanomechanical properties of MscL α helices: A steered molecular dynamics study

N. Bavi[a,b,‡], O. Bavi[c,‡], M. Vossoughi[c,d], R. Naghdabadi[c,e], A.P. Hill[a], B. Martinac[a,b], and Y. Jamali[f,g]

[a]Division of Molecular Cardiology and Biophysics, Victor Chang Cardiac Research Institute, Darlinghurst, NSW, Australia; [b]St Vincent's Clinical School, Faculty of Medicine, University of New South Wales, Darlinghurst, NSW, Australia; [c]Institute for Nanoscience and Nanotechnology, Sharif University of Technology, Tehran, Iran; [d]Biochemical & Bioenvironmental Research Center (BBRC), Tehran, Iran; [e]Department of Mechanical Engineering, Sharif University of Technology, Tehran, Iran; [f]Department of Mathematics, Tarbiat Modares University, Tehran, Iran; [g]Computational Physical Sciences Research Laboratory, School of Nano-Science, Institute for Research in Fundamental Sciences (IPM), Tehran, Iran

ABSTRACT

Gating of mechanosensitive (MS) channels is driven by a hierarchical cascade of movements and deformations of transmembrane helices in response to bilayer tension. Determining the intrinsic mechanical properties of the individual transmembrane helices is therefore central to understanding the intricacies of the gating mechanism of MS channels. We used a constant-force steered molecular dynamics (SMD) approach to perform unidirectional pulling tests on all the helices of MscL in *M. tuberculosis* and *E. coli* homologs. Using this method, we could overcome the issues encountered with the commonly used constant-velocity SMD simulations, such as low mechanical stability of the helix during stretching and high dependency of the elastic properties on the pulling rate. We estimated Young's moduli of the α-helices of MscL to vary between 0.2 and 12.5 GPa with TM2 helix being the stiffest. We also studied the effect of water on the properties of the pore-lining TM1 helix. In the absence of water, this helix exhibited a much stiffer response. By monitoring the number of hydrogen bonds, it appears that water acts like a 'lubricant' (softener) during TM1 helix elongation. These data shed light on another physical aspect underlying hydrophobic gating of MS channels, in particular MscL.

Introduction

The mechanosensitive channel of large conductance, MscL acts as a safety valve in bacterial membranes allowing the bacteria to release the turgor pressure under hypoosmotic conditions.[1-3] For this to occur, tension is transmitted directly from the lipid bilayer to MscL resulting in a conformational change that leads to channel gating.[4,5] To date, the structure and function of MscL are well characterized using a plethora of experimental and computational approaches.[1,6-13] MscL is a homopentamer with each monomer consisting of 4 α-helices, 2 transmembrane (TM1 and TM2) and 2 cytoplasmic (N- and C-terminal) helices (Fig. 1).[14] The TM1 helix, which lines the pore, is coupled to the membrane via a juxtaposed horizontal amphipathic N-terminal helix residing at the lipid-solvent interface.[15,16] The TM2 helix

faces the bilayer and spans the full bilayer thickness (Fig. 2B) and is connected to a coiled-coil C-terminal helical bundle of the channel pentamer.[14,17] Due to in-plane expansion and thinning of the bilayer, the pore-lining TM1 helix is dragged by the N-terminus and tilts and rotates, resulting in solvation of a hydrophobic gate (Fig. 1C).[6,9,18-20] Therefore, both the TM1 helix and the N-terminus undergo a considerable axial force in the open state.[16,21] MscL activation leads to opening of a large non-selective pore with a diameter of ∼ 3 nm and a unitary conductance in the range of ∼ 3 nS.[6,11,20]

Gating in MscL occurs on a timescale in the order of milliseconds and is accompanied by series of movements resulting in large helical deformations that are dependent on the mechanical properties of each individual helix. In order to understand the intricacies of the gating

---

CONTACT B. Martinac ✉ b.martinac@victorchang.edu.au

Color versions of one or more of the figures in this article can be found online at www.tandfonline.com/kchl.

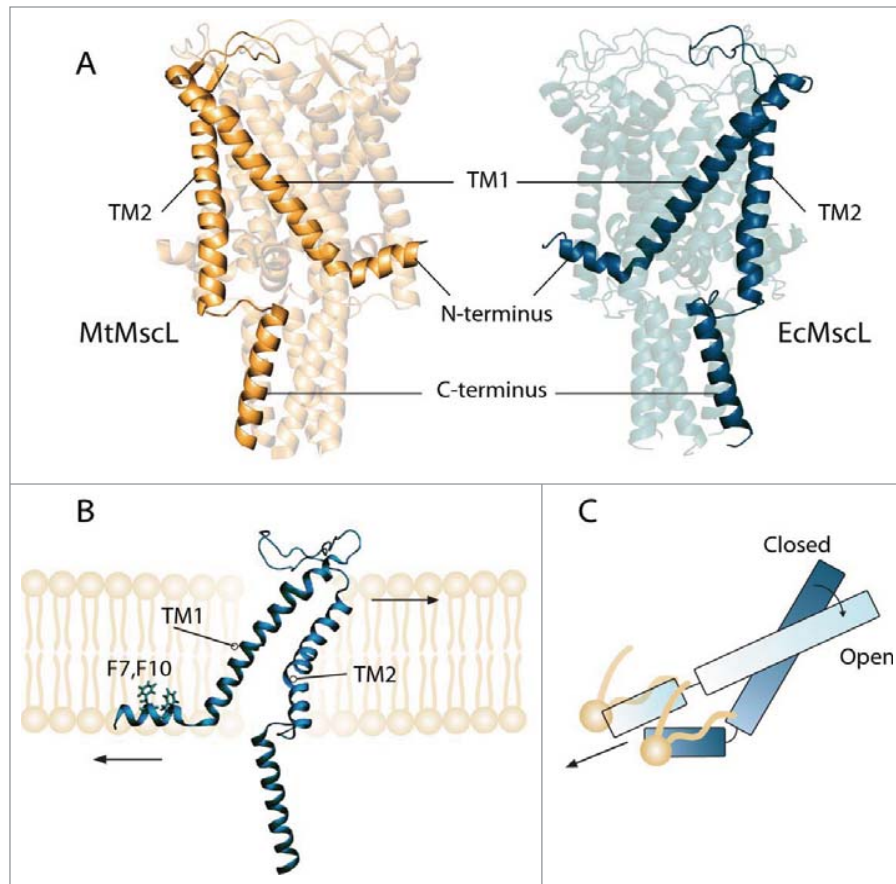‡ These authors have equal contribution.

Figure 1. Three dimensional structures of the closed (resting) state of (A) MtMscL (PDB code: 2OAR) on the left and a homology model of EcMscL obtained based on 2OAR and 4LKU on the right side.[14,16,17] (B) A subunit of EcMscL has been shown after equilibrated in POPE lipid bilayer. The residues that anchor the protein to the membrane (F7, F10) have been highlighted.[15] (C) TM1 helix becomes aligned with the N-terminus in the open state.[16]

mechanisms of these MS channels it is important that we fully determine the intrinsic mechanical properties of the individual TM helices. This information will also provide useful inputs and constraints for future computational analyses including coarse-grain molecular dynamics (MD) and continuum mechanics simulations that are routinely employed for investigating the global structural changes during MS channel activation.[22-29] Furthermore, given the growing interest in using MscL as nanosensor and/or nanovalve in biotechnology,[30-37] there are still unanswered questions regarding the intra-molecular mechanics of this family of MS channels. For example, how much force does each α-helix bear during the gating process? How do the helix properties differ in different environments (e.g., in water)? Also, is there any difference between mechanical properties of the helices in different MscL homologs?

The mechanical properties of different proteins have been studied using various theoretical[38-40] and experimental techniques such as steered molecular dynamics (SMD), atomic force microscopy (AFM), and laser optical tweezers.[38,39,41-45] These methods, in combination with X-ray crystallography and cryo-EM structures, have greatly advanced our knowledge of protein structure, mechanical strength and function. Among these approaches, SMD provides atomistic descriptions of the mechanical behavior of different proteins.[46-48] This can be achieved using 2 different approaches, either by applying a constant-force (CF) or a constant-velocity (CV). The advantages and disadvantages of these approaches are however not entirely clear.

In this study, we compared both CV and CF SMD for performing unidirectional pulling tests on the TM helices of MscL from *M. tuberculosis* and *E. coli* homologs. Using large number of simulations and the TM1 helix of MscL as our model α-helix, we demonstrated that the CF method is more reliable and accurate compared to the CV method in determining the

mechanical properties of α-helices but more expensive in terms of the computational costs. We also examined the effect of water on the elastic behavior of the pore lining TM1 helix of MscL. We showed that in its hydrated state, the TM1 helix of MtMscL became more than 5 times more flexible, while the elasticity of the TM1 helix in EcMscL did not vary significantly. The framework and mechanical properties estimated here have important consequences for 'hydrophobic lock-dependent gating'[49-54] of ion channels and may apply to many other prokaryotic and eukaryotic ion channels and proteins in general.

Materials and methods

All simulations were performed with the NAMD 2-10 package, where CHARM36 Force Field was employed. Visual Molecular Dynamics (VMD)[55] and Pymol were

used for all visualizations. The crystal structure of the *M. tuberculosis* MscL (2OAR) was used from the Protein Data Bank (Fig. 1A). The 3D structure of EcMscL (Fig. 1B) were generated based on the crystal structure of the MscL homolog of *M. tuberculosis* (PDB ID: 2OAR) and crystal structure of *E. coli* C-terminus (PDB ID: 4LKU)[17] using Phyre2[56] and Swiss-Model.[57]

Steered molecular dynamics (SMD) simulation

In SMD, external forces/velocities are applied to biomolecules to manipulate them in order to probe and determine their different mechanical properties.[46,58,59] The application of external forces/velocities accelerates processes that are otherwise too slow to model by using non-steered molecular simulations.[6,28] We used 2 different types of steered molecular dynamics simulation, namely constant-velocity (CV) and constant-force (CF). The CV method is also called "Moving Constraints" method in some versions of NAMD and other studies.[60] In this method, we have restrained the 2 α carbons of the first 2 residues (e.g., ILE14 and VAL15 in the
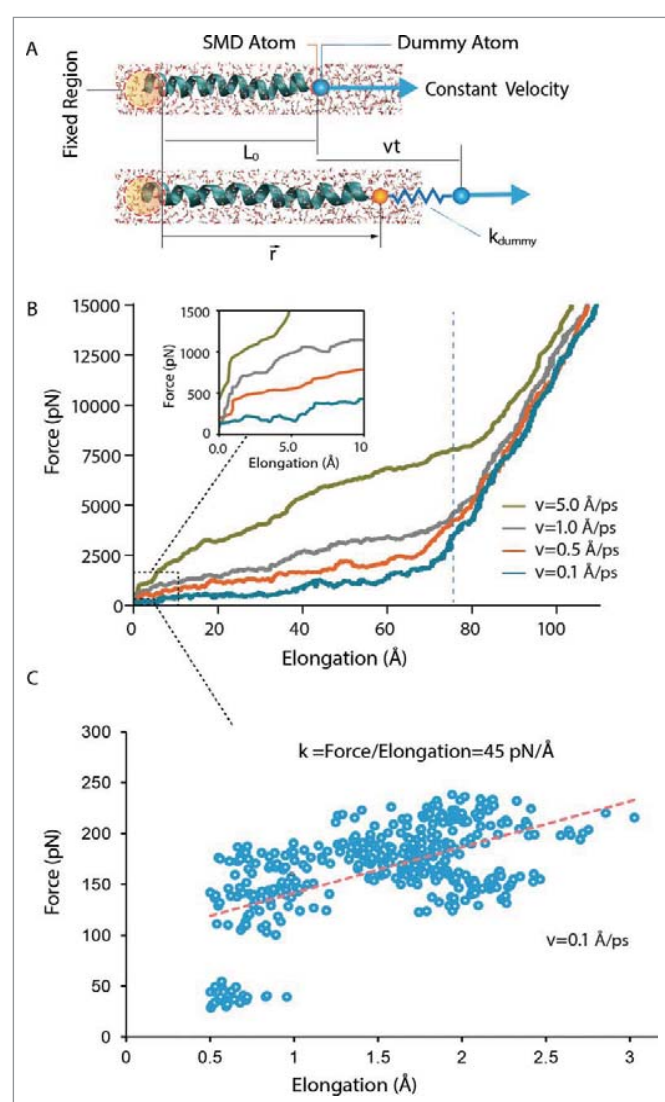

Figure 2. Steered molecular dynamics (SMD) simulation using constant-velocity (CV) method. In this method, the α carbons of the first 2 residues (ILE14 and VAL15) in TM1 helix of MtMscL have been fixed on the left hand side. Helical properties such as helix initial length, L_0, pulling rate, v, time t, vector position of the helix end, $\vec{r}$, and the assigned spring constant of the dummy atom, k_{dummy}, have been indicated. (A) A schematic unidirectional pulling test on the TM1 helix of MtMscL solvated in water. (B) The force versus elongation (ΔL) curve during constant-velocity simulation. The typical spring constant here is 3 kcal/mol/Å^2 (i.e. $\sim$210 pN/Å). Four different constant velocities have been assigned to the α carbon of the dummy atom, from 0.1 Å/ps, to 5 Å/ps. The helix elongation trend can be divided into 2 main quasi-linear regions. As shown in the inset multiple regions can be observed in the first regions which are indicative of sequential rupture of the hydrogen bonds (i.e., breakage of the hydrogen bonds during the pulling test). The length of TM1 increases up to a maximum length ($>$100 % of elongation), when the helix becomes almost unfolded due to the applied stretch. Before this point, helix response is rate dependent, i.e. the higher the pulling rate, the stiffer is the helix response. After this point the helix behavior becomes much stiffer and not rate dependent. It should be noted that the rationale for testing the helix behavior upon application of such high forces and large elongations was to find the reason for the rate dependency observed in the CV simulations. (C) A typical helical behavior under low forces. The spring constant here was 0.6 kcal/mol/Å^2 (i.e., $\sim$42 pN/Å) and the pulling rate was 0.1 Å/ps. Similar to previous studies,[39] the slope of the best linear fit to the initial part of the diagram (dashed red line) indicates the elasticity modulus, which is $\sim$0.7 kcal/mol/Å^2 (i.e., $\sim$45 pN/Å).

case of TM1 helix of MtMscL) on each helix using a strong harmonic restrain constant of 12 kcal/mol/Å^2. Table S1 and S2 in the Supporting Material contain more details about all the helices studied here. The last α carbon at the end of the helix, which is called the SMD atom, is attached to another 'dummy' atom by a harmonic spring (e.g., ILE46 in the TM1). The dummy atom is then moved with a given constant-velocity vector (Fig. 2A). We used a wide range of velocities for the TM1 helix (0.1 to 5 Å/ps) to fully investigate the effect of this parameter on estimation of the elastic moduli of our helices. In the CV method the force vector, $\vec{F}$, that has been applied on the SMD atoms can be calculated using Eq. 1,[39]

$$\vec{F} = -\nabla \left(\frac{1}{2} k \left[vt - (\vec{r} - \vec{r}_0) \cdot \vec{n} \right]^2 \right) \qquad (1)$$

Where k is the stiffness of the system, v is the pulling velocity, t is time, $\vec{r}$ is the position of the helix end (i.e., $|\vec{r} - \vec{r}_0|$ is the displacement) and $\vec{n}$ is the vector that indicates the pulling direction. It is also noteworthy, that the elongation (or strain) presented in the figures of this study, are the helical elongation which is the distance between the fixed atom and the SMD atom. Therefore, the resulting k from the slope of force versus elongation diagrams only indicates the elasticity constant of the helix. To estimate the Young's modulus, E, from the spring stiffness k, we used Eq. 2 as follows.

$$E = k \times L_0 / A \qquad (2)$$

Where L_0 is the initial length of helix (Table S1 and S2), and A is the average cross-sectional area of helix.

For calculating the helical cross-sectional area, we needed to estimate a radius of gyration for each helix as an average radius to be able to calculate their cross-sectional area using Eqs 3 and 4. The radius of gyration here, r_{gyr}, is the root mean square distance of the atoms from the helix central axis as following.

$$r_{gyr} = \sqrt{\frac{\sum (d - d_{mean})^2}{N}} \qquad (3)$$

$$d = \sqrt{x^2 + y^2} \text{ and } d_{mean} = \sqrt{x_{mean}^2 + y_{mean}^2} \qquad (4)$$

Where d and d_{mean} are the in-plane coordinates of each atom and central axis, respectively. N is the total number of atoms. x and y are the coordinates of each atom on the helix except hydrogens when the helix is aligned to the z axis. x_{mean} and y_{mean} are the in-plane coordination of the central axis of the helix when the helix is aligned to the z axis. For example, in the case of the TM1 helix, Eq. 3 yields the helical radius of 2.98 Å and thus annular cross-sectional area of 27.9 Å^2, which is similar to previously estimated values for the MscL helices.[11,61]

In the CF method, a constant-force vector is applied onto selected atoms on one end of the helix, while the other end has been restrained. In this method, the α carbons of the first 2 residues (e.g., ILE14 and VAL15 in TM1 helix of MtMscL) were restrained, and the force was applied on the α carbon of the last residue (e.g., ILE46). See Table S1 and S2 for the information about the fixed residues and dummy atoms on each helix. In the case of TM1 for example, a constant-force in the range of 0.1-1.5 kcal/mol/Å ($\sim$7 to 104 pN) was applied on the α carbon atoms of the last residue in the direction defined by a vector. This vector links center of the mass of the fixed atoms to the SMD atom, i.e., it is along the helix axis. For the other helices, the force range may alter given that the applied force was gradually increased to reach the helical strain of $\sim$6 %. We chose to measure the elastic response of each α-helix in this range as it is the maximum range that the MscL helices undergo during gating. This is a common range that has previously been used for other proteins as well.[39,41] After application of each force, the system was allowed to run for 10 ns to stabilize the equilibrium length (Fig. S1). The resultant strain of each helix was calculated by dividing the length of elongation, ΔL, by the initial length of the helix, L_0 (i.e., $\Delta L / L_0 \times 100$). See Table S1 and S2 for the initial lengths of all the helices. The initial 0% strain corresponds to the non-stretched state. For each applied force, the system was permitted to equilibrate for 10 ns (Fig. S1). For calculating the stress resultant, we calculated force/cross-sectional area of the helix ($|\vec{F}/\vec{A}|$), where A is calculated using Eq. 3. The slope of the stress-strain diagram indicates the Young's modulus of the helix. It should be noted that each point on each stress-strain diagram (e.g., Fig. 3C) is the average of 3 separate simulations. Therefore, with the number of forces we used to create reliable stress-strain curves for each helix, we performed an average of 51 simulations for each individual helix.
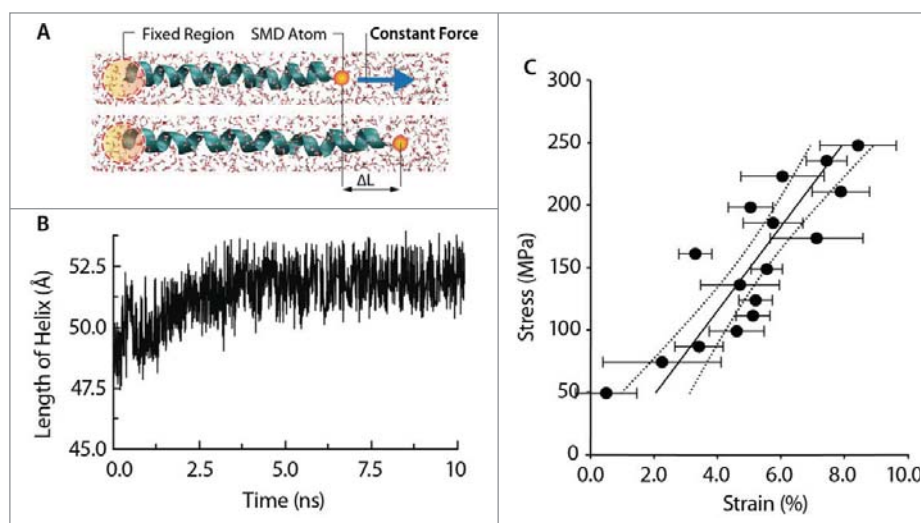
Figure 3. Mechanical behavior of the TM1 helix of MtMscL using constant-force (CF) method (A) A schematic unidirectional pulling of the TM1 helix of MtMscL solvated in water. (B) TM1 helix elongates over time as a result of constant pulling force applied on its end. The TM1 length increases to maximum length of ~52 Å then fluctuates around this value. (C) Stress-strain curve of the unidirectional traction applied to the TM1 helix in water. The range of axial force applied in these simulations ranges from 0.1 to 1.5 kcal/mol/Å (i.e., from ~7 to 70 pN). The Young's modulus of the TM1 helix can be calculated from the slope of this curve, which in this case is ~3.2 ± 0.9 GPa (Mean ± SEM). To obtain each point on the stress-strain curve, 3 simulations were performed. The strain at each force has been averaged over 3 simulations. The Young's modulus has been estimated based on 95 % confidence of both stress and strain axis.

In all of our simulations, a modified Nosé-Hoover Langevin piston pressure control provided in NAMD was utilized to control fluctuations in barostats (at 1 atm). This method is combined with a method of temperature control (at 300 K) (Langevin dynamics) to simulate the NPT ensemble. In order to study the role of water on the mechanical properties of the pore-lining α helix TM1, a series of SMD simulations were carried out in the NVT ensembles for 2 cases: (i) with water and (ii) without water (i.e. in vacuum). The TM1 helix was stretched along its axis in water and in vacuum using CF method. In the cases with water, the α helix was solvated in a 40 × 40 × 90–Å water box using the 'SOLVATE' module, with the TIP3P water molecule, in visual molecular dynamics (VMD) software. The helix was held fixed for the first 1 ns by restraining the atomic positions and then, only its backbone was maintained fixed while the rest of the system was allowed to relax for the following 1 ns. Thereafter, the whole system was equilibrated in a NPT ensemble for 10 ns with no restraint. An example of RMSD values during equilibration for the TM1 helix of MtMscL is shown in Figure S1. Care was taken of the charge neutrality in the simulations with water. We used HeliQuest and VMD for our bioinformatics data presented in Table S1 and S2.

Results

The mechanical response of the pore lining TM1 helix

We first compared the 2 SMD methods, constant-velocity (CV) and constant-force (CF), in determining Young's elasticity modulus of the TM1 helix of MtMscL solvated in water. In the CV method, the helix elongates as a result of assigning a velocity to the dummy atom attached to the end of the helix by a virtual spring, while the other end is fixed (Fig. 2A, Movie S1). Due to the helix elongation, force is generated in the helix which can be calculated from Eq. 1. The force vs. elongation was monitored over the simulation time for 4 different pulling velocities in the range 0.1 to 5 Å/ps (Fig. 2B). Two main semi-linear regions are evident (Fig. 2B). In the first, the slope of force versus elongation, representing the stiffness of the helix, is shallower and rate dependent. This region relates to hydrogen bonds and non-bonded interactions in general, which determine the secondary structure of the helix. In the second region the slope of force vs. elongation is steeper, corresponding to greater stiffness than the first region, and is independent of the pulling velocity. This region corresponds

to the scenario after all the hydrogen bonds have been broken, so represents the elasticity or stiffness of the helical backbone, which is mainly determined by bonded interactions. Importantly, the rationale for examining the helix behavior upon application of such high forces and large elongations was merely to understand the rate dependency observed in the CV simulations, which also occurs even at very low forces (e.g. <10 pN). It should be noted that the elasticity measurements (elastic constants and Young's moduli) and comparison between the CV and CF methods were done at forces <100 pN (~6% strain for TM1 helix) as described in the methods.

We have to note that the first region is not perfectly linear. This can be more clearly seen from the inset in Fig. 2B. As shown, first there was a steep jump in the force value with little to no change in the helix length, but then the helix length increased in multiple steps as the force increased. Each of these semi-linear domains is shown in the force versus elongation graph (Fig. 2B), which indicates the strain dependent behavior of TM1 helix in response to uniaxial force when the CV method was used. Since there was a slight non-linearity in the helical response and to be able to compare our results with the results obtained from the CF method, we measured the helical properties corresponding to strain < 6 % region (Fig. 2C). This is done similar to what has been done in previous studies,[39] by measuring the slope of the best linear fit to the portion of force-elongation diagram which is in the strain range of <6% (e.g., for TM1 helix, this strain value corresponds to 2.9 Å elongation). This is the range we chose to measure the elastic response of each α-helix throughout this study unless otherwise specified.

The rationale for doing it is that this is within the range of the strain that the α-helices of EcMscL experience during gating.[6,11,16] Also, this range has previously been used for other proteins in previous studies.[39,41] As described in the methods, for finding the apparent Young's modulus from the spring constant, we had to define the cross-section for the helix. For example, in the case of the TM1 helix, Eq. 3 yields the radius of 2.98 Å and thus annular cross-sectional area of 27.9 Å^2, which is similar to previously estimated values for the MscL helices, ~2.5 Å.[11,61] There is however, uncertainty in estimating the Young's elastic modulus of the α-helices from their spring constant (k), since they are not perfectly isotropic structures.

One way to overcome this problem is to divide each helix into multiple domains with different geometries. But this would require many more computations, a more complex theory and a detailed geometric model of the helix. Hence, we consider an α-helix to behave as a homogenous material so that the apparent Young's modulus, E, can be expressed as a simple scalar from Eq. 2. Although there are limitations in applying such a simplified model, it provides insight and describes well the overall mechanical behavior of different α-helices.[61] For future work, the helix cross-sectional area could be modeled as its van der Waals (vdW) shape, allowing stress values within the helix to be more precisely calculated based on force over local cross-section, instead of force over a uniform cross-section. This issue may be important if the helix dynamics are associated with bending (flexural) or torsional stiffness - where calculation of the actual cross-sectional area is more important. These more realistic surfaces will also better reflect the 'physicochemical' intricacies of MscL in future continuum models, such as when helical charge density has to be taken into account.[62]

In the constant-force (CF) method, an external constant-force has been applied on one end of the TM1 helix, while the other end was restrained (See Table S1 for the fixed and stressed residues for each individual helix). As a result of axial pulling force, TM1 helix elongates to a stable length very quickly (e.g., in 0.5 ns of simulation). However, we continued the simulation for at least another 10 ns to equilibrate helical length at each force value (Fig. 3A, B and Fig. S1). This procedure is repeated for the forces up to ~100 pN which is enough to stretch the helix beyond the length observed in the open state structure of MscL.[28] The stress-strain curve describing the helix response to a range of pulling forces is semi-linear (Fig. 3C). The slope of this curve indicates the Young's modulus of TM1 solvated in water, which is estimated to be 3.2 ± 0.9 GPa.

Comparison between constant-velocity (CV) and constant-force (CF) method

Given the differences observed in TM1 helix behavior in response to the axial force applied using the CV and CF methods (Figs 2B and 3C) we further investigated the role of the pulling rate and spring constant of the dummy atoms in our CV simulations in low strain regions (<6%). We performed

more than 200 SMD simulations using the CV method with pulling rates between 0.1 Å/ps to 5 Å/ps, as well as a wide range of dummy atom spring constant values from 0.1 kcal/mol/Å^2 to 2 kcal/mol/Å^2. Figure 4A shows that the helix Young's modulus is dependent on both the pulling
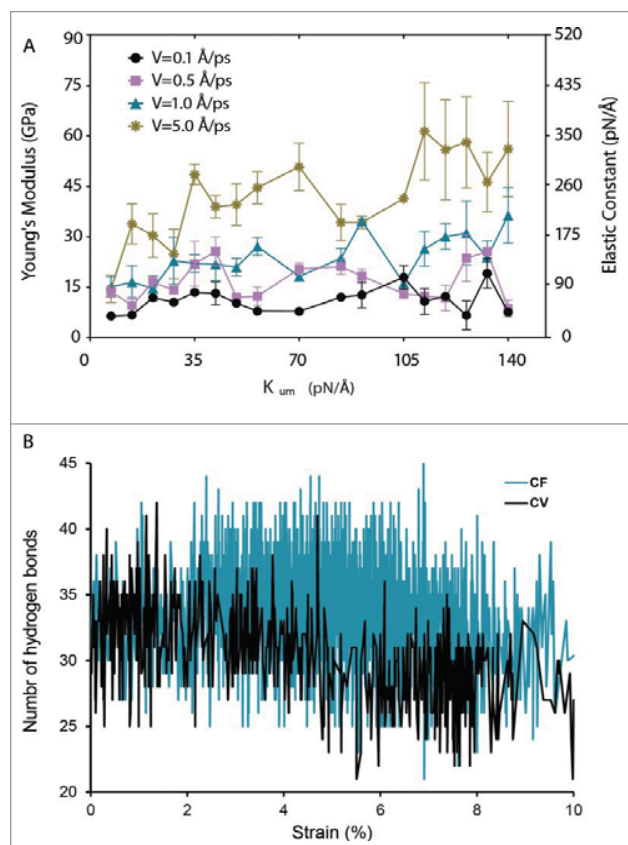

Figure 4. Comparing the constant-velocity (CV) method with the constant-force (CF) method for testing the mechanical behavior of α-helices using TM1 helix of MtMscL in water as an example. (A) The effect of pulling rate and stiffness of spring constant of the dummy atoms using constant-velocity method on the mechanical behavior of the TM1 helix of MtMscL. For higher pulling rates (> 1 Å/ps), there is a considerable fluctuation in the Young's modulus depending on the spring constant assigned to the dummy atoms. This fluctuation becomes larger as the spring constant becomes higher. As the rate of pulling decrease from 5.0 Å/ps to 0.1 Å/ps, the average of E values decreases from 42 to 11 GPa. (B) Change in the number of hydrogen bonds of TM1 α helix of MtMscL during the simulation time. The black trace shows the number of hydrogen bonds in the TM1 helix in the CV method, compared to those when the CF method was used. For this typical CV example, the spring constant is 0.6 kcal/mol/Å^2 (i.e. ~42 pN/Å) and the pulling velocity is 0.1 Å/ps. The force used in the CF method was 27 pN. The values of Young's moduli are Mean ± SEM. One-way ANOVA was used for statistical analysis with p-value < 0.05 and it was confirmed in groups with low n number using non-parametric Kruskal-Wallis test.

rate as well as the spring constant assigned to the dummy atoms. In general, for faster pulling rates, the Young's modulus was larger, i.e., the helix was stiffer. Specifically, as the rate of pulling decreased from 5.0 Å/ps to 0.1 Å/ps, the average of E values decreased from ~42 GPa to ~11 GPa. For some pulling rates (e.g., 5.0 Å/ps), higher spring constants of the dummy atoms resulted in a stiffer helix response. Also at higher pulling rates (i.e., 5 Å/ps), there was a considerable fluctuation in the Young's modulus of the helix which became larger as the spring constant of the dummy atoms increased. When we decreased the rate of pulling to 5×10^{-4} Å/ps the resulting spring stiffness of the TM1 reduced to ~25 pN/Å which corresponds to the Young's modulus ~4.3 GPa (Eq. 2; Fig. S2). This rate is closer to but still faster than the actual extension rate of this helix during the MscL gating, which is $< 5 \times 10^{-7}$ Å/ps, given that MscL gating occurs in several μs and TM1 helix elongates ~5 Å during gating.[16]

We next compared the number of hydrogen bonds in the TM helix after 10% strain in CV and CF simulation (Fig. 4B). As indicated in this figure, the number of hydrogen bonds in the TM1 helix only marginally decreased for the strain <10% compared to the CF method.

Comparing the mechanical properties of the α-helices in the MtMscL and EcMscL

A comparison of the mechanical properties of transmembrane helices between homologues of MscL from *M. tuberculosis* and *E. coli* is shown in Fig. 5. The TM1 helix and the N-terminus of MtMscL have similar Young's modulus to those in EcMscL, while the TM2 helix of MtMscL is about 4 times stiffer than in EcMscL. Conversely, the C-terminal helix of EcMscL is about 8 times stiffer than the C-terminal helix of MtMscL. There is no apparent correlation between the length and stiffness of the helix in either homolog (Fig. S3). There is also no correlation between the Young's modulus and hydrophobic moment or number of charges (Fig. S4 and S5 and Table S1 and S2). We also showed that the Young's moduli of the TM2 helix in MtMscL and EcMscL are vastly different, although they have very similar number of hydrogen bonds (Fig. S6).
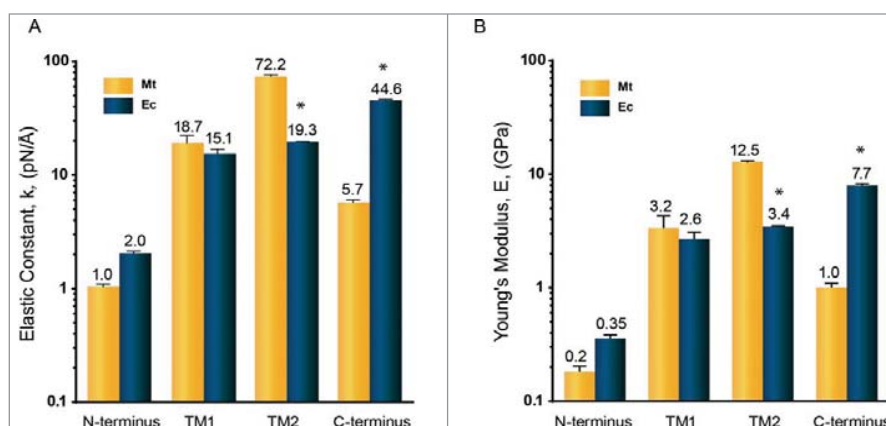
Figure 5. Mechanical properties of MtMscL and EcMscL α-helices in the presence of water measured by all-atom steered molecular dynamic (SMD) simulation. We used constant-force (CF) method here to estimate (A) the elasticity constant and (B) the Young's modulus. The elasticity constant is between 1.0 to 72.2 pN/Å (Young's moduli are between 0.2 to 12.5 GPa). Overall, the mechanical properties of MscL α-helices of both species are similar to each other except for their TM2 and C-terminal helices. TM2 helix in MtMscL is almost 4 times stiffer than the TM2 helix of EcMscL. But the C-terminal helix of EcMscL is about 8 times stiffer than the C-terminal helix of MtMscL. The values of Young's moduli are Mean $\pm$ SEM for n = 3. Each Young's modulus is obtained from the stress-strain graphs exemplified in Fig. 3. Student's t-test was used for statistical analysis between each α-helix in MtMscL with its corresponding α-helix in EcMscL. The differences were considered significant for *p-value < 0.05.

Applying steered forces on the specific parts of the pentameric MscL to gate the channel has been studied before to explore the gating mechanism of MscL.[6,63] Applying force on the MscL does not give us clear information about the material properties of each component because the result of such SMD simulation depends on: 1) the position on the protein that these forces are applied to, 2) the effect of surrounding lipid[64] and 3) the level of difference between the material properties of different helices and/or loops. Therefore, full atomistic calculations are required to derive physical parameters also useful for mesoscopic and continuum modeling of MscL in 'membrane protein lattices' models. This 'bottom-up' approach enables modeling multiple proteins (channels) in an implicit membrane to capture larger time and length scale phenomena.

Effect of water on the elasticity of TM1 helix

Figure 6 shows the influence of solvation in water on the properties of the TM1 helix obtained using constant-force method SMD simulation. We specifically chose TM1 helix as it forms the MscL pore and thus we were interested to see how its properties altered as it became hydrated. The intention here was to determine a range for the stiffness variation between these 2 conditions (hydrated and dehydrated). Solvation in water decreased the stiffness of the TM1 helix in both MtMscL and EcMscL ($E = 3.2 \pm 0.9$ GPa in water and 8.8 ± 0.2 in vacuo for MtMscL and $E = 2.6 \pm 0.5$ GPa in water and 3.5 ± 0.1 GPa in vacuo for EcMscL) (Fig. 6A and C). To examine why solvation resulted in a larger change in stiffness for MtMscL than EcMscL we determined the evolution of hydrogen bonds on the TM1 helix during solvation in each case. For MtMscL the number of hydrogen bonds was significantly reduced from $\sim$41 to $\sim$30 as the helix becomes solvated (Fig. 6B). However, the number of hydrogen bonds did not vary as much when the TM1 helix of EcMscL was solvated in water (Fig. 6D).

Discussion

Alpha helices play central roles in various biological processes such as molecular and cellular mechano-transduction, cell mechanics and tissue mechanics and are one of the most important elementary building components of proteins.[65] Due to a lack of understanding of how these secondary structural elements respond to mechanical force and how they interact with each other, the stiffness and unfolding of proteins remain unclear at atomic resolution. In this study we have used steered molecular dynamics approaches to investigate the mechanical properties of transmembrane α helices in MscL.
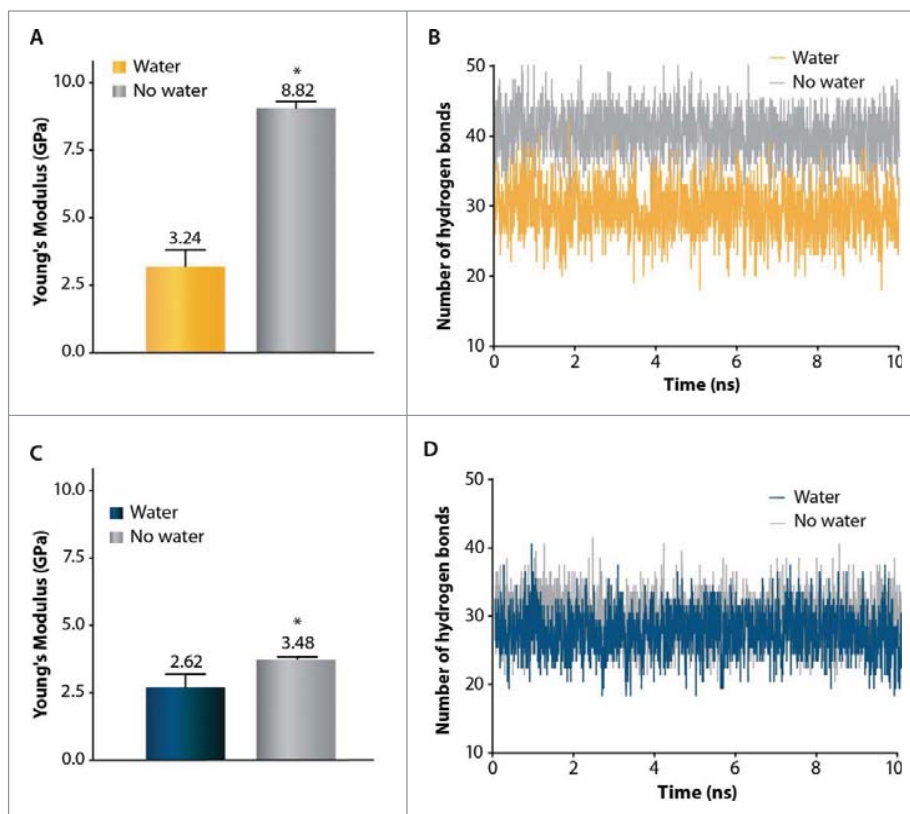
Figure 6. Effect of water on mechanical properties of the TM1 helix in MtMscL (A,B) and in EcMscL (C,D) using constant-force SMD simulation. (A) The Young's modulus of TM1 helix in MtMscL is $E = 3.2 \pm 0.9$ GPa when it is solvated in water, and $E = 8.8 \pm 0.2$ GPa in the absence of water (vacuum). Thus, in the absence of water (vacuum), TM1 helix is more than 3 times stiffer in MtMscL. (B) Change in number of the hydrogen bonds of TM1 α helix of MtMscL during 10 ns of SMD simulation. About 41 hydrogen bonds stabilize the secondary structure of TM1 helix in vacuum, while when it is solvated in water, the number of hydrogen bonds becomes significantly reduced to ∼30 bonds. This indicates that water acts as a 'lubricant' (softener) during TM1 helix elongation in water. (C) The Young's modulus of the TM1 helix of EcMscL solvated in water is $E = 2.6 \pm 0.5$ GPa whereas it is $E = 3.5 \pm 0.1$ GPa in the absence of water (vacuum). (D) The number of hydrogen bonds does not change considerably when the TM1 helix of EcMscL is solvated in water, thus its elasticity modulus only increases by ∼30 %. For all the hydrogen bond calculations, we used a donor-acceptor distance of 3.5 Å and angle cut-off of 40°. The values presented in (A) and (C) are Mean $\pm$ SEM for $n = 3$. Student's t-test was used for statistical analysis and differences were considered significant for *p-value < 0.05.

Constant-force SMD is a more reliable measure of helix stiffness than constant-velocity

We compared 2 widely used methods of steered molecular dynamics (SMD) namely, constant-velocity (CV) and constant-force (CF) in a more detailed and systematic way compared to previous studies using a large number SMD simulations.[66] We monitored the number of hydrogen bonds during pulling the TM1 helix using both methods. We showed that the number of hydrogen bonds in CV method, which determine/stabilize the secondary structure of the helix, quickly and dramatically decreased compared to the CF method during the stretching (Fig. 4B). Hence, we postulate that the

most important advantage of CF method over CV method is that the secondary structure of the helix remains better conserved during the pulling test in the former method compared to the latter one. Although, this is the case for common pulling rates (1-5 pÅ/s), we should note that the CV and CF methods will not be much different, in terms of breaking the H-bonds, if both performed at the same force level (Fig. 4B). The hydrogen bonding state of the helix was also reflected in the rate dependent unfolding during CV SMD which has also been shown in previous studies for different proteins.[39,67] Helix behavior was rate dependent only for the strains <100 % because the helical strain in this region is mainly due to the breakage

of hydrogen bonds (Fig. 2B and Movie S2). Whereas in higher strains, the helix behavior is not rate dependent as it manifests the helical backbone elasticity.[40,67] Therefore, unlike in the CF method, the Young's moduli obtained from CV method are dependent on the pulling rate and the assigned spring constant to the dummy atoms. For example, the Young's modulus of TM1 helix measured by CV method can vary from ∼11 GPa to ∼42 GPa depending on the puling rate (Figs 2B and 4A).

Consequently, the absolute Young's modulus obtained from CF method is generally more reliable and reproducible compared to those estimated by using CV method. This information is essential given the great need for employing precise tools for determining the mechanical properties of α-helices of membrane proteins, cytoskeletal elements and collagen-like microfibrils. For instance, it is essential to accurately determine the elasticity of tip links in hair cells given its importance in the force transduction in auditory physiology.[46] Previous studies have rigorously used the CV method combined with experiments for measuring the elasticity of tip links which is formed by protocadherin 15 and cadherin 23.[46,47] Instead, we suggest more accurate computational elasticity measurements by employing the CF method, which may be used to ensure the accuracy of elasticity constants. Also, provided the essential role of tip links in deafness-related structural defects, this may further uncover the molecular elasticity and physical principles underlying the function of tip links.[68,69] However, the down side of this approach is that the number of simulations required to be done to generate a stress-strain curve using the CF method is much larger than using the CV method (51 CF simulations vs. 3 CV simulations for each helix). Thus, the CF method requires a much larger computational cost. Moreover, it has recently been shown that SMD-like techniques can be vastly improved for relatively fast pulling rates, if one combines Minh-Adib's bidirectional estimator with nonlinear WHAM equations to reconstruct and assess PMFs from trajectories.[70]

Comparison of mechanical properties of T helices of MtMscL and EcMscL

Using the CF method, we determined the Young's modulus of all the helices of MtMscL and EcMscL (Fig. 5). The lowest Young's modulus was found for

the N-terminus of MtMscL which is ∼0.2 GPa and the highest determined is for the TM2 helix of MtMscL, which is ∼12.5 GPa. This is well in the range of the elasticity moduli previously measured using various experimental and computational approaches for different proteins ranging from 1 GPa to 30 GPa.[71-75] TM1 helix and N-terminal helices of MtMscL have similar mechanical properties to those in EcMscL, which could be due to their higher level of amino acid sequence conservation and identity in these regions. Among all the helices, the Young's modulus of the TM2 helix and the C-terminal helix appear to be vastly different between *M. tuberculosis* and *E. coli*. The TM2 helix in MtMscL is much stiffer than TM2 helix in EcMscL. Hence, overall in the transmembrane region, MtMscL is stiffer than EcMscL. Given that TM2 helix is embedded in the lipid bilayer and determines the bilayer hydrophobic length around the channel,[20,76] we suggest that the stiffer TM2 helix may also correspond to less sensitivity of MtMscL to bilayer thinning during the gating compared to EcMscL, as previously shown by patch-clamp experiments.[77] Conversely, the C-terminal helix in EcMscL is about 8 times stiffer than in MtMscL. However, removal of up to 20 amino acids from the end of EcMscL has been shown to have no significant effect on gating of MscL, but rather may be involved in pH sensitivity.[78] At this stage, we are not sure what would be the physiological meaning of having stiffer C-terminal bundle. This will remain to be addressed in the future studies to understand the physiological role of the C-terminus in MscL channels.

Previous reports have shown a dependence of the elasticity and strength of some helix types on their length.[67] For example it has been shown that the stiffness of the stack of α-helical ankyrin repeats increases with a decreasing number of repeats.[79] In our study, the elasticity modulus did not correlate with the helix length or hydrophobic moment or number of charged residues in this study. In addition, we demonstrated here that the charge and other factors such as hydrophobic moment did not correlate with the helix stiffness of MtMscL and EcMscL (Figs S3, S4, S5 and S6).

Effect of hydration on mechanical properties of TM helices of MscL

MD simulations have previously shown that TM1 helix, which forms the pore, is only partially hydrated

in the closed state and it becomes fully hydrated in the open state.[6,16] Therefore, we were interested to see how the TM1 helix elasticity changes when it is hydrated. By pulling the TM1 helix of both MtMscL and EcMscL in vacuum and water, we have found that exposure of the TM1 helix to water greatly affects its stiffness. Based on our results (Fig. 6 B, D), we suggest that water by interfering with the hydrogen bonds and electrostatic interactions within the helix, acts as a "lubricant" (softener) during the helix elongation. Thus, the Young's modulus of a helix like TM1 of MtMscL decreases significantly in the presence of water. This is not surprising given the previous reports on similar effects on different proteins such as the effect of water on collagen-like micro-fibrils, immuno-globulin domains and spectrin-like proteins.[60,80,81] In fact, the physiological function of this class of proteins is regulated by water since they should become softer and thus unfold easier as they become hydrated.[80] However, there are other studies which suggest that the elasticity of those α-helices that are primarily determined by the backbone hydrogen bonds do not change significantly when the helix is solvated in water.[82] An interesting point here is that water did not change the stiffness of TM1 helix of EcMscL to the same extent as it did in MtMscL. In fact, the effect of water on the elasticity of the TM1 helix in MtMscL was much larger than on the elasticity of the TM1 helix of EcMscL (Fig. 6A, C). We showed that this is analogous to the change in the number of the hydrogen bonds in vacuum and in water (Fig. 6B, D). The exact physiological meaning of this difference is unclear at this point. Given the recent computational MscL study, which showed that MscL gates in the presence of water easier than in vacuum, our results further support the importance of hydrophobic interactions for the gating of MS channels and nanopores.[49,52,83-85]

Conclusion

In summary, we calculated Young's moduli and elastic constants for all the helices in MtMscL and EcMscL, which are 2 important members of the bacterial MS channel family. Given a considerable number of all-atom MD simulations, we demonstrated in this study that the widely used constant-velocity approach is less reliable compared to the constant-force method, which is more accurate for determining Young's

modulus of α-helices, although it is computationally much more expensive. Interestingly, we showed not only the helical properties among the helices of MscL were quite different, but also the properties of some of the MscL helices (e.g. TM2 helix) turned out to be different between *E. coli* and *M. tuberculosis* homologs. Therefore, in these cases we checked if there was any correlation between the elastic properties and helical length, charge or amino acid sequence. We also demonstrated that water could act as a 'lubricant' (softener) during TM1 helix elongation, which lines the channel pore in MscL. Consequently, the data and methods resulting from this study have wide implications for understanding the force-enduring properties of the α-helices of MscL and their mechanistic role in MscL gating. In addition, atomistic calculations to derive parameters are also useful for a mesoscopic bead-spring and 'hybrid continuum-atomistic' models of channels using energy and force matching. This "bottom-up" approach will allow us to assemble multiple protein structures by springs (or elastic beam/rods) for capturing larger time and length scale phenomena, such as modeling of a cluster of proteins (channels) in lipid patches or attached to other intra-/extra-cellular elements.

Author contributions

N.B., O.B., B.M. and Y.J. designed the research; N.B. and O.B. performed the simulations. M.V., R.N., A.P.H., B.M. and Y.J.

contributed the computational/analytic tools; N.B., O.B., B.M. and Y.J. analyzed the data; and N.B., O.B., A.P.H., Y.J. and B.M. wrote the manuscript. All authors read and approved the final manuscript.

References

[1] Berrier C, Besnard M, Ajouz B, Coulombe A, Ghazi A. Multiple mechanosensitive ion channels from Escherichia coli, activated at different thresholds of applied pressure. J Membrane Biol 1996; 151:175-87; http://dx.doi.org/10.1007/s002329900068

[2] Meyer GR, Gullingsrud J, Schulten K, Martinac B. Molecular dynamics study of MscL interactions with a curved lipid bilayer. Biophys J 2006; 91:1630-7; PMID:16751236; http://dx.doi.org/10.1529/biophysj.106.080721

[3] Sukharev SI, Blount P, Martinac B, Blattner FR, Kung C. A large-conductance mechanosensitive channel in E. coli encoded by mscL alone. Nature 1994; 368:265-8; PMID:7511799; http://dx.doi.org/10.1038/368265a0

[4] Phillips R, Ursell T, Wiggins P, Sens P. Emerging roles for lipids in shaping membrane-protein function. Nature 2009; 459:379-85; PMID:19458714; http://dx.doi.org/10.1038/nature08147

[5] Kung C. A possible unifying principle for mechanosensation. Nature 2005; 436:647-54; PMID:16079835; http://dx.doi.org/10.1038/nature03896

[6] Corry B, Hurst AC, Pal P, Nomura T, Rigby P, Martinac B. An improved open-channel structure of MscL determined from FRET confocal microscopy and simulation. J Gen Physiol 2010; 136:483-94; PMID:20876362; http://dx.doi.org/10.1085/jgp.200910376

[7] Nomura T, Cranfield CG, Deplazes E, Owen DM, Macmillan A, Battle AR, Constantine M, Sokabe M, Martinac B. Differential effects of lipids and lyso-lipids on the mechanosensitivity of the mechanosensitive channels MscL and MscS. Proc Natl Acad Sci 2012; 109:8770-5; PMID:22586095; http://dx.doi.org/10.1073/pnas.1200051109

[8] Perozo E, Cuello LG, Cortes DM, Liu YS, Sompornpisut P. EPR approaches to ion channel structure and function. Novartis Found Symp 2002; 245:146-58; discussion 58-64, 65-8; PMID:12027005; http://dx.doi.org/10.1002/0470868759.ch10

[9] Sukharev S, Betanzos M, Chiang CS, Guy HR. The gating mechanism of the large mechanosensitive channel MscL. Nature 2001; 409:720-4; PMID:11217861; http://dx.doi.org/10.1038/35055559

[10] Battle A, Ridone P, Bavi N, Nakayama Y, Nikolaev Y, Martinac B. Lipid–protein interactions: Lessons learned from stress. Biochim Biophys Acta 2015; 1848:1744-56; PMID:25922225; http://dx.doi.org/10.1016/j.bbamem.2015.04.012

[11] Wang Y, Liu Y, Deberg HA, Nomura T, Hoffman MT, Rohde PR, Schulten K, Martinac B, Selvin P. Single molecule FRET reveals pore size and opening mechanism of a mechano-sensitive ion channel. Elife 2014; 3:e01834; PMID:24550255

[12] Gullingsrud J, Kosztin D, Schulten K. Structural determinants of MscL gating studied by molecular dynamics simulations. Biophys J 2001; 80:2074-81; PMID:11325711; http://dx.doi.org/10.1016/S0006-3495(01)76181-4

[13] Iscla I, Wray R, Eaton C, Blount P. Scanning MscL channels with targeted post-translational modifications for functional alterations. PLoS One 2015; 10: e0137994; PMID:26368283; http://dx.doi.org/10.1371/journal.pone.0137994

[14] Steinbacher S, Bass R, Strop P, Rees DC. Structures of the prokaryotic mechanosensitive channels MscL and MscS. In: Hamill OP, ed. Mechanosensitive Ion Channels, Part A. San Diego: Elsevier Academic Press, Inc., 2007:1-24.

[15] Iscla I, Wray R, Blount P. On the structure of the N-terminal domain of the MscL channel: helical bundle or membrane interface. Biophys J 2008; 95:2283-91; PMID:18515388; http://dx.doi.org/10.1529/biophysj.107.127423

[16] Bavi N, Cortes DM, Cox CD, Rohde PR, Liu W, Deitmer JW, Bavi O, Strop P, Hill AP, Rees D, et al. The role of MscL amphipathic N terminus indicates a blueprint for bilayer-mediated gating of mechanosensitive channels. Nat Commun 2016; 7:11984; PMID:27329693; http://dx.doi.org/10.1038/ncomms11984

[17] Walton TA, Rees DC. Structure and stability of the C-terminal helical bundle of the E. coli mechanosensitive channel of large conductance. Protein Sci 2013; 22:1592-601; PMID:24038743; http://dx.doi.org/10.1002/pro.2360

[18] Iscla I, Blount P. Sensing and responding to membrane tension: the bacterial MscL channel as a model system. Biophys J 2012; 103:169-74; PMID:22853893; http://dx.doi.org/10.1016/j.bpj.2012.06.021

[19] Blount P, Moe PC. Bacterial mechanosensitive channels: integrating physiology, structure and function. Trends Microbiol 1999; 7:420-4; PMID:10498951; http://dx.doi.org/10.1016/S0966-842X(99)01594-2

[20] Perozo E, Cortes DM, Sompornpisut P, Kloda A, Martinac B. Open channel structure of MscL and the gating mechanism of mechanosensitive channels. Nature 2002; 418:942-8; PMID:12198539; http://dx.doi.org/10.1038/nature00992

[21] Bavi N, Cox CD, Perozo E, Martinac B. Towards a structural blueprint for bilayer-mediated channel mechanosensitivity. Channels 2016; 7:00-.

[22] Bavi O, Vossoughi M, Naghdabadi R, Jamali Y. The Combined effect of hydrophobic mismatch and bilayer local bending on the regulation of mechanosensitive ion channels. PLoS one 2016; 11:e0150578; PMID:26958847; http://dx.doi.org/10.1371/journal.pone.0150578

[23] Bavi O, Cox CD, Vossoughi M, Naghdabadi R, Jamali Y, Martinac B. Influence of global and local membrane curvature on mechanosensitive ion channels: A finite element approach. Membranes (Basel) 2016; 6; PMID:26861405

[24] Bavi O, Vossoughi M, Naghdabadi R, Jamali Y. The effect of local bending on gating of MscL using a representative

volume element and finite element simulation. Channels (Austin) 2014; 8:344-9; PMID:25478623; http://dx.doi.org/10.4161/chan.29572

[25] Wiggins P, Phillips R. Analytic models for mechanotransduction: gating a mechanosensitive channel. Proc Natl Acad Sci U S A 2004; 101:4071-6; PMID:15024097; http://dx.doi.org/10.1073/pnas.0307804101

[26] Chen X, Cui Q, Tang Y, Yoo J, Yethiraj A. Gating mechanisms of mechanosensitive channels of large conductance, I: a continuum mechanics-based hierarchical framework. Biophys J 2008; 95:563-80; PMID:18390626; http://dx.doi.org/10.1529/biophysj.107.128488

[27] Bavi N, Nakayama Y, Bavi O, Cox CD, Qin QH, Martinac B. Biophysical implications of lipid bilayer rheometry for mechanosensitive channels. Proc Natl Acad Sci U S A 2014; 111:13864-9; PMID:25201991; http://dx.doi.org/10.1073/pnas.1409011111

[28] Deplazes E, Louhivuori M, Jayatilaka D, Marrink SJ, Corry B. Structural investigation of MscL gating using experimental data and coarse grained MD simulations. PLoS Comput Biol 2012; 8:e1002683; PMID:23028281; http://dx.doi.org/10.1371/journal.pcbi.1002683

[29] Sansom MS, Scott KA, Bond PJ. Coarse-grained simulation: a high-throughput computational approach to membrane proteins. Biochem Soc Trans 2008; 36:27-32; PMID:18208379; http://dx.doi.org/10.1042/BST0360027

[30] Cox CD, Bae C, Ziegler L, Hartley S, Nikolova-Krstevski V, Rohde PR, Ng CA, Sachs F, Gottlieb PA, Martinac B. Removal of the mechanoprotective influence of the cytoskeleton reveals PIEZO1 is gated by bilayer tension. Nat Commun 2016; 7:10366; PMID:26785635; http://dx.doi.org/10.1038/ncomms10366

[31] Nakayama Y, Mustapić M, Ebrahimian H, Wagner P, Kim JH, Al Hossain MS, Horvat J, Martinac B. Magnetic nanoparticles for "smart liposomes". Eur Biophy J 2015; 44:647-54; PMID:26184724; http://dx.doi.org/10.1007/s00249-015-1059-0

[32] Iscla I, Eaton C, Parker J, Wray R, Kovacs Z, Blount P. Improving the design of a MscL-based triggered nanovalve. Biosensors (Basel) 2013; 3:171-84; PMID:23678232; http://dx.doi.org/10.3390/bios3010171

[33] Yang LM, Wray R, Parker J, Wilson D, Duran RS, Blount P. Three routes to modulate the pore size of the MscL channel/nanovalve. ACS Nano 2012; 6:1134-41; PMID:22206349; http://dx.doi.org/10.1021/nn203703j

[34] Yang LM, Blount P. Manipulating the permeation of charged compounds through the MscL nanovalve. FASEB J 2011; 25:428-34; PMID:20930114; http://dx.doi.org/10.1096/fj.10-170076

[35] Kocer A, Walko M, Meijberg W, Feringa BL. A light-actuated nanovalve derived from a channel protein. Science 2005; 309:755-8; PMID:16051792; http://dx.doi.org/10.1126/science.1114760

[36] Kocer A, Walko M, Feringa BL. Synthesis and utilization of reversible and irreversible light-activated nanovalves derived from the channel protein MscL. Nat Protoc 2007; 2:1426-37; PMID:17545979; http://dx.doi.org/10.1038/nprot.2007.196

[37] Pacheco-Torres J, Mukherjee N, Walko M, Lopez-Larrubia P, Ballesteros P, Cerdan S, Kocer A. Image guided drug release from pH-sensitive Ion channel-functionalized stealth liposomes into an in vivo glioblastoma model. Nanomedicine 2015; 11:1345-54; PMID:25888277

[38] Buehler MJ. Atomistic and continuum modeling of mechanical properties of collagen: elasticity, fracture, and self-assembly. J Mat Res 2006; 21:1947-61; http://dx.doi.org/10.1557/jmr.2006.0236

[39] Lorenzo AC, Caffarena ER. Elastic properties, Young's modulus determination and structural stability of the tropocollagen molecule: a computational study by steered molecular dynamics. J Biomechan 2005; 38:1527-33; http://dx.doi.org/10.1016/j.jbiomech.2004.07.011

[40] Sikora M, Sułkowska JI, Cieplak M. Mechanical strength of 17 134 model proteins and cysteine slipknots. PLoS Comput Biol 2009; 5:e1000547; PMID:19876372; http://dx.doi.org/10.1371/journal.pcbi.1000547

[41] Buehler MJ, Keten S, Ackbarow T. Theoretical and computational hierarchical nanomechanics of protein materials: Deformation and fracture. Prog Mat Sci 2008; 53:1101-241; http://dx.doi.org/10.1016/j.pmatsci.2008.06.002

[42] Tskhovrebova L, Trinick J, Sleep J, Simmons R. Elasticity and unfolding of single molecules of the giant muscle protein titin. Nature 1997; 387:308-12; PMID:9153398; http://dx.doi.org/10.1038/387308a0

[43] Gautieri AV, Vesentini S, Redaelli A, Buehler MJ. Nanomechanics of collagen microfibrils from the atomistic scale up. Nano Lett 2011; 11:757-66; PMID:21207932; http://dx.doi.org/10.1021/nl103943u

[44] Wolny M, Batchelor M, Knight PJ, Paci E, Dougan L, Peckham M. Stable single α-helices are constant force springs in proteins. J Biol Chem 2014; 289:27825-35; PMID:25122759; http://dx.doi.org/10.1074/jbc.M114.585679

[45] Shayegan M, Forde NR. Microrheological characterization of collagen systems: from molecular solutions to fibrillar gels. PLoS One 2013; 8:e70590; PMID:23936454; http://dx.doi.org/10.1371/journal.pone.0070590

[46] Sotomayor M, Weihofen WA, Gaudet R, Corey DP. Structure of a force-conveying cadherin bond essential for inner-ear mechanotransduction. Nature 2012; 492:128-32; PMID:23135401; http://dx.doi.org/10.1038/nature11590

[47] Sotomayor M, Weihofen WA, Gaudet R, Corey DP. Structural determinants of cadherin-23 function in hearing and deafness. Neuron 2010; 66:85-100; PMID:20399731; http://dx.doi.org/10.1016/j.neuron.2010.03.028

[48] Marszalek PE, Lu H, Li H, Carrion-Vazquez M, Oberhauser AF, Schulten K, Fernandez JM. Mechanical unfolding intermediates in titin modules. Nature 1999; 402:100-3; PMID:10573426; http://dx.doi.org/10.1038/47083

[49] Aryal P, Sansom MS, Tucker SJ. Hydrophobic gating in ion channels. J Mol Biol 2015; 427:121-30; PMID:25106689; http://dx.doi.org/10.1016/j.jmb.2014.07.030

[50] Anishkin A, Sukharev S. Water dynamics and dewetting transitions in the small mechanosensitive channel MscS. Biophys J 2004; 86:2883-95; PMID:15111405; http://dx.doi.org/10.1016/S0006-3495(04)74340-4

[51] Yoshimura K, Batiza A, Schroeder M, Blount P, Kung C. Hydrophilicity of a single residue within MscL correlates with increased channel mechanosensitivity. Biophys J 1999; 77:1960-72; PMID:10512816; http://dx.doi.org/10.1016/S0006-3495(99)77037-2

[52] Beckstein O, Sansom MS. Liquid-vapor oscillations of water in hydrophobic nanopores. Proc Natl Acad Sci U S A 2003; 100:7063-8; PMID:12740433; http://dx.doi.org/10.1073/pnas.1136844100

[53] Sotomayor M, Schulten K. Molecular dynamics study of gating in the mechanosensitive channel of small conductance MscS. Biophys J 2004; 87:3050-65; PMID:15339798; http://dx.doi.org/10.1529/biophysj.104.046045

[54] Blount P, Moe PC. Bacterial mechanosensitive channels: integrating physiology, structure and function. Trends Microbiol 1999; 7:420-4; PMID:10498951; http://dx.doi.org/10.1016/S0966-842X(99)01594-2

[55] Humphrey W, Dalke A, Schulten K. VMD: visual molecular dynamics. J Mol Graph 1996; 14:33-8, 27-8; PMID:8744570; http://dx.doi.org/10.1016/0263-7855(96)00018-5

[56] Kelley LA, Mezulis S, Yates CM, Wass MN, Sternberg MJ. The Phyre2 web portal for protein modeling, prediction and analysis. Nat Protoc 2015; 10:845-58; PMID:25950237; http://dx.doi.org/10.1038/nprot.2015.053

[57] Biasini M, Bienert S, Waterhouse A, Arnold K, Studer G, Schmidt T, Kiefer F, Gallo Cassarino T, Bertoni M, Bordoli L, et al. SWISS-MODEL: modelling protein tertiary and quaternary structure using evolutionary information. Nucleic Acid Res 2014; 42:W252-8; PMID:24782522; http://dx.doi.org/10.1093/nar/gku340

[58] Ackbarow T, Chen X, Keten S, Buehler MJ. Hierarchies, multiple energy barriers, and robustness govern the fracture mechanics of alpha-helical and beta-sheet protein domains. Proc Natl Acad Sci U S A 2007; 104:16410-5; PMID:17925444; http://dx.doi.org/10.1073/pnas.0705759104

[59] Sotomayor M, Schulten K. The allosteric role of the Ca 2+ switch in adhesion and elasticity of C-cadherin. Biophys J 2008; 94:4621-33; PMID:18326636; http://dx.doi.org/10.1529/biophysj.107.125591

[60] Zhang D, Chippada U, Jordan K. Effect of the structural water on the mechanical properties of collagen-like microfibrils: a molecular dynamics study. Annal Biomed Eng 2007; 35:1216-30; http://dx.doi.org/10.1007/s10439-007-9296-8

[61] Tang Y, Cao G, Chen X, Yoo J, Yethiraj A, Cui Q. A finite element framework for studying the mechanical response of macromolecules: application to the gating of the mechanosensitive channel MscL. Biophys J 2006; 91:1248-63; PMID:16731564; http://dx.doi.org/10.1529/biophysj.106.085985

[62] Zhu L, Wu J, Liu L, Liu Y, Yan Y, Cui Q, et al. Gating mechanism of mechanosensitive channel of large conductance: a coupled continuum mechanical-continuum solvation approach. Biomech Model Mechanobiol 2016:1-20.

[63] Gullingsrud J, Schulten K. Gating of MscL studied by steered molecular dynamics. Biophys J 2003; 85:2087-99; PMID:14507677; http://dx.doi.org/10.1016/S0006-3495(03)74637-2

[64] Laganowsky A, Reading E, Allison TM, Ulmschneider MB, Degiacomi MT, Baldwin AJ, Robinson CV. Membrane proteins bind lipids selectively to modulate their structure and function. Nature 2014; 510:172-5; PMID:24899312; http://dx.doi.org/10.1038/nature13419

[65] Kendrew J, Dickerson R, Strandberg B, Hart R, Davies D, Phillips D, et al. Structure of myoglobin: A three-dimensional Fourier synthesis at 2 A. resolution. Nature 1960; 185:422-7.

[66] Lu H, Schulten K. The key event in force-induced unfolding of titin's immunoglobulin domains. Biophys J 2000; 79:51-65; PMID:10866937; http://dx.doi.org/10.1016/S0006-3495(00)76273-4

[67] Bertaud J, Hester J, Jimenez DD, Buehler MJ. Energy landscape, structure and rate effects on strength properties of alpha-helical proteins. J Phys Condens Matter 2009; 22:035102; PMID:21386278; http://dx.doi.org/10.1088/0953-8984/22/3/035102

[68] Alagramam KN, Goodyear RJ, Geng R, Furness DN, van Aken AF, Marcotti W, Kros CJ, Richardson GP. Mutations in protocadherin 15 and cadherin 23 affect tip links and mechanotransduction in mammalian sensory hair cells. PLoS One 2011; 6:e19183; PMID:21532990; http://dx.doi.org/10.1371/journal.pone.0019183

[69] Alagramam KN, Murcia CL, Kwon HY, Pawlowski KS, Wright CG, Woychik RP. The mouse Ames waltzer hearing-loss mutant is caused by mutation of Pcdh15, a novel protocadherin gene. Nat Genet 2001; 27:99-102; PMID:11138007

[70] Ngo VA, Kim I, Allen TW, Noskov SY. Estimation of potentials of mean force from nonequilibrium pulling simulations using both minh-adib estimator and weighted histogram analysis method. J Chem Theory Comput 2016; 12:1000-10; PMID:26799775; http://dx.doi.org/10.1021/acs.jctc.5b01050

[71] Solar M, Buehler MJ. Comparative analysis of nanomechanics of protein filaments under lateral loading. Nanoscale 2012; 4:1177-83; PMID:22193831; http://dx.doi.org/10.1039/C1NR11260K

[72] Hawkins RJ, McLeish TC. Dynamic allostery of protein alpha helical coiled-coils. J Royal Soc Interface 2006; 3:125-38; http://dx.doi.org/10.1098/rsif.2005.0068

[73] Knowles TP, Fitzpatrick AW, Meehan S, Mott HR, Vendruscolo M, Dobson CM, Welland ME. Role of intermolecular forces in defining material properties of protein nanofibrils. Science 2007; 318:1900-3; PMID:18096801; http://dx.doi.org/10.1126/science.1150057

[74] Kol N, Adler-Abramovich L, Barlam D, Shneck RZ, Gazit E, Rousso I. Self-assembled peptide nanotubes are uniquely rigid bioinspired supramolecular structures.

Nano Lett 2005; 5:1343-6; PMID:16178235; http://dx.doi.org/10.1021/nl0505896

[75] Heim AJ, Matthews WG, Koob TJ. Determination of the elastic modulus of native collagen fibrils via radial indentation. Applied Phys Lett 2006; 89:181902; http://dx.doi.org/10.1063/1.2367660

[76] Perozo E, Kloda A, Cortes DM, Martinac B. Physical principles underlying the transduction of bilayer deformation forces during mechanosensitive channel gating. Nat Struct Biol 2002; 9:696-703; PMID:12172537; http://dx.doi.org/10.1038/nsb827

[77] Mukherjee N, Jose MD, Birkner JP, Walko M, Ingolfsson HI, Dimitrova A, Arnarez C, Marrink SJ, Koçer A. The activation mode of the mechanosensitive ion channel, MscL, by lysophosphatidylcholine differs from tension-induced gating. FASEB J 2014; 28:4292-302; PMID:24958207; http://dx.doi.org/10.1096/fj.14-251579

[78] Kloda A, Ghazi A, Martinac B. C-terminal charged cluster of MscL, RKKEE, functions as a pH sensor. Biophys J 2006; 90:1992-8; PMID:16387769; http://dx.doi.org/10.1529/biophysj.105.075481

[79] Lee G, Abdi K, Jiang Y, Michaely P, Bennett V, Marszalek PE. Nanospring behaviour of ankyrin repeats. Nature 2006; 440:246-9; PMID:16415852; http://dx.doi.org/10.1038/nature04437

[80] Ortiz V, Nielsen SO, Klein ML, Discher DE. Unfolding a linker between helical repeats. J Mol Biol 2005; 349:638-47; PMID:15896349;http://dx.doi.org/10.1016/j.jmb.2005.03.086

[81] Lu H, Schulten K. Steered molecular dynamics simulation of conformational changes of immunoglobulin domain I27 interprete atomic force microscopy observations. Chem Phys 1999; 247:141-53; http://dx.doi.org/10.1016/S0301-0104(99)00164-0

[82] Choe S, Sun SX. The elasticity of α-helices. J Chem Phys 2005; 122:244912; PMID:16035821; http://dx.doi.org/10.1063/1.1940048

[83] Sawada Y, Sokabe M. Molecular dynamics study on protein–water interplay in the mechanogating of the bacterial mechanosensitive channel MscL. Eur Biophys J 2015; 44:531-43; PMID:26233760; http://dx.doi.org/10.1007/s00249-015-1065-2

[84] Kocer A. Mechanisms of mechanosensing - mechanosensitive channels, function and re-engineering. Curr Opin Chem Biol 2015; 29:120-7; PMID:26610201; http://dx.doi.org/10.1016/j.cbpa.2015.10.006

[85] Anishkin A, Akitake B, Kamaraju K, Chiang CS, Sukharev S. Hydration properties of mechanosensitive channel pores define the energetics of gating. J Phys Condens Matter 2010; 22:454120; PMID:21339607; http://dx.doi.org/10.1088/0953-8984/22/45/454120

Supplementary Information

Supplementary Figures

Movie S1

In this simulation the end-most segment of the TM1 helix (the pore lining helix in MtMscL) has been stretched to obtain its mechanical response to the axial force. The TM1 helix has been first solvated and equilibrated in water for 10 ns before the start of the constant velocity (CV) SMD simulation. The movie shows a typical elongation of the TM1 helix up to 4 % strain.
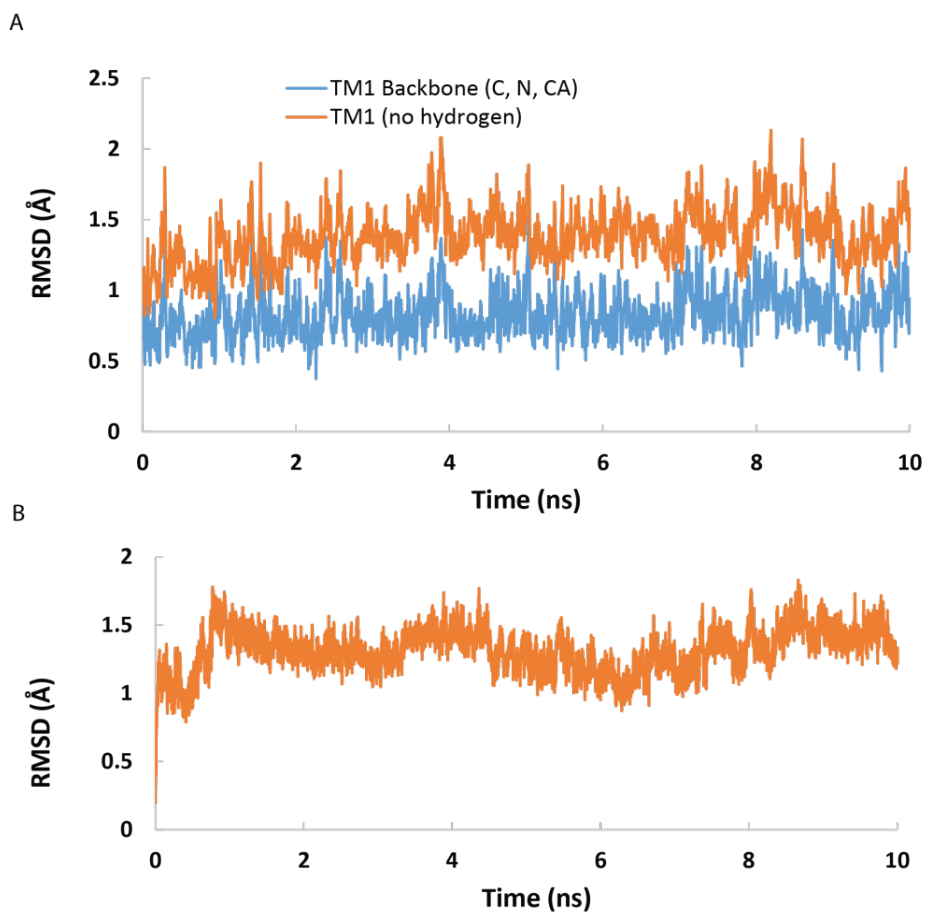
Figure S1. (A) Root Mean Square Deviation (RMSD) graph of the TM1 helix of MtMscL during equilibration in water using an NPT ensemble. This step has been done for all the helices in MtMscL and EcMscL before performing the pulling simulations. "Backbone carbons" and "no hydrogen" were plotted against the simulation time. All the helices are well equilibrated after 10 ns. **(B)** RMSD graph of TM1 helix during elongation using constant force (CF) method over 10 ns. As it is shown in this graph, the helix rapidly reaches the stable length (in ~ 1.0 ns).
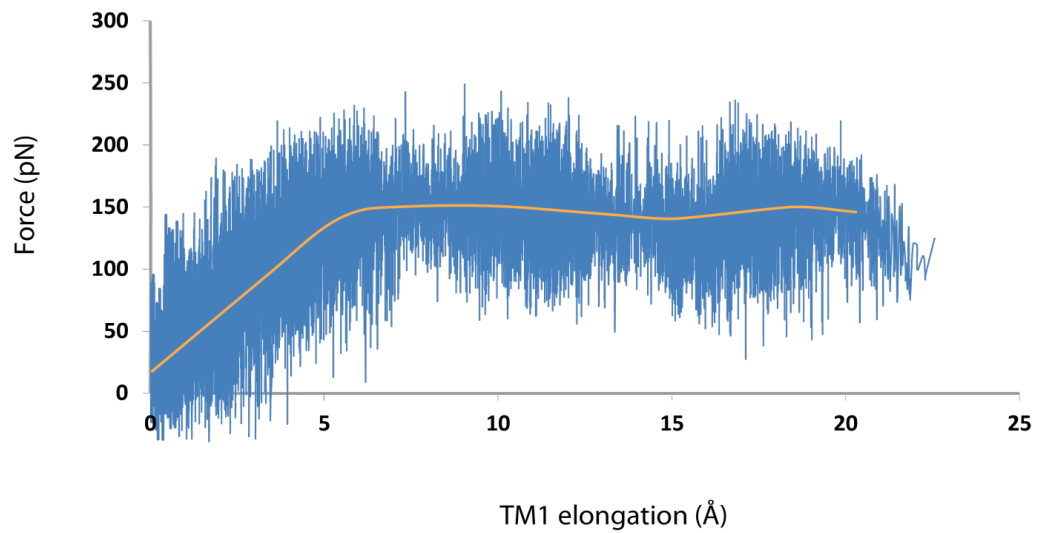
Figure S2. Typical force versus elongation curve of the TM1 helix of MtMscL using CV method. In order to better mimic the elongation rate which occurs during the MscL gating, the pulling rate here was much lower (5×10^{-4} Å/ps) compared to those used in previous studies. The dummy atom spring constant for this simulation was 0.6 kcal/mol/Å^2, and thus the helical elasticity constant, k, obtained from this curve is ~25 pN/Å (i.e. E=4.3 GPa).
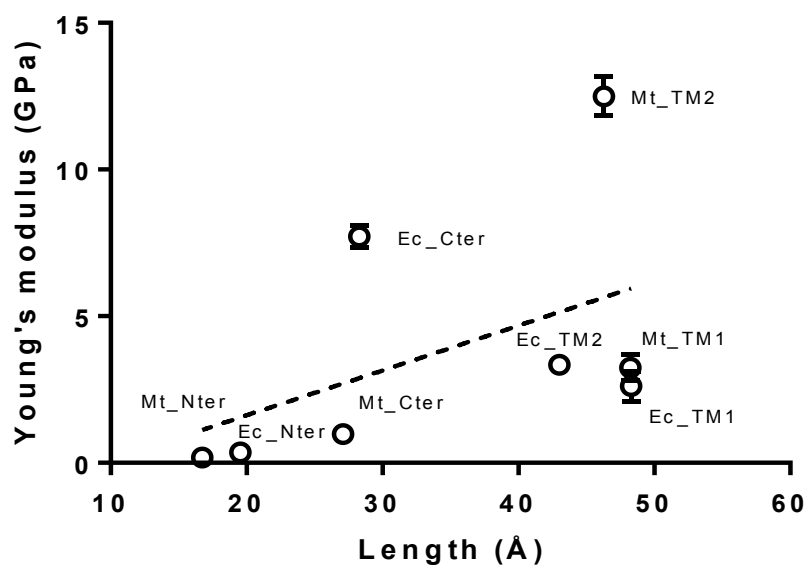
Figure S3. The figure shows weak correlation between the initial length of the helices and their Young's moduli. The obvious outliers were the TM2 helix in MtMscL (Mt_TM2) and the C-terminus in EcMscL (Ec_Cter). The Young's modulus values are Mean±SD for n=3.
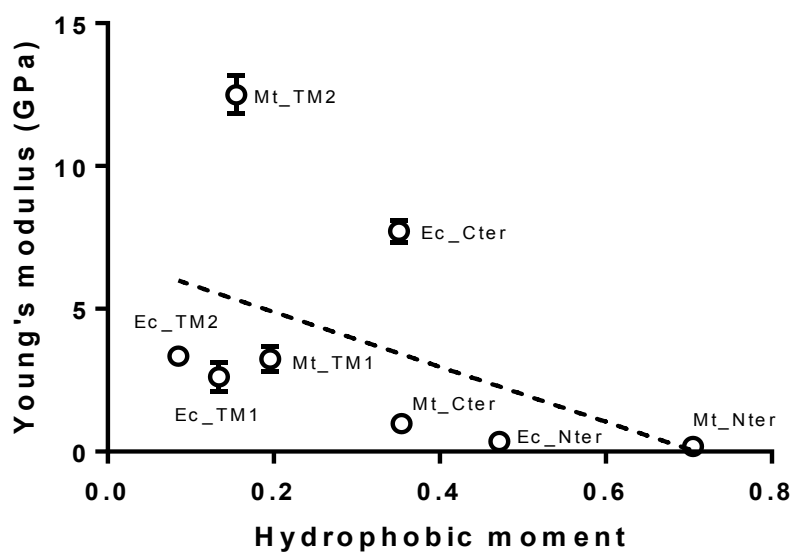
Figure S4. There is weak correlation between the hydrophobic moment of the helices and their Young's moduli. The outliers are again the TM2 helix in MtMscL (Mt_TM2) and the C-terminus in EcMscL (Ec_Cter). The Young's modulus values are Mean±SD for n=3.
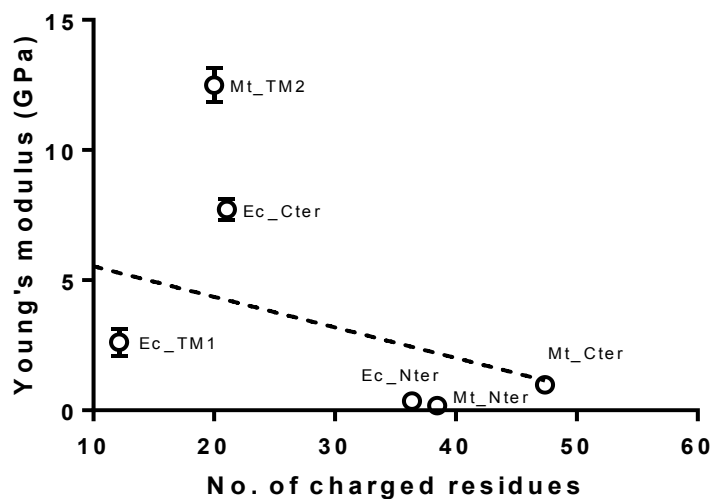
Figure S5. There is weak correlation between the number of charged residues on the helices and their Young's moduli. The outliers are the N-terminus of MtMscL (Mt_Nter), the TM2 helix in MtMscL (Mt_TM2) and the C-terminus in EcMscL (Ec_Cter). The Young's modulus values are Mean±SD for n=3.
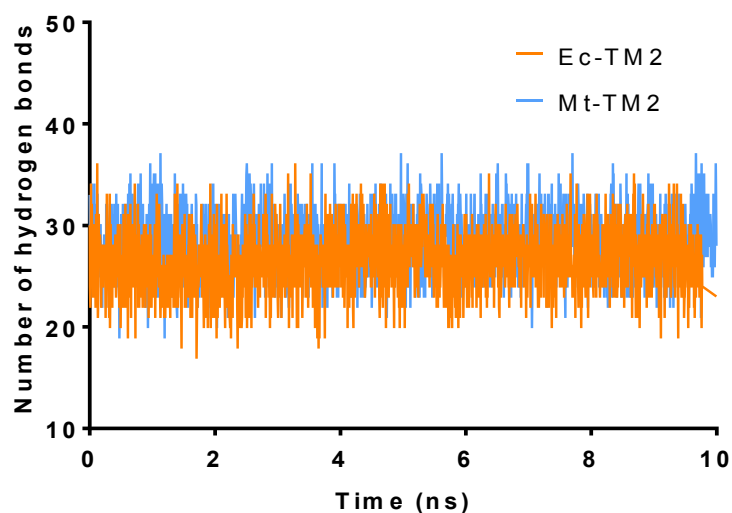
Figure S6. Comparing the number of hydrogen bonds of the TM2 helix of MtMscL with that of EcMscL during 10 ns of equilibration (NPT ensemble). The graph illustrates that the number of hydrogen bonds in both helices is similar. Hence, it is unlikely to correlate to the existing large difference between their Young's moduli.
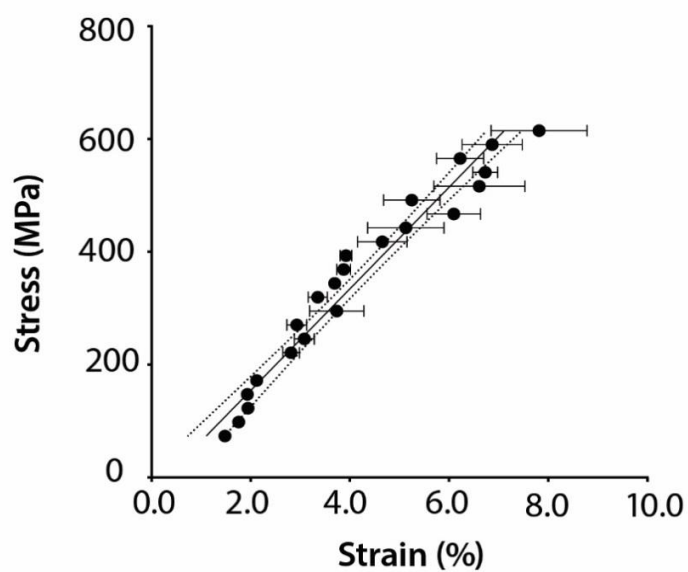
Figure S7. Typical stress-strain curve of the TM1 helix of MtMscL in vacuum using CF method. Compared to the corresponding stress-strain curve in water (Fig. 3C), the helix has much stiffer and more linear behaviour. The slop shows the Young's modulus which is $E=8.8\pm 0.2$ GPa (Mean±SEM, n=3).

Table S1. Amino acid sequence and helical information of all the α-helices in *Mycobacterium tuberculosis* MscL. We used HeliQuest for our bioinformatics calculations and VMD for our molecular measurements.

Mt	Helix (From res X to res Y)	Amino acid sequence	Length (Å)	Hydrophobicity <H>	Hydro phobic moment	Polar Residue % (n)	Charged Residue % (n)	Net charge (z)	Charged Residue
N-terminus	MET1 ARG11	MLKGFKEFLAR	16.7	0.45	0.71	45.4 (5)	36.3 (4)	2	LYS 2, ARG 1, GLU 1
TM1	ILE014 ILE046	IVDLAVAVVIGTAFTAL VTKFTDSIITPLINRI	48.2	0.75	0.20	36.4 (12)	12.1 (4)	0	LYS 1, ARG 1, ASP 2
TM2	LEU069 LYS100	LNVLLSAAINFFLIAFAV YFLVVLPYNTLRKK	46.3	0.84	0.16	25.0 (8)	9.4 (3)	3	LYS 2, ARG 1,
C-terminus	PRO106 THR124	PGDTQVVLLTEIRDLLA QT	27.1	0.49	0.35	52.6 (10)	21.0 (4)	-2	ARG 1, GLU 1, ASP 2

Table S2. Amino acid sequence and helical information of all the α-helices in *Escherichia coli* MscL. We used HeliQuest for our bioinformatics calculations and VMD for our molecular measurements.

Ec	Helix (From res X to res Y)	Amino acid sequence	Length (Å)	Hydrophobicity <H>	Hydrophobic moment	Polar Residue % (n)	Charged Residue % (n)	Net charge (z)	Charged Residue
N-terminus	MET1 ARG13	MSIIKEFREFAMR	19.5	0.43	0.47	46.1 (6)	38.5 (5)	1	LYS1, ARG2, GLU2
TM1	ASN015 LEU048	NVVDLAVGVIIG AAFGKIVSSLVAD IIMPPLGLL	48.3	0.80	0.13	29.4 (10)	8.8 (3)	-1	LYS1, ASP2
TM2	VAL77 LYS106	VFIQNVFDFLIVAFAIF MAIKLINKLNRKK	43.0	0.70	0.09	33.3 (10)	20.0 (6)	4	LYS4, ARG1, ASP1
C-terminus	LYS117 ARG135	KEEVLLTEIRDLLKEQN NR	28.3	0.07	0.35	68.4 (13)	47.4 (9)	-1	LYS2, ARG2, GLU4, ASP1

CHAPTER 5

Conclusions

5.1   Motivation and background

In this thesis, the basic principles and the significance of mechanotransduction processes in living cells were reviewed. The biological importance of the mechanical properties of lipid bilayers and stress distribution in them (lipid bilayer rheology) were also assessed. There is strong evidence from various studies that bilayer mechanical properties can modulate a large variety of membrane proteins, in particular MS channels. The simplest example to date being bilayer thickness, which affects MscL to a much greater extent than MscS. Membrane composition alters the lateral transbilayer pressure profile, bilayer thickness, line tension, surface tension, membrane spontaneous curvature, area compressibility modulus, bending stiffness and first and second moments of the pressure profile. All these physical properties are directly related to the lateral pressure profile and bilayer thickness. The parameter which has the greatest impact on channel function depends on the type of MS channel being mechanically stressed (i.e. shape of the pore, hydrophobic length, charged and non-bonded interactions on the interface of protein and lipid bilayer and solution).

5.2   Outcomes

After appraising the methods used in the literature to characterize bilayers, the evident consensus is that there is discrepancy between the measured mechanical properties of lipid bilayers and their material reality. The pros and cons of these techniques, specifically the micropipette aspiration (MA) method as a "gold standard method" used for bilayer material characterization, were discussed. Thus, the possible variables that can modify these paradigms, which are of importance for the function of MS channels

were investigated in Chapter 2. Moreover, the way that mechanical forces are transmitted to mechanosensitive channels through the lipid bilayer has been investigated. The main outcomes of these studies are listed below:

a) The mechanical properties of azolectin, as a mixed lipid, were characterised.

b) Two new analytical models were introduced for measuring the mechanical properties of lipid bilayers, resulting in much smaller values for the bilayer elasticity (i.e. $K_a \cong 15$ mN/m compared to 112 mN/m). In other words this means that lipid bilayers are much softer than previously determined by MA method.

c) Excised liposome patch fluorometry was proposed to be used as a new experimental paradigm for the characterization of mechanical properties of lipid bilayers.

d) Stress-strain development in biological membranes was studied (membrane rheology). Stress analysis of the membrane patch revealed marked stress heterogeneity in the patch area previously thought to be uniform.

e) FE analysis showed that Laplace's equation leads to an under/overestimation of bilayer tension depending on patch configuration and vesicle radius.

f) In the excised configuration, the maximum membrane stress of the outer monolayer was at least 30% greater than that of the inner monolayer. In contrast, in the cell-attached configuration there was a negligible difference between the membrane stresses of both monolayers.

In addition, different gating paradigms for presently identified MS channels including force-from-lipids and force-from-filament were discussed. The mechanosensitive channel of large conductance MscL, acts as an osmoprotective valve in bacteria where it gates in response to membrane tension due to cellular turgor. As a prototypical mechanosensitive (MS) channel, MscL has provided many insights into the basic biophysical principles of mechanosensory transduction. Moving from membrane mechanics to channel structural dynamics, in Chapter 3, a combination of experiment and simulation was used including site-directed spin labelling electron paramagnetic resonance (SDSL EPR) spectroscopy (In collaboration with Perozo Lab, University of Chicago), patch-clamp electrophysiology, molecular dynamics (MD) simulation and

finite element (FE) modelling to study the gating cycle of MscL. The main outcomes were:

a) Lipids tightly interact with the N-terminus which sits at the lipid-water interface.

b) Removal of the N-terminus or extending the Glycine linker between the N-terminus and TM1 helices, results in the channel becoming less sensitive to membrane tension. These mutations and truncations also reduced the cell survival shown under hypo-osmotic shocks.

c) The N-terminus is the main cytoplasmic mechanosensor in MscL.

d) Upon membrane stretch, the lipids move away, but they also drag the N-terminus and the pore lining helix TM1 with it.

e) The role of the MscL amphipathic N-terminus indicates a blueprint for bilayer-mediated gating of mechanosensitive channels.

Since the lipid environment plays a significant role in the function of membrane proteins, it is important to better understand how it controls membrane protein dynamics, particularly in MS channels. The increasing interest in using MscL as a nanosensor and/or a nanovalve makes understanding of the lipid bilayer-protein interactions increasingly important. For this, the mechanical properties of the channel itself, as it is the protein scaffold, must be measured. To do so, over 200 steered MD simulations were performed using constant-velocity (CV) and constant-force (CF) methods to accurately measure the mechanical properties of the alpha helices in EcMscL and MtMscL homologues. First, it was shown that the CF method is more accurate in estimating the Young's moduli of different helices compared to the CV method. The pulling rates usually used in the CV method, although in the order of Å/ps, are much faster than the equilibrium rates. Furthermore, the selection of a spring constant adds a degree of freedom that makes interpretation of the data more difficult than the CF method. Apart from this, the CV method has the advantage that it is considerably less expensive computationally than the CF method. Using the CF method, it was estimated that the Young's moduli of the MscL helices are between 0.2 and 12.5 GPa, where the TM2 helix is the stiffest and the N-terminus is the softest helix. It was also shown that water softens the TM1 (the pore-forming) helix with a much greater effect on the TM1 in MtMscL.

5.3   Future directions

The rheological studies of lipid bilayers, presented in this thesis, imply that lipid membranes should be seen as a viable "drugable" target for channelopathies as well as other membrane protein associated diseases. This is because of their central role in the structural integrity and function of membrane proteins, in particular MS channels. Meaning that in order to regulate the function of various membrane proteins, including MS channels, the lipid bilayer can be modulated externally by compounds such as surface active agents or drugs rather than direct targeting of membrane proteins themselves.

Given these findings and the collective data available in the literature, hydrophobic pockets such as those identified in MscL are widely present in other MS channels such as MscS, TRP, K_{2P} and likely Piezo channels. It is possible that in all these inter-subunit pockets, there is a horizontal helix (similar to the MscL N-terminus), which is directly linked to the pore-lining helix, usually via a Gly hinge. This is likely the case at least in K2P channels, where the C-terminal helix seems to be important in mechanically driven gating. Furthermore, it is crucial to investigate whether similar structures play a mechanosensitive role in Piezo and TRP channels. Knowing such a structural blueprint of MS channels is imperative for identification, discovery and modulation of MS channels.

MscL is an excellent candidate to be used as a nanovalve in liposomal drug delivery systems and several groups have already investigated this. It was determined that the N-terminus of MscL is the main mechanosensor at the cytoplasmic side of the cell membrane. This short amphipathic helix is located at the lipid-solvent interface hence it is easily accessible from the cytoplasm for attaching it to auxiliary actuators such as nanoparticles. However, using molecular dynamics, it was shown that this helix has a relatively low stiffness compared to the other helices, which means that at high forces required for gating of MscL, the N-terminal helix unravels. Therefore, it is suggested to double or triple the N-terminal helix length for two reasons: i) to increase the efficiency of force transmission to the pore (i.e. sensitizing the channel) and ii) to increase the mechanical stiffness of the N-terminus.

Also, given our recent inclusive understanding of the intricacies of MscL gating, and the knowledge of the movement of each MscL helix during its gating cycle as well as their mechanical resilience, MscL seems to be a worthy candidate to be used as a molecular tension sensor in cell membranes. This is because of its high structural flexibility despite its simple structure and large structural deformation and conformational changes in response to membrane tension. For this purpose, MscL needs to be coupled with, for example, a FRET pair. This could be a tool for the long-standing need in current mechanobiology to provide a molecular probe that can accurately measure membrane tension in response to different stimuli.